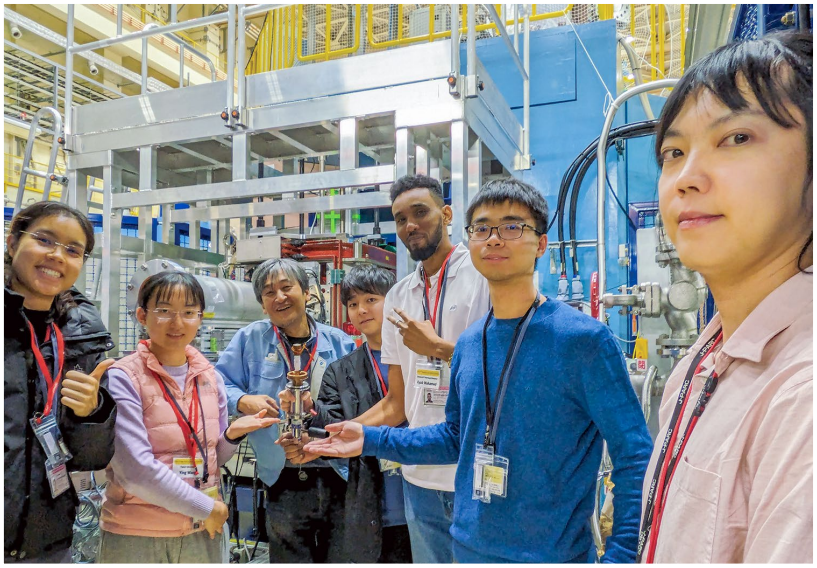

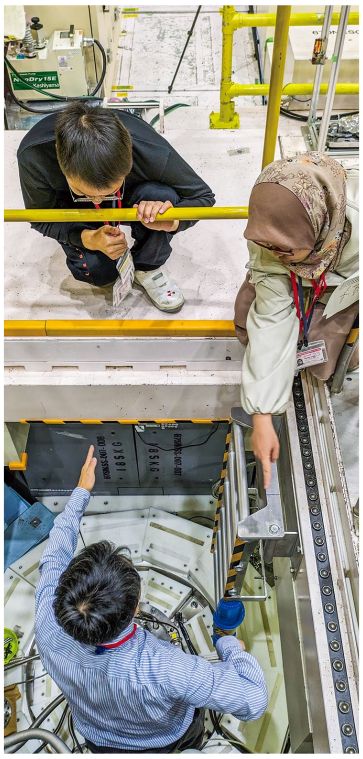

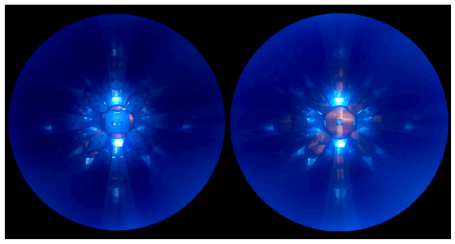

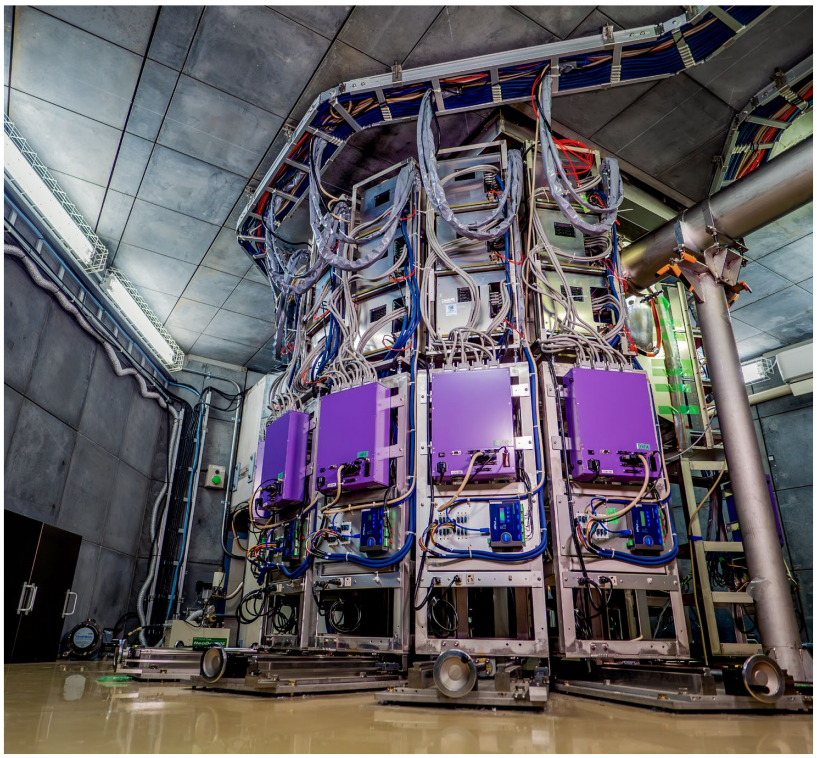

J-PARC

ANNUAL REPORT 2023

Vol.2: Materials and Life Science Experimental Facility

MLF ANNUAL REPORT

Cover photographs

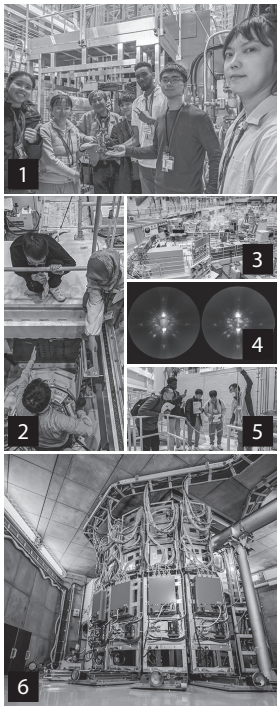

1 : Hands on experiment at the 7th Neutron and Muon School (Muon S1)

2 : Hands on experiment at the 7th Neutron and Muon School (BL01)

3 : MLF Experimental Hall-2

4 : The vacuum duct and slits at Muon D line

5 : Hands on experiment at the 7th Neutron and Muon School (BL02)

6 : Single crystal neutron diffractometer BL18 SENJU

J-PARC MLF
Materials and Life Science Division
J-PARC Center
https://mlfinfo.jp/en

J-PARC was jointly constructed and is now operated by the High Energy Accelerator Research Organization (KEK) and the Japan Atomic Energy Agency (JAEA).

Comprehensive Research Organization for Science and Society
https://neutron.cross.or.jp/en

J-PARC 24-02

Preface

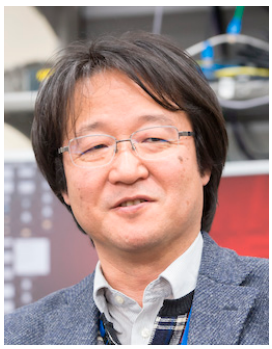

Toshiya Otomo
Division Head of Materials and Life Science Division, MLF

In FY2023, we almost reached the designed proton beam power, 1 MW, by developing neutron and muon targets and proton beam transports and especially by securing one-year lifetime of the neutron target vessel. Progress was also made in the upgrades and development of detectors, neutron polarization devices and the new ultra-slow muon beamline. More than 250 papers were published in 2023 through 350 experiments, with results in various fields ranging from fundamental physics to industrial applications. These activities and outcomes will be covered in detail in this annual report. Also, efforts to expand the user community have been made through hosting the international annual school for scientists from the younger generations, the annual meeting of the neutron industrial application, the 4th International Training School on Sample Environment at the Scattering Facilities ISSE School and the 11th Workshop on Neutron Wavelength-Dependent Imaging (NEUWAVE-11).

On the other hand, because of accidents and malfunctions, the beamtime of the user program was reduced: 1) two fire accidents in the Hadron Facility and the Main Ring occurred during the 2023A period, 2) malfunctions of the cryogenic hydrogen system of the MLF moderator system occurred shortly before the launch of 2023B. The availabilities of the beam operation for the user program in FY2023 were 64.6% in 2023A and 77.1% in 2023B. The rising cost of electricity remains a pressure that causes reduction of the operating hours. It is critical for the MLF to improve its robustness by countering degradation, securing the operating budget, and ensuring the long-term availability of human resources.

The MLF will continue to strive for robustness, accompanied by continuous improvement of the MLF to produce more results with greater scientific impact.

Materials and Life Science Division, Japan Proton Accelerator Research Complex
https://mlfinfo.jp/en

Preface

Mitsuhiro Shibayama
Director, CROSS

The Comprehensive Research Organization for Science and Society (CROSS), a partner institution of the Materials and Life Science Experimental Facility (MLF), is honored to release the J-PARC MLF ANNUAL REPORT 2023 (MLF-AR2023), which includes sections on R&D Highlights, Neutron Sources, Neutron Science, Muon Science and more. The Neutron Science and Technology Center (NSTC) of the CROSS is a registered organization of the J-PARC's Specific Neutron Beamline Facility, appointed by the Japanese government in 2011. It supports the activities of the 7 public beamlines of the MLF (BL01 4SEASONS, BL02 DNA, BL11 PLANET, BL15 TAIKAN, BL17 SHARAKU, BL18 SENJU, and BL22 RADEN), provides high-quality user support to the MLF users, both academic and industrial researchers, and promotes the use of the facility. The CROSS established a new base, the Neutron Industrial Application Promotion Center (NIAPC) in April 2023, and from 2023, this center is in charge of the two beamlines of Ibaraki Prefecture (BL03 iBIX and BL20 iMATERIA).

In FY2023, the beamtime was shortened from 140 to 114 days due to several accidents. Apart from those interruptions, the neutron beam at the MLF was stably operated. The total numbers of (short term) neutron proposals submitted and accepted in the two proposal rounds in FY2023 were 587 and 318, respectively, and those for the Public Beamlines were 268 and 158, respectively. As of the outcome, 200 scientific papers (excluding proceedings) were published from the MLF in 2023, among which were 71 papers from the Public Beamlines. The details are included in the Research and Development Highlights collected in this volume. The numbers of press releases were 25 from the MLF and 6 from the Public Beamlines, and 3 from the Ibaraki Prefecture Beamlines. These numbers illustrate the high activities of the Public Beamlines and the MLF, which have been used by a wide range of users from academia and various industries. The special program for new users "New User Promotion (NUP)", which started in 2016, continued its operation in 2023, and 9 NUP neutron users conducted experiments at the MLF.

Regarding public relations, "J-JOIN", operated by the J-PARC MLF, Ibaraki Prefecture, JRR-3 (JAEA and the University of Tokyo), and the CROSS, welcomes potential users. (https://jrr3ring.jaea.go.jp/jjoin/index_en.php).

I hope this Annual Report will provide useful information about the current status of the MLF operations and recent scientific achievements, the technical R&D reports, and so on. On behalf of the CROSS, I sincerely welcome your visit to the MLF.

Neutron Science and Technology Center, Comprehensive Research Organization for Science and Society
https://neutron.cross.or.jp/en

Contents

Research and Development Highlights

Neutron Source

Neutron Science

Muon Science

MLF Safety

MLF Operations in 2023

Organization Chart

Organization Chart of J-PARC Center

- Director, J-PARC Center
  - Deputy Director (JAEA, KEK, Safety)
    - Safety Division
  - Accelerator Division
  - Materials & Life Science Division
    - Neutron Source Section
    - Neutron Science Section
    - Neutron Instrumentation Section
    - Muon Science Section
    - Technology Development Section
  - Particle & Nuclear Physics Division
  - Nuclear Transmutation Division
  - Cryogenics Section
  - Information System Section
  - Public Relations Section
  - Facility Engineering Section
  - Administration and Operations Support Division
    - Users Office

Organization Chart of CROSS

CROSS is "Registered Institution for facility Use Promotion" for the public-access neutron beam facilities at J-PARC.

- President
  - CROSS Head Office
  - Research Center for Science and Society
  - Neutron Science and Technology Center
    - Director, Neutron Science and Technology Center
      - Science Coordinators
      - R&D Division
      - Utilization Promotion Division
      - Industrial Collaboration Promotion Division
      - Safety Division
      - Administration Division
  - Neutron Industrial Application Promotion Center
  - New Business Creation Division

The Role of CROSS

Under the terms of the legislation that supports the Public Neutron Beam Facility, CROSS is entrusted with specific responsibilities. In practical terms, the core functions of CROSS can be summarized as follows:

- *Proposal Selection and Beamtime Allocation on the Public Beamlines*
- *User Support on the Public Beamlines*
- *Establishment of an Information Resource for Facility Users*
- *Outreach and Facility Utilization Promotion*
- *Contract Beamline Assessment and Selection*

J-PARC Map

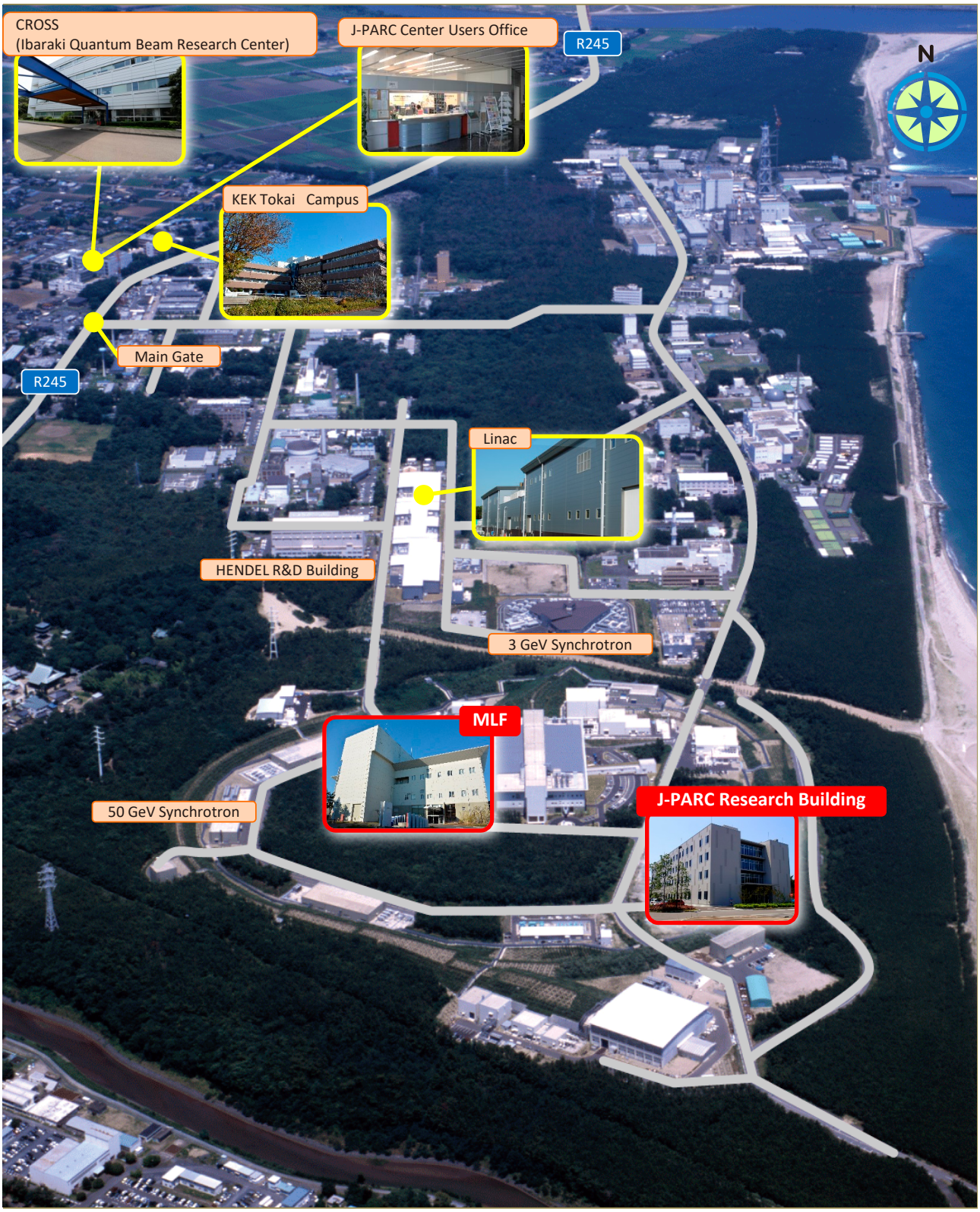
CROSS
(Ibaraki Quantum Beam Research Center)
J-PARC Center Users Office
R245
N
KEK Tokai Campus
Main Gate
R245
Linac
HENDEL R&D Building
3 GeV Synchrotron
MLF
J-PARC Research Building
50 GeV Synchrotron

Muon and Neutron Instruments

Muon Source

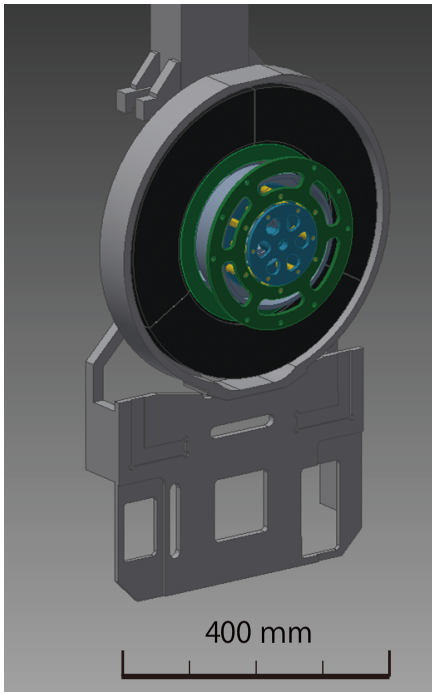

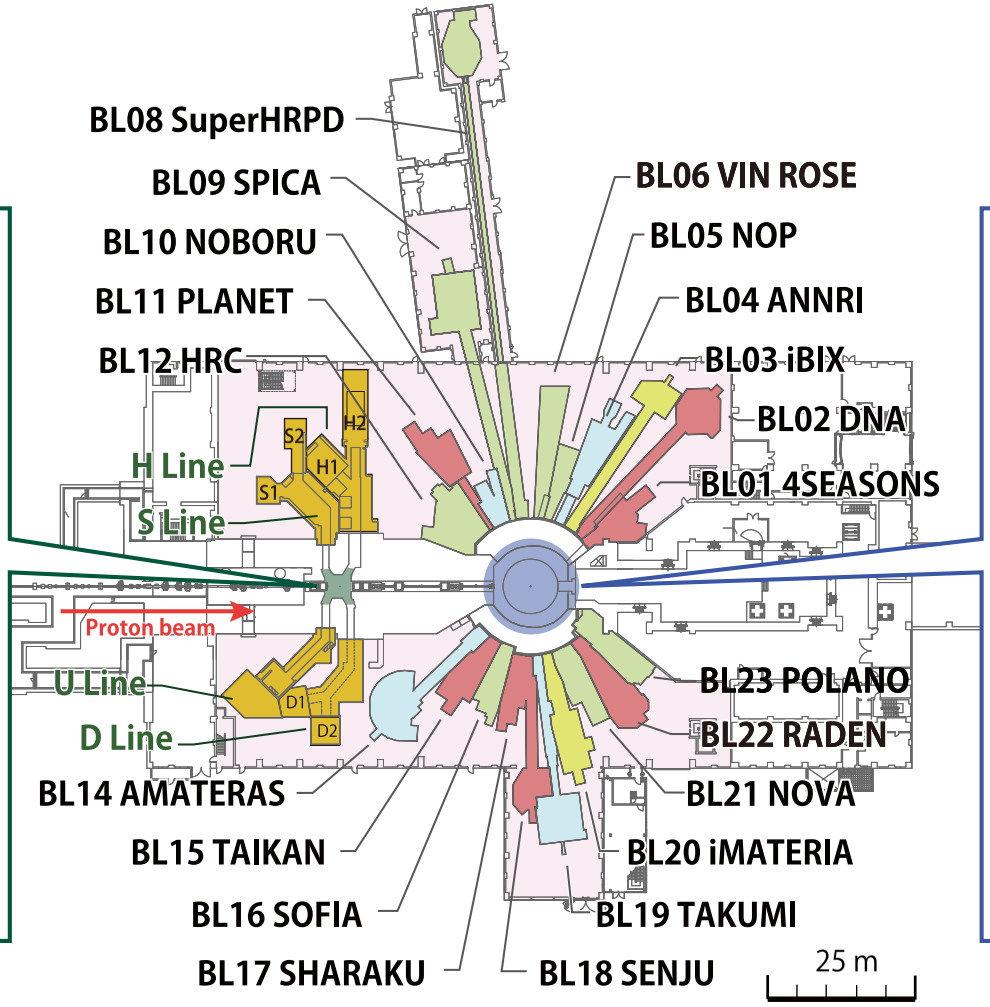

Neutron Source

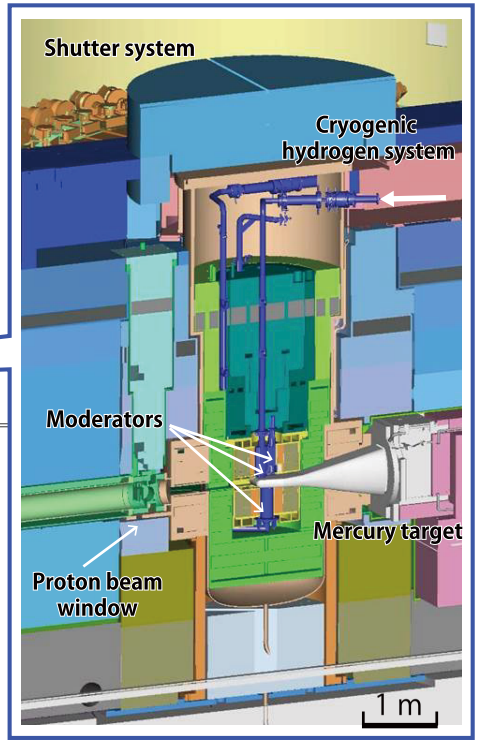

Muon Instruments

Neutron Instruments

JAEA

KEK

Public beam lines

Ibaraki Pref.

As of March 2023

Research and Development Highlights

Observation of Topological Magnon Polarons in a Multiferroic Material

1. Introduction

Magnons and phonons, quanta of spin waves and lattice vibrations respectively, constitute two fundamental collective excitations in ordered magnets. While they typically propagate independently, under conditions of strong magnon-phonon coupling, they can hybridize to form novel elementary excitations known as magnon polarons (Fig. 1(a)). Due to their hybrid nature, magnon polarons play a crucial role in various spintronic and magnetic phenomena. However, despite long-standing experimental efforts, the direct spectroscopic evidence of their existence has been elusive.

$Fe_2Mo_3O_8$ (FMO) is a type-I multiferroic material with an antiferromagnetic ordering temperature $T_N \sim 60$ K. Previous studies have reported a number of intriguing phenomena in FMO, such as the giant thermal Hall effect [1], colossal linear magnetoelectricity [2] and electromagnon resonance [3], all of which suggest a strong coupling between spin and lattice degrees of freedom. These properties make FMO a promising platform for probing the long-sought magnon polarons. Consequently, we conducted inelastic neutron scattering (INS) experiments on high-quality single crystals of FMO on 4SEASONS of J-PARC.

2. Anomalous phonons at low energies

Figure 1(c) shows the full profile of excitation spectra along the [100] direction in FMO at 6 K. In the same energy and momentum window, three types of excitations are observed: i) Magnons appear at higher energies, around 11 and 14 meV. These excitations exhibit strong scattering intensities but weak dispersion. They disappear just above T_N and correspond to two doubly degenerate magnons, consistent with the linear spin-wave theory. ii) Phonons stem from lower energies, and in contrast to magnons, they display weak scattering intensities but strong dispersion. iii) Magnon polarons form near the anticrossing regions between the magnon and phonon bands.

We first discuss the anomalous behavior of the phonons. A closer view of a specific low-energy phonon mode at 6 K is shown in Figs. 1(d) and (f). This mode has an onset energy around 5.3 meV along the [100] direction (Fig. 1(d)), corresponding to the maximum excitation energy along the [001] direction (Fig. 1(f)), suggesting a saddle point in the phonon spectra. At 100 K, these excitations become invisible at small momenta (Fig. 1(e)) yet remain observable at larger momenta (Fig. 1(g)). This anomalous temperature-dependent

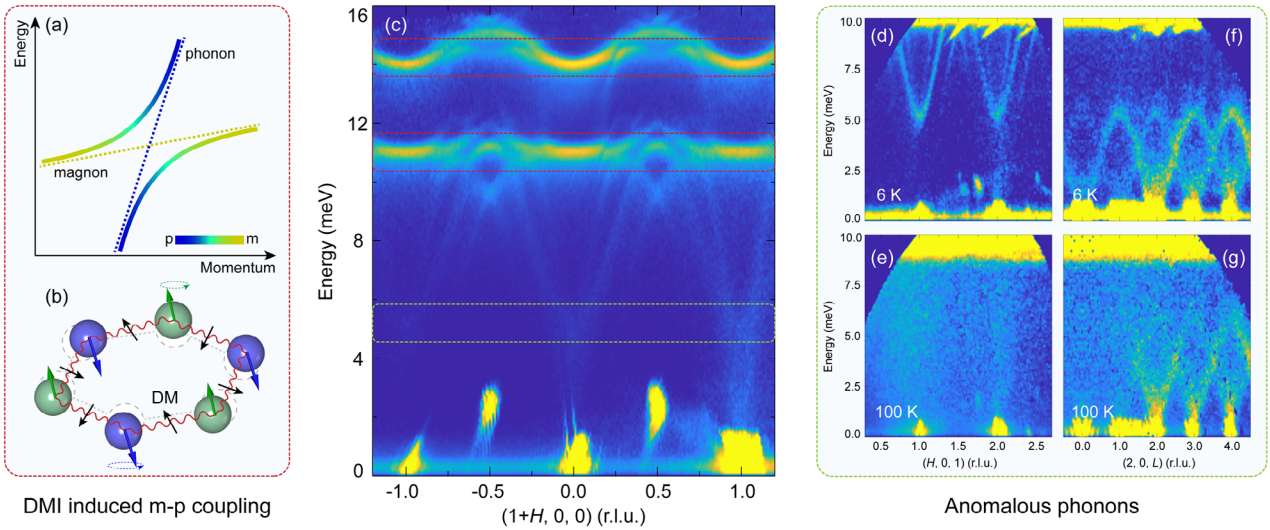

Figure 1. (a) Schematic of the magnon-polaron bands. (b) Schematic of DMI-induced magnon-phonon coupling in FMO. (c) INS results of the excitation spectra measured at 6 K along [100] direction. (d) and (e) Low-energy phonon spectra along [100] direction at 6 K and 100 K. (f) and (g) Same as in (d) and (e) but measured for [001] direction.

behavior suggests that these low-energy phonons acquire some spin components through the strong magnon-phonon coupling, leading to additional magnetic scattering intensities at small momenta at 6 K. However, at 100 K, as the magnons collapse, phonons recover their original properties and can only be observed at large momenta, where the intrinsic dynamic structure factors are sufficiently large.

This interpretation is further supported by our parallel research employing magneto-Raman measurements, which reveal that the zone-center phonons, with an energy of approximately 5.3 meV, correspond to a pair of low-lying chiral phonons carrying substantial magnetic moments of up to 0.68 μ_B [4].

3. Formation of magnon polarons

The appearance of phonons at small momenta together with magnons enables us to examine the interaction effects between them. We now focus on the regions where the weak and dispersive phonons tend to intersect with the intense and relatively flat magnons (Fig. 1(c)). A series of constant-energy scans along the [100] direction is plotted for higher (Figs. 2(a)–(c)) and lower (Figs. 2(e)–(g)) anticrossing regions. In each panel, two sets of excitations on either side of the origin (zone center) are observed, representing two magnon-polaron bands separated by a gap. As the energy increases, a shift in the peaks is accompanied by a transfer of spectral weight between the two magnon-polaron bands, indicating magnon-phonon interconversion during propagation.

To better clarify this behavior, we extract relative peak position (Δq) and the ratio of the spectral weight for each band to the total spectral weight of the two magnon-polaron bands for various energies and plot them in Figs. 2(d) and (h) for the higher and lower

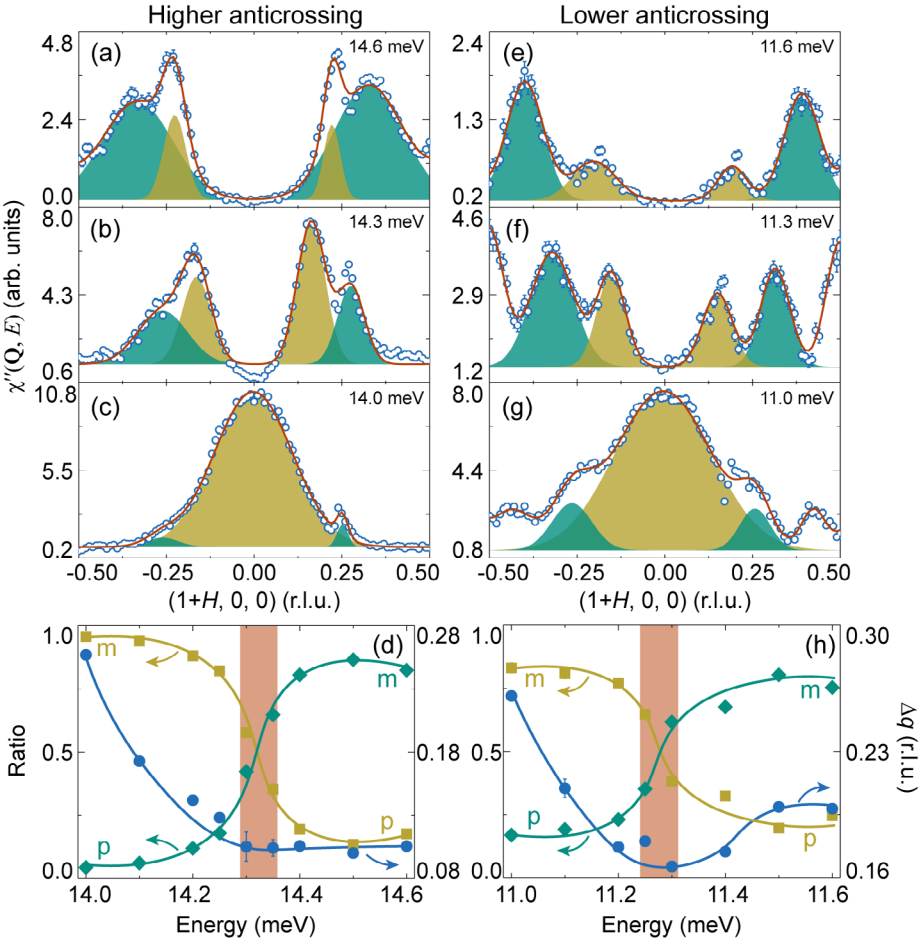

Figure 2. (a)–(c) and (e)–(g) Constant-energy scans at different energies near the higher and lower anticrossing regions, respectively. (d) and (h) Ratio of the extracted spectral weight (left axis) and the peak interval (right axis) as a function of energy for the higher and lower anticrossing regions.

anticrossing regions, respectively. From the perspective of scattering intensities, it is found that approaching the anticrossing from low energies, the two magnon-polaron bands are of primarily magnonic (m) and phononic (p) natures respectively. At the anticrossing point, where Δq reaches its minimum, the strongest hybridization happens so that the m and p components become comparable. Across this position, the main components of the two bands are reversed, and so are their relative intensity ratios. These results elaborate the band inversion between the original magnon and phonon bands. Together with the observed gaps in the dispersions (Fig. 1(c)), these constitute the hallmarks for the magnon polarons.

We attribute the formation of magnon polarons to the Dzyaloshinskii–Moriya interaction (DMI)-induced magnon-phonon coupling, which give rise to the coherent hybridizations between in-plane phonons and magnons, as illustrated in Fig. 1(b). Additionally, we demonstrate that the magnon-polaron excitations are topologically nontrivial, consistent with the observed band inversion between magnons and phonons (more details are available in Ref. [5]).

4. Summary

The strong DMI-induced magnon-phonon coupling in FMO leads to the formation of topological magnon polarons in the magnon-phonon resonant region. Additionally, it gives rise to other intriguing phenomena even away from the anticrossing region, such as the phonon magnetic moments [4], electric-dipole-active excitations [3], and the emergence of thermal Hall effect [1]. These results, which show strong magnon-phonon coupling and hybrid excitations in FMO, suggest that it could be a prime candidate in developing phonon-controllable spintronic devices. This work has been published in Ref. [5].

References

[1] T. Ideue et al., Nat. Mater. **16**, 797 (2017).
[2] Y. Chang et al., Phys. Rev. Lett. **131**, 136701 (2023).
[3] T. Kurumaji et al., Phys. Rev. B, **95**, 020405 (2017).
[4] F. Wu et al., Nat. Phys. **19**, 1868 (2023).
[5] S. Bao et al., Nat. Commun. **14**, 6093 (2023).

S. Bao[1], Z.-L. Gu[1], Y. Shangguan[1], Z. Huang[1], J. Liao[1], X. Zhao[1], B. Zhang[1], Z.-Y. Dong[2], W. Wang[3], R. Kajimoto[4], M. Nakamura[4], T. Fennell[5], S.-L. Yu[1], J.-X. Li[1], and J. Wen[1]

[1]National Laboratory of Solid State Microstructures and Department of Physics, Nanjing University; [2]Department of Applied Physics, Nanjing University of Science and Technology; [3]School of Science, Nanjing University of Posts and Telecommunications; [4]Neutron Science Section, Materials and Life Science Division, J-PARC Center; [5]Laboratory for Neutron Scattering and Imaging, PSI

Quasielastic Neutron Scattering Probing H^- Dynamics in the H^- Conductors $LaH_{3-2x}O_x$

1. Introduction

Hydrogen is widely known to exhibit very large diffusion coefficients in metals. For example, the diffusion coefficient of hydrogen in a body-centered cubic Fe metal reaches $10^{-9} \sim 10^{-8}$ m^2/s around 300 K, which is comparable with atomic diffusion in liquids at room temperature [1]. Understanding of the large hydrogen diffusion coefficients in metals is not only essential for the industrial use of materials, as exemplified by hydrogen embrittlement (hydrogen-induced cracking) and hydrogen storage etc., but also has attracted fundamental interest in anomalous hydrogen diffusion.

In metals with low solid solubility of hydrogen, such as Cu, Ni, and Fe, hydrogen migrates through interstitial spaces, specifically, a tetrahedral site or an octahedral site composed of metal frameworks. In case of metals with high hydrogen solubility, hydrogen gradually fills the interstitial spaces with increasing concentration of hydrogen, and then, forms stoichiometric hydrides, e.g. TiH_2 and ZrH_2. As a result, the hydrogen diffusion coefficient at a given temperature goes to zero when the interstitial spaces are fully occupied. Strangely, in contrast, a diffusion coefficient of hydrogen in $LaH_{x'}$ ($2 < x' < 3$) continues to increase with increasing x'. Although a "collective" motion of hydrogens is suggested for the origin of these anomalous diffusions, much remains unclear about microscopic hydrogen dynamics in $LaH_{x'}$.

Recently, Fukui et al. reported high conductivities of hydrogen ions in a series of oxyhydrides $LaH_{3-2x}O_x$ ($x \neq 0$), which are derivative materials of LaH_3 by a partial substitution of O^{2-} ions for hydrogen ions (see Fig. 1) [2, 3]. They have also established that conductive hydrogen in these materials is not a proton H^+, but a hydride ion H^-. Because the diffusion coefficients of H^- in these materials, especially with $x < 0.25$, are comparable to those in $LaH_{x'}$, a similar H^- conduction mechanism is expected. Elucidation of unique H^- dynamics in $LaH_{x'}$ and $LaH_{3-2x}O_x$ will provide useful guidelines for designing other H^- conductive materials, which have attracted growing interest in their potential to realize novel energy storage and conversion devices with high energy densities [4].

To reveal the unique dynamics of H^- in $LaH_{x'}$ and $LaH_{3-2x}O_x$, we performed quasielastic neutron scattering (QENS) experiments [5].

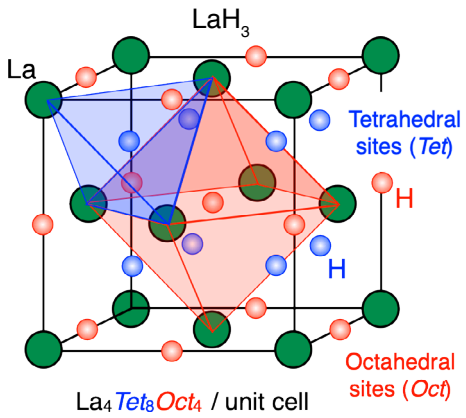

Figure 1. Crystal structure of $LaH_{3-2x}O_x$ [5]. There are two kinds of anion sites, the tetrahedral (Tet) and the octahedral (Oct) sites, center of the La_4 tetrahedron and La_6 octahedron, respectively. A partial substitution of O^{2-} for H^- introduces a vacant site to preserve charge neutrality.

2. Experiments

The QENS measurements with the time-of-flight method were performed using the near-backscattering spectrometer with high energy resolution, DNA, installed at BL02 in MLF, J-PARC. The final neutron energy of 2.08 meV was selected using Si (111) analyzers. The frequencies of the pulse-shaping choppers and their slit sizes were set to 225 Hz and 3 cm × 3 cm, respectively, which led to an energy resolution of 3.6 μeV at $E = 0$ eV (full width at half maximum) and an observable energy range of -40 μeV $< E <$ 100 μeV. The resolution functions of each sample were measured below 10 K. All the samples used in this study were in polycrystalline powder form. The details of the sample preparation for the QENS measurements are described in Ref. [5].

3. Results and discussion

Figure 2(a) shows the typical neutron scattering spectra of the end member $LaH_{3-\delta}$ ($\delta < 0.09$). We successfully identified two kinds of microscopic H^- dynamics in $LaH_{3-\delta}$; a jump diffusion and a localized motion. These dynamics are corroborated by our molecular dynamical simulations. Although the QENS intensities are smaller, the H^- dynamics in $LaH_{3-2x}O_x$ ($x \neq 0$) look similar to that in $LaH_{3-\delta}$ according to our mode distribution analyses.

As shown in Fig. 2(b), a diffusion length l increases with increasing a temperature T. Because the length between the Tet and (adjacent) Oct sites is the shortest

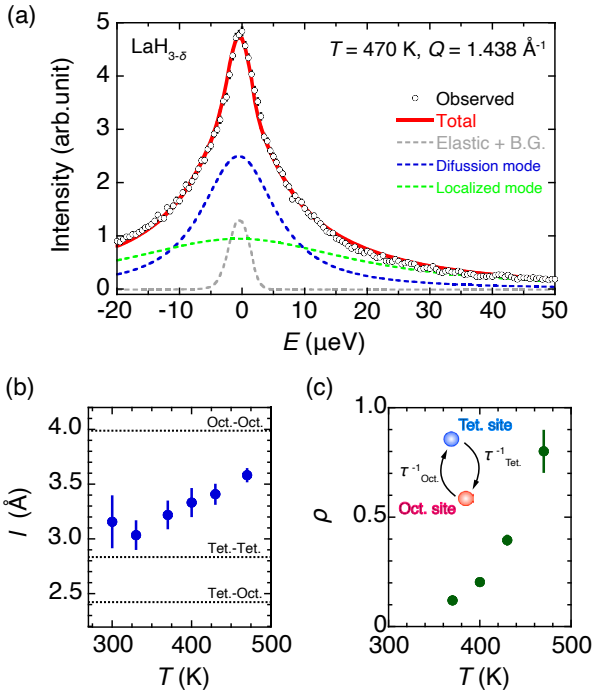

Figure 2. (a) Typical fitting results of the neutron scattering spectra for $LaH_{3-\delta}$ at 470 K [5]. (b) T dependence of the jump length l in the diffusion mode. (c) T dependence of a ratio, $\rho \equiv \tau_{Oct} / \tau_{Tet}$ of the residence times τ_{Oct} and τ_{Tet} in the localized mode.

in $LaH_{3-\delta}$, we can assume that H^- ions always migrate through this path as an elementary jump process. A possible interpretation of the increase of l is as follows: at lower T, the H^- migration that looks like the jump between the Tet sites is dominant in the time scale of our measurement, although the elementary jump process is the jump between the Tet and (adjacent) Oct sites; with increasing T, the proportion of the H^- migration that looks like the jump between the Oct sites increases owing to the growing thermal fluctuation.

The localized motion can be described by a model of a back and forth jump between neighboring tetrahedral and octahedral sites. As shown in Fig. 2(c), a ratio of mean residence times, ρ, increases with increasing T. Because the residence time at the Tet sites τ_{Tet} is longer than that at the Oct sites τ_{Oct}, ρ is defined as τ_{Oct} / τ_{Tet}. This indicates that at lower T, τ_{Tet} is much longer than τ_{Oct}, while with increasing T, they become similar to each other due to the growing thermal fluctuation.

We consider these dynamics to be interconnected with each other, based on the common elementary jump process between the Tet and adjacent Oct sites, and their relatively close activation energies (159 meV for the diffusion mode and 101 meV for the localized mode). In addition, our QENS results indicate that the key factor in the high mobility of H^- in $LaH_{3-2x}O_x$ is a concentration of H^-. These results corroborate a concerted migration mechanism, where cooperative migrations of multiple ions are important for the fast ion conductions. $LaH_{3-2x}O_x$ would be an example of H^- ion conductors governed by the concerted migration mechanism.

4. Conclusion

Our QENS measurements directly determined the two kinds of H^- dynamics in $LaH_{3-\delta}$; the long-range diffusion and the localized jump between the Tet and Oct sites. Also, our mode distribution analyses for the QENS results suggest that the H^- dynamics in $LaH_{3-2x}O_x$ ($x \neq 0$) are similar to those in $LaH_{3-\delta}$. These dynamics are consistent with the concerted migration mechanism. This study provides the detailed microscopic picture of H^- dynamics in $LaH_{3-2x}O_x$ which results in the anomalous diffusion with high conductivity.

References

[1] Y. Fukai, *The Meal-Hydrogen System,* Springer Series in Materials Science (GmbH, Springer-Verlag, Berlin, 1993).
[2] K. Fukui et al., Nat. Commun. **10** 2578 (2019).
[3] K. Fukui et al., J. Am. Chem. Soc. **144** 1523 (2022).
[4] G. Kobayashi et al., Science **351** 1314 (2016).
[5] H. Tamatsukuri et al., Phys. Rev. B, **107** 184114 (2023).

H. Tamatsukuri[1], K. Fukui[2], S. Iimura[3,4,5], T. Honda[6,7], T. Tada[3,8], Y. Murakami[3,6], J. Yamaura[3], Y. Kuramoto[6], H. Sagayama[6,7], T. Yamada[9], M. Matsuura[9], K. Shibata[1], M. Kofu[1], Y. Kawakita[1], K. Ikeda[6,7], T. Otomo[6,7], and H. Hosono[3,5]

[1]Neutron Science Section, Materials and Life Science Division, J-PARC Center; [2]Graduate Faculty of Interdisciplinary Research, University of Yamanashi; [3]Materials Research Center for Element Strategy, Tokyo Institute of Technology; [4]Japan Science and Technology Agency, PRESTO; [5]National Institute for Materials Science; [6]Institute of Materials Structure Science, KEK; [7]Department of Materials Structure Science, The graduate University for Advanced Studies; [8]Kyushu University Platform of Inter/Transdisciplinary Energy Research, Kyushu University; [9]Neutron Science and Technology Center, CROSS

Neutron Crystallography of a Semiquinone Radical Intermediate of Copper Amine Oxidase

1. Introduction

Hydrogen atoms comprise almost half of the atoms in proteins, and the transfer of protons and hydrogen atoms plays an essential role in many enzyme-catalyzed reactions [1]. Therefore, experimental determination of hydrogen/proton positions of enzymes provides atomic-level insight into the structural basis of the catalytic mechanism. Neutron diffraction resulted from the interaction between neutrons and atom nuclei. The scattering intensities of hydrogen and deuterium atoms are comparable to the scattering cross-sections of heavy atoms constituting proteins. Therefore, even at moderate resolution, the locations of hydrogen and deuterium atoms, including their cationic forms, can be obtained as neutron scattering length density (SLD) maps.

The target enzyme of this study is a copper amine oxidase (CAO), which is ubiquitous in a wide range of aerobic organisms and plays multiple physiological roles by catalyzing oxidative deamination of primary amines. All CAOs structurally characterized to date are homodimers of a ~70 – 95 kDa subunit, each containing a Cu(II) ion and the peptidylquinone cofactor, topaquinone (TPQ) [2]. The catalytic reaction of CAO has been shown to proceed through a ping-pong mechanism consisting of two half-reactions (Fig. 1). We have recently determined the neutron crystal structure of the substrate-free form of CAO from *Arthrobacter globiformis* (AGAO) containing oxidized TPQ (TPQ_{ox}) [3, 4]. SLD maps of TPQ_{ox} revealed that the cofactor is in keto/enolate equilibrium and is involved in an unusual proton sharing with the

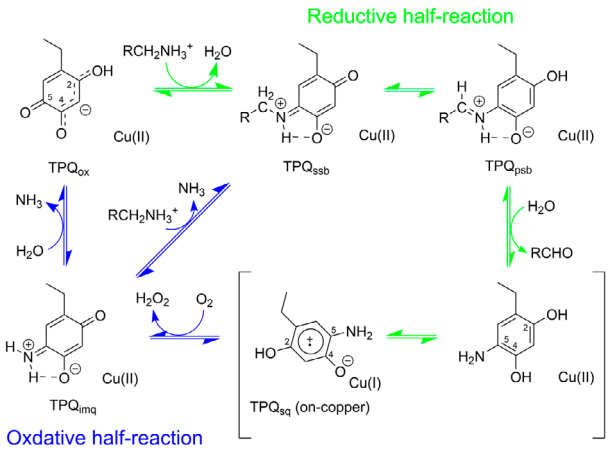

Figure 1. Presumed catalytic mechanism of CAO. Green and blue arrows indicate the steps of reductive and oxidative half-reactions, respectively.

catalytic base. These surprising findings have not been obtained in previous X-ray crystallography. In this study, we determined the neutron crystal structure of the catalytic intermediate of AGAO reduced by the substrate amine and identified the positions of hydrogen atoms and protons in this enzyme [5].

2. Sample preparation and diffraction method

Various catalytic intermediates of the AGAO can be generated by the reaction with substrates in both solution and crystal [6]. In these intermediates, a semiquinone radical form (TPQ_{sq}) is observed as a stable one at the end of the former reductive half-reaction.

A high-quality and extra-large AGAO crystal (3.94 mm^3) was treated in deuterated solution in the following processes for deuterium exchange to reduce a large incoherent scattering mainly derived from solvent H atoms. The crystal was further reacted with a high-affinity substrate, 2-phenylethylamine (2-PEA), at pD 9.0 in an anaerobic chamber. The color change from brownish red to pale green started at the peripheral region of the crystal and gradually spread to the center regions, showing that 2-PEA penetrated the crystal. After completion of the color change (about 24 h of soaking) and subsequent dialysis against the deuterium cryo buffer, the crystal was flash-frozen under a cold N_2 gas stream (100 K) in the chamber.

The prepared crystal exhibited an absorption spectrum identical to that of TPQ_{sq} in the enzymes reduced in both solution and crystal. With this crystal, the neutron diffraction data were collected at 100 K using BL03, Ibaraki biological crystal diffractometer iBIX, at the Materials and Life Science Experimental Facility (MLF) of the Japan Proton Accelerator Research Complex (J-PARC, Tokai, Japan) and the X-ray diffraction data were collected at BL5A in the Photon Factory (PF, Tsukuba, Japan). The obtained neutron and X-ray diffraction data sets at 1.67 and 1.09 Å resolution, respectively, were used for the joint structural refinement.

3. Structure of TPQ_{sq}

The overall protein structure was nearly identical to that determined via neutron/X-ray crystallography using a non-reduced AGAO [3]. A noticeable difference was observed at the active site. A stick model of the active site, including TPQ_{sq} and the nearby residues, is shown

in Fig. 2A, together with $2F_o - F_c$ electron density (ED) and SLD maps (Fig. 2B). The heavy atom coordinates of the determined structures were very similar to those of TPQ_{sq} state obtained by X-ray crystallography [6]. TPQ_{sq} was in the on-copper conformation, in which the 4-OH group of TPQ_{sq} is ligated axially onto the Cu(I) ion. Notably, the SLD map provided novel information for the protonation state of TPQ_{sq}. We found that the 4-hydroxyl group of TPQ_{sq} is deprotonated upon the ligation onto the Cu(I) ion (Fig. 2). Simultaneously, the O4 atom of TPQ_{sq} formed a hydrogen bond with the hydroxyl group of Tyr284 via a water molecule (W1). The 2-hydroxyl group of TPQ_{sq} was deprotonated, and this O2 atom of TPQ_{sq} was also linked to the hydroxyl group of Tyr296 by a hydrogen bond. Furthermore, the TPQ ring was stabilized by NH-π interaction with Asn381 and CH-π interaction with His433 (not shown here).

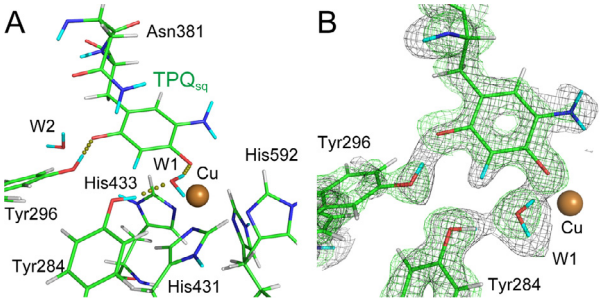

Figure 2. Active-site structure of AGAO containing TPQ_{sq}. (A) The active-site structure is shown as a stick model with TPQ_{sq} (green) and the Cu atom (brown sphere). Dotted lines indicate H-bonds. (B) $2F_o - F_c$ ED map (green) and $2F_o - F_c$ SLD map (grey) around TPQ_{sq}, respectively, superimposed on a stick model.

4. Deuterium exchange in the peptide bond of TPQ

The hydrogen atom of the main-chain NH of TPQ382 was not deuterated in the TPQ_{ox} form, probably by a strong hydrogen bond with the main-chain carbonyl O atom of Ile379 (NH···O distance, 2.0 Å; Fig. 3A). However, this hydrogen atom was exchanged for deuterium in the TPQ_{sq} form as shown in the $F_o - F_c$ omit SLD map (Fig. 3B). The ND group in TPQ_{sq} formed a weak hydrogen bond (ND···O distance, 2.7 Å). Interestingly, the deuterium exchange was observed exclusively in the peptide bond of TPQ_{sq}, strongly suggesting that deuterium is incorporated during the reductive half-reaction. Furthermore, the conformational change of the cofactor was not limited to the side chain quinone ring but was also accompanied with the movement of the main-chain peptide bond.

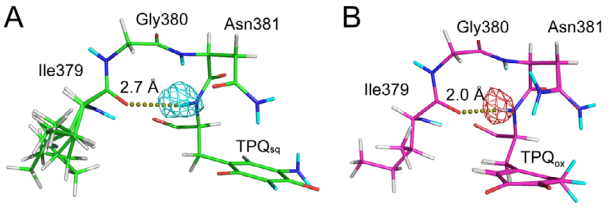

Figure 3. Main-chain hydrogen bonds between the peptide N atom of TPQ and O atom of Ile379. $F_o - F_c$ polder omit SLD maps (positive and negative contours are indicated in cyan and red, respectively), without contributions of the hydrogen and deuterium atoms of the peptide N atoms, superimposed on a stick model of TPQ_{sq} (A) and TPQ_{ox} (B).

5. Identification of the bound amine substrate

Neutron crystallography revealed the binding of a ligand in the hydrophobic pocket as shown in the SLD map (Fig. 4). This molecule has been considered a reaction product, phenylacetaldehyde (PAA), in a previous X-ray crystallographic study [6]. However, the SLD map in this study indicated that three D atoms (positive SLDs) were attached to the terminal heavy atom (previously assigned as O), indicating that the distal group was not an aldehyde group but an amino group. The substrate amine, 2-PEA, taking protonated form, was bound to the substrate-binding pocket. The positively charged amino group of 2-PEA formed a hydrogen bond with the carboxyl group of Asp298, which is highly conserved in CAOs and acts as a catalytic base (Fig. 4). The lack of residual SLD corresponding to an H (D) atom on the Oδ2 atom indicates that the carboxyl group of Asp298 is dissociated and involved in the hydrogen bonding network

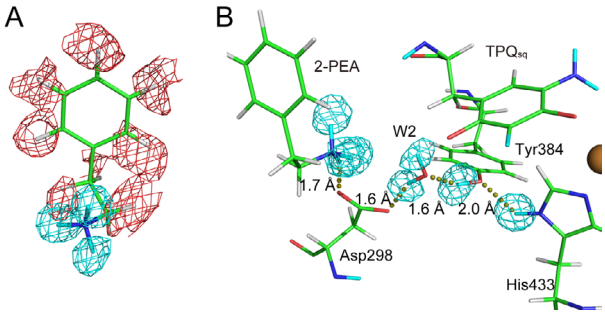

Figure 4. Structure of the amine substrate (2-PEA) bound to the active site. (A) $F_o - F_c$ polder omit SLD map of the deuterium atoms (positive and negative contours are indicated in cyan and red, respectively), without contributions of the hydrogen and deuterium atoms, superimposed on a stick model of 2-PEA. (B) $F_o - F_c$ polder omit SLD maps (positive contours are indicated in cyan), without contributions of the deuterium atoms of Tyr384, His433, H_2O (W2), and 2-PEA, superimposed on stick models. Dotted lines indicate hydrogen bonds together with bond distances.

through a water molecule (W2), OH of Tyr384, and Nδ1 atom of His433.

6. Conclusion

This study revealed an interesting structural feature of AGAO. A surrounding hydrogen-bonding network, as well as CH-π and NH-π interactions with both sides of the TPQ ring, stabilized the radical species, TPQ_{sq}, demonstrating a high chemical reactivity [5]. Furthermore, neutron diffraction analysis showed the number of deuterium/hydrogen atoms covalently bonded to the terminal heavy atom of the ligand bound to the hydrophobic pocket adjacent to TPQ, leading to the conclusion that the amine substrate replaced the product aldehyde in the pocket. These results demonstrate that additional binding of the substrate triggers a conformational change of TPQ in the reductive half-reaction and that the subsequent oxidative half-reaction proceeds with the substrate amine, not with the product aldehyde [5].

References

[1] T. P. Silverstein, Protein Sci. **30** 735 (2021).
[2] S. M. Janes et al., Science **248** 981 (1990).
[3] T. Murakawa et al., PNAS **117** 10818 (2020).
[4] T. Murakawa et al., IUCrJ **9** 342 (2022).
[5] T. Murakawa et al., ACS Catal. **13** 12403 (2023).
[6] T. Murakawa et al., J. Biol. Chem. **290** 23094 (2015).

T. Murakawa[1], K. Kurihara[2], K. Kusaka[3], M. Adachi[2], and T. Okajima[4]
[1]*Faculty of Medicine, Osaka Medical and Pharmaceutical University;* [2]*Institute for Quantum Life Science, National Institutes for Quantum Science and Technology;* [3]*Neutron Science and Technology Center, CROSS;* [4]*SANKEN, Osaka University*

Development of Correction Method for Sample Density Effect on PGA

1. Introduction

In prompt γ-ray analysis, a sample is irradiated with neutrons to excite the nuclei, and a target nuclide is quantified by measuring the γ-rays emitted during the de-excitation process [1]. The γ-ray emission rate varies in samples containing neutron-scattering materials, such as hydrogen, due to the following two factors. The first is the effect of the apparent neutron flux. When neutrons are incident on a sample containing scattering materials, the scattered neutrons change their flight path and length. Consequently, the apparent neutron flux in the sample and the nuclear reaction rate varies. Suppressing the change in the path length using spherical samples can minimize the effect [2, 3]. The second factor is the change in neutron energy caused by scattering. The neutron energy is changed by the contribution of up-scattering, which receives energy from the thermal motion of the nucleus during scattering for cold neutron irradiation, and the contribution of down-scattering that gives energy to the nucleus for epithermal neutron irradiation. In both cases, reaction probabilities vary, as the applied cross-section is energy-dependent. Recently, in developing the PGA technique, we discovered that the neutron energy depends not only on the contents but also on the density of the scattering materials in the sample [4]. This is because the number of neutron scatterings depends on the scattering materials' contents as well as density. L. Szentmiklósi et al. [5] proposed a correction method for this scattering effect. However, this method is complicated because it requires Monte Carlo simulations for each sample. A simpler correction method is required because PGA is used in various fields, and many users are unfamiliar with Monte Carlo simulation techniques. In this study, we developed a straightforward correction method for the sample density effect on nuclear reaction rates, which is essential to PGA, and evaluated its performance using simulations and experiments.

2. Correction method

In developing the correction method, we used the simulation code PHITS 3.16 [6]. In the simulation, JENDL 4.0 and the thermal neutron data of S(α, β) were applied to accurately reproduce the neutron behavior [7]. To simplify the development of the correction method, hydrogen was employed as both the scattering material affecting the measurement and the element to measure the γ-ray emission rate affected by the scattering material. First, the hydrogen density effect is quantitatively demonstrated using the difference of γ-ray counts in different hydrogen density samples. The samples were spherical to minimize the effect of apparent neutron flux, and their densities were set to 1/1 (1.05 g/cm^3), 1/2, 1/5, 1/10, and 1/50 of that of simple-substance polystyrene. The γ-rays emitted from the hydrogen in the polystyrene samples were counted during irradiating cold neutrons at 5 meV and epithermal neutrons at 1 eV. Figure 1 shows the correlation between γ-ray counts and hydrogen content under cold neutron irradiation. As shown in Fig. 1, γ-ray counts vary depending on the

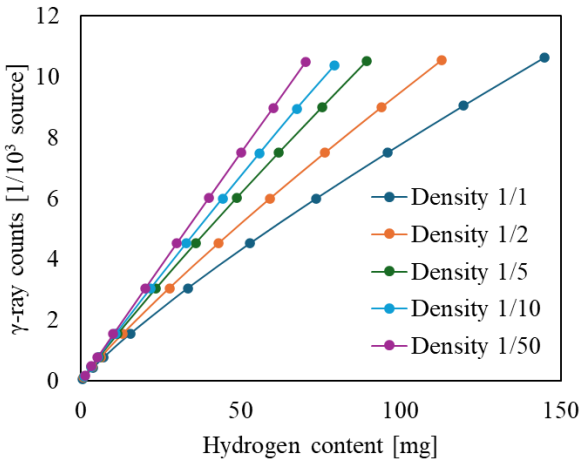

Figure 1. Simulated correlations between γ-ray counts and hydrogen content for various sample densities relative to polystyrene under cold neutron irradiation.

sample density, even when the hydrogen content is the same. The slopes of the correlation curves vary up to 30%. Similarly, for epithermal neutron irradiation, the slopes vary up to 29%. The hydrogen content from these results would yield significantly inaccurate values.

We developed a correction method for the density effect applicable to samples with unknown hydrogen densities. In the simulation, since the amount of hydrogen (the element to be measured; true hydrogen content) is known from the input file, the ratios of the hydrogen content estimated from the γ-ray counts to the true hydrogen content were defined as the correction factors.

First, the scattering effect was reduced by applying a correction factor based on hydrogen content, ignoring density. A correction factor curve for hydrogen content was obtained by fitting a quadratic function to the correlation between the correction factor and the hydrogen content estimated from γ-ray counts. These correction factors can be applied regardless of the hydrogen density, effectively reducing the hydrogen content effect even for samples with unknown densities. Since the corrected hydrogen content does not account for density effects, it is referred to as the tentative hydrogen content. Similarly, the hydrogen density calculated from the tentative hydrogen content and the sample's spherical volume is referred to as the tentative hydrogen density.

Quadratic correlations between the correction factors and tentative hydrogen densities were observed for both cold and epithermal neutron irradiation data. Using these correlations, the hydrogen density effect can be corrected for samples with unknown densities through the following procedure: First, correction factor curves are obtained for the required neutron energy. Next, tentative hydrogen contents are calculated by applying the correction to the measured γ-ray counts of samples with unknown hydrogen densities. Then, tentative hydrogen densities are calculated, and correction factors are obtained using the quadratic correlation for each tentative hydrogen content. Finally, the results are corrected using the correlation curves. Figure 2 shows the corrected results obtained using the method described above. Compared to Fig. 1, the hydrogen density effect is suppressed across all data, and the slope discrepancy is improved from 30% to 0.81%. Similarly, applying corrections to the epithermal neutron irradiation reduced the slope discrepancy from 29% to 1.3%. Since the slope corresponds to γ-ray counts per hydrogen content, measurement uncertainty is improved by approximately 30% for all samples. In this method, since the facility manager obtains correction curves before the experiment, users are not required to perform Monte Carlo simulations.

The correction method was experimentally verified at the ANNRI. ANNRI provides neutrons over a broad energy range, from cold to epithermal, and enables γ-ray energy spectra to be obtained for each neutron energy using the time-of-flight method. Spherical polystyrene samples with densities approximately 1/5 that of simple-substance polystyrene and diameters of 10, 13, 15, and 20 mm (weighing 87.3, 201.6, 303.3, and 713.6 mg, respectively) and samples with densities approximately 1/10 that of simple-substance polystyrene and diameters of 10, 13, 15, and 20 mm (weighing 52.1, 115.3, 166.8, and 418.5 mg, respectively) were measured. Measurements were conducted at a beam power of 600 kW for 2 to 14 hours to maintain statistical

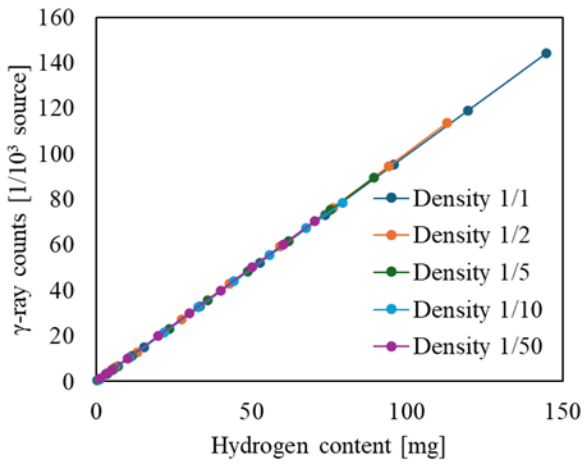

Figure 2. Corrected results for correlations under cold neutron irradiation from the simulations in Fig. 1.

uncertainties within 3% in epithermal neutron irradiations depending on the hydrogen content.

Tentative hydrogen contents and densities were derived by applying the hydrogen content correction. Corrected hydrogen contents were then calculated for each sample using the developed correction method, as described in the previous section. Since samples of two densities were used in the experiment, the performance of the correction method for the hydrogen density effect was verified by directly comparing the slopes of the correlation curves obtained from each measurement. Table 1 shows the ratio of the slopes of the correlation curves before and after correction for each incident neutron energy and sample density. When the slopes agree, the ratio is one. Before correction, significant discrepancies were observed in the slope ratios for both neutron energies. However, after applying the correction, the slopes agreed within the uncertainties, confirming that the developed correction method effectively reduces uncertainties due to sample density to a level comparable to the measurement uncertainty.

Table 1. Comparison of slopes of the correlation curves before and after correction.

	Cold neutron	Epithermal neutron
Before correction	1.035 ± 0.014	0.963 ± 0.022
After correction	0.993 ± 0.015	0.993 ± 0.024

3. Conclusion

In this research, we developed a straightforward correction method for addressing the sample density effect in PGA and verified it experimentally. The developed correction method can suppress the density effect even for samples with unknown hydrogen densities by using simulation-derived correction factor curves based on incident neutron energy. Since the correction method does not require simulations for each measurement sample, it allows even users unfamiliar with simulation techniques to quickly apply corrections. The correction method is expected to reduce the uncertainty due to the density effect from 30% to 0.81% for cold neutron irradiations and from 29% to 1.3% for epithermal neutron irradiations. This level of uncertainty meets the requirements of most users.

References

[1] M. P. Failey, D. L. Anderson, et al., Anal Chem 51: 2209-2221 (1979).
[2] E. A. Mackey, G. E. Gordon, et al., Anal Chem 63: 288-292 (1991).
[3] E. A. Mackey, G. E. Gordon, et al., Anal Chem 64: 2366-2371 (1992).
[4] M. Maeda, M. Segawa, et al., Sci Rep 12: 6287 (2022)
[5] L. Szentmiklósi, Z. Kis, et al., J Anal At Spectrom 36: 103-110 (2021).
[6] T. Sato, Y. Iwamoto, et al., J Nucl Sci Technol 55: 684-690 (2018).
[7] K. Shibata, O. Iwamoto, et al., J Nucl Sci Technol 48: 1-30 (2011).

M. Maeda[1], M. Segawa[2], Y. Toh[2], S. Endo[2], S. Nakamura[2], and A. Kimura[2]
[1]*Nuclear Science and Engineering Center, JAEA;* [2]*Neutron Science Section, Materials and Life Science Division, J-PARC Center*

Discovery of Novel Ionic Conductors and Their Structure Science

1. Introduction

The development of clean energy technologies, such as solid oxide fuel cells (SOFCs) and proton ceramic fuel cells (PCFCs), is an essential pathway to achieve a carbon-neutral society. To develop better SOFCs and PCFCs, electrolytes (i.e. oxide-ion conductors and proton conductors) with high ionic conductivity at low temperature are required. Since ionic conductivity in ceramic materials is strongly dependent on their crystal structures, it is also important to elucidate the mechanism of the ion conduction and the origins of high ionic conductivity. In particular, the neutron diffraction method is the most important technique to clarify the structural information (atomic positions, atomic displacement parameters, and occupancy factors) of a relatively light oxide ion and proton in ceramic materials. Our research group has been exploring new oxide-ion conductors and proton conductors by various strategies. Through synthesis, conductivity measurements, structural analysis including neutron diffraction, and theoretical calculations, we have discovered top-level oxide-ion conductors [1-3], a dual oxide-ion and proton conductor [4], and proton conductors [5-8], and revealed the ion conduction mechanisms and origins of high ionic conductivity. In this highlight, our recent research topics are briefly introduced.

2. High oxide-ion conductivity in Sillén oxychlorides

The oxyhalides are mixed-anion compounds containing both oxide ions and halide ions that exhibit a variety of material properties. Several oxyhalides exhibit halide ion conduction. However, oxide ion conduction in oxyhalides is rare and therefore worthy of study. We focused on Bi-containing Sillén oxychlorides because many Bi-containing materials show high oxide-ion conductivity and the Sillén oxyhalides with the triple fluorite-like layers contain possible interstitial oxygen sites, leading to high oxide-ion conduction. Indeed, we found that the Sillén oxychlorides, such as $Bi_{1.9}Te_{0.1}LaO_{4.05}Cl$ and $Bi_{1.9}Te_{0.1}LuO_{4.05}Cl$ exhibit very high oxide ion conductivity [1, 2]. In particular, the bulk conductivity of $Bi_{1.9}Te_{0.1}LuO_{4.05}Cl$ reaches 10^{-2} S cm^{-1} at 431°C, which is much lower than 644°C of $(ZrO_2)_{0.92}(Y_2O_3)_{0.08}$ (YSZ) and 534°C of $La_{0.8}Sr_{0.2}Ga_{0.83}Mg_{0.17}O_{2.815}$ (LSGM) (Fig. 1a).

The crystal structures of $Bi_{1.9}Te_{0.1}LuO_{4.05}Cl$ and the parent material Bi_2LuO_4Cl were analyzed using neutron powder diffraction (ND) data measured at the BL08 (SuperHRPD, MLF, J-PARC) in situ between 25 and 700°C, in order to discuss the origins of the high oxide ion conductivity. The crystal structures of $Bi_{1.9}Te_{0.1}LuO_{4.05}Cl$ and Bi_2LuO_4Cl were successfully refined by the Rietveld method based on the tetragonal *P*4/*mmm* Sillén phase

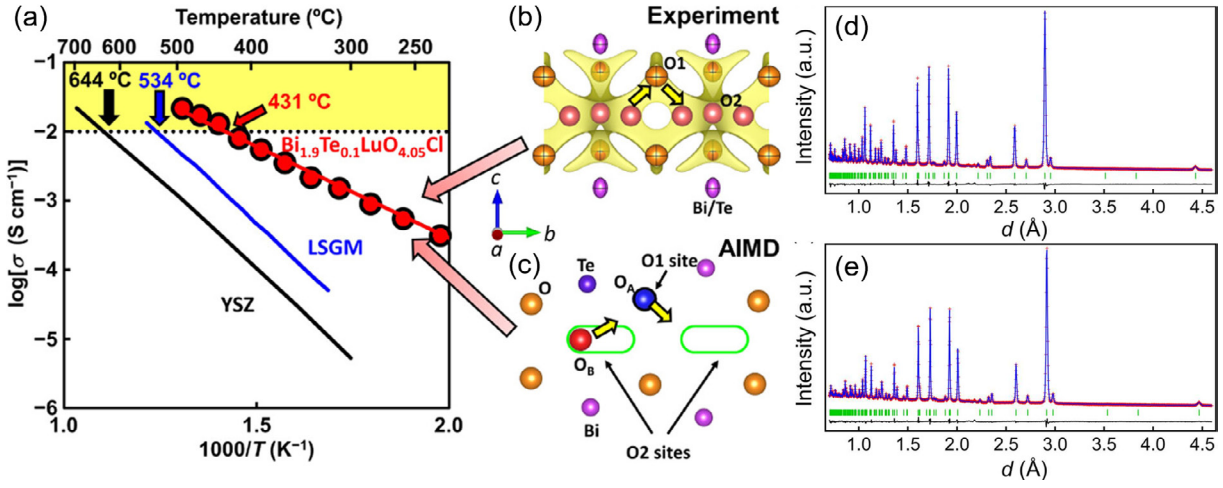

Figure 1. (a) Comparison of the bulk conductivity σ_b of $Bi_{1.9}Te_{0.1}LuO_{4.05}Cl$ with $(ZrO_2)_{0.92}(Y_2O_3)_{0.08}$ (YSZ) and 534°C of $La_{0.8}Sr_{0.2}Ga_{0.83}Mg_{0.17}O_{2.815}$ (LSGM). The black dotted line denotes the conductivity of 0.01 S cm^{-1}, and the yellow area stands for the region where the conductivity is higher than 0.01 S cm^{-1}. (b) Neutron scattering length density (NSLD) distribution at 400°C in $Bi_{1.9}Te_{0.1}LuO_{4.05}Cl$. (c) Snapshot of the Ab initio molecular dynamics (AIMD) simulations of $Bi_{16}Te_2Lu_9O_{37}Cl_9$. (d,e) Rietveld patterns of $Bi_{1.9}Te_{0.1}LuO_{4.05}Cl$ for neutron powder diffraction data measured in situ at (d) 25°C, (e) 400°C.

in the whole temperature range (Fig. 1d, e). The Rietveld analysis of ND data indicated that there was no interstitial oxygen in the parent material Bi_2LuO_4Cl. In contrast, the existence of an interstitial oxygen atom at the interstitial O2 site in the Te-doped material $Bi_{1.9}Te_{0.1}LuO_{4.05}Cl$ was confirmed (Fig. 1b). The oxygen atom at the interstitial O2 site was localized at 25°C, while it exhibited larger spatial distributions at a higher temperature of 400°C which corresponded to the higher oxide ion conductivity at 400°C. The neutron scattering length density analyses indicated the oxide-ion diffusion in the triple fluorite-like layer, which is also supported by bond valence-based energy calculations, static DFT calculations, and ab initio molecular dynamics simulations (Fig. 1b, c). The oxide-ion diffusion in the triple fluorite-like layer enables the high oxide-ion conductivity with the low activation energy in $Bi_{1.9}Te_{0.1}LuO_{4.05}Cl$. Further investigation of Sillén oxyhalides with triple fluorite-like layers will lead to the discovery of superior oxide ion conductors.

3. Dimer-mediated cooperative mechanism of ultrafast-ion conduction in hexagonal perovskite-related oxides

Ion conduction in hexagonal perovskite-related materials is rare, and the mechanism of ion diffusion is unclear. Previously, we have found that $Ba_7Nb_{3.9}Mo_{1.1}O_{20.05}$ showed very high oxide-ion conductivity [3]. However, there is still lack in the detail study on $Ba_7Nb_4MoO_{20}$-based materials. We have synthesized and measured electrical conductivity of $Ba_7Nb_{4-x}Mo_{1+x}O_{20+x/2}{\cdot}y\ H_2O$ (x = 0, 0.02, 0.04, 0.06, 0.08, 0.1, 0.12, 0.14, 0.16, 0.18, 0.2, 0.22, 0.25, 0.3). Here, y is the water content in $Ba_7Nb_{4-x}Mo_{1+x}O_{20+x/2}{\cdot}y\ H_2O$. Because $Ba_7Nb_{3.8}Mo_{1.2}O_{20.1}$ showed the highest conductivity, we examined the characteristics of this material. Then, we found that high oxide-ion and proton conductivity (bulk conductivities in wet air: 11 and 2.7 mS cm^{-1} at 537 and 326°C, respectively), high chemical, and electrical stability were exhibited in the new hexagonal perovskite-related oxide $Ba_7Nb_{3.8}Mo_{1.2}O_{20.1}$ [3].

Oxide-ion transport number t_O^{2-} of $Ba_7Nb_{3.8}Mo_{1.2}O_{20.1}$ was evaluated using an oxygen-concentration cell in dry conditions. The obtained t_O^{2-} were 0.95–0.98 between 697 and 903°C in (dry air)/(dry 10% air in N_2), 0.92–1.0 between 697 and 903°C in (dry air)/(dry O_2), and 1.0 at 596°C in (dry air)/(dry 5% H_2 in N_2), demonstrating that $Ba_7Nb_{3.8}Mo_{1.2}O_{20.1}$ is an oxide-ion conductor with negligible electronic contribution in dry conditions. The bulk conductivity in dry air of $Ba_7Nb_{3.8}Mo_{1.2}O_{20.1}$ is higher than other $Ba_7Nb_4MoO_{20}$-based oxides (Fig. 2a). The total DC electrical conductivity of $Ba_7Nb_{3.8}Mo_{1.2}O_{20.1}{\cdot}y\ H_2O$ in wet air is higher than that in dry air, indicating proton conduction. At 537°C, $Ba_7Nb_{3.8}Mo_{1.2}O_{20.1}{\cdot}0.11\ H_2O$ exhibits much higher bulk conductivity compared with representative proton conductors. Therefore, $Ba_7Nb_{3.8}Mo_{1.2}O_{20.1}{\cdot}y\ H_2O$ has a higher potential as a dual-ion solid electrolyte in a ceramic fuel cell.

The neutron diffraction study at 800°C revealed the existence of interstitial oxygen in $Ba_7Nb_{3.8}Mo_{1.2}O_{20.1}$ and oxide-ion migration path through the interstitial oxygen was suggested from the neutron scattering length density distribution (Fig. 2b). The result suggests the interstitially oxide ion diffusion in this material. Combined with the ab initio molecular dynamics (AIMD) simulations, we found that the excess oxygen atoms are incorporated by the formation of both 5-fold coordinated $(Nb/Mo)O_5$ monomer and its $(Nb/Mo)_2O_9$ dimer with a corner-sharing oxygen atom and that the breaking and reforming

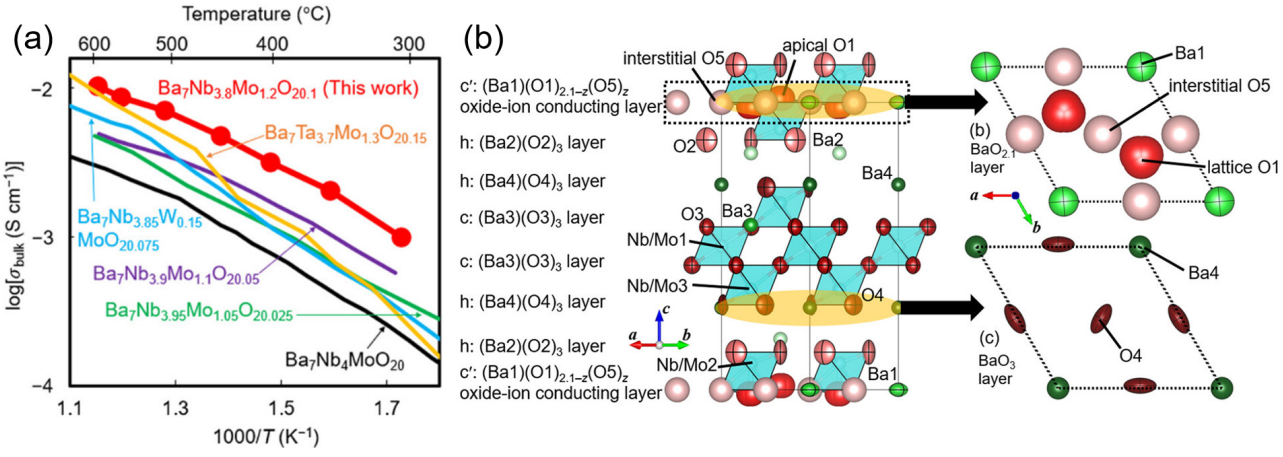

Figure 2. (a) Comparison of bulk conductivity of $Ba_7Nb_{3.8}Mo_{1.2}O_{20.1}$ and other $Ba_7Nb_4MoO_{20}$-based oxides in dry air. (b) Crystal structure of $Ba_7Nb_{3.8}Mo_{1.2}O_{20.1}$ at 800°C. Copyright © 2023 The Authors of ref. [4].

of the dimers lead to a high oxide-ion conduction. AIMD simulations showed that high proton conduction can be attributed to proton migration in the hexagonal close-packed BaO_3 layers of $Ba_7Nb_{3.8}Mo_{1.2}O_{20.1}$. The present findings of high oxide-ion, proton and dual-ion (oxide ion and proton) conduction and unique migration mechanisms in $Ba_7Nb_{3.8}Mo_{1.2}O_{20.1}$·$y$ H_2O would develop the science and engineering of oxide-ion, proton, and dual-ion (oxide ion and proton) conductors.

4. Summary

We have successfully discovered top-level ionic conductors. The crystal structure analyses based on the neutron diffraction data played a very important role in clarifying the origin of the high ionic conductivity of our new materials.

K. Fujii, Y. Sakuda, and M. Yashima
School of Science, Institute of Science Tokyo

References

[1] H. Yaguchi et al., Adv. Func. Mater., **33** 2214082 (2023).
[2] N. Ueno et al., J. Am. Chem. Soc., **146** 11235 (2024).
[3] M. Yashima et al., Nat. Commun., **12**, 556 (2021).
[4] Y. Sakuda et al., Chem. Mater., **35** 9774 (2023).
[5] R. Morikawa et al., Commun. Mater., **4** 42 (2023).
[6] K. Saito and M. Yashima, Nat. Commun., **14**, 7466 (2023).
[7] K. Saito et al., J. Mater. Chem. A, **12** 13310 (2024).
[8] K. Matsuzaki et al., J. Am. Chem. Soc., **146** 18544 (2024).

Neutron Diffraction Measurements for Developing Li Superionic Conductors in Complex Compositional Systems

1. Introduction

Lithium superionic conductors can be applied as solid electrolytes and thus become essential components for all-solid-state lithium batteries, which potentially have a wider operation temperature range and higher power properties, compared with lithium-ion batteries using liquid electrolytes [1-3]. Among lithium superionic conductors, $Li_{10}GeP_2S_{12}$ [4] and its structural derivatives (LGPS-type phases) [5] show high ionic conductivities exceeding 10 mS cm^{-1} at around room temperature and thus all-solid-state batteries using them have been reported to show high discharge performance [3, 6]. Since solid electrolytes with even higher ionic conductivity will make it possible to build high-energy all-solid-state lithium-metal batteries [7] employing thick cathode [8, 9], new LGPS-type materials have been searched for. Such material search is supported by neutron diffraction techniques that complement X-ray diffraction (XRD), because the sensitivity to elements and the *d*-space dependent attenuation of diffraction intensity are different between neutron diffraction and XRD. This article reports on the synthesis for new LGPS-type solid-solution phases of $Li_{9.54}[Si_{1-\delta}M_\delta]_{1.74}P_{1.44}S_{11.1}Br_{0.3}O_{0.6}$ ($LiSiM_\delta PSBrO$, where *M* represents Ge or Sn as well as δ and 1−δ ranging from 0 to 1 mean the molar ratios of M^{4+} and Si^{4+} in the target composition, respectively), and neutron diffraction studies on one end composition at δ = 0 (i.e., LiSiPSBrO) [10].

2. Development of new solid electrolytes

The synthesis of $LiSiM_\delta PSBrO$ was motivated by earlier leading studies of high-entropy design for alkali ion conductors, where multiple elemental substitutions and the resultant increase in configurational entropy were attempted to appropriately distort the crystal lattice and thereby flatten energy barriers for ion migration [11]. With this design approach, various lithium conductors having LISICON [12], NASICON [11], Garnet [11], or Rock-salt [13] -type structure have been synthesized so far. In this study, the target composition series of $LiSiM_\delta PSBrO$ was selected thus increasing the compositional complexity and forming a target crystalline structure (i.e., LGPS-typephase) [10]. Two compositional metrics were derived and used when selecting the compositions that meet both criteria [10]. Consequently, a series of $LiSiM_\delta PSBrO$ were selected as example compositions to investigate the applicability of the high-entropy design to LGPS-type crystal structures.

Samples were synthesized by solid-state reaction after mechanical milling of six reagents as starting materials (i.e. Li_2S, P_2S_5, SiS_2, GeS_2 or SnS_2, P_2O_5, and LiBr). The samples' quality was investigated by XRD techniques. For monophasic samples, all peaks were indexed by the same space group as the target LGPS-type crystal (i.e., $P4_2/nmc$). The XRD data were analyzed to investigate lattice parameter changes induced by multiple chemical substitutions for the original LGPS and thereby confirm substitutions of guest elements such as Si, Sn, Br, and O.

Neutron diffraction data were measured at −269°C (4 K) for LiSiPSBrO using a time-of-flight diffractometer (SPICA) installed on the BL09 beamline at J-PARC. The data were analyzed by the Rietveld method to obtain a crystal structure model. Figure 1 shows the recorded and refinement patterns. Some of the diffraction peaks could not be indexed. These peaks might be due to secondary phases that could not be detected by XRD but detected by neutron diffraction. They were excluded

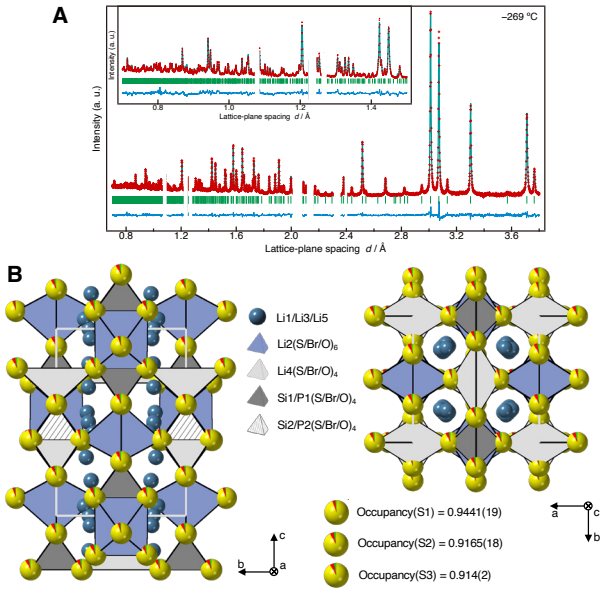

Figure 1. (A) Neutron Rietveld refinement pattern at −269°C (4 K). Red, cyan, and blue lines indicate the observed and calculated patterns as well as the residual differences, respectively. The positions of Bragg reflections are indicated by green bars. Lattice-plane spacing *d* ranges excluded from the analysis are not shown. (B) A crystal structure model of the LiSiPSBrO as obtained by Rietveld analysis. Figures are adapted from Ref. [10] with minor modifications.

from the refinement. In the refinement process, Br and O atoms tended to occupy anion sites evenly. The distribution of Li atoms was similar to that of the original LGPS phase [14]. Using the obtained model, first-principles-based calculations were performed to estimate the effect of substitution on ion-migration energy barriers. Results of climbing image nudged elastic band (NEB) calculations indicate that even a small degree of substitution by bromine atom potentially decreases the migration barrier around substituent sites.

The bulk ionic conductivity was measured for $LiSiGe_{0.4}PSBrO$, which was selected because the sample powder showed a high-phase purity and low ionic resistance including grain-boundaries. Figure 2 shows the Arrhenius plots of the ionic conductivity measured by electrochemical impedance spectroscopy for a sintered sample. The ionic conductivity for $LiSiGe_{0.4}PSBrO$ was 32 mS cm^{-1} at 25°C, which is 2.5 times larger than that of the original LGPS phase (12 mS cm^{-1}). It should be noted that the measured bulk ionic conductivity for $LiSiGe_{0.4}PSBrO$ might be an underestimated value,

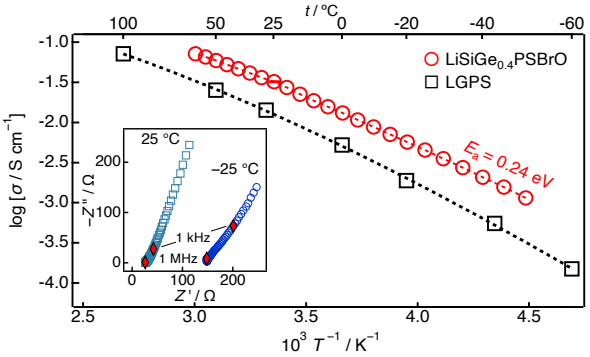

Figure 2. Arrhenius plots for the bulk conductivities of $Li_{9.54}[Si_{0.6}Ge_{0.4}]_{1.74}P_{1.44}S_{11.1}Br_{0.3}O_{0.6}$ ($LiSiGe_{0.4}PSBrO$) and LGPS. Inset: typical impedance plots for the former phase measured at −25°C (right) and 25°C (left). The figure is adapted from Ref. [10] with minor modifications.

because the sample possibly contained undesirable secondary phases that were not detected by XRD but might be detected by neutron diffraction, as is the case for LiSiPSBrO (Fig. 1).

3. Concluding remarks

In summary, new LGPS-type superionic conductors $Li_{9.54}[Si_{1-\delta}M_\delta]_{1.74}P_{1.44}S_{11.1}Br_{0.3}O_{0.6}$ ($LiSiM_\delta PSBrO$, M = Ge, Sn) were developed with the help of high-entropy design. The observed improvement for $LiSiGe_{0.4}PSBrO$ compared with the original LGPS phase indicates that the synthesis of an LGPS-type crystal in the complex chemical compositions is a promising direction for developing solid electrolytes with an enhanced ionic conductivity. By complementing XRD, neutron diffraction assists such future studies, especially in the preparation of high-quality samples.

References

[1] K. Takada, Acta Mater., 61, (2013) 759.
[2] J. Janek, et al., Nat. Energy, 1, (2016) 16141.
[3] Y. Kato, et al., Nat. Energy, 1, (2016) 16030.
[4] N. Kamaya, et al., Nat. Mater., 10, (2011) 682.
[5] Y. Kato, et al., Adv. Energy Mater., 10, (2020) 2002153.
[6] L. Ye, et al., Nature, 593, (2021) 218.
[7] Y. G. Lee, et al., Nat. Energy, 5, (2020) 299.
[8] A. Bielefeld, et al., ACS Appl. Mater. Interfaces, 12, (2020) 12821.
[9] Y. Kato, et al., J. Phys. Chem. Lett., 9, (2018) 607.
[10] Y. Li, et al., Science, 381, (2023) 50.
[11] Y. Zeng, et al., Science, 378, (2022) 1320.
[12] Y. Deng, et al., ACS Appl. Mater. Interfaces, 9, (2017) 7050.
[13] D. Bérardan, et al., J. Mater. Chem. A, 4, (2016) 9536.
[14] T. Yajima, et al., J. Mater. Chem. A, 9, (2021) 11278.

S. Hori[1] and T. Saito[2, 3]
[1]Institute of Integrated Research, Institute of Science Tokyo; [2]Institute of Materials Structure Science, KEK; [3]School of High Energy Accelerator Science, The Graduate University for Advanced Studies (SOKENDAI)

Orientation Mapping of $YbSn_3$ Single Crystals Based on Bragg-dip Analysis Using a Delay-line Superconducting Sensor

1. Introduction

Neutron imaging is of great importance in the application of non-destructive inspection techniques since it allows us to collect a wealth of information about material structure through a change in transmission as a function of neutron energy. The dip structure in the transmission spectrum induced by Bragg diffraction can provide information about crystal structure, crystallinity, crystal grain, lattice strain, and grain orientation [1].

We have developed a ^{3}He-free superconducting neutron detector based on a current-biased kinetic-inductance detector (CB-KID) [2]. The two-dimensional neutron imager operates in a wide temperature range below the superconducting transition temperature T_c and achieves high spatial resolution by using a delay-line technique (delay-line CB-KID) [3, 4].

2. Experimental

Figure 1(a) schematically shows the structure of the delay-line CB-KID. The superconducting Nb ground plane, two mutually orthogonal Nb meanderlines, and ^{10}B neutron conversion layer are stacked sequentially on a Si substrate, whereas each layer is separated by SiO_2 insulating layers. The meanderlines have the following specifications; a pitch p = 1.5 μm, 50 nm in thickness, segment h = 15.1 mm in length, 10,000 times in repetition, and a total length 151 m, as schematically shown in Fig. 1(a).

A charged particle from nuclear reaction between a neutron and ^{10}B atom in the neutron conversion layer creates a local hot spot in two meanderlines. When DC currents are biased across meanderlines, a transient reduction in Cooper pair density generates voltage signals at the hot spot. Signals propagate toward both ends of the meanderlines as electromagnetic waves. Then, the hot spot position (x, y) is determined by delay-line method as follows:

$$x = \mathrm{Ceil}\frac{(t_{\mathrm{Ch4}} - t_{\mathrm{Ch3}})v_x p}{2h},\quad y = \mathrm{Ceil}\frac{(t_{Ch2} - t_{\mathrm{Ch1}})v_y p}{2h}.$$

Here, t_{Ch1}, t_{Ch2}, t_{Ch3}, and t_{Ch4} are the corresponding timestamps of signals received at Ch1, Ch2, Ch3, and Ch4, signal propagation velocities are v_x and v_y. The neutron wavelength is determined by the time-of-flight method.

We performed neutron imaging experiments with pulsed neutrons at BL10 of the Material and Life Science Experimental Facility (MLF), J-PARC [5]. The detector was cooled down below T_c by using a Gifford-McMahon refrigerator, as shown in Fig. 1(b).

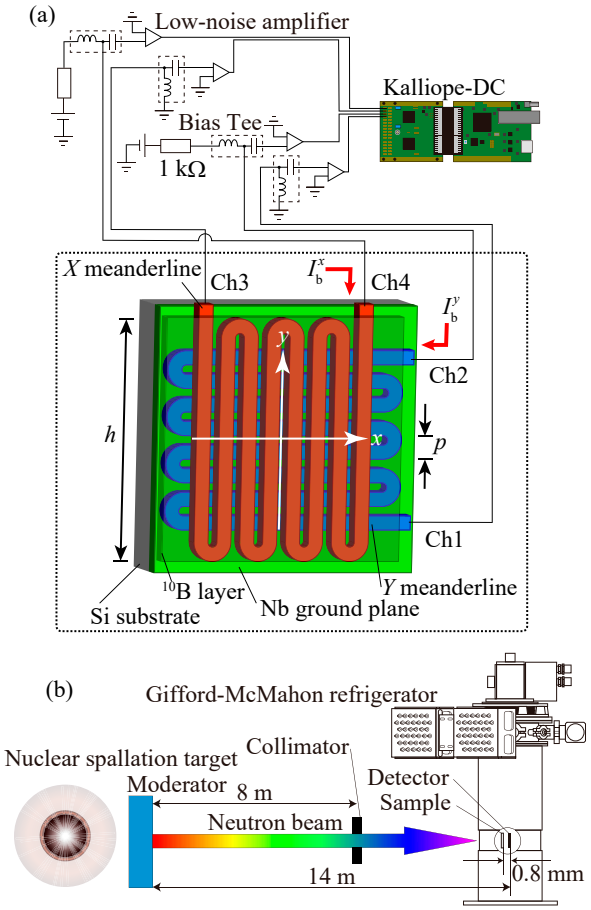

Figure 1. (a) Measurement system consisting of room-temperature instruments and a cryogenic detector. Objects surrounded by the dashed line were cooled down to 7.9 K. DC bias currents of 30 μA were fed to meanderlines, and signals were acquired by the Kalliope-DC board. (b) Schematic illustration of the measurements system.

3. Results and discussion

We grew an intermetallic compound $YbSn_3$ as a test crystal sample. An optical photograph of the test sample is shown in Fig. 2(a). The upper left $YbSn_3$ single crystal (#1) and the lower right one (#2) are bonded together by a diagonal thin layer of Sn.

Figures 2(b) and (c) show neutron transmission

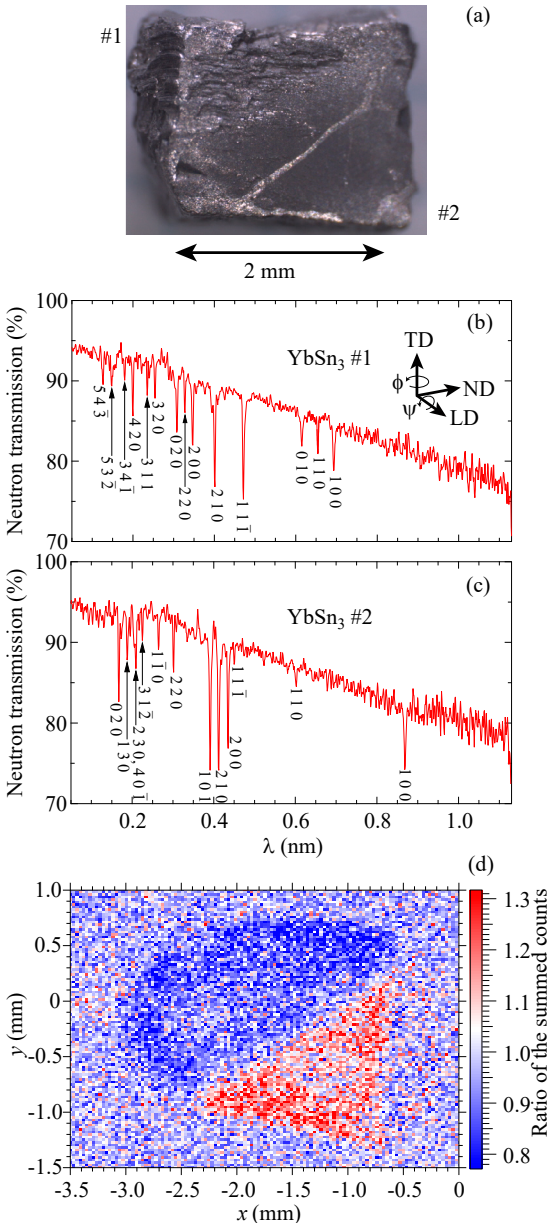

Figure 2. (a) Optical photograph of the test sample. (b) (c) Neutron transmissions of $YbSn_3$ summing the upper left and lower right areas in Fig. 2(a). (d) Neutron transmission image emphasizing the difference in Bragg-dip positions between crystals #1 and #2. The pixel size is 30 × 23 μm^2.

spectra for the upper left and lower right single crystals, respectively. Bragg dips are clearly observed in $YbSn_3$ single crystals due to the high neutron scattering cross section of Yb. All Bragg dips in single crystals #1 and #2 are successfully assigned as indices shown in Figs. 2(b) and (c).

We assume that the [100] direction is rotated by an azimuthal angle ϕ and a longitudinal angle ψ from the vertical line, as shown in the inset of Fig. 2(b). ϕ and ψ in a cubic crystal are given in

$$\phi = \arcsin\left(\frac{\lambda_{110}}{a} - \frac{\lambda_{100}}{2a}\right), \psi = \arccos\left(-\frac{\lambda_{100}}{2a\cos\phi}\right),$$

where, a is the lattice constant, λ_{100} and λ_{110} are 100 and 110 Bragg dips [1].

By using these equations, we estimated the orientation of the [100] direction of the crystal #1(#2) as ϕ = 41.0 (20.9) degrees and ψ =169.0 (173.3) degrees.

To emphasize the difference in Bragg-dip positions between crystals #1 and #2, we computed a neutron transmission ratio image. The total number of events NoE (denoted NoE#1) is summed up over λ = 0.345 to 0.348 nm (the 200 dip), 0.399 to 0.402 nm (the 210 dip), and 0.469 to 0.474 nm (the 11-1 dip) for crystal #1. In the same way, the total NoE (denoted as NoE#2) is summed up over λ = 0.389 to 0.393 nm (the 101 dip), 0.410 to 0.414 nm (the 210 dip), and 0.433 to 0.437 nm (the 200 dip) for crystal #2. The ratio image NoE#1/NoE#2 is denoted in Fig. 2(d). Regions of crystal #1 and #2 exhibit uniform color, while their colors are different from each other. It indicates that the $YbSn_3$ sample consists of two single crystals with different orientations from each other.

4. Summary

In this study, we demonstrated that the delay-line CB-KID could be used to conduct Bragg-dip analyses of neutron transmission spectrum and transmission imaging. We successfully assigned Bragg dips and determined the [100] axis orientations of the $YbSn_3$ crystals.

References

[1] J. R. Santisteban, J. Appl. Cryst. **38** 934 (2005).
[2] T. Ishida *et al.*, J. Low Temp. Phys. **176** 216 (2014).
[3] H. Shishido *et al.*, Phys. Rev. Appl. **10** 044044 (2018).
[4] H. Shishido *et al.*, J. Appl. Cryst. **56** 1108 (2023).
[5] K. Oikawa *et al.*, Nucl. Instrum. Methods Phys. Res. A **589** 310 (2008).

H. Shishido[1], T. D. Vu[2,3], K. Aizawa[3], K. M. Kojima[2,4], T. Koyama[2], K. Oikawa[3], M. Harada[3], T. Oku[3], K. Soyama[3], S. Miyajima[5], M. Hidaka[6], S. Y. Suzuki[7], M. M. Tanaka[8], S. Kawamata[2], and T. Ishida[2]

[1]*Equipment Sharing Center for Advanced Research and Innovation, Osaka Metropolitan University;* [2]*Division of Quantum and Radiation Engineering, Osaka Metropolitan University;* [3]*Materials and Life Science Division, J-PARC Center;* [4]*Center for Molecular and Materials Science, TRIUMF and Stewart Blusson Quantum Matter Institute, University of British Columbia;* [5]*Advanced ICT Research Institute, National Institute of Information and Communications Technology;* [6]*Advanced Industrial Science and Technology;* [7]*Computing Research Center, Applied Research Laboratory, KEK;* [8]*Institute of Particle and Nuclear Studies, KEK*

An X-ray and Neutron Scattering Study of Aqueous $MgCl_2$ Solution in the Gigapascal Pressure Range

1. Introduction

Understanding of the nature of Mg^{2+} solvation is an important issue since Mg^{2+} plays an essential role in various application fields, such as biological systems, environmental aerosols, and geological processes in the Earth. For example, Mg^{2+} is the second most common cation in seawater and lake water after Na^+; thus, Mg^{2+} affects the properties of sea salt aerosols in an atmospheric environment. Investigation under high pressure is required to understand the geological process, but most studies on Mg^{2+} solvation in aqueous solutions have been conducted only in ambient conditions. When high pressure of several gigapascals (GPa) is applied to aqueous solutions, the hydrogen bonding of solvent water is expected to be greatly perturbed up to around 4 GPa since liquid water behaves like normal liquids above 4 GPa [1, 2].

In this study, we performed X-ray and neutron scattering measurements on a 2 *m* (= mol/kg) $MgCl_2$ aqueous solution at ambient condition of up to 4 GPa and 300 – 500 K. The empirical potential structure refinement (EPSR) modeling method was employed to analyze the X-ray and neutron scattering data simultaneously to extract the site-site pair distribution functions, coordination number distributions, angle distribution (orientational correlation), and spatial density functions (3D structure) of ion solvation and association and the solvent structure [3].

2. Experimental

A 2 *m* $MgCl_2$ aqueous solution was prepared by dissolving dried $MgCl_2$ into degassed H_2O to a required amount by weight. For the neutron scattering experiments, a 2 *m* $MgCl_2$ aqueous solution in D_2O was prepared in a nitrogen-filled glove box to avoid contamination of light water (H_2O). The X-ray scattering experiments were carried out on BL14B1 at SPring-8. A sample solution was kept in a diamond cylindrical cell (1.5 mm inner diameter and 1.2 mm height) capped with a thin gold foil and sealed in a high-pressure cell assembly. The neutron scattering experiments were carried out on the PLANET diffractometer installed at BL11 in J-PARC MLF. The measured thermodynamic conditions were 0.1 MPa (hereafter abbreviated as 0 GPa)/300 K, 1 GPa/300 K and 500 K, 2 GPa/500 K, and 4 GPa/500 K. EPSR calculations were performed in a unit cell, including 40 Mg^{2+} cations, 80 Cl^- anions, and 1000 D_2O molecules to reproduce the composition of the sample solution.

3. Results and discussion

Figure 1 shows the X-ray and neutron experimental interference functions, $F(Q)$, and the corresponding radial distribution functions, $G(r)$ obtained by the experiments (black dots) and EPSR modeling (red lines). Symbols X and N denote X-ray and neutron scattering, respectively. In the neutron interference functions, a hump observed at $Q \sim 4$ Å^{-1} at 0 GPa/300 K gradually decreases and becomes a plateau at 4 GPa/500 K. On the other hand, the X-ray interference function has first double peaks at 2 – 3 Å^{-1} at 0 GPa/300 K, merging into a single sharp peak at 4 GPa/500 K. These characteristic features suggest the disruption of the tetrahedral hydrogen-bonded network in water with increasing pressure and temperature.

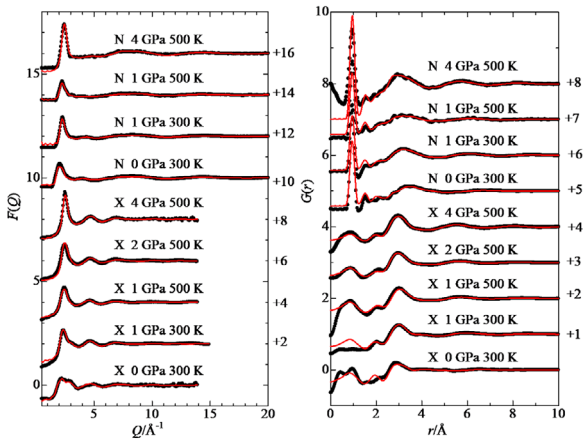

Figure 1. The X-ray and neutron interference functions (left frame) and the radial distribution functions (right frame) obtained by experiments (black dots) and EPSR modeling (red lines) of 2 *m* $MgCl_2$ aqueous solutions as a function of pressure and temperature. X and N denote X-ray and neutron scattering, respectively.

Table 1 summarizes the structure parameters obtained by EPSR modeling combined with X-ray and neutron scattering data.

Mg^{2+} solvation: Mg^{2+} is a structure-making ion. The first neighbor Mg–O_W(I) distance is almost constant at 1.92 Å over the pressure range measured, suggesting a rigid solvation shell. Here, "I" denotes the first coordination

Table 1. Interatomic distances (*r*) and coordination numbers (*CN*) of the individual atom pairs in a 2 *m* $MgCl_2$ aqueous solution at various pressures and temperatures. (I) denotes the first coordination shells. r_{max} is the upper limit of integration of radial distribution function to define the coordination shell. The uncertainties in the interatomic distance are estimated as 0.02 Å.

P, T		Mg–Ow(I)	Mg–Hw(I)	Cl–Ow(I)	Cl–Hw(I)	Ow-Ow(I)	Ow-Hw(I)	Mg–Cl(I)
0 GPa/	*r*/Å	1.92	2.58	3.18	2.32	2.76	1.80	2.37
300 K	*CN*	6.0±0.2	12.0±0.4	8.2±1.2	6.7±1.1	4.6±1.7	1.1±0.90	0.01±0.12
	r_{max}/Å	2.40	3.15	4.05	3.00	3.39	2.04	3.21
1 GPa/	*r*/Å	1.92	2.58	3.14	2.24	2.79	2.07	2.33
300 K	*C.N.*	5.0±1.3	10.2±2.6	8.2±1.8	6.2±2.0	6.3±1.8	1.3±1.0	0.78±0.90
	r_{max}/Å	2.37	3.09	3.87	2.91	1.8	2.13	3.15
1 GPa/	*r*/Å	1.92	2.61	3.21	2.31	2.85	1.98	2.19
500 K	*C.N.*	4.2±2.0	8.6±4.0	8.4±2.2	4.0±2.0	7.6±1.7	1.5±1.1	1.12±1.27
	r_{max}/Å	2.58	3.18	4.17	2.88	3.78	2.22	2.85
2 GPa/	*r*/Å	1.92	…	3.12	…	2.71	……	2.35
500 K	*CN.*	5.3±0.9	…	14.2±1.5	…	9.5±1.5	……	0.65±0.75
	r_{max}/Å	2.32	…	4.19	…	3.63	……	3.00
4 GPa/	*r*/Å	1.93	2.61	3.14	2.18	2.74	1.74	2.36
500 K	*CN*	5.6±0.7	11.4±1.2	14.0±1.4	6.2±1.6	8.4±1.6	0.88±0.84	0.33±0.54
	r_{max}/Å	2.31	3.07	4.15	2.72	3.69	1.98	3.30

shells. Ow and Hw mean oxygen and hydrogen atoms, respectively, in a water molecule. Despite the constant Mg-O_W(I) distance, the Mg-H_W(I) distance is sensitive to pressure and temperature. At 300 K, the compression to 1 GPa does not significantly affect the Mg-H_W(I) distance at 2.58 Å but the latter becomes longer and reaches 2.61 Å at 500 K.

Cl^- solvation: Cl^- is a structure-breaking ion and has no distinct solvation shell under ambient conditions. The Cl–O_W (I) and Cl–H_W (I) distances follow an expected change with pressure and temperature, i.e., both distances decrease upon compression and increase with elevating temperature. The *CN* of Cl-Ow(I) shows a substantial pressure dependence from 8 at 0 GPa/300 K to 10 at 4 GPa/500 K. On the contrary, the *CN* of Cl-H(I) does not change significantly with pressure and temperature, suggesting linear Cl…H hydrogen bonds. It should be noted that the third peak evolved at 8 Å at 4 GPa/500 K and that Cl^- behaves like a structure-making ion. With elevating temperature and pressure, the first peak gradually becomes more asymmetrical toward the longer distance, suggesting more water molecules entering the solvation shell of Cl^-.

Solvent Water

As seen in Table 1, the *CN* of Ow(I)-Ow(I) increases from 4.6 at 0 GPa/300 K to 8.4 at 4 GPa/500 K, demonstrating the transformation from the tetrahedral network structure to a dense random packing structure in the GPa pressure range. However, the *CN* of the intermolecular Ow(I)-Hw(I) does not change significantly with temperature and pressure, suggesting a linear Ow(I)…Hw(I) hydrogen bond in the GPa pressure range. The 3D structure obtained by EPSR is shown in Fig. 2.

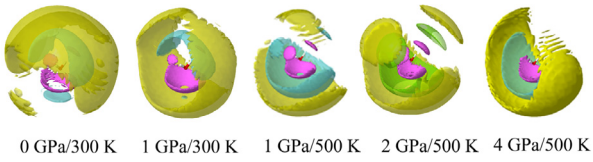

Figure 2. Spatial density functions of the water molecules around a central water molecule as a function of temperature and pressure.

References

[1] Y. Katayama et al., Phys. Rev. B, **81**, 014109 (2020).
[2] T. Yamaguchi et al., J. Mol. Liq., **176**, 44 (2012).
[3] T. Yamaguchi et al., Liquids, **3**, 288 (2023).

T. Yamaguchi[1,2], N. Fukuyama[2], K. Yoshida[2], Y. Katayama[3], S. Machida[4], and T. Hattori[5]
[1]*Key Laboratory of Salt Lake Resources Chemistry of Qinghai Province, Qinghai Institute of Salt Lakes, Chinese Academy of Sciences;* [2]*Faculty of Science, Fukuoka University;* [3]*Synchrotron Radiation Research Center, National Institutes for Quantum and Radiological Science and Technology;* [4]*Neutron Science and Technology Center, CROSS;* [5]*Neutron Science Section, Materials and Life Science Division, J-PARC Center*

Field Control of Quasiparticle Decay in a Quantum Antiferromagnet

The concept of a quasiparticle has been successful in explaining various types of low-energy excitations in many-body systems, including charge, spin, and lattice. Using a spectroscopic approach, a weakly coupled quasiparticle with a long lifetime can be probed as a well-defined excitation, allowing identification of the effective Hamiltonian and basic understanding of the system. Momentum-resolved spectroscopy has permitted investigations into the intricate structure of spectra, revealing the effect of quasiparticle interactions that results in the renormalization of the dispersion and instability of the quasiparticle.

The microscopic phenomena in the spectra affect bulk properties of materials. In the thermoelectric material PbTe, the interaction between longitudinal acoustic and transverse optical modes (here, the quasiparticles are phonons) induces the decay and overdamping of the former phonon in the low energy region, leading to low conductivity of thermal current [1]. The instability of the quasiparticle is key for the current to exist in bulk property.

Two examples illustrate the fact that the instability of the quasiparticle is changed by the interaction between the one-quasiparticle and two-quasiparticle continuum [2]. An example for a case of strong interaction is found in the longitudinal sound wave, phonon, in superfluid ^{4}He [3]. The spectrum in low energy exhibits a local minimum with energy Δ, called a roton, whose qualitative behavior is explained by the Feynman and Cohen (FC) harmonic dispersion. However, the spectrum does not exceed the critical energy level of 2Δ, which is the lower boundary of the two-phonon continuum. The strong interaction between the one-phonon and continuum reduces the one-phonon energy, and the one-phonon stays at 2Δ outside the continuum. On the FC dispersion beyond the critical energy, bare one-phonon decays into a pair of rotons, and a remnant of one-phonon which is ascribed to the bound state of two-phonon waswere observed. The phenomenon is considered universal in bosonic systems and has also been observed in a spin-gap antiferromagnet $BiCu_2PO_6$ [4].

An example for the weak interaction is found in a two-dimensional quantum magnet, piperazinium hexachlorodicuprate (PHCC) [3]. This case is simple; the quasiparticle decays in the continuum, and a remnant one-magnon is probed as a broad excitation. This work tests is that if one tunes the interaction between a quasiparticle and the continuum in an identical material by applying an external field, would the quasiparticle decay behavior change?

This study [5] examines magnon decay in a triangular lattice quantum antiferromagnet $RbFeCl_3$. Magnetism of Fe^{2+} ion surrounded by Cl^- octahedra with trigonal distortion is effectively described by an S = 1 spin with strong easy-plane anisotropy. Fe^{2+} ions form one-dimensional ferromagnetic chain along the crystallographic *c*-axis, and the interchain interaction in the triangular lattice in the *ab*-plane is antiferromagnetic. At low temperatures the compound exhibits a non-collinear 120° structure due to the frustration. The spectrum was qualitatively similar to that of the pressure-induced ordered state in the isostructural compound $CsFeCl_3$ near the quantum critical point (QCP) [6], which cannot be explained by standard linear spin wave theory. Instead, the strong hybridization of the transverse and longitudinal fluctuations resulting from the non-collinear magnetic structure renormalizes the magnetic excitation, as explained by the linear extended spin wave theory (LESW) [3]. Because a non-collinear magnetic structure is realized near the QCP and the excitation is strongly hybridized with longitudinal fluctuation, magnon decay is anticipated in wide four-dimensional momentum-energy space. Furthermore, gapless behavior and a large dispersion perpendicular to the triangular lattice yield a two-magnon continuum covering the whole region of one-magnon excitation.

In this study, we performed inelastic neutron scattering (INS) measurements on $RbFeCl_3$ in zero field at the High Resolution Chopper (HRC) spectrometer installed at BL12 to identify the spin Hamiltonian as shown in Fig. 1.

Then, we performed INS measurements in the magnetic field to study the magnon decay and the interaction between single magnons and the two-magnon continuum. We observed a simple magnon decay in a low field, where the interaction is small, and a magnon avoiding decay in a high field, where the interaction was large, as shown in Fig. 2. Thus, we succeeded in controlling the magnon decay using the field. In contrast, with the avoided phonon decay in superfluid ^{4}He and magnons in magnetic materials previously reported [2, 4], the phenomenon was observed in the presence of a two-quasiparticle continuum, indicating that the phenomenon is not limited to outside the continuum, but also occurs inside.

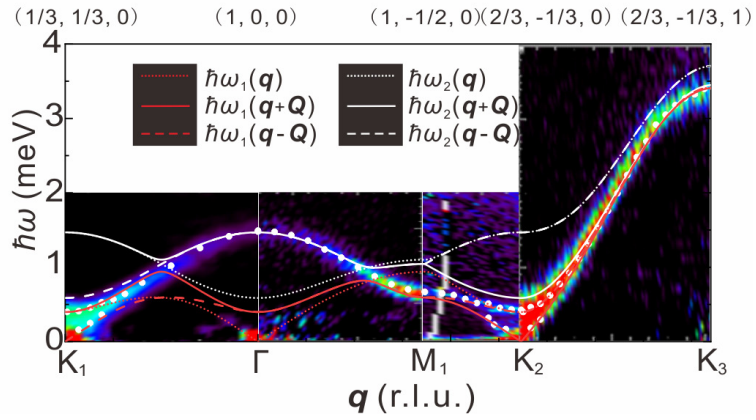

Figure 1. Inelastic neutron scattering (INS) spectra measured at zero field. False color map of the INS spectra acquired at HRC. White circles represent peak energy obtained from fitting results of constant ***q*** cuts. White and red curves are dispersion relations calculated by applying the linear extended spin wave theory using the best fit parameters.

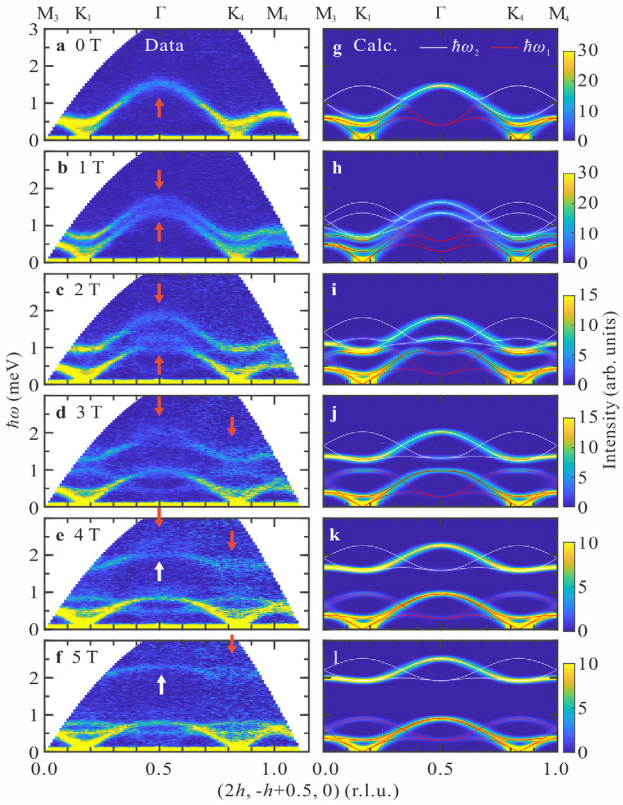

Figure 2. False color map of inelastic neutron scattering (INS) spectra and calculated two-magnon density of state in $RbFeCl_3$. **a-l**: Magnetic field (*H* // *c*-axis) dependences of the false color maps for observed (**a-f**) and calculated (**g-l**) INS spectra. Red arrows in **a-f** indicate broadening linewidth. White arrows in **e** and **f** indicate magnons avoiding decay. White and red solid curves in **g-l** are one-magnon dispersion relations of $\hbar\omega_1$ and $\hbar\omega_2$ modes calculated using linear extended spin wave theory (LESW) using the best fit parameters. The calculated spectra are convoluted by the instrumental resolution.

References

[1] O. Delaire, J. Ma, K. Marty, A. F. May, M. A. McGuire, M. H. Du, D. J. Singh, A. Podlesnyak, G. Ehlers, M. D. Lumsden, and B. C. Sales, Nat. Mater. **10**, 614 (2011).

[2] R. Verresen, R. Moessner, and F. Pollmann, Nat. Phys. **15**, 750 (2019).

[3] M. B. Stone, I. A. Zaliznyak, T. Hong, C.L. Broholm, and D. H. Reich, Nature (London) **440**, 187 (2006).

[4] K. W. Plumb, K. Hwang, Y. Qiu, L. W. Harriger, G. E. Granroth, A. I. Kolesnikov, G. J. Shu, F. C. Chou, C. Rüegg, Y. B. Kim, and Y-J. Kim, Nat. Phys. **12**, 224 (2016).

[5] S. Hasegawa, H. Kikuchi, S. Asai, Z. Wei, B. Winn, G. Sala, S. Itoh, and T. Masuda, Nat Commun **15**, 125 (2024).

[6] S. Hayashida, M. Matsumoto, M. Hagihala, N. Kurita, H. Tanaka, S. Itoh, T. Hong, M. Soda, Y. Uwatoko, and T. Masuda, Sci. Adv. **5**, eaaw5639 (2019).

S. Hasegawa[1], H. Kikuchi[1], S. Asai[1], Z. Wei[1], B. Winn[2], G. Sala[2], S. Itoh[3], and T. Masuda[1,3,4]

[1]*Institute for Solid State Physics, The University of Tokyo;* [2]*Neutron Scattering Division, Oak Ridge National Laboratory;* [3]*Institute of Materials Structure Science, High Energy Accelerator Research Organization;* [4]*Trans-scale Quantum Science Institute, The University of Tokyo*

Direct Observations of Spin Fluctuations in Hedgehog–anti-hedgehog Spin Lattice States in $MnSi_{1-x}Ge_x$ (x = 0.6 and 0.8) in Zero Magnetic Field

1. Introduction

The interplay between conduction electrons and magnetism has been attracting remarkable attention in condensed matter physics. In particular, noncoplanar magnetic orders showing anomalous Hall effects of unconventional origins have been intensively investigated. One example is the topological Hall effect arising from magnetic skyrmion lattices. The magnetic skyrmions, which were discovered in a noncentrosymmetric cubic helimagnet MnSi [1], are topologically nontrivial vortex-like spin objects. Their non-coplanar spin arrangements have finite scalar spin chirality defined by three neighboring magnetic moments as $S_i \cdot (S_j \times S_k)$, which can induce an effective magnetic field acting only on conduction electrons. This effect is termed a topological Hall effect, and was indeed observed in the previous Hall resistivity measurements on MnSi [2].

The topological Hall effect was also found in a short-period helimagnet MnGe [3]. This material is isostructural to MnSi, which belongs to the cubic space group of $P2_13$, but exhibits a different kind of topological spin order. The magnetic ground state of MnGe was determined to be a triple-q state composed of q-vectors of (q,0,0), (0,q,0), and (0,0,q), which results in a hedgehog–anti-hedgehog spin lattice (HSL) state. By calculating the effective magnetic fields arising from the scalar spin chirality, it turns out that the HSL state has an equal number of effective magnetic monopoles and antimonopoles. Although the effective magnetic fields between the effective monopoles and antimonopoles are canceled out at zero external magnetic field, an application of an external magnetic field leads to the displacement of the monopoles and antimonopoles, which induces a net effective magnetic field acting on the conduction elections in the sample.

Several unsolved problems in the topological Hall effect in MnGe still remain. One is the sign reversal of the Hall resistivity near the critical temperature. The sign of the topological Hall effect is determined by the direction of the effective magnetic field and the coupling between the conduction electrons and localized magnetic moments, which are supposed to be independent of temperature. Nevertheless, the Hall resistivity in MnGe changes from positive to negative as the temperature is lowered below the critical temperature [3]. A recent theoretical study suggested that the positive Hall resistivity can be explained by skew scattering due to the spin fluctuations of the locally correlated spin clusters with a nonzero average of sign-biased scalar spin chirality [4]. To corroborate this scenario, we need to quantitatively investigate how such spin fluctuations develop with varying temperature.

In the present study, we investigate the spin fluctuations of polycrystalline $MnSi_{1-x}Ge_x$ samples with $x = 0.6$ and 0.8, which exhibit the HSL states, by means of time-of-flight (TOF) neutron inelastic scattering and neutron resonance spin-echo spectroscopy.

2. Experiment

Polycrystalline samples of $MnSi_{1-x}Ge_x$ with $x = 0.6$ and 0.8 were grown by high-pressure synthesis method. These samples were also used in the previous small-angle neutron scattering studies to determine the magnetic structures [5]. TOF neutron inelastic scattering experiments were performed at the High-Resolution Chopper spectrometer (HRC) at BL12 [6] in the Materials and Life Science Experimental Facility (MLF) of J-PARC to obtain the magnetic scattering intensity distribution in the wide Q-E space with varying temperature. We also performed neutron spin echo (NSE) measurements at BL06 in the MLF of J-PARC. Specifically, we employed the Modulation of IntEnsity by Zero Effort (MIEZE) method in the NSE measurements [7], by which we can detect fluctuations of the magnetic moments in the timescale of pico-to-nano second. The polycrystalline samples were loaded in Al sample cell with a small amount of He gas for thermal exchange. We employed a closed-cycle refrigerator to cool the samples to low temperatures.

3. Results and discussions

In this report, we focus on the results of neutron spin echo measurements on the x = 0.8 sample, which exhibits the same magnetic ground state as that in undoped MnGe. Figures 1(a) – 1(d) depict the intensity profiles as a function of momentum Q in the $x = 0.8$ sample at four representative temperatures of $T = 50$, 100, 130, and 150 K. We observed the sharp peak attributed to the long-range order at 50 K, which was well below the

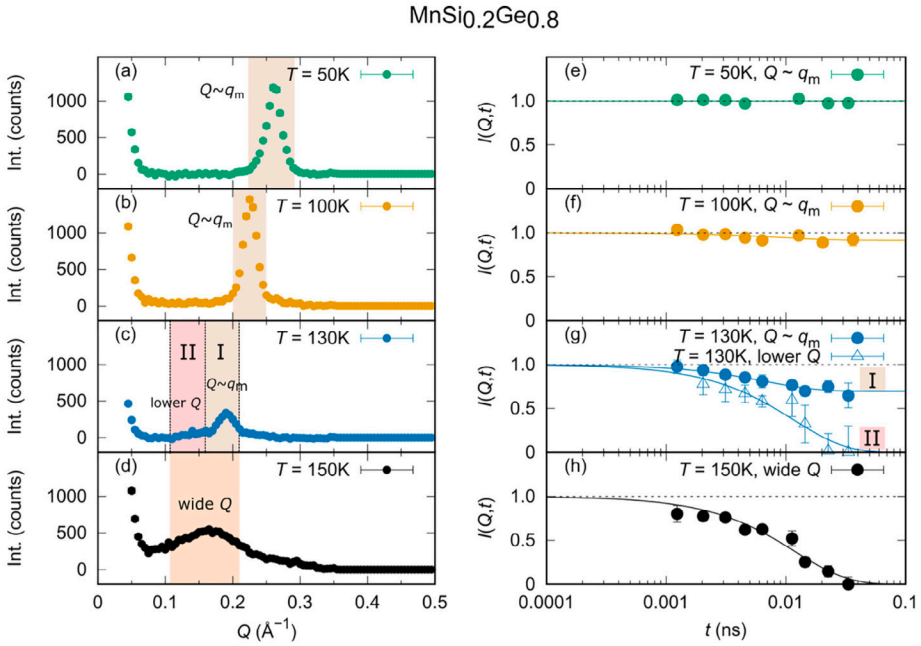

Figure 1. MIEZE-NSE experimental results for x = 0.8. [(a) – (d)] Q dependence of intensity at four representative temperatures, and [(e) – (h)] the intermediate scattering function of $I(Q, t)$ deduced from the selected Q range given in (a) – (d). This figure is taken from Ref. [8].

critical temperature of this sample (150 K). As the temperature increases, the peak moves toward the low-Q region, and broadens. At the critical temperature of 150 K, it completely becomes a broad diffuse scattering.

To distinguish the contributions from the static and fluctuating spin components, we obtained the intermediate correlation function $I(Q, t)$ for the selected Q-ranges highlighted by the colored area in Figs. 1(a) – 1(d) from the NSE data. At 50 K, the observed I(Q, t) values remain in a state of unity up to approximately 0.1 ns, which means that the magnetic moments are static in the timescale of up to 0.1 ns (Fig. 1(e)). However, at 100 K, we observed a slight deviation of $I(Q, t)$ from the unity (Fig. 1(f)). This unambiguously shows that spin fluctuations start to develop at this temperature. The observed $I(Q,t)$ data at high temperatures clearly show the temporal decay of the spin correlations, and are well described by the exponential decay functions as shown in the solid lines in Figs. 1(g) and 1(h). We compared these results with the temperature dependence of the Hall resistivity of this sample, revealing that the sign reversal of the Hall resistivity occurs in the temperature range where the spin fluctuations are detected.

We also performed MIEZE-type NSE measurements on the x = 0.6 sample and demonstrated that the sign reversal of the Hall resistivity is attributed to the spin fluctuations. Details of the analysis and comparisons between the neutron results obtained at BL06 and BL12 and the Hall resistivity data are covered in the published paper [8].

References

[1] S. Mühlbauer *et al.*, Science **323**, 915 (2009).
[2] A. Neubauer *et al.*, Phys. Rev. Lett. **102**, 186602 (2009).
[3] N. Kanazawa *et al.*, Phys. Rev. Lett. **106**, 156603 (2011).
[4] H. Ishizuka and N. Nagaosa, Sci. Adv. **4**, eaap9962 (2018).
[5] Y. Fujishiro *et al.*, Nat. Commun. **10**, 1059 (2019).
[6] S. Itoh *et al.*, Nucl. Instrum. Methods Phys. Res., Sect. A **631**, 90 (2011).
[7] T. Oda *et al.*, Rev. Sci. Instrum. **87**, 105124 (2016).
[8] S. Aji *et al.*, Phys. Rev. B **108**, 054445 (2023).

S. Aji[1], T. Oda[1], Y. Fujishiro[2], N. Kanazawa[3], H. Saito[1], H. Endo[4,5], M. Hino[6], S. Itoh[4,5], T-h Arima[2,7], Y. Tokura[2,8,9], and T. Nakajima[1,2]
[1]Institute for Solid State Physics, The University of Tokyo; [2]RIKEN Center for Emergent Matter Science; [3]Institute of Industrial Science, The University of Tokyo; [4]Neutron Science Section, Materials and Life Science Division, J-PARC Center; [5]Institute of Materials Structure Science, KEK; [6]Institute for Integrated Radiation and Nuclear Science, Kyoto University; [7]Department of Advanced Materials, Science, The University of Tokyo; [8]Department of Applied Physics and Quantum Phase Electronics Center, The University of Tokyo; [9]Tokyo College, The University of Tokyo

Bond-Dependent Anisotropy and Magnon Decay in Cobalt-Based Kitaev Triangular Antiferromagnet

1. Introduction

Finding a quantum state of matter, such as quantum spin liquid (QSL), is arguably one of the most important topics in condensed matter physics [1]. The Kitaev model, which spins on a honeycomb lattice with bond-dependent Ising-like anisotropic interactions, is the rare example of QSL ground state as an exact solution [2]. Unfortunately, most of the Kitaev model candidates not only have bond-dependent anisotropy but also have magnetic order due to the finite non-Kitaev type interactions [3]. However, the bond-dependent anisotropy itself manifests unusual spin dynamics even with magnetic order. Recent research suggests that bond-dependent anisotropy can stabilize exotic magnetic phases on the geometrically frustrated lattice, such as triangular lattice [4]. In this report, we describe our studies of the spin dynamics of the first example of triangular lattice with strong bond-dependent anisotropy: CoI_2 [5]. Because of the spin-orbit entanglement in Co^{2+} ions and edge-sharing networks of CoI_6 octahedrons, CoI_2 is the ideal candidate for exploring the potential bond-dependent anisotropy in the triangular lattice.

2. Experimental Methods

To uncover the existence of bond-dependent anisotropy, we measured the dynamical spin structure factor using the inelastic neutron scattering (INS) technique. All the INS measurements were performed using the cold-neutron disk chopper spectrometer AMATERAS at J-PARC in Japan [6]. The 5-gram CoI_2 single crystal was prepared using the Bridgman method. The single crystal was aligned and mounted on an aluminum holder and covered with the CYTOP. After the mounting, the sample was cooled down to $T = 4$ K for the ordered state and 13 K for the paramagnetic state. We used three different incident energy values $E_i = 52.43$, 17.26, and 8.48 meV via repetition-rate multiplication method.

3. Results and Discussions

First, to find the signature of bond-dependent anisotropy, we measured the dynamical spin structure factor (DSSF) of the paramagnetic state at 13 K, which is just above the magnetic ordering temperature $T_N = 9$ K. Analyzing the paramagnetic state allows us to extract the exchange interaction of the system without considering the quantum fluctuations. Figure 1(a) shows the magnetic diffuse scattering intensity. For the microscopic analysis, we started with a magnetic Hamiltonian with J_1-J_2-J_3 further nearest neighbor model and J_1-$J_{\pm\pm}$-J_3, which includes the bond-dependent anisotropy $J_{\pm\pm}$. Figure 1(b) shows a comparison of the magnetic diffuse scattering pattern of the best parameter set of each model. From the hexagonal pattern inside the Brillouin zone, it becomes clear that the J_1-$J_{\pm\pm}$-J_3 model is well-matched with the data. Furthermore, using the semiclassical Landau-Lifshitz dynamics [7],

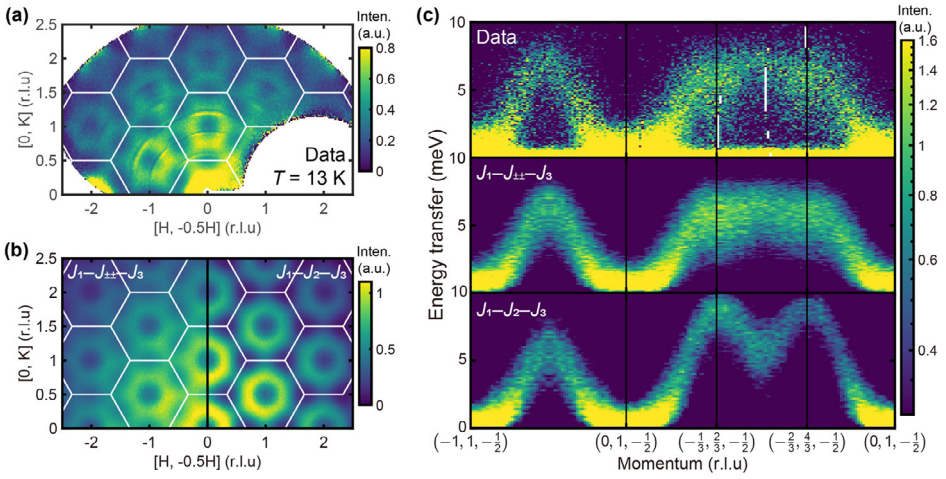

Figure 1. Energy-resolved magnetic diffuse scattering in the paramagnetic state of CoI_2. (a) Magnetic diffuse scattering intensity measured at $T = 13$ K and integration by energy transfer $E = [1, 6]$ meV and along L direction with $L = [-0.7, 0.7]$ r.l.u. (b) Comparison of the J_1-$J_{\pm\pm}$-J_3 model and J_1-J_2-J_3 model. (c) Energy-momentum slice of the scattering intensity along the high-symmetric points in the Brillouin zone and comparison with the model.

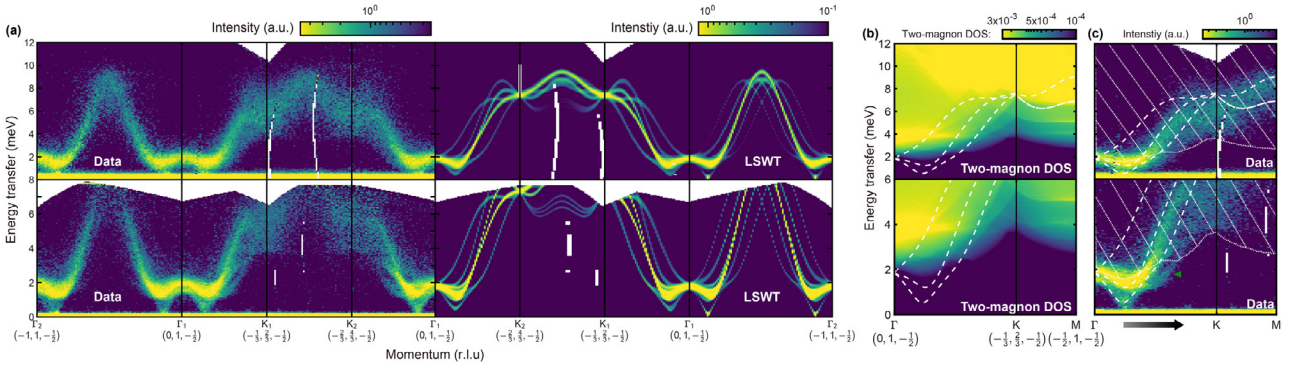

Figure 2. (a) Energy- and momentum-resolved INS data (left) and LSWT simulation (right) at the magnetically ordered state T = 4 K. The logarithmic scale was used to improve the presentation of data. The upper row data is used incident energy E_i = 17 meV and the lower row data is used E_i = 8 meV. (b) Two-magnon density-of-states simulation based on the LSWT. (c) INS data compared to the kinematic extent of the two-magnon continuum. The dotted line represents the boundary of the two-magnon continuum, and the dashed lines indicate the LSWT solution.

we can also simulate the energy-resolved magnetic diffuse scattering. Figure 1(c) represents the measured DSSF signal at the paramagnetic state and simulation of each model. The minimal model with bond-dependent anisotropy (J_1-$J_{\pm\pm}$-J_3) perfectly overlapped with the data, especially for the Brillouin zone boundary. We found the best parameter set as J_1 = –2.73 meV, $J_{\pm\pm}$ = –0.41 meV, and J_3 = 1.01 meV.

With this knowledge, we measured the spin-wave spectrum of CoI_2 at T = 4 K in the ordered phase to understand the spin dynamics. Figure 2(a) shows the comparison between the energy and momentum-resolved INS data and the linear spin-wave theory (LSWT) simulations. The experimental data show strong linewidth broadening near the Brillouin zone boundary. From the previous magnetic diffuse scattering analysis, we calculated the LSWT, including the instrumental resolution effect. However, our simulation cannot explain the strong broadening intensity, which indicates the intrinsic quantum fluctuation.

To estimate the intrinsic magnon decay, we calculated the two-magnon density of states (DOS) using the LSWT formalism (See Fig. 2(b)). Our DOS simulation perfectly matched the region where broadening starts. The origin of the strong magnon decay can, in principle, arise from the three-magnon interaction term, which can be caused by either non-collinear magnetic order [8] or bond-dependent anisotropy [9]. Fortunately, CoI_2 fulfilled both conditions. Therefore, we concluded that the strong magnon decay is realized from the interplay of bond-dependent anisotropy and the non-collinear magnetic order.

4. Summary

In summary, we found the bond-dependent anisotropy on the quantum spin triangular lattice antiferromagnet CoI_2 by INS measurement. We further revealed the rich spin dynamics of the Kitaev physics cooperating with the geometrical frustration. We also observed the substantial magnon decay and selectively avoided decay over the broad momentum space. Our findings are essential for understanding the complex interplay between bond-dependent anisotropy and geometrical frustration in quantum magnets.

References

[1] L. Balents, Nature **464**, 199-208 (2010).
[2] A, Kitaev, Ann. Phys. -New York **321**, 2-111 (2006).
[3] H. Takagi *et al*. Nat. Rev. Phys. **1**, 264 (2019).
[3] P. Maksimov *et al*. Phys. Rev. X **9**, 021017 (2019).
[4] C. Kim *et al*. Nat. Phys. **19**, 1624 (2023).
[5] K. Nakajima *et al*. J. Phys. Soc. Jpn 80, SB028 (2011).
[6] https://github.com/SunnySuite/Sunny.jl
[7] A. Chernyshev *et al*. Phys. Rev. B 79, 144416 (2009).
[8] S. M. Winter *et al*. Nat. Comm. 8, 1152 (2017).

C. Kim[1,2], S. Kim[3], P. Park[1,2], T. Kim[1,2], J. Jeong[1,2], S. Ohira-Kawamura[4], N. Murai[4], K. Nakajima[4,5], A. L. Chernyshev[6], M. Mourigal[7], S.-J. Kim[3], and J.-G. Park[1,2]

[1]*Center for Quantum Materials, Seoul National University;* [2]*Department of Physics and Astronomy, Seoul National University;* [3]*Department of Chemistry and Nano Science, Ewha Womans University;* [4]*Neutron Science Section, Materials and Life Science Divi-sion, J-PARC Center;* [5]*Materials Science Research Center, JAEA;* [6]*Department of Physics and Astronomy, University of California, Irvine;* [7]*School of Physics, Georgia Institute of Technology*

Neutrons and the Muddy Clay/Water Interface

1. Introduction

Water is not only one of most abundant molecules on Earth, but also one of the most anomalous due to its unusual thermodynamic properties. The interaction of water with rocks at the solid/water interface has led to the creation of complex systems, including clay minerals [1]. In turn, the interaction mechanisms of water and clay mineral surfaces, or more specifically water and hydrated ions, at the nanoscale controls various aspects of geology, environmental science, petroleum and geotechnical engineering, seismology, atmospheric science, astrobiology and catalysis [2].

One fascinating point to consider is that the timescale associated with a particular experimental approach will give information specific to a dynamical process occurring in the muddy world of clay minerals, as shown in Fig. 1. Vibrational transitions will be detected in the timescale from 10^{-15} to 10^{-12} s, while considerably slower motions (10^{-11} to 10^{-3} s) are observed in NMR, EPR, or neutron scattering [3]. In this sense, the main advantage of incoherent quasi-elastic neutron spectroscopy (QENS) is its power to provide details on total water diffusion.

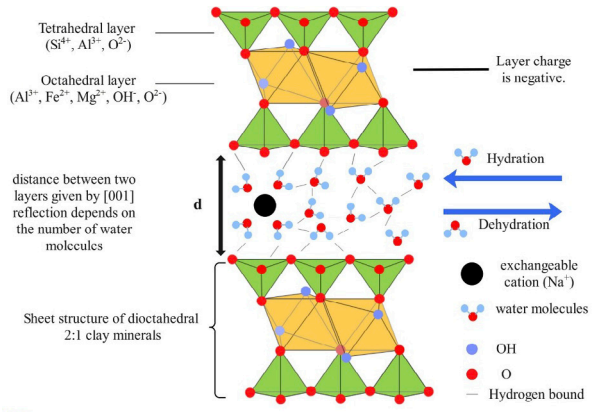

Figure 1. Atomic structure of a 2:1 clay mineral that consists of two basic units, an octahedral sheet (pink) and a tetrahedral sheet (green) with water molecules and exchange cations in the interlayer. The number of water molecules controls the distance, d, between the layers.

Nevertheless, differentiating the dynamic behavior of the water populations in the interlayer space from those in the external surfaces remains a challenge. To overcome this, we carried out QENS studies at variable temperature on sodium forms of two different smectite clay mineral powders, montmorillonite (Mt) and hectorite (Ht) hydrated at a pseudo one-layer hydration (1LH) state, using AMATERAS (BL14) at MLF (J-PARC, Japan). Mt and Ht were selected due to their different layer charges and different octahedral and tetrahedral layer compositions. Before the QENS experiments, the hydration levels of the samples were verified using NOVA (BL21).

The results obtained from the analysis of QENS data using an improved jump-diffusion and rotation-diffusion model (rJRM) [4] better described the behavior of the confined water giving direct evidence of differences in H-bonding of interlayer water with surface oxygens in low hydration states that are crucial for improving functional properties [5].

2. Multiscale relaxation processes: Critical role of water–cation and water–surface interactions

In complex systems that show multiscale relaxation, such as hydrated clay minerals, the srJRM model provided excellent fits of QENS data. From the obtained fitting parameters, several important conclusions were drawn and contributed to a novel and realistic description of these nanomaterials at the atomic scale. For instance, it was possible to fully describe the rotational dynamics and translational diffusion of two distinct populations of interlayer water: confined, consisting of remaining water molecules, including those not bonded directly to cations or surfaces, residing within the interlayer, and ultraconfined, which is the nearest-neighbor coordination water bonded to the interlayer cations or surface.

Moreover, the information extracted from the QENS spectra clearly shows the impact of higher layer charge, and thus a greater concentration of interlayer cations in Mt, with higher layer charge, had stronger H-bonding between water and the interlayer surfaces compared to Ht. Slower translational and rotational diffusion were thus observed in Mt. These results can be directly related to a polarization effect induced on the water molecules by both the exchangeable cation and surface charge within the interlayer.

Another interesting point was the strong evidence for a dynamic crossover of both translational and rotational water diffusion that occurred at a lower temperature in Mt (~230 K) than in Ht (~250 K) for confined water, as indicated by the values for Q = 0.4 $Å^{-1}$. Since this dynamic crossover phenomenon was not evidenced for ultraconfined water, we suggest that the shift to lower temperature in Mt was probably controlled mainly by the stronger interaction of water with the higher layer charged surface.

3. Broader implications of our results

Our results have direct relevance to how clay minerals undergo hydration and dehydration processes, form uniaxially isotropic films and control the freezing point of water [6, 7]. They also inform various reactions such as Brønstad acidity or diffusion [8] controlled by exchange cation hydration as well as reactions of water at (bio) interfaces. The latter is also an important question in biology since the local hydration in proteins plays crucial role in preserving their structures and functions. Indeed, it is speculated that in charged proteins the interactions between water and the protein surface are the main driver of diffusive interactions due to the strong binding of water by the acidic amino acids [9]. However, existing experimental techniques still do not offer complete capability for probing such dynamics. By demonstrating that higher layer charge, and thus the presence of more interlayer cations, binds water more strongly, inducing a slowdown of the water molecules points towards the idea that it is the net charge on proteins that governs their solubility. Additionally, knowing that a key requirement for enzymatic function is the presence of bound water–water having significantly slower dynamics than that of bulk water at protein surfaces, our approach can also be applied to the understanding of intercellular function.

4. Future plans

With this work, we have clearly demonstrated that higher layer charge results in greater overall mobility of both structural OH and interlayer water [10, 11]. From these results we also suppose that one cause of the difference observed in the temperature of the dynamic crossover is related to differences in the orientation of OH vectors within the layer structure between the two smectites, which would have different impacts on the H-bonding of water at the interlayer surfaces. To confirm this hypothetic direct effect of anisotropy due to total layer charge, the phenomenon ought to be analyzed in smectite thin films. Such understanding is crucial for improving functional properties. To answer this question, we are analyzing QENS experiments on clay films at different orientations combining AMATERAS (BL14) and DNA (BL02) [11] as part of the J-PARC Long-Term Proposal (proposal no.2018L1000), as shown in Fig. 2. This combination would allow to cover an extended time range between 70 ps and 0.2 ns and explore the mechanism of the local environment in the translational diffusion of the water molecules.

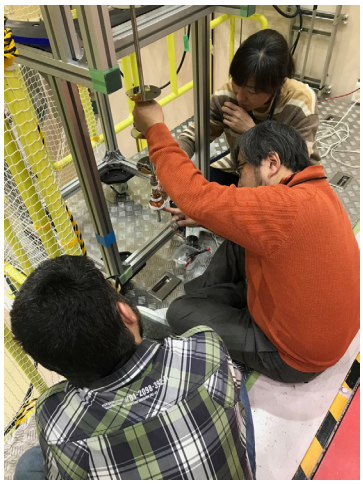

Figure 2. Users placing a sample in BL14. Photo taken by H. N. Bordallo and used with permission from F. J. Villacorta, Seiko Ohira-Kawamura and Yukinobu Kawakita.

References

[1] W. P. Gates et al., Microporous and Mesoporous Materials, **324** 111267 (2021).

[2] M. L. Whittaker et al., Proc. Natl. Acad. Sci. USA, **116** 22052-22057 (2019).

[3] M. L. Martins et al., Applied Clay Science, **96** 22-35 (2014).

[4] Y. H. Chen et al., Physica B, **627** 413542 (2022).

[5] H. Li, et al., The Journal of Physical Chemistry A **128** 261-270 (2024).

[6] W. P. Gates et al., Applied Clay Science **147** 97-104 (2017).

[7] W. P. Gates et al., Applied Clay Science **201** 105928 (2021).

[8] R. Ignazzi et al, The Journal of Physical Chemistry C **121** 23582-23591 (2017).

[9] B. Qiao et al., Proc. Natl. Acad. Sci. USA, **116** 19274-19281 (2019).

[10] M. H. Petersen et al., The Journal of Physical Chemistry C **125** 15085-15093 (2021).

[11] Y. Jin, MSc. thesis, University of Copenhagen (2024).

Hua Li [1], Yin-Hao Zheng[1], W. P. Gates[2], F. J. Villacorta[3], Seiko Ohira-Kawamura[4], Yukinobu Kawakita[4], Kazutaka Ikeda[4,5], and H. N. Bordallo[6]

[1]Department of Physics, Jinan University, Guangzhou; [2]Institute for Frontier Materials, Deakin University; [3]ESS-Bilbao; [4]Neutron Science Section, Materials and Life Science Division, J-PARC; [5]Neutron Industrial Application Promotion Center, CROSS; [6]The Niels Bohr Institute, University of Copenhagen

Mesomorphism in Ionic Liquid-Water

1. Introduction

Ionic liquids (ILs), consisting of cations and anions, have been demonstrated to exhibit self-organizing properties, and size tunable nano-structures are among their most fascinating properties [1]. The nano-heterogeneity of the ILs was evaluated by a prepeak on the small- and wide-angle X-ray scattering patterns (SWAXS). 1-Alkyl-3-methylimidazolium, $[C_n\text{mim}]^+$, where n denotes the alkyl-chain length, is a representative cation. The density functional theory provided conformational degrees of freedom of $[C_{10}\text{mim}]^+$ [2]. Liquid and crystal structures of $[C_n\text{mim}][NO_3]$ were simulated using molecular dynamics (MD) [3]. Experimentally, crystal polymorphs of $[C_{10}\text{mim}][NO_3]$ at low temperature and high pressure were observed using SWAXS [4], where the crystal polymorphs were influenced by conformational and packing polymorphs. Also, nano-confined water (water pocket) in $[C_8\text{mim}][NO_3]$-H_2O was visualized by MD (Fig. 1) [5]. Experimentally, the water pocket was observed in $[C_4\text{mim}][NO_3]$-D_2O using small- and wide-angle neutron scattering (SWANS) [6]. With increasing n, a large water pocket formed in $[C_n\text{mim}][NO_3]$-D_2O (n = 6 and 8) [7]. The spontaneously formed water pocket in $[C_4\text{mim}][NO_3]$-D_2O possessed a slow dynamic property using incoherent quasielastic neutron scattering [8]. Also, the anomalous hydrogen bonding of the water pocket was examined using Raman spectroscopy [9].

2. Experiments

SWANS experiments were conducted on the BL15 (TAIKAN) at J-PARC. Here, the scattering vector Q was defined as $4\pi(\sin\theta)/\lambda$ (Å^{-1}). Considering neutron scattering length density, D_2O was selected as an additive to enhance the water pocket.

3. Results and discussion

$[C_{10}\text{mim}][NO_3]$-D_2O indicated complicated phase behaviors in addition to the water pocket [10]. Using SWANS, the phase diagram was determined (Fig. 2). The 001 Bragg reflection at the position of the prepeak

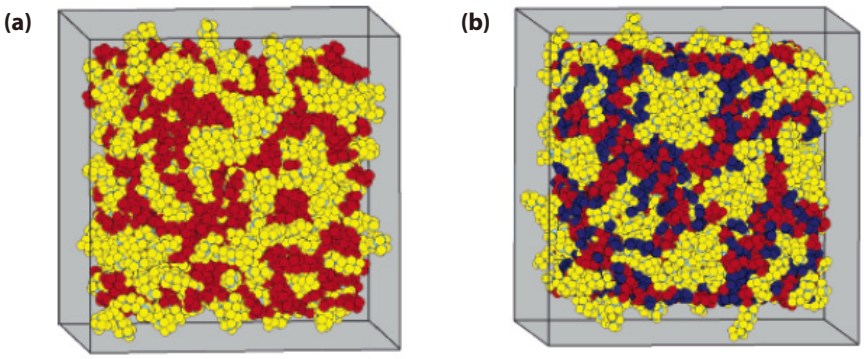

Figure 1. Molecular dynamics simulations of (a) pure $[C_8\text{mim}][NO_3]$ and (b) $[C_8\text{mim}][NO_3]$-80 mol% H_2O. The polar groups, nonpolar groups, and water are colored red, yellow, and dark blue, respectively.

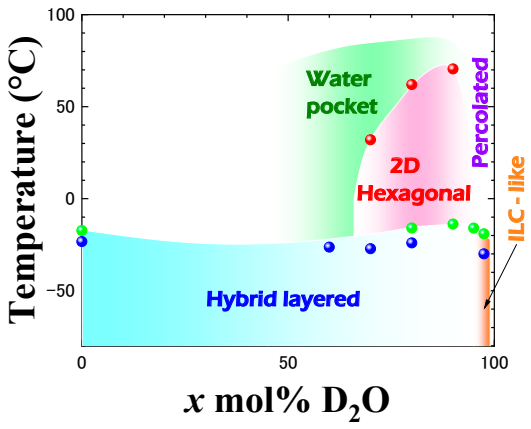

Figure 2. Phase diagram of $[C_{10}\text{mim}][NO_3]$-x mol% D_2O.

was derived from the Ionic liquid crystal (ILC). Two-dimensional (2D) hexagonal structure appeared in the water-rich region. Hybrid layered structure having the longer stacking layer was characterized by 00ℓ Bragg reflections [4]. The sizes of each phase are shown in Fig. 3. Depending on the water concentration, sizes and phases changed sensitively. Self-organized morphologies were derived from a competition between molecular packing coupled with conformations and the water network via hydrogen bonding in the IL.

A more complicated phase diagram was obtained in $[C_{12}mim][I]$-D_2O using SWANS [11]. A water pocket, a smectic A (SmA) phase, a 2D columnar hexagonal (Col_{hex}) phase as a lyotropic mesophase, a bicontinuous cubic (Cub_{bi}) phase as a double gyroid, and a layered crystal phase (Fig. 4) were observed. Additionally, a double gyroid structure in Fig. 5 appeared in the narrow water concentration region. This implies that a specific geometrical factor contributes to the mesomorphic double gyroid structure. For instance, the molar ratio of I^- : D_2O = 1 : 12 provides a concentration of 92.3 mol% D_2O. We deduced that the icosahedral D_2O cluster at the center of I^- was formed [11]. The double gyroid was rigid, reflecting the specific water-mediated network.

Mesoscopic morphologies were spontaneously induced even in a simple IL-water system. Since drastic phase changes were caused by slight changes of the water concentrations, water could play a different role at each circumstance. The phase varieties in the IL-water system are derived from (i) conformational and packing polymorphs, (ii) hydrogen bonding and water network, and (iii) icosahedral hydration.

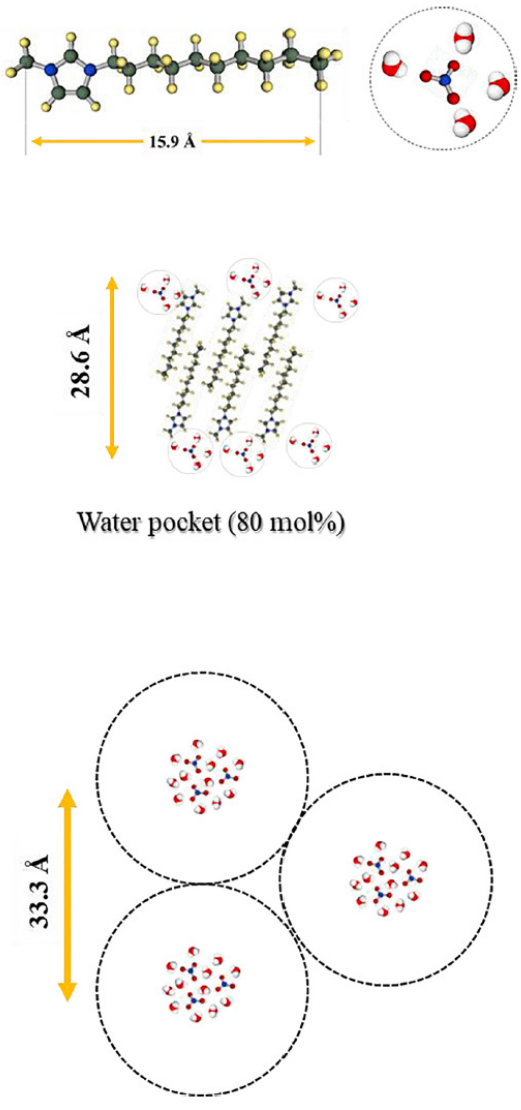

Figure 3. Molecular structure of $[C_{10}mim]^+$, water pocket, and 2D hexagonal structure of $[C_{10}mim][NO_3]$.

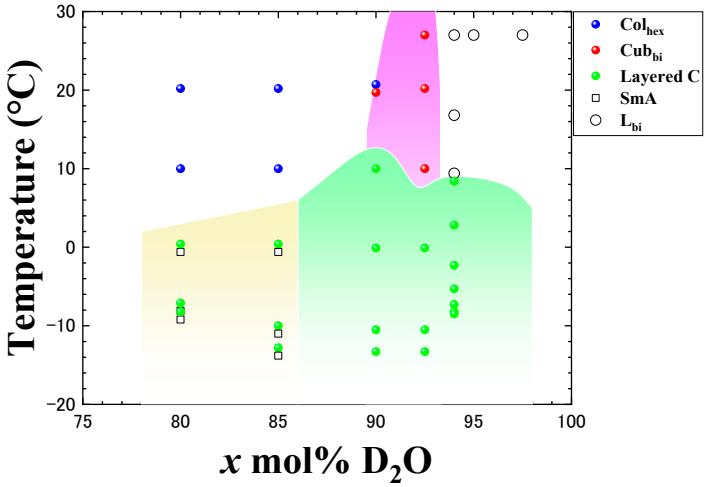

Figure 4. Phase diagram of [C_{12}mim][I]-*x* mol% D_2O.

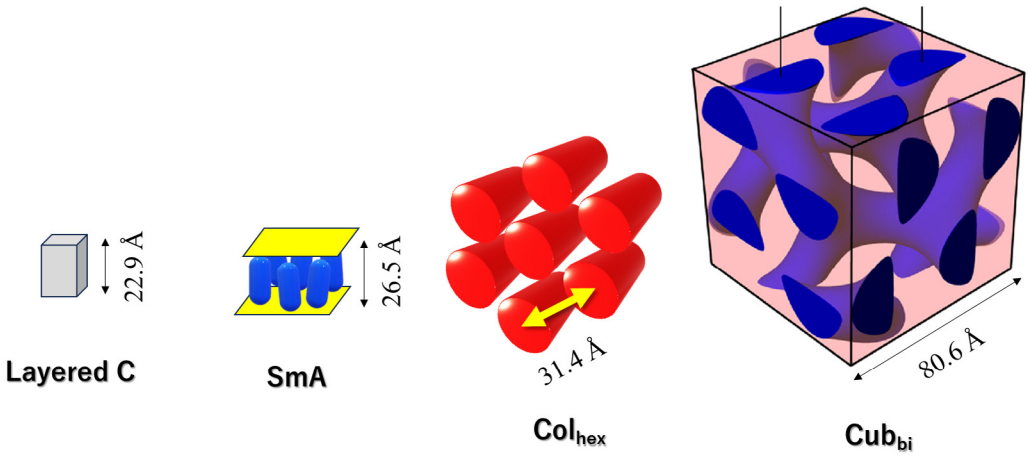

Figure 5. Sizes of layered crystal (C), smectic A (SmA), 2D hexagonal (Col_{hex}), and double gyroid (Cub_{bi}).

References

[1] A. Triolo et. al., J. Phys. Chem. B, **111** 4641 (2007).
[2] H. Abe et al., J. Phys. Chem. Lett., **15** 10668 (2024).
[3] W. Cao et al., J. Phys. Chem. B, **122** 229 (2018).
[4] H. Abe et al., Chem. Phys. Lett., **827** 140685 (2023).
[5] W. Jiang et al., J. Phys. Chem. B, **111** 4812 (2007).
[6] H. Abe et al., J. Phys. Chem. Lett., **5** 1175 (2014).
[7] H. Abe et al., J. Mol. Liq. **346** 117035 (2022).
[8] H. Abe et al., J. Mol. Liq., **264** 54 (2018).
[9] H. Abe et al., J. Mol. Liq., **367** 120383 (2022).
[10] H. Abe et al., J. Mol. Liq., **386** 122551 (2023).
[11] H. Abe et al., J. Mol. Liq. **404** 124952 (2024).

H. Abe[1], F. Nemoto[1], K. Hiroi[2], and S. Takata[2]
[1]*Dept. of Mater. Sci. & Eng. National Defense Academy;* [2]*Neutron Science Section, Materials and Life Science Division, J-PARC Center*

Equation Elucidating the Catalyst-Layer Proton Conductivity in a Polymer Electrolyte Fuel Cell Based on the Ionomer Distribution Determined Using Small-Angle Neutron Scattering

1. Introduction

The performance of polymer electrolyte fuel cells depends on the proton conductivity of the catalyst layers where the proton reacts with oxygen to generate electricity. Because the catalyst layer consists of platinum-supported carbon particles coated with proton-conducting ionomer, the distribution of the ionomer coating must be optimized to enhance proton conduction.

Our previous study using contrast-variation small-angle neutron scattering has revealed that homogeneously adsorbed ionomers and heterogeneously deposited ionomers coexist in a catalyst layer [1]. Since the homogeneously adsorbed ionomers form thin films on the carbon particles, their proton conductivity is believed to be suppressed [2]. Here, we model the proton conduction in the catalyst layer based on the ionomer distribution, taking into account the conductivity suppression by thinning [3].

2. Experimental

The samples were catalyst layers with different types of platinum-supported carbon (Pt/C) and different ionomer-to-carbon weight ratio (I/C). Vulcan and Ketjenblack were selected as a solid and nanoporous carbon support, respectively.

For the catalyst layers, scanning electron microscope (SEM) images were obtained using a Hitachi High-Tech S-5500, and small-angle neutron scattering (SANS) measurements were performed using the instrument at BL15 of J-PARC under 100% relative humidity (RH). The proton conductivity (σ) of the catalyst layers was measured at various RHs by electrochemical impedance spectroscopy (EIS).

3. Results and discussion

Figure 1 shows SEM images of the two types of catalyst layers with four I/C. The aggregation of Pt/C and the adsorbed ionomers (indicated by circles) formed a porous structure. Pt nanoparticles (the white dots indicated by arrows) were more clearly observed in Vulcan than in Ketjenblack. The deposited ionomers (indicated by squares) were found around the aggregates and were more abundant in Vulcan than in Ketjenblack.

Figure 2 shows the SANS spectra of the catalyst layers and the Pt/Cs (I/C = 0). In all cases, the intensity of the peak at q = 0.15 $Å^{-1}$ increased with increasing I/C. The peak corresponds to a periodicity of approximately

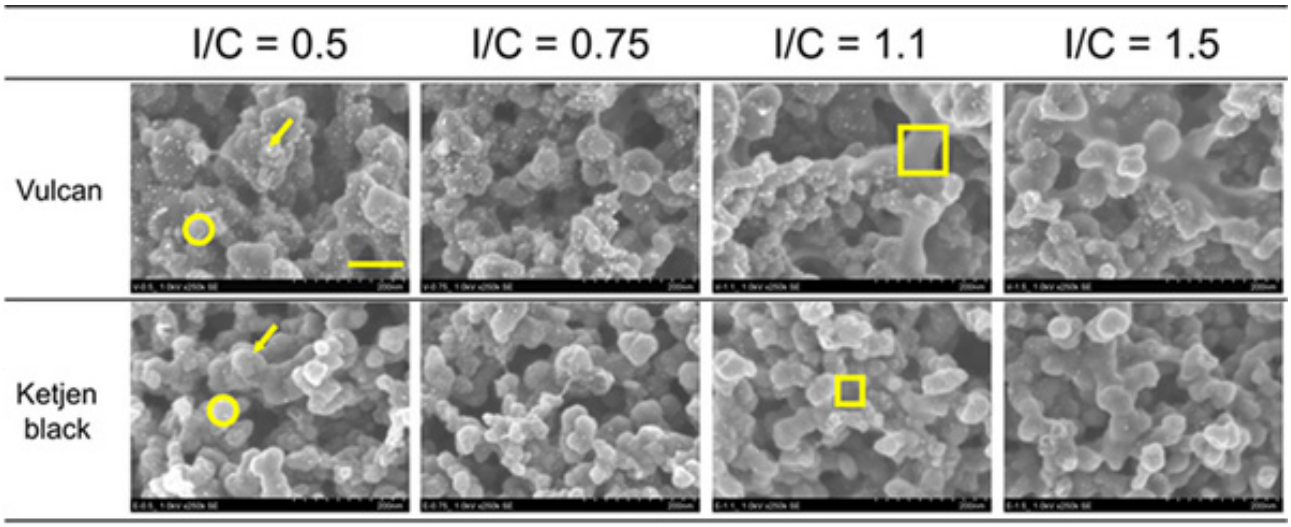

Figure 1. Scanning electron microscopy images of the liquid-nitrogen fractured cross sections of the two types of catalyst layers with various ionomer-to-carbon mass (I/C) ratios (scale bar in the top-left image: 100 nm). The aggregated particles are Pt/C-coated with ionomers where the boundaries are unclear (indicated with circles), and several ionomer bridges are observed between the particles in certain images (indicated with squares). The small white spots on the particles correspond to the Pt catalyst (indicated with arrows).

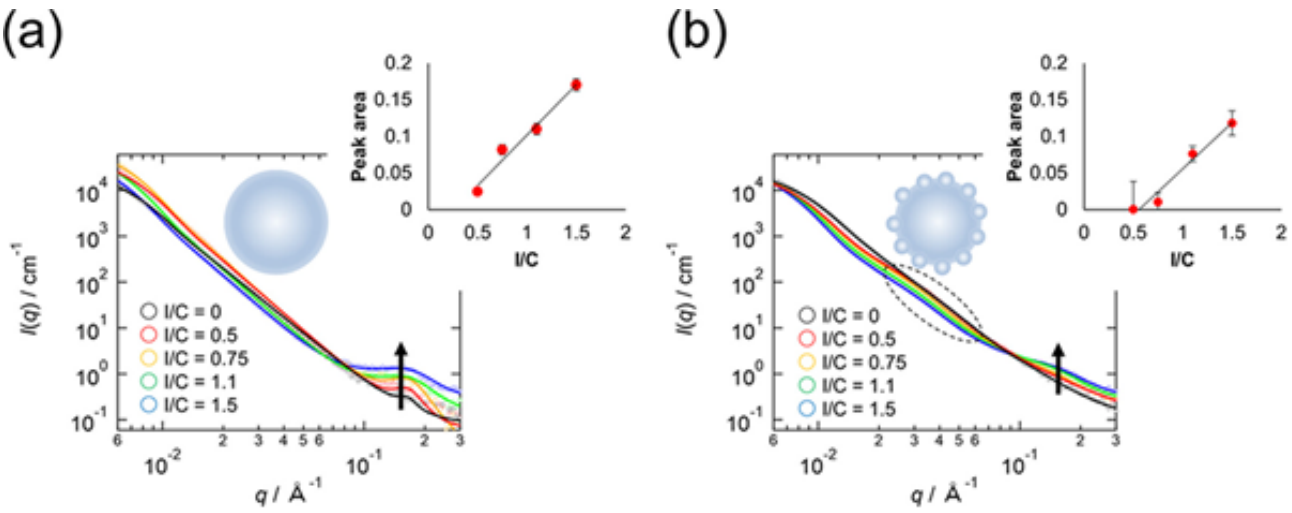

Figure 2. The Small-angle neutron scattering (SANS) spectra of two types of catalyst layer with varying ionomer/carbon weight ratio: (a) Vulcan and (b) Ketjenblack, noting that SANS data for I/C = 0 were acquired using Pt/C powder on an Si substrate. The insets show the peak areas as functions of I/C for q = 0.15 Å^{-1}, along with lines of best fit. Copyright © 2023 American Chemical Society.

40 Å and was attributed to the ion clusters of the ionomer. Since the adsorbed ionomer forms a thin film, it is considered that it does not contribute to the peak. We, therefore, assumed that the peak area (insets of Fig. 2) was proportional to the volume fraction of the deposited ionomer ϕ_{depo}, and estimated the volume fractions of adsorbed ionomer ϕ_{adso} by the difference from the total volume fraction of the ionomer.

We also assumed that the proton conductivity of the adsorbed ionomer (σ_{adso}) and that of the deposited ionomer (σ_{depo}) were the same as the conductivity of the thin ionomer [2] and the bulk membrane, respectively. Then, the proton conductivity of the catalyst layer (σ) was modeled in terms of the volume-weighted average of the proton conductivities of the adsorbed and deposited ionomers:

$$\sigma = \sigma_{adso}\,\phi_{adso} + \sigma_{depo}\,\phi_{depo} \quad (1)$$

Equation 1 corresponds to a parallel circuit model of the adsorbed and deposited ionomers, wherein protons mainly conduct through the deposited ionomer.

Figure 3 shows the proton conductivity calculated using Equation 1, plotted against the proton conductivity of the catalyst layer determined from the EIS spectra. These values correlate well with a correlation coefficient of r = 0.96. The obtained result suggests that this simple model essentially expresses the proton conduction mechanism in the catalyst layers.

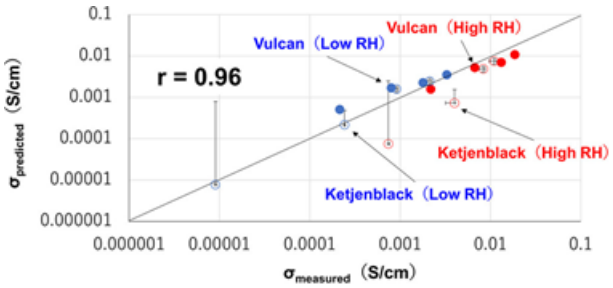

Figure 3. Predicted proton conductivities ($\sigma_{predicted}$) of the catalyst layers prepared using Vulcan and Ketjenblack at high and low relative humidities (RHs) as functions of the measured proton conductivities ($\sigma_{measured}$). The straight line, which corresponds to a perfect correlation, is provided for guidance purposes. Copyright © 2023 American Chemical Society.

4. Conclusion

A simple conductivity model of catalyst layers has been proposed by considering the ionomer distribution on Pt/C. The model was verified for catalyst layers with 2 different types of carbon supports (solid and nanoporous).

References

[1] M. Harada et al., ACS Omega, **6** 15257 (2021).
[2] X. Gao et al., Solid State Ionics, **357** 115456 (2020).
[3] M. Harada et al., ACS Applied Materials & Interfaces, **15** 42594 (2023).

M. Harada[1], S. Takata[2], H. Iwase[3], S. Kajiya[1], T. Suzuki[1], N. Hasegawa[1], A. Shinohara[1], and S. Kato[1]
[1]Toyota Central R&D Labs., Inc.; [2]Neutron Science Section, Materials and Life Science Division, J-PARC Center; [3]Neutron Science and Technology Center, CROSS

Layer Structure of Polymer Brush Film and Polymer Adsorption Film Revealed by Neutron Reflectometry

1. Introduction

Oil is commonly used to lubricate mechanical systems. This study aimed to establish water-based lubrication as a new technology to replace oil lubrication. Water-based lubrication has the potential to achieve ultralow friction, high durability, and high recyclability, which cannot be achieved with oil lubrication. One of the major reasons why water is not widely used for lubrication is its low load-bearing capacity owing to its low viscosity. If the viscosity is low, the fluid film drains out of the sliding gaps, leading to direct contact between the solid surfaces. The lubrication required for such a condition is called boundary lubrication (BL) and is typically achieved by the thin film formed on the sliding surfaces. However, BL's friction coefficient is generally ten times higher than that of fluid-mediated lubrication (Hydrodynamic lubrication). Therefore, it is essential to establish low-friction BL technology that can be applied to water-based lubrication.

We focused on hydrated MPC polymer brush films as lubricious coatings (MPC: 2-Methacryloyloxyethyl phosphorylcholine). MPC polymer is used as a coating for sliding surfaces in artificial joints. Moro et al. reported that MPC polymer coatings reduced the coefficient of friction (COF) in artificial joints to 0.1 and increased the service life of the joint [1]. In addition, Tairy et al. used a surface force apparatus (SFA) and they found that the COF can be as low as 10^{-5} on an atomically flat substrate, which agrees with the definition of superlubricity [2]. The high lubricity of MPC polymer coatings is attributed to their ability to absorb the surrounding water to form a gel-like thin film. The lubricity of a hydrated gel-like surface is known as hydration lubrication [3].

Our previous research found that when an aqueous solution containing the same type of hydrated polymer was applied to the hydrated polymer brush film, the friction coefficient decreased to approximately 1/10 of that of the water-only case. Based on our previous results, we hypothesized that the brush film surface interacts with the polymer in aqueous solution to form a bilayer structure that achieves high lubricity. When the sliding surface applies a shear force to the film, the interfacial slip between the adsorbed and brush layers can lead to low friction. This study aimed to elucidate the bilayer structure (brush and adsorbed layers) using neutron reflectivity measurements.

2. Experimental

The hydrated MPC polymer brush film was made by using the surface-initiated graft polymerization method. When hydrated, the MPC polymer brush film became a thin gel film. Heavy water (D_2O) was used for hydration. A silicon plate (10 mm thick) with a parylene film coating (20 nm thick) was used as substrate. An aqueous solution of several wt% MPC polymers was used as the polymer solution to form the adsorption film. The experimental setup is illustrated in Fig. 1. Using a diaphragm pump, we applied a pressure flow of D_2O with and without MPC polymer into the cell that contained the substrate coated with MPC polymer brush film on its top surface. Neutron reflectivity was measured using a Soft Interface Analyzer (SOFIA, BL-16) at the J-PARC's Materials and Life Science Experimental Facility. The experimental procedure was as follows. First, we measured the reflectivity only with the MPC polymer brush film under a flow of D_2O. Next, we conducted measurements under a flow of D_2O with the MPC polymer (0.5wt%). Finally, we conducted measurements under D_2O flow. These experiments were performed sequentially, that is, all brush films were measured at the same position and only the solutions were switched. The flow rate was 5 ml/min. We analyzed the SLD profiles using software (GenX) and calculated the volume fraction of the MPC polymer (brush and adsorbed) with respect to the

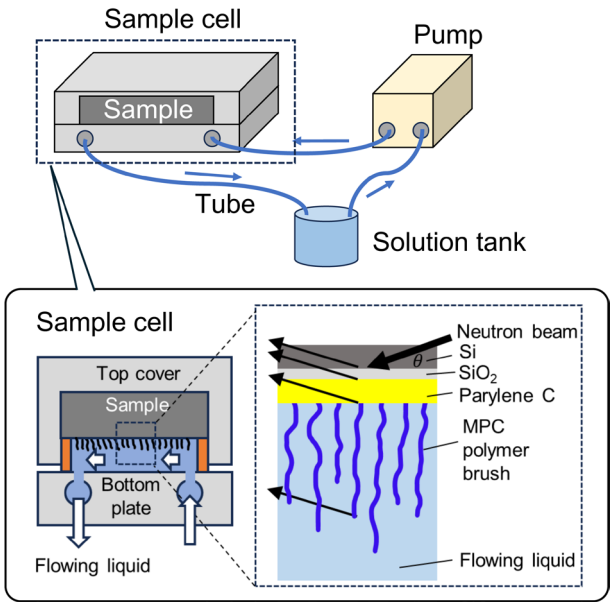

Figure 1. Experimental setup for neutron reflectometry.

distance from the parylene film surface.

3. Results and discussion

Figure 2 shows the results of measuring volume fractions versus distance from the substrate [4]. From top to bottom: (a) polymer brush film with the flow of D_2O, (b) with the flow of polymer dissolved in D_2O, and (c) with the flow of D_2O measured after the measurement of (b). The results in Fig. 2(a) are in qualitative agreement with a previous study that measured the same type of polymer brush film [5]. This indicates that the measurements were successfully performed in the presence of flow. When D_2O with polymer was introduced into the cell (Fig. 2(b)), the volume fraction of the polymer at the interface increased. This indicates that the polymer in the D_2O was adsorbed on the surface. Interestingly, the density of the polymer adsorbed on the brush film was higher than that near the substrate where the brush film was formed. This is presumably due to the size exclusion effect of the brush film. Figure 2(c) shows that the adsorbed polymer was almost completely removed from the brush film surface since the result in Fig. 2(c) is nearly identical to the result in (a).

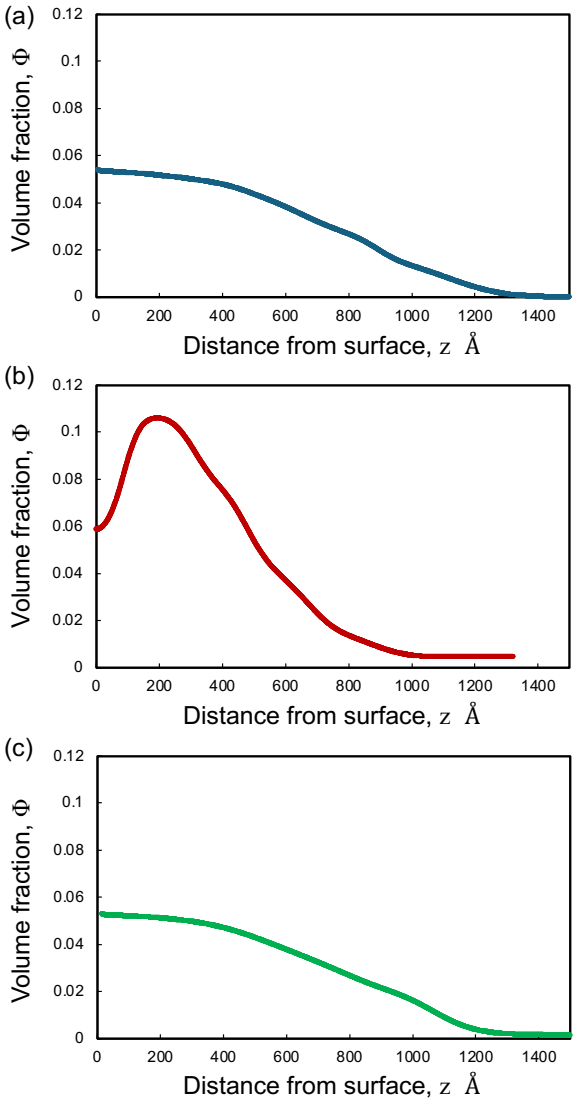

Figure 2. Volume fractions of polymer versus distance from the substrate (a) with the flow of D_2O, (b) with the flow of polymer dissolved in D_2O, and (c) with the flow of D_2O measured after the measurement of (b).

From the above results, it was found that a layer with a low polymer density (containing a large amount of water) formed near the substrate, where the brush film was dominant, and that the average polymer density increased owing to the adsorption of suspended polymers. A layer with low polymer density has low shear resistance and contributes to low friction, and the increase in average polymer density is thought to contribute to the increase in load resistance due to osmotic pressure. The adsorbed layer is easily peeled off and removed by friction, but it is thought that the polymer in the solution is re-adsorbed and regenerated.

4. Summary and future plans

The experimental results indicated that the polymer in water formed an adsorption layer on the surface of the brush film. The polymer density of the adsorption layer was greater than that of the area near the substrate where the brush film was present. These layered structures can be a factor in reducing shear resistance while supporting loads, thereby reducing the coefficient of friction. In the future, we will clarify how combinations of water-dissolved polymers and polymer brushes with different chemical and molecular structures change the layer structure and, consequently, the friction properties.

References

[1] T. Moro et al., Nat. Mater., **3 (11)**, 829–836 (2004).
[2] O. Tairy, et al., Macromolecules, **48 (1)**, 140–151 (2015).
[3] J. Klein, Friction, **1 (1)**, 1–23 (2013).
[4] F. Lin et al., Tribol. Int., **191**, 109189 (2024).
[5] M. Kobayashi et al., Sci. Polym. Ed., **25 (14–15)**, 1673–1686 (2014).

S. Itoh[1,2]
[1]*Department of Micro/Nano mechanical science and engineering, Nagoya University;* [2]*JST PRESTO*

Neutron Reflectivity Study on Water Accumulation at Epoxy Resin Interface

1. Introduction

Epoxy resin adhesives, widely used as structural adhesives, often exhibit various interfacial characteristics that significantly influence their failure mechanisms. Numerous studies have shown that moisture absorption can reduce the mechanical properties of epoxy resin, and water molecules tend to accumulate at the polymer interface, especially where the substrate surface is hydrophilic [1]. Additionally, some reports indicate that the polymer structure near the interface can also affect water accumulation significantly [2]. For the application of epoxy resin adhesives, the curing reaction must occur on the adherent's surface. This process creates a network structure near the interface that may be altered by interfacial constraints, resulting in interfacial conditions different from those in the bulk region [3]. Investigating the behavior of epoxy resin interfaces in humid environments is essential for understanding and enhancing advanced applications of epoxy resin adhesives.

Neutron Reflectometry (NR) is an excellent research method for quantitatively studying the distribution of moisture in a layer structure system. Neutron beams can penetrate resin materials and produce reflections at the interfaces of layered structures within the material system. By analyzing the oscillation of the reflection, which is caused by the interference between reflected signals, researchers can extract structural information, such as layer thickness, roughness, and scattering length density (SLD) [4]. NR also has a key advantage for studying moisture distribution: neutrons strongly scatter from deuterium (D_2O), allowing NR to sensitively detect the distribution of D_2O in the material system [5]. By analyzing the SLD profile, which represents substance distribution, one can obtain a special water distribution with the layer structure in the objects.

2. New release

In FY2023, we fully utilized the NR reflectometer at MLF BL17, along with its associated humidity control system, to quantitatively investigate water accumulation at the interface of epoxy resin adhesives [6]. In these studies, water molecules were observed to accumulate at the SiO_2/epoxy resin interface after exposure to a relative humidity (RH) of 85%. A water-enriched layer approximately 1 nm thick was detected, with its thickness varying depending on curing conditions and epoxy resin components. Additionally, water accumulation at the interface was found to be influenced by high-temperature and high-humidity environments, even after fully curing.

With the in-situ measurement and precise humidity control provided by the neutron reflectometer at MLF BL17, this quantitative study of water distribution in epoxy resin offers new insights into the cured structure of epoxy resins near interfaces. Based on observations of water distribution in different epoxy resin systems, we propose that water accumulation at the epoxy resin interface is associated with the structure of the epoxy resin near the interface. The formation of this interface layer in epoxy resin is likely influenced by interfacial constraints, which affect the cross-linked polymer chains during the curing reaction.

3. Spatial distribution of water molecules in epoxy resin

Figure 1 shows the NR data for an epoxy resin thin film, diglycidyl ether of bisphenol A (DGEBA)/1,4-cyclohexanebis(methylamine) (CBMA) before (black dots) and after (blue dots) exposure to RH of 85% (D_2O) at room temperature (RT) [7]. In both NR profiles, oscillations in reflectivity against momentum transfer (Q) were observed up to $Q = 3\ nm^{-1}$, which allows for the estimation of interface layer structures on the angstrom scale. The NR data for the DGEBA/CBMA film were analyzed using optimized fitting (solid lines), which provides estimates for the SLD, thickness, and roughness of each layer within the epoxy resin system.

In Fig. 1(b), the black and blue profiles represent the SLD distribution of the DGEBA/CBMA thin film on the Si/SiO_2 substrate, extending from the Si/SiO_2 interface (0 nm on the X-axis) to the surface of the epoxy resin under dry and humid conditions. In the dry state, a 0.8 nm thick layer with an SLD of $3.47 \times 10^{-4}\ nm^{-2}$, corresponding to the SiO_2 layer, can be observed on the Si substrate, which itself has an SLD of $2.07 \times 10^{-4}\ nm^{-2}$. A homogeneous layer with an SLD of $1.27 \times 10^{-4}\ nm^{-2}$, representing the DGEBA/CBMA thin film, is also visible on the substrate. Upon exposure to humidity, an increase in the SLD of the DGEBA/CBMA layer is observed, indicating that D_2O has diffused into the bulk of the epoxy resin. At the interface, a notable increase in SLD to $4.10 \times 10^{-4}\ nm^{-2}$ with thickness of 0.7 nm suggests a water accumulation at the interface. According

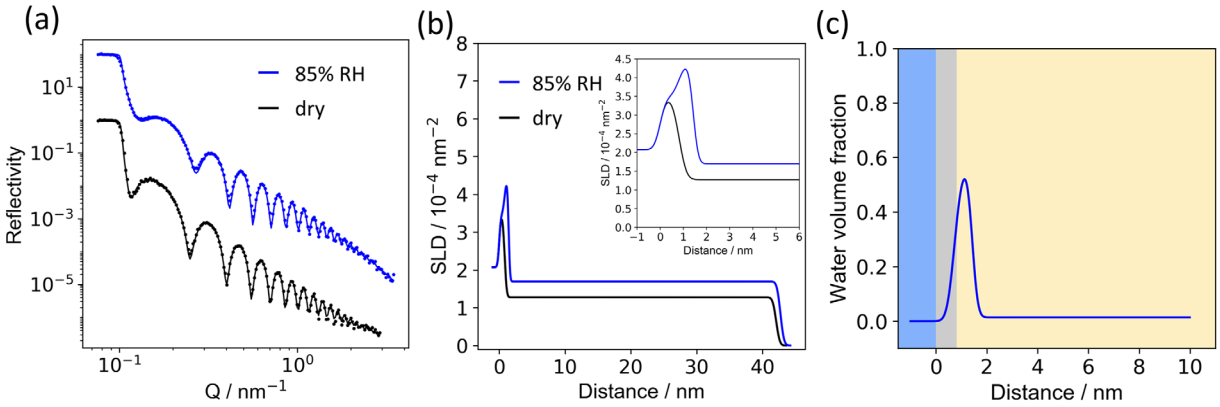

Figure 1. (a) The NR data and fitting curves of the DGEBA/CBMA thin film cured at 100°C in the dry state and under RH of 85% (vertically shifted); (b) The related SLD profiles the dry state and under RH of 85%. The inserted figure shows the SLD profiles near the substrate interface; (c) The water volume fraction at the interface of DGEBA/CBMA cured at 100°C under RH of 85%. Adapted with permission from Liu, Y., et al., " Neutron reflectometry analysis of condensed water layer formation at a solid interface of epoxy resins under high humidity." ACS Langmuir, 2023, 39, 12345–12350. Copyright 2024 American Chemical Society.

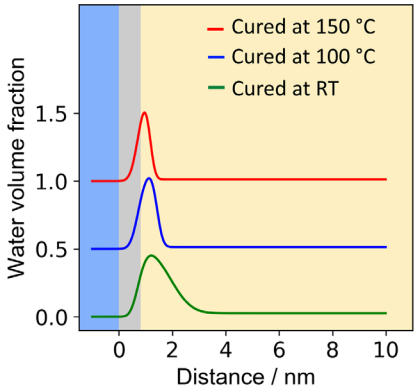

Figure 2. The water volume fraction at the interface of DGEBA/CBMA thin film cured at RT, 100°C, and 150°C under RH of 85% with offset value of 0.5. Adapted with permission from Liu, Y., et al., " Neutron reflectometry analysis of condensed water layer formation at a solid interface of epoxy resins under high humidity." ACS Langmuir, 2023, 39, 12345–12350. Copyright 2024 American Chemical Society.

to the SLD profiles obtained in the dry and humid states, the special distribution of the water in the DGEBA/CBMA thin film was calculated. In Fig. 1(c), the distribution of absorbed water in the DGEBA/CBMA thin film at 85% RH at RT is presented. A water-enriched layer with a thickness of 0.7 nm and a maximum fraction of 43% can be observed at the interface between the DGEBA/CBMA thin film and the Si substrate. Using this NR technique, we quantitatively compared the water distribution in the DGEBA/CBMA thin film cured in different conditions. In Fig. 2, in the RT cured DGEBA/CBMA (green solid line), the absorbed water formed the 1.4 nm thick condensed water layer with the maximum water volume fraction of 45% at the interface, whereas the water fraction was 2.6% in the bulk region. The water volume fraction profiles of DGEBA/CBMA thin films cured at 100°C (blue solid line) and 150°C (red solid line) indicate the presence of 0.7 and 0.6 nm thick condensed water layers with maximum water fractions of 52 and 50% at the interface, respectively, with the corresponding water fractions of 1.4 and 1.2% in the bulk region. Our FT-IR analysis of the epoxy resin bulk shows that the consumption ratios of the epoxy group of DGEBA after the curing reaction at RT, 100°C, and 150°C were evaluated to be 57, 89, and 100%, respectively. It indicates that the water accumulation at the interface was related to the curing degree of epoxy resins at the interface.

This study systematically invested the water distribution in the epoxy resins with various environment conditions. The quantitative data provide important information to understand the situation of the epoxy resin interface under humidity. We explored factors, such as chemical features of epoxy components and temperature, and discussed the relevant mechanism.

We proposed that the curing structure of epoxy resin adhesive near the interface is likely different from that of the bulk because of interfacial constraints. In our investigation, we think that the moisture accumulation at the epoxy resin adhesive interface is related to this phenomenon. Furthermore, this phenomenon may also be relevant to other behaviors of epoxy resin adhesives at their interfaces.

4. Future plans

According to the results obtained in this study, we propose that the mechanical failure of epoxy resin under humidity may be influenced by the cured structure near the interface. We conducted mechanical tests and performed related research on interfacial modification. The latest results demonstrate a significant improvement in adhesion strength after altering the structure of the epoxy resin near the interface. The publication is in progress.

References

[1] L. Tam, et al., Polymer (Guildf). **57** 28 (2015).
[2] T. Koga, et al., Phys. Rev. Lett. 2011, **107** 22 (2011).
[3] T. Hirai, et al., Phys. Chem. Chem. Phys., **14** 39 (2012).
[4] K. Jo, et al., ACS Macro Lett. **9** 2 (2020).
[5] H. Kiessig, et al. Ann. Phys. **402** 7 (1931).
[6] Y. Liu, et al., Langmuir **39** 29 (2023).
[7] H. Arima-Osonoi, et al., Rev. Sci. Instrum. **91** 10 (2020).

Y. Liu[1] and H. Aoki[2,3]
[1]*Center for Synchrotron Radiation Research, JASRI;* [2]*Institute of Materials Structure Science, KEK;* [3]*Neutron Science Section, Materials and Life Science Division, J-PARC Center*

Spin Rotation to Evaluate Perfect Crystals

1. Introduction

Perfect crystals can be used to tackle the mysteries of particle physics and astrophysics. The permanent electric dipole moment of neutrons (nEDM) breaks the time reversal symmetry, which is one of the most sensitive probes of the new physics search beyond the standard model of particle physics [1]. Time-reversal symmetry breaking is also related to the mechanism of matter formation in the universe. Today's nEDM search experiments [2] are conducted by measuring spin rotation in the electric field of stored ultra-cold neutrons (UCNs), which have very low kinetic energy, however, no finite values have been measured despite 50 years of searching. The sensitivity is limited by the number of UCNs. There is also a limit to the electric field that can be applied to the UCN storage cell. One of the other methods uses diffraction by crystals of thermal neutrons [3]. A comparable sensitivity could be achieved using thermal neutrons that are available in significantly larger numbers than UCNs.

2. Dynamical diffraction with perfect crystal

Using the strong electric field that exists inside the crystal can be considered. When neutrons simply pass through the crystal, the integral of the effect of the electric field is canceled. However, when neutrons are injected into a perfect crystal to satisfy the diffraction conditions, the neutron waves are scattered on the lattice planes and create standing waves in the crystal (Fig. 1). The effect of the electric field may not be cancelled out when integrated over the path of the standing wave in a noncentrosymmetric crystal. This means that the nEDM can be searched using dynamical diffraction of polarized neutrons. The key to this method is to know the electric field, which interacts with the neutrons in the crystal, and to evaluate the systematic uncertainty due to imperfections of the crystal.

Dynamic diffraction can also be used to evaluate crystals [4]. In the case of an electric field that is perpendicular to the direction in which the standing wave travels, the neutron feels the magnetic field due to relativistic effects and the neutron spins precesses about the field (Fig. 2). By measuring the spin precession, the electric field in the crystal can be estimated. Neutrons are polarized to incident direction. The neutrons are injected into the crystal with diffraction condition, and only those that are dynamically diffracted are analyzed for polarization.

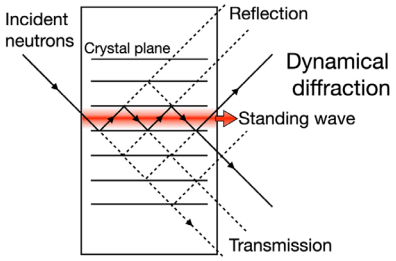

Figure 1. Conceptual drawing of dynamical diffraction. The interference of the neutron wave components can be regarded as a standing wave propagating.

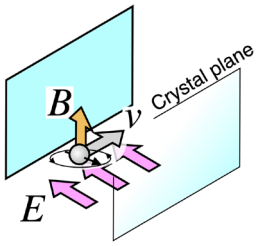

Figure 2. Spin precession around magnetic field by relativistic effect with electric field between the crystal planes.

We have already constructed a method to measure the dynamical diffraction by crystals using a pulsed neutron beam [5]. Neutron wavelengths that satisfy the diffraction conditions for each crystal plane are selected to create peaks on the TOF spectrum. Reflected waves go out in various directions, however, in the case of dynamical diffraction, there is a component that goes out in the same direction as the incident direction due to multiple reflections. By blocking a simple transmitted beam, dynamically diffracted neutrons in multiple planes can be measured with a single detector simultaneously.

3. Spin rotation with dynamical diffraction

The experiment was performed at BL17 (Sharaku) at the MLF in J-PARC, as a part of the S-type program 2019S03. A neutron beam was injected into single crystal alpha-SiO_2 and diffraction peaks from several crystal planes were detected simultaneously (Fig. 3). The neutrons were polarized, as shown in the figure, and the arrangement was such that the spins rotated when an electric field perpendicular to the crystal plane was present. The spin rotation angle varied with the tilt of the crystal, which corresponded to the length of the electric field. As a result of the experiment, the spin rotation of dynamically diffracted neutrons from the (110) crystal plane in a symmetric Laue configuration was found to be consistent with the spin rotation calculated from the electric field with the plane reported in previous

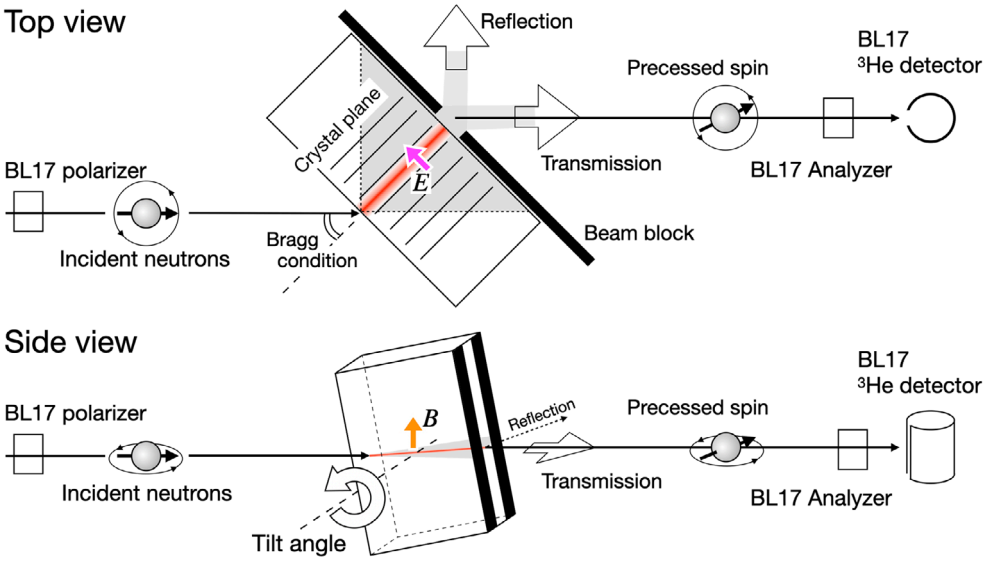

Figure 3. Experimental setup to measure the spin rotation at BL17 SHARAKU.

studies (Fig. 4) [6]. The electric field strength was obtained as $E_{(110)} = (2.2 \pm 0.2^{stat} \pm 0.5^{syst}) \times 10^8$ V/cm. This can be used for EDM searches.

Furthermore, spin rotations from the $(0\bar{2}1)$, (011), and $(11\bar{1})$ crystal planes, which are in an asymmetric Laue configuration, were investigated. Research on spin rotation in these crystal planes has not been conducted before. The experiment revealed significant spin rotation even in the $(0\bar{2}1)$ and $(11\bar{1})$ crystal planes, where the electric field was expected to be zero [6].

When neutrons injected into the crystal exactly satisfy the Bragg condition at one crystal plane, the neutron wave field in the crystal can be described by four Bloch waves, that are two transmitted waves and two reflected waves. Some of the interference terms of the partial wave components form the standing waves that feel the electric field on the crystal plane. The other terms progress across the plane and feel positive and negative electric fields periodically, so the effect of the electric field is smeared out, if the crystal is perfect. The present results suggested that the electric field was not completely canceled due to imperfections in the crystal. This causes systematic uncertainties in the EDM searches.

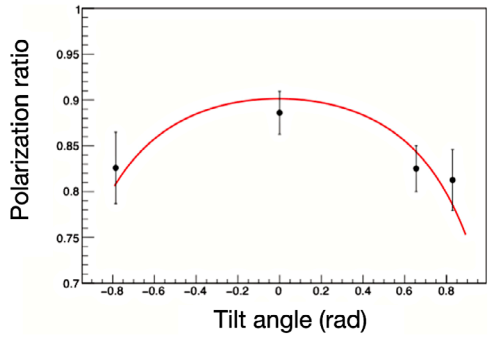

Figure 4. Change of the neutron polarization due to the spin rotation with dynamical diffraction by (110) plane of the crystal. The red curve is the result of fitting with the electric field.

4. Future plans

The results of this study indicate the need for detailed investigation of the influence of interference terms in nEDM search experiments using crystal diffraction. Future research should aim to clarify the electric field in the crystal and spin rotations from multiple crystal planes in both symmetric and asymmetric Laue configurations, through further experimental verification and theoretical considerations. We plan to continue to conduct systematic research in the future.

References

[1] M. Pospelov, A. Ritz, Ann. Physics **318** 119–169 (2005).
[2] C. Abel, et al., Phys. Rev. Lett. **124** 081803 (2020).
[3] V. Fedorov, et al., Nucl. Instr. Meth. Phys. Res. B 201, 230–242 (2003).
[4] V. Fedorov, et al., Physica B 297, 293–298 (2001).
[5] S. Itoh, et al., Nucl. Instr. Meth. Phys. Res. A 908, 78–81(2018).
[6] S. Itoh, et al., Nucl. Instr. Meth. Phys. Res. A 1057, 168734 (2023).

S. Itoh[1], S. Fukumura[1]*, T. Fujiie[1], M. Kitaguchi[1,2], and H. M. Shimizu[1]**
[1]*Department of Physics, Nagoya University;* [2]*Kobayashi-Maskawa Institute, Nagoya University*
**Present address: Department of Physics, Niigata University;* ***Present address: Department of Physics, Rikkyo University*

Development of an Iron(II) Complex Exhibiting Double Proton-transfer-coupled Spin Transition

1. Introduction

The control of proton dynamics through external stimuli such as temperature, light, and electric fields has garnered significant attention in the development of functional materials, including ferroelectric compounds, luminescent materials, and catalysts. In particular, designing molecules and hydrogen bonds (HBs) that exhibit unique proton movements is anticipated to enable novel approaches for regulating physical properties derived from proton dynamics. In studies of proton transfer phenomena, multiple proton transfers that result in the same molecular structure are common, as exemplified by proton transfer in carboxylic acid dimers. However, the controlled manipulation of multiple proton transfers leading to distinct molecular structures (protonation states) in crystalline materials remains a significant challenge. Successfully controlling multiple proton transfers could lead to substantial changes in molecular states and physical properties, such as dipole moment magnitude and the absorption/emission wavelengths of light.

In this study, we developed a novel iron(II) complex that exhibits double proton transfer coupled with spin transition. Previous studies have reported iron(II) complexes where single proton transfer occurs cooperatively with spin transitions [1–3]. However, temperature- and photo-controlled multiple proton transfers have not been previously demonstrated. We synthesized an iron(II) complex, **[Fe(HL)$_2$]**, where H_2L is a tridentate ligand (Fig. 1(a)). This complex contains a short HB, reflecting the small pKa difference between the hydrazone-N (N_{Hyd}) and phenol-O (O_{Phe}) groups, which suggests that proton transfer can occur in response to subtle changes in pKa. In this molecule, the positions of two protons can be reversibly controlled by temperature and photoirradiation within the crystalline state, resulting in distinct protonation states. The photo-response behavior of **[Fe(HL)$_2$]** is beyond the scope of this introduction and is not discussed here.

2. Results and discussion

Magnetic property measurements of **[Fe(HL)$_2$]** were conducted under temperature between 50 K and 300 K. The product of the magnetic susceptibility and temperature ($\chi_m T$) showed an abrupt change indicative of the spin transition phenomenon (Fig. 1(b)).

To investigate the dependence of the protonation state on the spin state, the molecular structure of **[Fe(HL)$_2$]** at 300 K (HS state) and 90 K (LS state) was determined using single-crystal X-ray diffraction. In all structures, two HL ligands formed an intramolecular short HB with an N_{Hyd}–O_{Phe} distance of 2.45 – 2.49 Å. Hereafter, the ligands in which the distance between N_{Hyd} and O_{Phe} is relatively short and long are denoted as HL(S) and HL(L), respectively. The protonation state was analyzed based on the coordination angles centered on N_{Hyd} ($NN_{Hyd}C$) and the O_{Phe}–C distance (Fig. 1a). Reference values for these structural parameters at the protonated and deprotonated states were obtained from density functional theory calculations. These calculations showed that the $NN_{Hyd}C$ angle decreased from 115º to 110º, and the O_{Phe}–C distance increased from 1.27 to 1.32 Å during the proton transfer from N_{Hyd} to O_{Phe}. Based on these reference values, we analyzed the dependence of the protonation state of HL(S) and HL(L) on the spin state (Figs. 2a and 2b). At 90 K (LS state), the $NN_{Hyd}C$ angle and O_{Phe}–C distance in HL(S) were 110.1º and 1.311 Å, respectively, whereas these values in HL(L) were 109.6º and 1.313 Å. This indicates that the proton in both HL(S) and HL(L) is located on the O_{Phe}

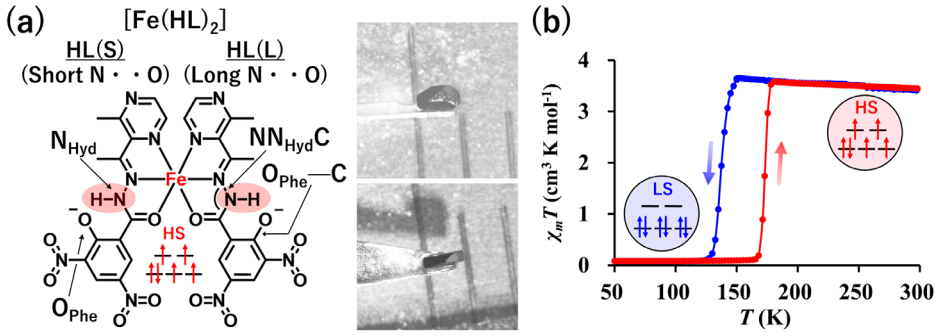

Figure 1. (a) Molecular structure of [Fe(HL)$_2$] and crystal size for neutron diffraction measurement. (b) $\chi_m T$–T plot of [Fe(HL)$_2$].

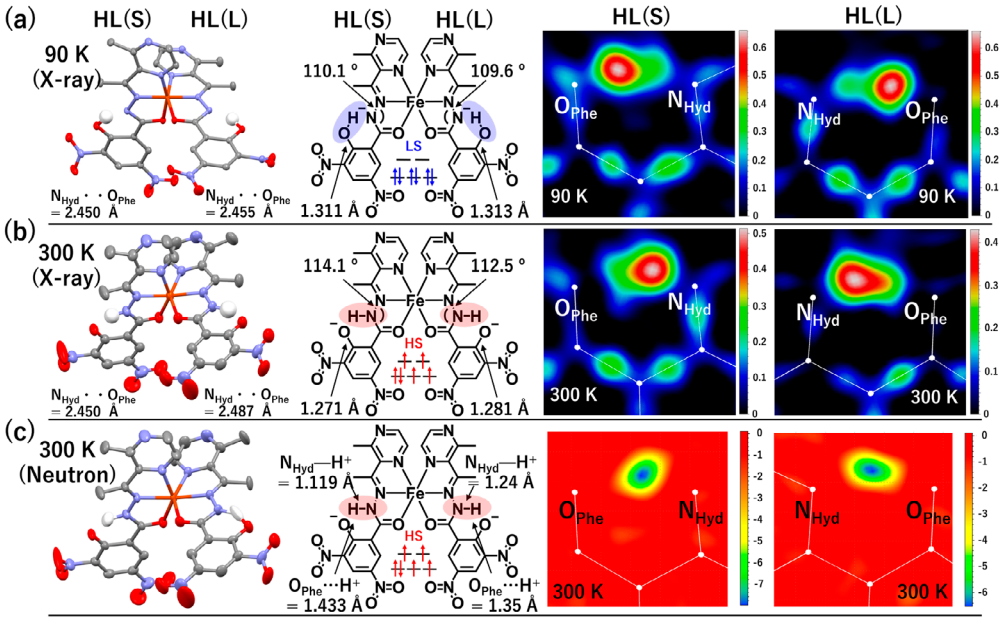

Figure 2. X-ray structure of the **[Fe(HL)$_2$]** complex with the N_{Hyd}–O_{Phe} and O_{Phe}–C distances, $NN_{Hyd}C$ angle, and difference Fourier map around the intramolecular HB in HL(S) and HL(L) at (a) 90 K and (b) 300 K. (c) The neutron structure, the N_{Hyd}–H+ and O_{Phe}–H+ distances, and the difference Fourier map of HL(S) and HL(L) at 300 K.

side (Fig. 2a). The difference Fourier maps around the intramolecular HB in HL(S) and HL(L) are consistent with these results (Fig. 2a).

Conversely, at 300 K (HS state), the $NN_{Hyd}C$ angle and O_{Phe}–C distance in HL(S) were 114.1º and 1.271 Å, respectively, whereas in HL(L) these values were 112.5º and 1.281 Å. This indicates that the proton in both HL(S) and HL(L) is located on the N_{Hyd} side (Fig. 2b). The difference Fourier map shows that the electron density attributed to the hydrogen atom is located on the N_{Hyd} side in both HL(S) and HL(L).

In addition, the single-crystal neutron structure at 300 K was successfully determined using the single crystal shown in Fig. 1(a) at BL-18 in J-PARC. The obtained structure provided further evidence of proton positions in the HS state (Fig. 2c). In HL(S), nuclear density corresponding to the proton was observed near the N_{Hyd} side, with an N_{Hyd}-H distance of 1.12 Å, slightly longer than the typical N-H bond length of 1.03 Å. Similarly, in HL(L), the nuclear density of the proton was observed near the N_{Hyd} side, with an N_{Hyd}-H distance of 1.24 Å and an O_{Phe}-H distance of 1.35 Å (Fig. 2d). These measurements indicate that in the HS state, the proton in HL(L) is also located near the N_{Hyd} side. The deviations in N_{Hyd}-H bond lengths from the typical values can be attributed to the formation of short HBs. These findings demonstrate that **[Fe(HL)$_2$]** undergoes thermally induced double proton transfer coupled with spin transition, enabling the reversible control of two protons through temperature changes.

3. Summary

In this study, we developed a novel proton-coupled spin transition complex **[Fe(HL)$_2$]** forming the short HBs and achieved the manipulation of multiple proton transfers, leading to distinct protonation states in a crystalline system. These results suggest that designing molecules with short HBs is a promising strategy for achieving multiple proton transfers in crystalline systems. This study provides valuable insights into the molecular design of proton-electron coupling systems and advances our understanding of proton dynamics in crystalline materials.

References

[1] T. Nakanishi et al., *J. Am. Chem. Soc.* **2019**, 141, 14384-14393.

[2] T. Nakanishi et al., *Angew. Chem. Int. Ed.* **2020**, 59, 14781-14787.

[3] T. Nakanishi et al., *Phys. Chem. Chem. Phys.* **2023**, *25*, 12394-12400.

T. Nakanishi[1,2], Y. Hori[3], Y. Shigeta[3], H. Sato[4], R. Kiyanagi[5], K. Munakata[6], T. Ohhara[5], A. Okazawa[7], R. Shimada[8], A. Sakamoto[8], and O. Sato[1]

[1]*Institute for Materials Chemistry and Engineering & IRCCS, Kyushu University;* [2]*Institute for Materials Research, Tohoku University;* [3]*Center for Computational Sciences, University of Tsukuba;* [4]*Rigaku Corporation;* [5]*Neutron Science Section, Materials and Life Science Division, J-PARC Center;* [6]*Neutron Science and Technology Center, CROSS;* [7]*Department of Electrical Engineering and Bioscience, Waseda University;* [8]*Graduate School of Science and Engineering, Aoyama Gakuin University*

Strong and Ductile Maraging Medium-entropy Alloy

1. Introduction

Development of ultrastrong and ductile alloys is crucial to ensure the safety of the component during service and reduce environmental concerns; such materials enable minimizing the component thickness and reducing the weight without sacrificing the component safety, which leads to benefits in production cost, fuel economy, and greenhouse gas emissions [1, 2].

In this work, we propose a novel medium-entropy alloy (MEA) that is ultrastrong and ductile by simultaneously harnessing the advantages of the high-entropy alloys and maraging steels. Most conventional maraging steels used to lack in the strain hardenability despite their high strength [3]. On the other hand, our MEA exhibits considerable strain hardening ability and uniform ductility, which are essential to enhance the load-bearing capability of structural materials, via harnessing deformation-induced martensitic transformation of reverted austenite phase. Our experimental results validate the hypothesis that the maraging concept can be successfully adapted to high-entropy alloy design to overcome limits in both groups of materials and achieve both ultrahigh strength and strain hardening ability.

2. Materials and methods

An ingot of the MEA with the $Fe_{60}Co_{25}Ni_{10}Mo_5$ (at%) chemical composition was cast via vacuum induction melting. The as-cast ingot was homogenized at 1100°C for 6 h in Argon atmosphere. The homogenized ingot was hot rolled (HR) at 1150°C from 7 mm to 1.5 mm and air-cooled at room temperature. The HR sheets were then treated by aging at 600, 650, and 700°C for 10 min in Argon atmosphere, then air-cooling at room temperature. The aged samples are hereinafter denoted by A600, A650, and A700 according to the aging temperatures.

Uniaxial tensile tests were conducted at room temperature at a strain rate of 1×10^{-3} s^{-1}. Microstructural evolution before and after tensile deformation was analyzed using electron backscatter diffraction (EBSD), transmission electron microscopy (TEM), and atom probe tomography (APT), etc. In situ neutron diffraction analysis accompanied by tensile loading was conducted at BL19 "TAKUMI" of Materials and Life Science Experimental Facility of Japan Proton Accelerator Research Complex.

3. Results and discussion

The microstructural characterization of the HR and aged MEAs (Fig. 1a) reveals that nanoscale precipitates have formed during the aging process. The HR MEA shows a typical lath martensite structure containing high-density dislocations, similar to the solutionized state in maraging steels. After aging, the general lath martensite structure does not change while profuse Mo-rich μ phase precipitates appear homogeneously throughout the matrix. Besides the spherical nano-precipitates, long μ phase particles that have been nucleated along the lath boundaries are also observed. Additionally, reverted FCC phase is visible in A650 and A700. The formation of the long μ phase particles led to depletion of Mo and relative enrichment of FCC stabilizer Ni, promoting the reversion into FCC.

Figure 1b shows the tensile properties of the MEA. The HR MEA exhibits a high-yield strength (YS) of ~1 GPa, ultimate tensile strength (UTS) of ~1.16 GPa, and total elongation (TE) of ~21.0%, but a very limited strain hardening ability with only ~3.3% of uniform elongation (UE). On the other hand, the aging process of only 10 min brings significant increases in strength. The YS increases to ~1.55 GPa in A700, and to ~2.02 GPa in A650. A600 shows an extremely high YS of ~2.41 GPa and UTS of ~2.51 GPa, with TE of ~9.4%. However, the most salient feature of the aged samples is the excellent strain hardening capability. Unlike the HR MEA, the A650 and A700 samples can sustain substantial strain hardening that leads to balanced strength and uniform ductility: UTS of ~2.18 GPa and UE of ~6.0% in A650 and UTS of ~1.85 GPa and UE of ~9.2% in A700, respectively. The tensile properties are quite encouraging because existing maraging steels show low uniform ductility inversely proportional to the high strength.

The most noticeable difference of A650 and A700 with the extraordinary strain hardenability from the other samples is the reverted FCC phase; this lets us know that controlling the FCC reversion is the key to enhancing the strain hardening ability and UE. EBSD phase maps of A700 tensile deformed to varying true strains show that the FCC phase fraction decreases with increasing strain (Fig. 1c). This suggests that the reverted Ni-rich FCC phase goes through deformation-induced martensitic transformation (DIMT) into the BCC phase upon strain.

In situ neutron diffraction study under tensile loading of A700 was conducted to quantitatively understand the effect of DIMT on the mechanical behavior: the contributions of constituent phases to strain hardening and

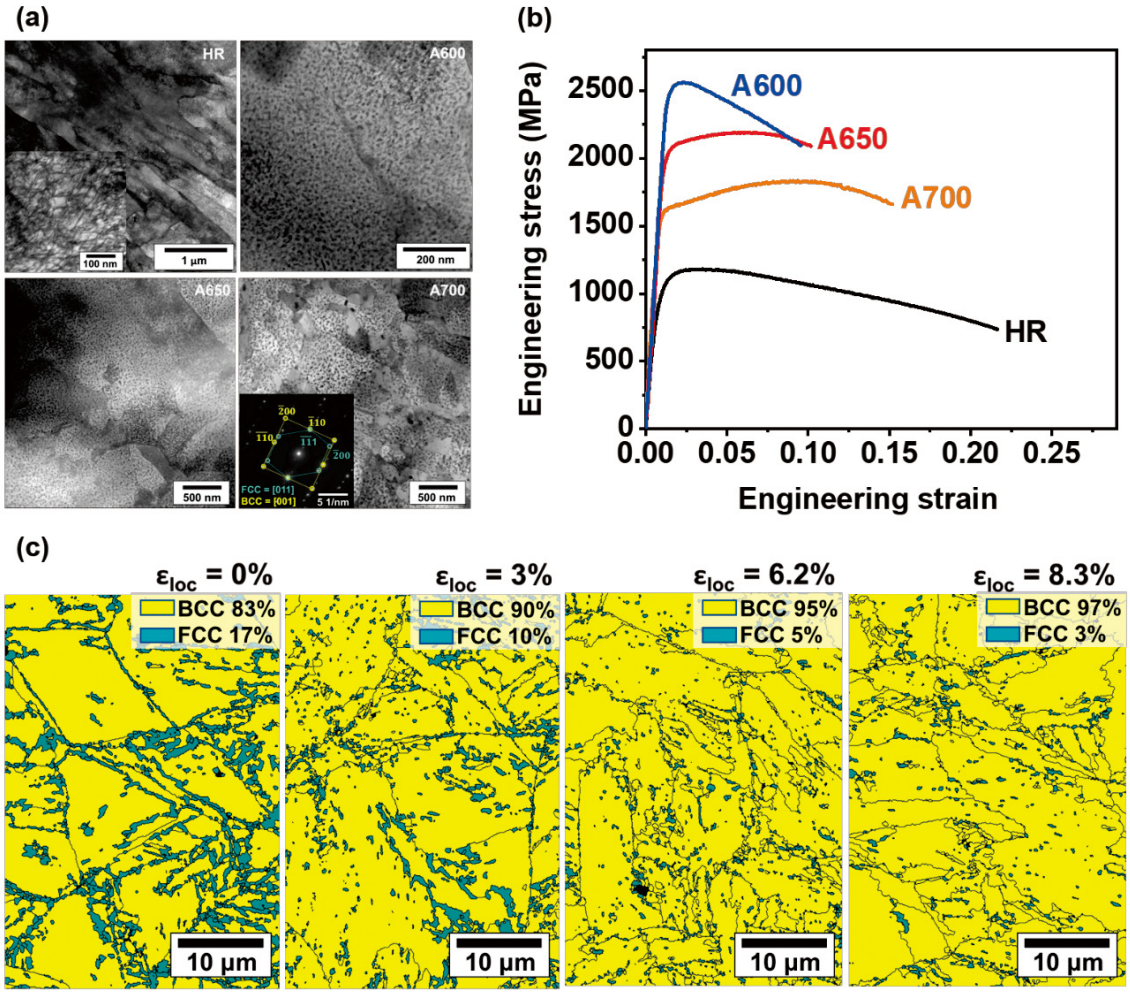

Figure 1. Microstructures and mechanical properties of the maraging MEA. (a) STEM images. (b) Tensile properties. (c) EBSD phase maps of A700 MEA deformed to different true strains.

sustaining plastic deformation. The neutron diffraction patterns presented in Fig. 2a show that FCC peaks diminish with tensile strain, and the (200) and (220) FCC peaks nearly vanish at later stages of plastic deformation. The FCC phase fraction does not change during the elastic deformation and starts decreasing in the plastic regime, which shows the mechanical martensite is generated by strain-induced martensitic transformation.

Lattice strain induced by increased lattice spacing of each orientation (ε_{hkl}) can be calculated by shifting of each hkl diffraction peak as follows [4]:

$$\varepsilon_{hkl} = \frac{d_{hkl} - d^0_{hkl}}{d^0_{hkl}}, \quad (1)$$

where d_{hkl} is the lattice spacing, and d^0_{hkl} is the initial lattice spacing before tensile loading. The lattice strains plotted against applied true stress (Fig. 2b) show substantial anisotropy. In the BCC phase, (200) grains exhibit the highest lattice strains, which means they act as hard grains that share a larger load, while the (110) grains show the lowest lattice strains. On the other hand, (200) grains and (111) grains show largest and lowest lattice strains in the FCC phase, respectively. This behavior is in good accordance with typical materials, showing that stress partitioning occurs among phases and grains with different crystal orientations. The stress partitioning and contribution of each phase to the flow stress can be shown by computing phase stresses of the FCC and BCC (σ_i) via Hooke's law, i.e. $\sigma_i = E_i\varepsilon_i$, where E_i is Young's modulus and ε_i is averaged lattice strain of phase i. The phase stresses calculated using $E_{FCC} = 214$ GPa and $E_{BCC} = 246$ GPa [5] are plotted against applied true strain in Fig. 2c. The phase stress of the BCC phase is far higher than that of the FCC phase, which indicates a noticeable stress partitioning onto the BCC phase. This shows that the BCC phase contributes more to the flow stress, and its contribution is predicted to become larger due to increasing BCC fraction with increasing applied strain that will further share the load. Therefore, the dynamic stress-strain partitioning by DIMT to BCC explains the extraordinary strain hardenability of the A650

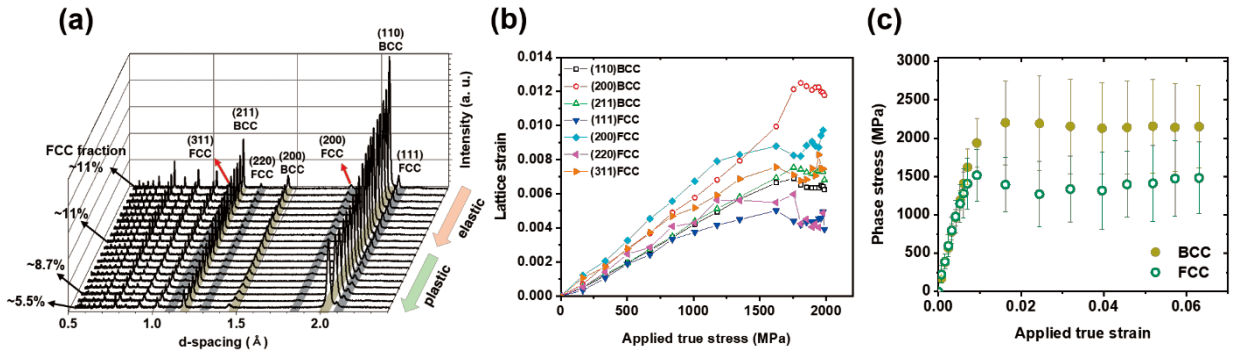

Figure 2. In situ neutron diffraction study of A700 MEA. (a) In situ neutron diffraction patterns under tensile loading. (b) Lattice strains plotted against applied true stress. (c) Phase stresses plotted against applied true strain.

and A700 MEAs.

4. Conclusions

$Fe_{60}Co_{25}Ni_{10}Mo_5$ MEA was designed by combining concepts of maraging steels and high-entropy alloys. The alloy exhibited a martensite lath structure in the HR condition, and 10 min of aging at 600~700°C introduced high density of nanosized μ phase precipitates, along with partial phase reversion into the Ni-rich FCC. The microstructure enabled superior tensile properties, especially with A650 showing UTS of ~2.2 GPa and UE of ~6%. While the nanoprecipitates largely contributed to the strength, transformation-induced plasticity from the DIMT of the reverted FCC into BCC was responsible for the strain hardening and improved UE. The current combination of ultrahigh strength and strain hardening ability has been unprecedented in conventional maraging steels. The fact that these properties are achieved through a simple route (hot rolling and a short single-step aging) without multiple heat treatment steps makes the current alloy more attractive for future challenging applications. Our work provides a useful insight into high-performance novel alloys by overcoming the limits of conventional materials through the high-entropy design approach.

References

[1] D. Raabe et al., Scr. Mater., **60** 1141 (2009).
[2] J. Inoue et al., Scr. Mater., **59** 1055 (2008).
[3] S. Jiang et al., Nature, **544** 460 (2017).
[4] S. Harjo et al., Sci. Rep., **7** 1 (2017).
[5] J.W. Bae et al., Scr. Mater., **165** 60 (2019).

H. Kwon[1], P. Sathiyamoorthi[2], M.K. Gangaragu[2], A. Zargaran[3], J. Wang[1], Y.-U. Heo[3], S. Harjo[4], W. Gong[4], B.-J. Lee[1], and H.S. Kim[1,3,5]
[1]Department of Materials Science and Engineering, POSTECH; [2]Indian Institute of Technology (BHU); [3]Graduate Institute of Ferrous & Energy Materials Technology, POSTECH; [4]Neutron Science Section, Materials and Life Science Division, J-PARC Center; [5]Advanced Institute for Materials Research (WPI-AIMR), Tohoku University

Neutron Diffraction and μ⁺SR Reveal Unusually Large Magnetic Moment and Tricritical Behavior in $NaCr_2O_4$

1. Introduction

Mixed-valence transition metal oxides display a rich variety of physical properties, including unconventional superconductivity and colossal magnetoresistance (CMR). Among them, $NaCr_2O_4$, a chromium oxide with Cr^{3+} and Cr^{4+} ions, attracted attention due to its rare mixed-valence state, stabilized via high-pressure synthesis [1, 2]. The compound's unique crystal structure features distorted CrO_6 octahedra forming zig-zag chains along the b-axis with two different Cr sites (Fig. 1a), giving rise to complex magnetic and electronic behaviors.

$NaCr_2O_4$ exhibits an antiferromagnetic (AFM) transition and anomalous CMR below the Néel temperature. Unlike typical CMR materials, where resistivity decreases near a ferromagnetic transition, $NaCr_2O_4$ shows a continuous decrease in resistivity with cooling, even at temperatures far from the AFM transition. This suggests a novel CMR mechanism potentially related to field-induced increased mobility of localized Cr electrons or spin re-orientation effects. Additionally, $NaCr_2O_4$ displays coexistence of positive and negative charge transfer states and a dual itinerant/localized nature of the Cr electrons [3], further complicating its electronic structure.

Our study [4, 5], including neutron diffraction and muon spin rotation measurements, revealed a canted AFM order in $NaCr_2O_4$, along with an incommensurate modulation of its magnetic structure. The interplay between high-spin and low-spin Cr sites, coupled with 2D magnetic interactions, challenges earlier interpretations of spin frustration within the zig-zag chains. These findings suggest that $NaCr_2O_4$'s CMR behavior may be driven by complex metamagnetic phenomena.

2. Experimental methods

Polycrystalline $NaCr_2O_4$ samples were synthesized from $NaCrO_2$, Cr_2O_3, and CrO_3 at 1300°C under 7 GPa pressure at the National Institute for Material Science, Japan. X-ray diffraction confirmed that the samples had a single-phase $CaFe_2O_4$-type Pnma structure. Temperature-dependent muon spin rotation (μ⁺SR) spectra were measured at the Paul Scherrer Institute, using approximately 500 mg of powder in an aluminum-coated Mylar envelope mounted on a helium cryostat (1.6 K to 300 K). Neutron powder diffraction (NPD) measurements were conducted at J-PARC's iMATERIA and SPICA instruments in Japan, with samples sealed in vanadium cells at temperatures from 2 K to 300 K. The instruments provided high-resolution structural data and allowed identification of magnetic Bragg peaks. Data analysis was performed using FullProf for NPD data and musrfit for μ⁺SR data, VESTA was used for structural visualization, Igorpro for temperature dependent parameter fitting.

3. Results and discussion

Both μ⁺SR and NPD revealed the nature of the transitions between paramagnetic (PM) and antiferromagnetic (AFM) phases in $NaCr_2O_4$.

The μ⁺SR measurements were conducted in weak transverse field (wTF), which confirmed the AFM transition at TN ≈ 125 K, and zero-field (ZF) configurations.

The ZF μ⁺SR measurements revealed multiple magnetic environments at low temperatures, with two distinct muon precession frequencies in the AFM state at 2 K. As the temperature increased, only one frequency remained above T_μ = 62 K, indicating a simpler magnetic environment. These magnetic changes occurred

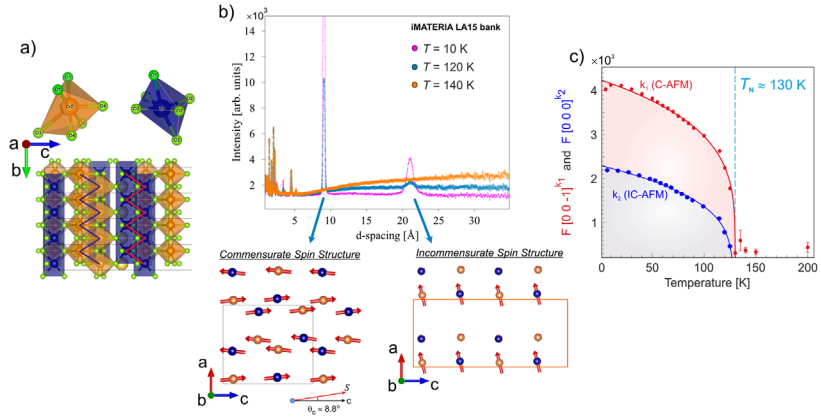

Figure 1. a) $NaCr_2O_4$ crystal structure, the zig-zag chains are evidenced. b) High d-spacing diffraction patterns showing the magnetic peaks at 9 and 20 Å and corresponding magnetic structures. c) Magnetic order parameters for the two magnetic structures.

without detectable structural or additional magnetic transitions in the NPD data, suggesting that they were independent of atomic rearrangements.

NPD patterns show the appearance of magnetic peaks below 130 K, specifically at d = 9 Å and d ≈ 20 Å (Fig. 1 b). Above 130 K, diffuse scattering around d ≈ 20 Å indicated short-range magnetic correlations, which condensed into a long-range AFM order as the temperature decreased.

The NPD refinement revealed two distinct magnetic phases at low temperatures: a commensurate AFM (C-AFM) phase with propagation vector k_1 = (1 0 1), and an incommensurate AFM (IC-AFM) phase with k_2 = (0 0 0.497) related to the magnetic peaks at d = 9 Å and d ≈ 20 Å respectively (Fig. 1 b). The C-AFM phase showed ferromagnetic alignment of Cr spins within zig-zag chains along the c-axis and antiferromagnetic coupling between chains. The IC-AFM phase, in contrast, displayed a cycloidal modulation of spins along the b-axis.

These phases were characterized by values of the Cr moment equal to 4.3 μB for the C-AFM and 2.2 μB for the IC-AFM. The value of the moment for the C-AFM phase is unusually large, greater than expected for $Cr^{3.5+}$ ions. This is consistent with the negative charge transfer state in $NaCr_2O_4$, with holes localized on oxygen sites rather than Cr, resulting in an effective Cr valence closer to Cr^{2+}. This interpretation aligns with the previous findings for $NaCr_2O_4$.

Temperature-dependent magnetic order parameters, based on the intensity of the C-AFM magnetic Bragg peaks (Fig. 1 c), suggested tricritical behavior, implying the C-AFM-PM transition may exhibit mixed first- and second-order characteristics. Slight changes in lattice parameters with temperature, particularly an inversion in the c-axis trend around 60 K, support a weak coupling between magnetic order and the lattice.

The results suggest a complex magnetic behavior in $NaCr_2O_4$ driven by both ferromagnetic and antiferromagnetic interactions, potentially mediated by ligand holes on oxygen sites. The interplay of localized and itinerant electron behavior appears to influence magnetic order. Future studies under applied magnetic fields may further clarify these magnetic transitions.

4. Conclusions

High-resolution NPD on $NaCr_2O_4$ reveals two distinct magnetic phases: a canted commensurate AFM (C-AFM) phase with propagation vector k_1 = (1 0 1) and an incommensurate cycloidal (IC) AFM phase with vector k_2 = (0 0 ½ - δ). Following the temperature evolution of the magnetic reflections, an unconventional critical behavior for the k_1 phase transition was observed, possibly near a tricritical point, with indications of a hidden metamagnetic phase. Weak coupling between crystal and magnetic structures, supported by μ^+SR and NPD data, aligns with the absence of geometric frustration. The unusually high Cr moment value in the C-AFM phase is consistent with a double exchange mechanism via itinerant Cr electrons (ligand-hole hopping), while the lower moment in the IC phase suggests exchange coupling between localized Cr spins. The precise value of the Cr spin canting angle in the C-AFM phase was determined as θ = 8.8°, and a combination of FM double-exchange and AFM itinerant electron hopping interactions was concluded to likely drive the k1 magnetic transition in $NaCr_2O_4$.

References

[1] H. Sakurai et al., Angewandte Chemie, **51** (27) 6653–6656 (2012).
[2] M. Taguchi et al., Physical Review B **96** (24) 245113 (2017).
[3] T. Toriyama et al., Proceedings of SCES2013, p. 017003 (2014).
[4] E. Nocerino et al., Journal of Physics: Materials **6.3**, 035009 (2023).
[5] E. Nocerino, Ph.D. thesis, KTH – Royal Institute of Technology (2022).

E. Nocerino[1,2#], O. K. Forslund[3,4#], H. Sakurai[5], A. Hoshikawa[6#], N. Matsubara[7], D. Andreica[8], A. Zubayer[9], F. Mazza[10], T. Saito[11], J. Sugiyama[12,13], I. Umegaki[14], Y. Sassa[7#], and Martin Månsson[7]

[1]Department of materials and environmental chemistry, Stockholm University; [2]PSI Center for Neutron and Muon Sciences, Villigen, CH-5232, Switzerland; [3]Physik-Institut, Universität Zürich; [4]Department of Physics and Astronomy, Uppsala University; [5]National Institute for Materials Science (NIMS); [6]Research and Education Center for Atomic Sciences, Ibaraki University; [7]Department of Applied Physics, KTH Royal Institute of Technology; [8]Faculty of Physics, Babes-Bolyai University; [9]Department of Physics, Chemistry and Biology (IFM), Linköping University; [10]Insitute of Solid State Physics, TU Wien; [11]Neutron Science Section, Materials and Life Science Division, J-PARC Center, Institute of Materials Structure Science, KEK; [12]Neutron Science and Technology Center, CROSS; [13]Advanced Science Research Center, Japan Atomic Energy Agency; [14]Muon Science Section, Materials and Life Science Division, J-PARC Center, Institute of Materials Structure Science, KEK. [#]Current affiliations

Relationship between Intramolecular Bond Lengths and Their Stretching Frequencies of Organic Molecules in the Liquid State

1. Introduction

Molecules in the liquid state receive strong intermolecular interactions from other molecules and/or ions that surround them. This interaction should cause certain changes in the intramolecular bond length. However, due to the small magnitude of the change in length (expected to be ca. 1/100 Å at most), it has been difficult to obtain experimental evidence for the change in intramolecular geometry. Recently, intramolecular bond length in the liquid state has been determined with higher precision (less than several 1/1000 Å) by employing high performance TOF neutron spectrometer with a new generation high power pulsed neutron source. The r_{OD}–ν_{OD} relationship has been successfully obtained for liquid D_2O and concentrated aqueous Li-salts solutions in D_2O, in which intermolecular hydrogen bonds are extensively destroyed [1, 2].

In the present study, we carried out TOF neutron diffraction measurements on deuterated methanol and concentrated methanolic solutions involving $LiClO_4$ and LiTFSA ($TFSA^-$: $N^-(SO_2CF_3)_2$) [3]. The least-squares fitting analysis was applied to the observed interference term to determine the O–D bond length (r_{OD}) of the methanol molecule in the liquid state. Scattering data observed at forward scattering angles have been employed to avoid apparent shrinkage in bond lengths due to the inelasticity effect [4]. ATR-IR spectroscopic measurements were carried out for the methanolic solutions with natural abundance to obtain the average O–H stretching vibrational frequency (ν_{OH}) of the methanol molecules in the liquid state. The relationship between r_{OD} and ν_{OH} has been discussed.

2. Neutron diffraction measurements

Pure CD_3OD (99.8% D), 10 and 20 mol% $LiClO_4$–CD_3OD, and 10 and 33 mol% LiTFSA- CD_3OD solutions were sealed in thin walled cylindrical vanadium cell (10 mm in diameter, 0.1 mm in wall thickness). Neutron diffraction measurements have been carried out at 25°C using the NOVA (BL21) spectrometer installed at the MLF high intensity pulsed neutron source in the J-PARC. The incident proton beam power was 812 kW. The acquisition time for each sample was 4h. Measurements for the empty cell, standard vanadium rod (9.5 mm ϕ), and background have been made. The total interference term, $i(Q)$, was derived by subtracting the coherent self-scattering term. In the present study, the least-squares fitting analysis for the $i(Q)$ has been carried out in the range of $10 \le Q \le 40$ Å^{-1}, employing the sum of calculated intramolecular interference terms for CD_3OD and anion. In the present fitting analysis, independent parameters, O–D_a, C–D_m, and C–O bond lengths (D_a: alcoholic D atom, D_m: methyl D atom), bond angles, $\angle D_aOC$ and $\angle D_mCO$, and root-mean-square amplitudes for both bonding and non-bonding atom pairs, l_{CO}, l_{ODa}, l_{CDm}, l_{ODm}, l_{DaDm}, l_{CDa}, and $l_{DmDm'}$, for the CD_3OD molecule, were employed. In the least squares fitting procedure, the intramolecular geometry of CD_3OD described in the Z-matrix form was converted to the Cartesian coordinates (x_i, y_i, z_i), and then all intramolecular distances were evaluated. Tetrahedral geometry of ClO_4^- was assumed. Intramolecular r_{ClO}, l_{ClO}, and l_{OO} were treated as independent parameters. The intramolecular geometry of $TFSA^-$ was fixed to that determined by single crystal X-ray diffraction studies [5,6] during the present fitting analyses of $(LiTFSA)_{0.1}(CD_3OD)_{0.9}$ and $(LiTFSA)_{0.33}(CD_3OD)_{0.67}$ solutions.

3. Results and discussion

Figure 1 represents $i(Q)$ observed for pure liquid CD_3OD and $(LiX)_x(CD_3OD)_{1-x}$ solutions. In the present study, scattering cross sections observed from forward

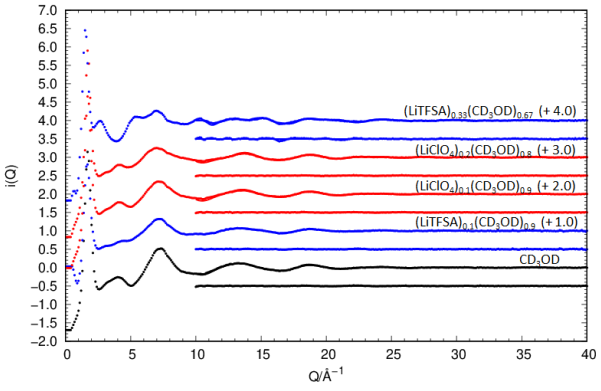

Figure 1. Total interference term observed for pure deuterated methanol and concentrated methanolic solutions (dots). The residual functions are indicated below.

scattering angle detector pixels located at $1.9 \leq 2\theta \leq 54.9°$ were combined at Q interval of 0.1 Å^{-1} and adopted for the subsequent analyses. The oscillatory features found in the observed $i(Q)$ in the high-Q region above $Q \geq 10$ Å^{-1} can be regarded as intramolecular interference contributions from CD_3OD and from polyatomic anions in the solution.

The best-fit of the calculated intramolecular interference term is compared with the observed total interference term in Fig. 1. Satisfactory fit was obtained in the range $10 \leq Q \leq 40$ Å^{-1}. Although the contribution from the intramolecular O–D_a interaction of the methanol molecule is relatively small, the O–D_a distance has been determined with favorable accuracy. In order to take into account the effect of thermal vibration of atoms, the observed r_{a_ODa} has been converted to r_{g_ODa} ($r_{g\_ODa} = r_{a\_ODa} + l_{ODa}^2/r_{a\_ODa}$). The r_{ODa} values determined for the present liquid methanol and methanolic solutions are, on average, ca. 0.01 Å shorter than those reported for water and aqueous solutions [1, 2].

Figure 2 represents the relationship between ν_{OH} and r_{g_OD} observed for the methanol molecule in various phases. In this plot, the ν_{OH} and r_{OD} data for the solid and gaseous states are involved. The $r_{g\,OD}$ and ν_{OH} values for pure liquid methanol and methanolic Li-salt solutions exhibit an intermediate position between the values reported for the solid (fully hydrogen-bonded) and gaseous (completely isolated) states. Although the data points are somewhat scattered, the ν_{OH}–$r_{g\,OD}$ relationship can be well approximated by a linear function of ν_{OH}. The functional form, $r_{g\_OD} = (-6 \pm 1) \times 10^{-5} \times \nu_{OH} + (1.16 \pm 0.05)$, was determined by least-squares fitting analysis. The value, $d\nu_{OH}/dr_{g\,OD} = -(17000 \pm 3000)$ cm^{-1}Å^{-1}, was evaluated from the slope of the fitted line. Recently, the value, $d\nu_{OD}/dr_{g\,OD} = -(21000 \pm 1000)$ cm^{-1}Å^{-1} has been reported for the D_2O molecule in various states [1]. If we assume a simple relationship of stretching vibrational frequencies for the O–H and the O–D groups, $\nu_{OD}/\nu_{OH} = (1/2)^{1/2}$, the $d\nu_{OD}/dr_{g\,OD}$ value for the present methanol molecule can be roughly estimated to be $-(12000 \pm 2000)$ cm^{-1}Å^{-1}, which is significantly smaller

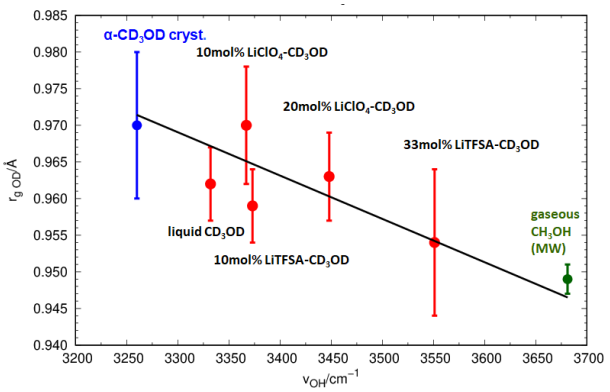

Figure 2. The relationship between observed O-H stretching frequency (ν_{OH}) and O-D bond length ($r_{g\,OD}$) observed for methanol molecules in various states.

than that observed for D_2O. Since the strength of intermolecular hydrogen-bonded interaction between methanol molecules is known to be weaker than that for water, the smaller value of $d\nu_{OD}/dr_{g\,OD}$ obtained for methanol may indicate that the O–D bond length of methanol sensitively reflects intermolecular hydrogen-bonded interaction.

It has been shown that it is possible to determine the effect of intermolecular hydrogen-bonded interaction on the intramolecular structure in the liquid state by using high precision neutron scattering data obtained from the TOF spectrometer installed at the high-intensity pulsed neutron source. The ν_{OH}–$r_{g\,OD}$ relationship for methanol molecules in the liquid state can be well represented by a linear function which has been found for D_2O molecules in the liquid state.

References

[1] Y. Kameda et al., J. Phys. Chem. B, **125** 11285 (2021).
[2] Y. Kameda et al., J. Mol. Liq., **382** 121927 (2023).
[3] Y. Kameda et al., J. Phys. Chem. B, **127** 7758 (2023).
[4] Y. Kameda et al., Bull. Chem. Soc. Jpn., **94** 2800 (2021).
[5] R. W. Berg et al., J. Pjys. Chem. B, **113** 8878 (2009).
[6] R. Tatara et al., J. Phys. Chem. C, **124**, 15800 (2020).

Y. Kameda[1], Y. Amo[1], T, Usuki[1], K. Ikeda[2], T. Honda[3], and T. Otomo[3]
[1]*Faculty of Science, Yamagata University;* [2]*Neutron Science and Technology Center, CROSS;* [3]*Institute of Materials Structure Science, KEK*

Internal Structural Changes in Lithium-ion Batteries during Heating Tests Observed by In-situ Neutron Imaging

1. Introduction

Electric vehicles (EVs) are experiencing a rapid increase in popularity as a means of reducing greenhouse gas emissions. Lithium-ion batteries (LIBs) are most commonly used in EVs because of their high energy and power density, and long-life cycles. Given the high added value of LIBs even when used, it is imperative to reuse used products to achieve carbon neutrality. Among the various tests for used batteries, the thermal abuse test is crucial for evaluating the stability of LIBs. The inside of LIBs is not directly observable, necessitating the observation of changes in the LIBs during the heating process. Although X-ray-based experiments have been conducted, the changes in the electrolyte and separator have not been observed. Therefore, an attempt was made to observe the inside of the battery using neutrons.

2. Experiments

A commercially available LIB was used as the sample. The dimensions of the LIB were 35 × 35 × 6.1 mm, and its capacity was 1 Ah. The battery comprised a $LiNi_{0.81}Co_{0.15}Al_{0.04}O_2$ cathode, a graphite anode, and a separator made of stacked polyethylene (PE) and polypropylene (PP) films. The cathode and anode were coated on Al and Cu foil, respectively. The laminated cathode, separator, and anode were sealed together with the liquid electrolyte into an aluminum package. A fully charged, pristine battery was used as the imaging sample.

Neutron imaging experiment was conducted at BL22 RADEN in J-PARC MLF (Japan Proton Accelerator Research Complex, Materials and Life Science Experimental Facility) with a proton beam power of 800 kW. Neutron transmission images were acquired using a CMOS camera with a resolution of 2048 × 2048 pixels. The field of view and the exposure time were 47.6 × 47.6 mm and 0.48 s, respectively.

3. Results and discussion

We have designed and built a double-layered airtight chamber consisting of an inner and outer box specifically for neutron experiments as shown in Fig. 1. This specialized chamber was developed over a period of two years, repeating trial manufacture and testing to ensure the safety of experiments at the neutron facility. Before the battery sample reaches the thermal runaway,

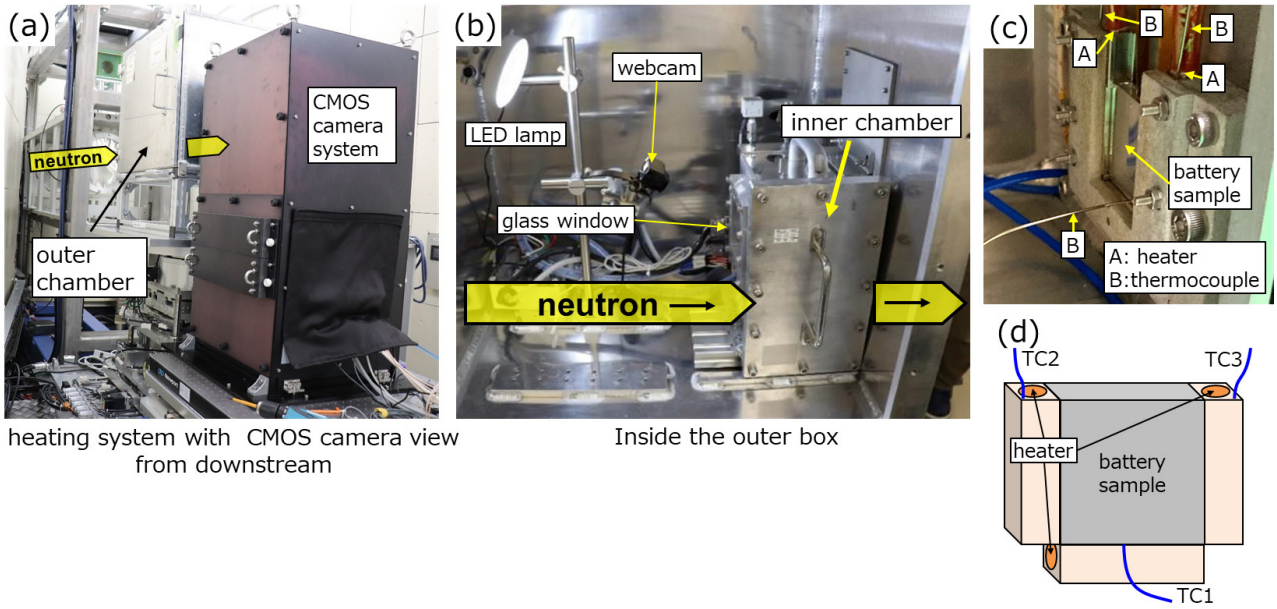

Figure 1. The pictures of the heating experiment at BL22 (RADEN); (a) outer chamber and CMOS camera system viewed from downstream, (b) inside the outer chamber with the webcam and LED lamp, and (c) battery sample fixed to the holder inside the inner chamber. (d) Three cartridge heaters are placed on both sides and the bottom of the sample, and three thermocouples (TC) are attached to the bottom and the top of a heater holder. Thermocouples TC1 measure the sample temperature. TC2 and TC3 are for temperature control and the over-temperature prevention, respectively.

the liquid electrolyte spews out of the battery can due to increased internal pressure, and high temperature particles are released. Even in such a situation, it was confirmed that our airtight chamber confined all particles and gases for a month.

To avoid blocking the neutron beam transmitted through the sample, heaters were placed on both sides and at the bottom of the battery sample. The sample was heated at a rate of 5°C/min. According to a preliminary experiment, the spatial resolution was evaluated as 248 μm, and the transmission of the center of the battery sample was about 27%.

The sample temperature (T_s) and the voltage (V_s) as a function of the heating time are shown in Fig. 2 with neutron transmission images. At room temperature, V_s was about 4.2 V and almost constant up to 90°C. Around 125°C, there was an obvious contrast between the upper and lower parts of the battery in the transmission image. This is caused by the so-called separator shutdown mechanism, in which the electrolyte seeps out of the separator. Thereafter, V_s gradually decreased and dropped suddenly at 157°C. Since this phenomenon occurs near the melting point of PP (approximately 160°C), it is believed to be caused by the complete insulation of the separator. As T_s rose further, the film-like material was seen to deform as shown in Fig. 2 (right upper panel). Another experiment revealed that the deformed material was the plastic film insulation between the battery can and the electrodes. Above 170°C, T_s rises quickly around 190°C due to thermal runaway.

4. Conclusion

We established an in-situ neutron imaging technique while heating the LIB by fabricating a special chamber system. Consequently, we succeeded in observing the internal structural change in LIB up to thermal runaway with a time resolution of a few seconds.

Reference

[1] H. Nozaki et al., Scientific Reports, **13** 22082 (2023).

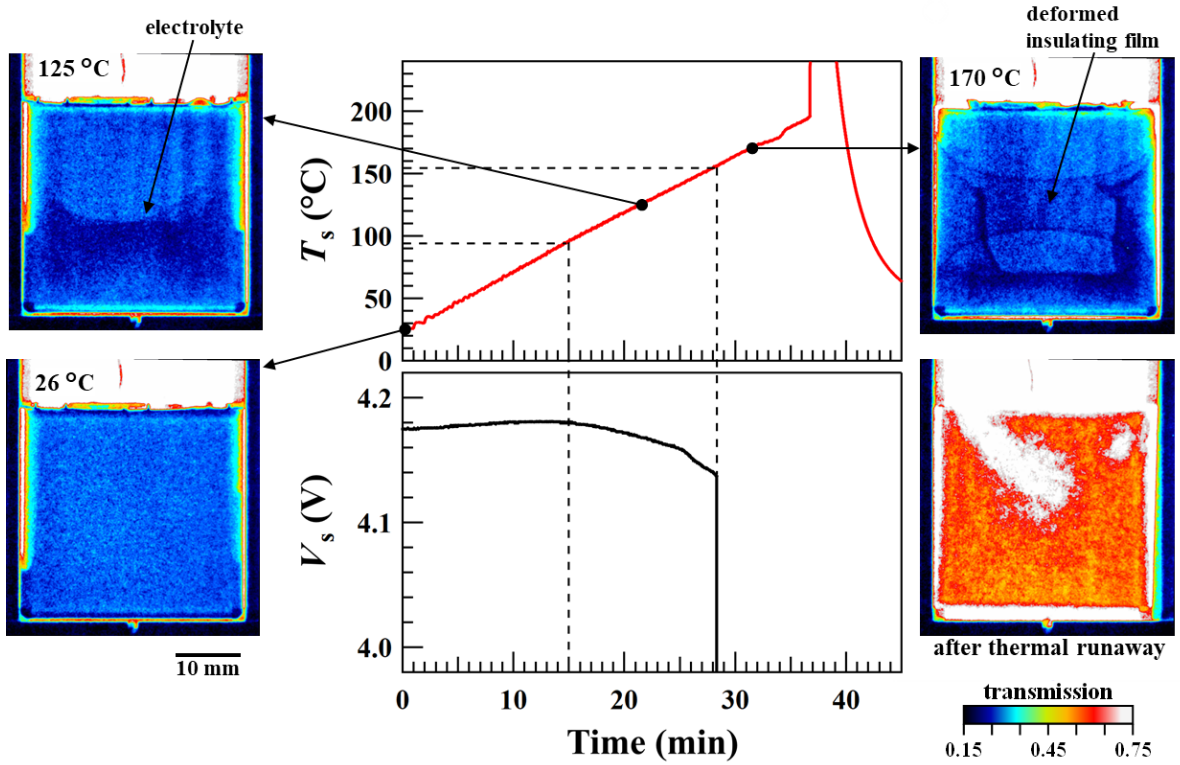

Figure 2. Temporal dependence of the voltage and temperature. Variations in the temperature and voltage of the battery sample as a function of time. Transmission images are shown at different temperatures with a visually distinguishable contrast. Figure of the neutron experiment. Copyright © 2023, The Authors, Springer Nature Ltd., (H. Nozaki et al., CC BY 4.0, No changes [1]).

H. Nozaki[1], H. Kondo[1], T. Shinohara[2], D. Setoyama[1], Y. Matsumoto[3], T. Sasaki[1], K. Isegawa[1,2], and H. Hayashida[3]

[1]*Toyota Central Research and Development Laboratories Inc.;* [2]*Neutron Science Section, Materials and Life Science Division, J-PARC Center;* [3]*Neutron Science and Technology Center, CROSS*

Revealing Hydrogen Dynamics in Zeolites as Catalyst Support

1. Introduction

In hydrogenation reactions, the charge state of hydrogen directly determines its reactivity and interactions with the catalyst. The dissociation and diffusion of hydrogen on the catalyst surface, as well as charge transfer processes, significantly influence the reaction progress and selectivity. Therefore, understanding the charge state of hydrogen is crucial for optimizing specific reactions and designing appropriate catalysts and reaction conditions for a wide range of applications. However, the dynamic nature of these species, coupled with the complexity of catalytic environments, makes it difficult to directly observe and quantify the hydrogen charge state under reaction conditions.

In recent years, K. Motokura et al. developed a catalyst composed of Pd nanoparticles supported on zeolites, which facilitates the direct coupling reaction between alkanes and benzene [1]. The proposed reaction scheme is illustrated in Scheme 1. While conventional methods for synthesizing alkylbenzenes typically produce substantial quantities of by-products, this approach generates only hydrogen or water as by-products. A critical aspect of this reaction is the transfer of hydrogen atoms from the acidic sites of the zeolite to the Pd nanoparticles. Nonetheless, the precise charge state of the transferred hydrogen remains unidentified, impeding a full understanding of the reaction mechanism.

In the present study, we aimed to elucidate the charge state of hydrogen during the diffusion process. To achieve this, we employed μ^+SR measurements to probe the electronic state of hydrogen atoms under reaction temperature. By comparing with previous reports, we investigated whether the atomic hydrogen on zeolite had enogh life time for the reaction using muonium (Mu) as a peudoisotope of hydrogen. The Mu mixture initially formed upon muon implantation is typically far from thermal equilibrium and contains an excessive proportion of metastable Mu species [2, 3]. This may mimic the reaction intermediate in/on the zeolites. Our findings from the study of metastable Mu are expected to provide critical insights into the fundamental role of hydrogen charge states in catalytic transformations, providing a molecular-level understanding of the reaction mechanism.

2. Experimental

Pulsed μ^+SR measurements were performed on H-mordenite and H-ZSM-5 powders in the D1 area of MLF at J-PARC, utilizing a spin-polarized surface muon beam in double-bunch operation mode. The zeolite powders were dried at 150°C for 1 hour in a ^{4}He atmosphere and subsequently sealed in a titanium cell using a gold wire ring gasket, maintaining the ^{4}He atmosphere. The sample cell, mounted on the cold finger of a conventional ^{4}He flow cryostat, was placed in the μSR spectrometer. Positive muons penetrated the 50 μm-thick titanium window (24 mm diameter) of the sample cell and were implanted into the bulk of the zeolite. Measurements were conducted in longitudinal geometry, where the muon spins were polarized along the incident beam direction. The time evolution of the

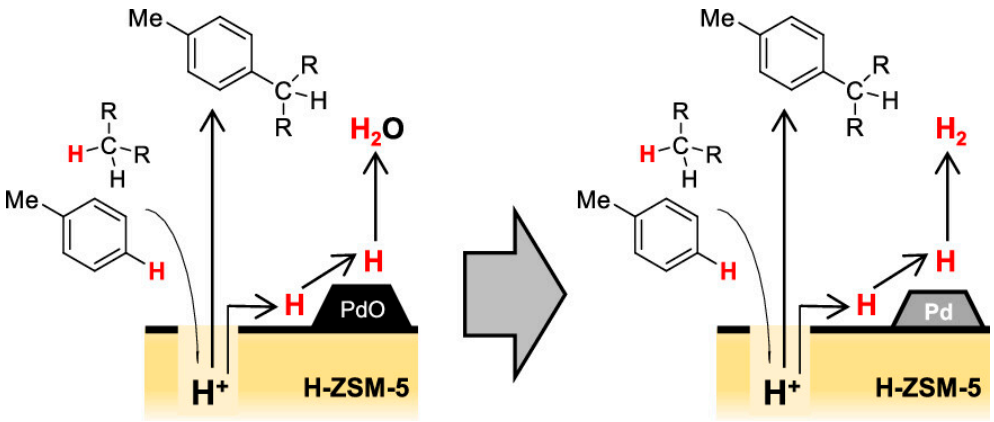

Scheme 1. Reaction pathway of the present study. Scheme from ACS Catalysis, 18, 2023, 12281 ©2023, ACS Publications.

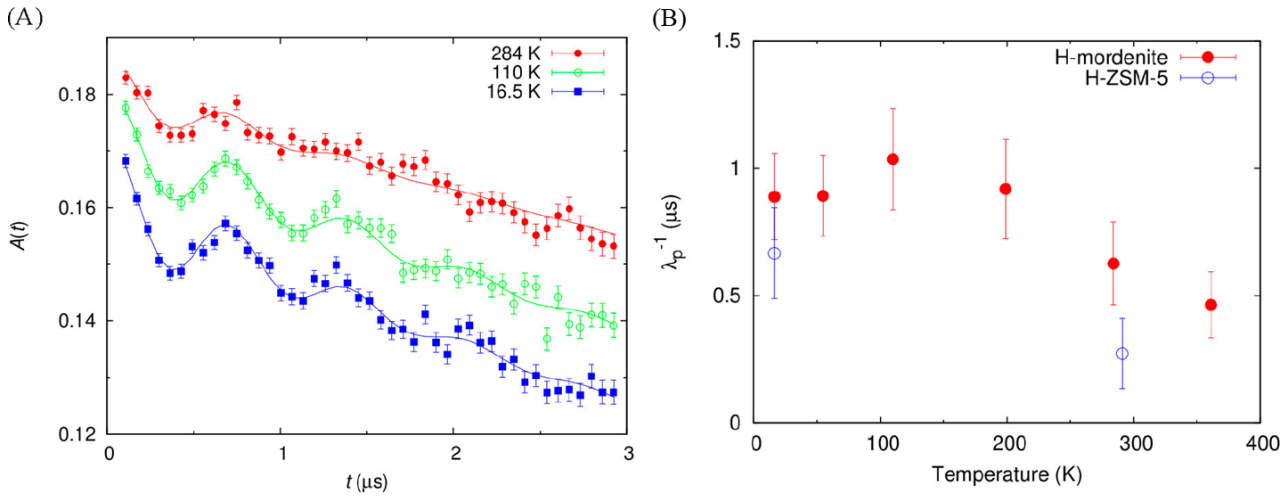

Figure 1. (A) μ⁺SR time spectra of H-mordenite under TF (0.10 mT) at 16.5, 110, and 284 K. (B) Temperature dependence of λ_p^{-1} for H-mordenite and H-ZSM-5. Reprinted with permission from ACS Catal. 2023, 13, 18, 12281−12287. © 2023 American Chemical Society.

forward-backward asymmetry of muon beta decay, $A(t)$, was recorded using scintillation counters surrounding the sample. The time origin (t = 0) was set to the arrival of the second muon pulse at the sample.

3. Results and discussion

Figure 1(A) presents the μ⁺SR time spectra, A(t), of H-mordenite under a transverse field (TF) of 0.10 mT over a wide temperature range. The spin-triplet component of paramagnetic atomic muonium was observed as a characteristic damped cosine oscillation with a frequency of 1.44 MHz at 0.10 mT. A similar spin-triplet Mu signal was detected in H-ZSM-5 under a TF of 0.13 mT.

The chemical lifetime of the initially formed atomic Mu (τ_{Mu}) was estimated from the depolarization rate (λ_p) of the spin-triplet Mu signals using the relation $\lambda_p = \tau_{Mu}^{-1} + \lambda_0$, where λ_0 represents the depolarization rate arising from other origins, such as the distribution of nuclear dipolar fields (Fig. 1(B)). The λ_p values are consistent with those reported for other sodium-based aluminosilicates [4]. At temperatures near 400 K, the chemical lifetime of the atomic Mu was found to be in the sub-microsecond range or longer for both zeolites. In comparison, the chemical lifetime of secondary carbocations during chemical transformations has been reported to lie in the femto- to picosecond range [5, 6]. These findings suggest that the chemical lifetime of atomic hydrogen species is sufficiently long to facilitate their diffusion and participation in reactions both within and on the surfaces of H-ZSM-5 and H-mordenite, thereby enabling the elucidation of the reaction pathway outlined in Scheme 1.

4. Conclusion

In this study, we investigated the charge state and chemical lifetime of hydrogen species in H-mordenite and H-ZSM-5 zeolites using pulsed μ⁺SR measurements. The results revealed that the atomic muonium formed upon μ⁺ implantation exhibits a chemical lifetime in the sub-microsecond range or longer, even at elevated temperatures near 400 K. This lifetime is significantly longer than that of secondary carbocations, suggesting that atomic hydrogen species possess sufficient stability to enable diffusion and catalytic reactions within the zeolite framework and on its surface.

References

[1] S. Misaki et al., ACS Catalysis **13** 12281 (2023).
[2] L. R. Lichti et al. Phys. Rev. Lett. **101** 136403 (2008).
[3] T. U. Ito, e-J. Surf. Sci. Nanotech. **20** 128 (2022).
[4] D. J. Arseneau et al., Physica B **326** 64 (2003).
[5] R. Pemberton et al., Chem. Sci. **5** 3301 (2014).
[6] W. Chen et al., Chem. Soc. Rev. **51** 4337 (2022).

H. Miwa[1,2], T.U. Ito[3], and K. Motokura[4]
[1]*Innovation Research Center for Fuel Cells and Hydrogen, The University of Electro-Communication;* [2]*Graduate School of Informatics and Engineering, The University of Electro-Communications;* [3]*Advanced Science Research Center, Japan Atomic Energy Agency;* [4]*Department of Chemistry and Life Science, Yokohama National University*

New Precision Measurements of Muonic Helium Hyperfine Structure

1. Introduction

Muonic helium is composed of a helium atom with one of its electrons replaced by a negative muon (μ^-). The muon is so closely bound to the helium nucleus that it nearly completely screens one proton charge, producing a "pseudonucleus" with a positive effective charge and a magnetic moment nearly equal to that of a negative muon. It can be regarded as a heavy hydrogen isotope, similar to muonium, another hydrogenlike atom made of a bound state of a positive muon and an electron (Fig. 1). The ground-state hyperfine structure (HFS) of muonic helium results from the interaction of the negative muon magnetic moment and the remaining electron and is very similar to that of muonium but inverted because of the different signs of their respective muon magnetic moments.

Muonic helium HFS has only been measured twice in the 1980s directly at zero magnetic field [1] and indirectly at high field [2]. New precision measurements of the muonium HFS interval using a microwave magnetic resonance technique are now in progress at J-PARC by the Muonium Spectroscopy Experiment Using Microwave (MuSEUM) Collaboration [3]. The same method can be used to precisely measure the muonic helium HFS interval $\Delta\nu$, which is a sensitive tool to test three-body atomic systems and bound-state quantum electrodynamics theories. Measurements at high field also allow us to determine the fundamental constants of the negative muon magnetic moment and mass. The world's most intense pulsed negative muon beam at the Muon Science Facility (MUSE) of J-PARC allows improving previous measurements and testing further *CPT* invariance by comparing the magnetic moments and masses of positive and negative muons (second-generation leptons).

What makes muonic helium HFS measurements more challenging is that the initial μ^- polarization (~100%) is strongly reduced to ~5% during the muon cascade process in He due to Auger transition and collisional Stark mixing. This value should be compared to the case of muonium (50%), as we need to expand the measurement period by 100 times to get similar statistics. Also, when a He atom captures a μ^- ejecting both electrons via Auger transitions in the process, and a $[\mu^- {}^4He^{++}]^+$ ion in its ground $1s$ state is formed, it cannot capture an electron from the neighboring He atoms because its electron binding energy is similar to that in hydrogen (13.6 eV). Thus, to form a neutral μHe atom, the prerequisite to measuring HFS, a collision with a foreign gas atom acting as an electron donor is necessary. Here, CH_4 was preferred to Xe used previously [1, 2] because of its reduced total charge ($Z = 10$), which makes it less likely to capture muons (Fermi-Teller Z law), a similar ionization potential (12.5 eV), and CH_4 is also believed to give a larger residual polarization compared to Xe, making it more advantageous for the experiment.

2. Experiment details

The experiment was performed at the J-PARC MUSE D-line. The apparatus enclosed in a magnetic shield box made of permalloy for zero-field measurements is shown in Fig. 2. Pulsed polarized μ^- were stopped into a microwave cavity located inside a gas chamber containing pressurized He gas with an admixture of 2% CH_4 as an electron donor to form neutral μHe atoms efficiently. The muon spin was flipped by applying a microwave

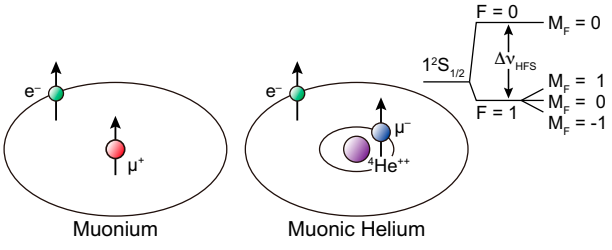

Figure 1. Comparison between a muonium atom (left) and a muonic helium atom (right), showing a diagram of its ground-state hyperfine structure and low-field Zeeman splitting (insert).

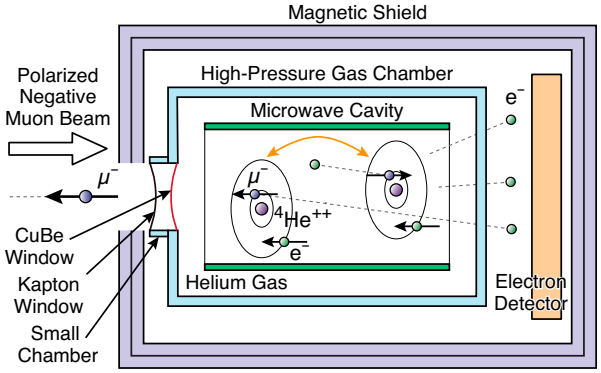

Figure 2. Schematic view of the experimental setup to measure muonic helium HFS at zero field.

magnetic field in the cavity. Electrons (e^-) from μ^- decay were emitted preferentially in the direction antiparallel to the μ^- spin. At the resonance, the microwave field induced the μ^- spin flip, changing the angular distribution of decay electrons, which were detected with segmented scintillation counters placed downstream. Muonic helium HFS measurements were performed by scanning the microwave frequency and measuring the decay e^- asymmetry with and without microwave ($N_{ON}/N_{OFF} - 1$) to determine the resonance frequency $\Delta\nu$.

3. Results

Muonic helium HFS resonance curves measured at three different He gas pressures of 3.0, 4.0, and 10.4 atm are shown in Fig. 3. The resonance curve centers were determined by fitting a theoretical resonance line shape using the "old muonium" method [4]. The three frequency values $\Delta\nu$ measured with He + CH_4(2%) are shown in Fig. 4 as a function of the gas density in atmosphere at 0°C and corrected for nonideal gas behavior (closed circle). Previous results from [1, 2] measured with He + Xe(1.5%) are also shown for comparison. The HFS frequency at zero pressure $\Delta\nu(0)$ of a free μHe atom was obtained by fitting a linear pressure shift to the data (solid line). By fitting our measured values with $\Delta\nu(p) = \Delta\nu(0) + Ap$ we obtained $\Delta\nu(0)$ = 4464.980(20) MHz (4.5 ppm). The uncertainty indicated is mainly statistical (details reported in [5]).

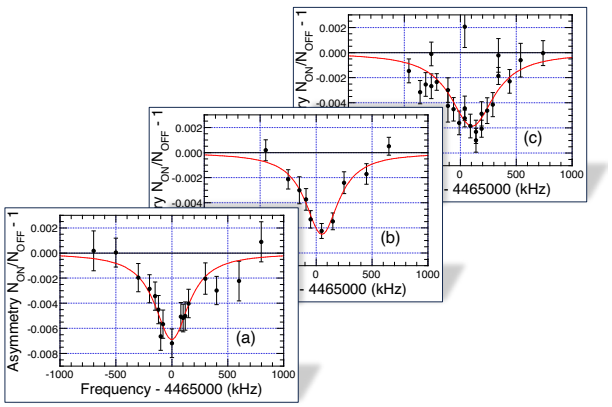

Figure 3. Muonic helium HFS resonance curve measured at zero field with He + CH_4(2%) at (a) 3.0, (b) 4.0, and (c) 10.4 atm, respectively.

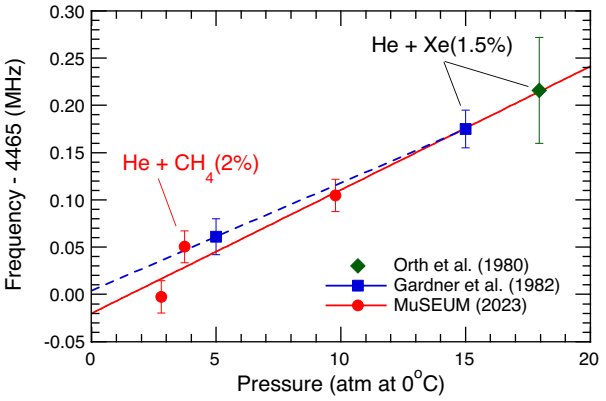

Figure 4. Δν as a function of He + CH_4 (2%) gas pressure (closed circle). The solid line shows the linear fit to the data to determine Δν (0). Previous results measured with He + Xe(1.5%) [1, 2] are shown.

4. Summary and future plans

After nearly 40 years, new precise measurements of the muonic helium HFS were performed, and the achieved precision was 3 times better than the previous measurement at zero field [1]. Our result is also more precise than the high field measurement [2], improving the current world record by a factor of 1.5, and it was the first one performed with CH_4 admixture to efficiently form neutral μHe atoms.

High-field measurements are now in progress at the H-line, using higher μ^- intensity than at the D-line and longer measurement time, we aim to improve the determination of the negative muon magnetic moment and mass by nearly 100 times over the previous measurement [2].

References

[1] H. Orth *et al.*, Phys. Rev. Lett. **45**, 1483 (1980).
[2] C. J. Gardner *et al.*, Phys. Rev. Lett. **48**, 1168 (1982).
[3] S. Kanda *et al.*, Phys. Lett. B **815**, 136154 (2021).
[4] W. Liu *et al.*, Phys. Rev. Lett. **82**, 711 (1999).
[5] P. Strasser *et al.*, Phys. Rev. Lett. **131**, 253003 (2023).

P. Strasser[1,2,3], S. Fukumura[4], R. Iwai[1], S. Kanda[1,2,3], S. Kawamura[4], M. Kitaguchi[4,5], S. Nishimura[1,2], S. Seo[6], H. M. Shimizu[4], K. Shimomura[1,2,3], H. Tada[4], and H. A. Torii[7]

[1]Institute of Materials Structure Science, KEK; [2]Muon Science Section, Materials and Life Science Division, J-PARC Center; [3]Materials Structure Science Program, Graduate Institute for Advanced Studies, SOKENDAI; [4]Department of Physics, Nagoya University; [5]Kobayashi-Maskawa Institute, Nagoya University; [6]Graduate School of Arts and Sciences, The University of Tokyo; [7]School of Science, The University of Tokyo

Hydrogen Trapping in Aluminum Alloys Via Muon Spin Relaxation Method and First-Principles Calculations

1. Introduction

While hydrogen embrittlement is a widely known phenomenon in metallic materials, experimental data on the hydrogen atoms' kinetics in metals are limited due to the difficulty of direct observation. Metallurgical analyses using large synchrotron radiation facilities and high-resolution electron microscopy have revealed that delamination and fracture occur at the interface between precipitated particles and aluminum in high-strength aluminum alloys. In contrast, alloys with precipitated and dispersed specific particles suppress hydrogen embrittlement, although the direct interaction with hydrogen is unknown [1]. Recent studies based on first-principles calculations (DFT) revealed that certain precipitated particles may strongly trap hydrogen inside [2]. The present study focused on the usefulness of muons, which show similar behavior to hydrogen in metals, as a medium to link calculation-based predictions with experimental data. Using muons and DFT, the locations and binding energies of hydrogen atoms trapped in aluminum alloys are evaluated to search for groups of solute elements that can strongly bind and trap hydrogen and thus strongly suppress hydrogen embrittlement.

In this work, zero-field muon spin relaxation experiments were carried out for Al-0.5%Mg, Al-0.011% Ti, Al-0.015% V, and Al-0.2% Cu (at. %). The experimental results indicate that the temperature variations of the dipole field widths (Δ) have revealed three peaks for Al-0.5%Mg, Al-0.011%Ti, Al-0.015%V, and four peaks for Al-0.2%Cu alloys. Atomic configurations of the muon trapping sites corresponding to the observed Δ peaks are well assigned using the DFT results for hydrogen binding energies around a solute and solute-vacancy pair. Detailed descriptions have been given elsewhere [3].

2. Experimental

The materials used in this study were prepared in two ways. First, the Al-Mg and Al-Cu alloys were cast in the steel mold by melting pure Al with Mg or Cu and homogenized at 743 K for 24 h in air. The Al-Ti and Al-V alloys were melted in an argon arc furnace with Al and Ti or V and homogenized at 873 K for 12 h in a vacuum quartz tube. The resulting ingots were formed into 1.0 mm thick plates by hot and cold rolling, then sample plates of approximate dimensions, $25 \times 25 \times 1$ mm^3, were cut out.

The zero-field muon spin relaxation spectra were obtained in the S1 area. Relaxation spectra were acquired with 30 million positron counts (events) recorded at each temperature point from 6 to 302 K. We have interpreted the measured relaxation spectra using a Monte Carlo simulation, in which four fitting parameters were employed: the dipolar width (Δ), trapping rate (vt), detrapping rate (vd), and a fraction of initially trapped muons (P0) [4].

3. Results

The observed relaxation spectra with the Al-0.011%Ti sample were plotted in Fig. 1, divided into three temperature regions. From 6 to 58 K, the largest relaxation rate was found at 30 K, and the smallest at 6 K (Fig. 1a). The relaxation rates were large and almost constant between 67 and 96 K, and between 117 and 199 K, indicating the existence of a clear boundary near 108 K (Fig. 1b). Above 199 K, the relaxation rates decreased as the temperature rose (Fig. 1c).

Similar relaxation spectra were taken for other samples. Figure 2 shows the temperature variations of the deduced Δ values by the Monte Carlo simulation for the four samples, in which arrows indicate identified peak temperatures of Δ (T_Δ). There are three peaks for Al-Mg, Al-Ti, and Al-V, and four peaks for Al-Cu alloys. The Δ peak temperatures for Al-0.011%Ti are well correlated with the variations of the observed spectra. Similar depolarization rate peaks have been found in previous studies, but detailed explanations have hardly

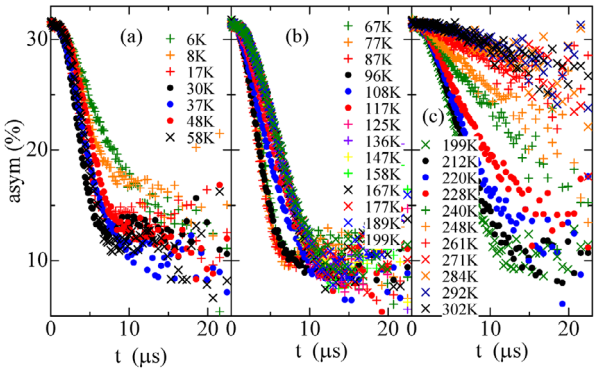

Figure 1. Observed zero-field relaxation spectra with Al-0.011%Ti sample in the temperature regions: (a) 6 – 76 K, (b) 84 – 190 K, and (c) 201 – 302 K.

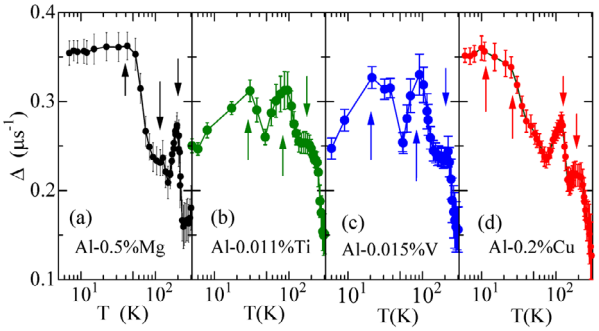

Figure 2. Deduced dipole field widths vs temperatures for (a) Al-0.15%Mg, (b) Al-0.011%Ti, (c) Al-0.015%V, and (d) Al-0.2%Cu.

been found [5]. Since the Δ values mainly depend on the atomic configurations of the muon trapping sites, it is of interest to examine which kind of atomic configurations are associated with these Δ peaks.

We adopted hydrogen binding energies with solute and solute-vacancy pairs from the DFT results to determine the atomic configurations. Figure 3 illustrates possible muon trapping sites with solute Ti atoms and/or vacancies. The hydrogen binding energies from DFT calculations locating H atom at the muon position in Fig. 3 were found to be 0.043, 0.248, and 0.340 eV for the atomic configurations of Ti-2NN, Ti-1NN, and Ti-vac-2NNA, respectively [3]. Similar assignments were done for the three Δ peaks of Al-Mg and Al-V alloys. For Al-Cu, the third peak was assigned to trapping muons in a Cu-vacancy pair and the fourth to trapping in a Cu-vac-2NNA site [3].

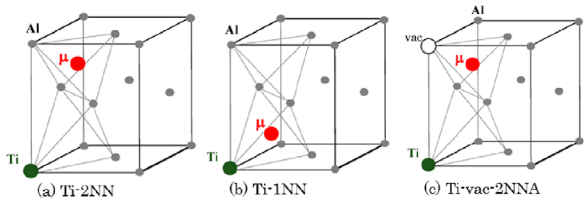

Figure 3. Atomic configurations for muon trapping sites with Al-Ti alloys: (a) second nearest neighbor site of Ti, (b) nearest neighbor site of Ti, and (c) nearest neighbor site of vacancy with Ti in the second nearest neighbor.

Figure 4 plots the relationship between the T_Δ and H binding energies (E_H). Atomic configurations of the muon trapping sites corresponding to the T_Δ are well assigned using E_H of hydrogen around a solute and solute-vacancy pair, resulting in the linear relationship in Fig. 4 ; T_Δ [K] = 430 × E_H [eV] (note: there is approximately 20 times difference between T_Δ and E_H, the intrinsic physical meaning is unclear)

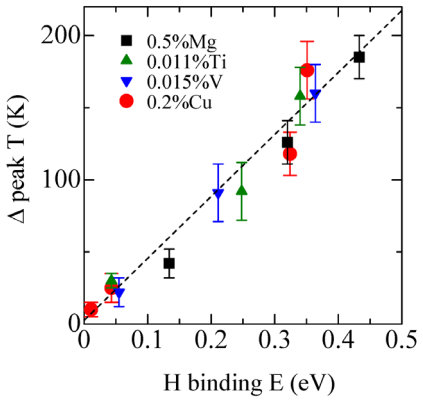

Figure 4. A plot of the observed Δ peak temperature vs. trap energy of hydrogen around a solute or solute-vacancy pair.

4. Future Plans

The combination of the μSR and the first-principles calculation shows that the Δ peak temperatures have a clear linear relationship with the trap energies for the particular configurations. This approach, based on muon Δ peak temperature and hydrogen binding energy, enables us to predict the existence of unknown trap sites and to explore the potential alloying elements that trap hydrogen in Al alloys. This method has already been successfully applied to Al_6Mn compound [6].

References

[1] Y. Wang et al., Nature Comm. **13** 6860 (2022).
[2] T. Tsuru et al., Sci. Rep. **10** 1 (2020).
[3] T. Tsuru et al., Metall. Mater. Trans. A **54** 2374 (2023).
[4] S. Wenner et al., Phys. Rev. B **86** 104201 (2012).
[5] W.J. Kossler et al., Hyperfine Interact. **6** 295 (1979).
[6] K. Shimizu et al., Scripta Mater. **245** 116051 (2024).

K. Nishimura[1], K. Matsuda[1], T. Namiki[1], W. Higemoto[2], T. Tsuru[3], K. Shimizu[4], and H. Toda[5]
[1]Graduate School of Science and Engineering, University of Toyama; [2]Advanced Science Research Center, Japan Atomic Energy Agency; [3]Nuclear Science and Engineering Center, Japan Atomic Energy Agency; [4]Faculty of Engineering, Tottori University; [5]Department of Mechanical Engineering, Kyushu University

Neutron Source

Neutron Source Section

1. Operational overview

The beam operation for the user program in fiscal year 2023 started on April 16 with beam power of 930 kW at the outlet of the 3 GeV rapid cycling synchrotron (RCS) (820 kW at the MLF). The beam power was raised up to 950 kW at the outlet of RCS (840 kW at the MLF) on April 20. However, the beam operation was suspended by a fire accident at the 30 GeV main ring (MR), which occurred on April 26. The operation resumed on May 14. Due to rising external temperatures, the beam power at MLF dropped to 800 kW on June 2 and further to 750 kW on June 8. A second fire accident at the MR on June 22 brought the beam operation to an end, starting a long maintenance period.

Following issues with the cryogenics loop system, the resumption of the beam operation after the maintenance was delayed. The operation restarted on December 3 with a beam power of 660 kW at the MLF, despite some pressure loss in the cooling water flow and the mercury flow in the new target. The beam operation was suspended again on December 25 for the holiday season and resumed on February 5 after replacement of the cooling system of the air conditioner at the MLF building. With the sufficient bubbling effect in the target confirmed, the beam power at MLF was restored to 810 kW on February 12.

The availability of the beam operation for the user program in FY2023 was 64.6% before the long outage and 77.1% afterward.

2. Maintenance work overview

Some important remote-handling operations in the hot cell were performed. One of these was the replacement of the used proton beam window at the shielding plug with a new one via remote handling. The proton beam window is mounted on the shielding plug and integrated into one unit. The unit of the proton beam window was replaced in the previous year. The assumed lifespan of the proton beam window is approximately 10,000 MWh. The operation was successfully completed.

Another notable operation was the remote handling test of the moderator and reflector assembly, conducted using a spare assembly, as in the previous year. An assembly consists of three moderators, a reflector, and a shielding plug. Only the used moderators and reflector are replaced, while the shielding plug is reused, similar to the proton beam window. Because the operating lifetime of a moderator and reflector assembly is relatively long, 30,000 MWh, equivalent to 8 years at 1 MW, the previous remote handling operation was conducted during the commissioning period before the MLF beam operation began more than 10 years ago. Therefore, inheriting skills and experience is crucial. During the detailed checks of the remote handling procedures, several issues requiring resolution were identified. These issues will be addressed, and the procedures will be re-evaluated using full remote handling for actual radioactive assembly in the near future.

On September 4, specimens were cut from the forefront wall of the used target vessel, which operated with 2,273 MWh and 950 kW/pulse at maximum. A picture of the specimen is shown in Fig. 1. The damage to the inner wall of the mercury vessel, which was protected against pitting damage by micro-bubble injection into mercury

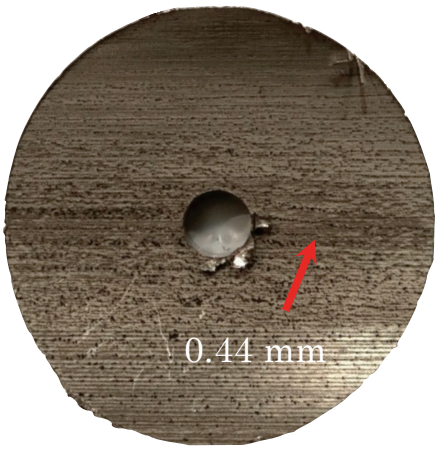

Figure 1. The picture of a PIE specimen at the inner mercury vessel wall with the integrated beam power of 2,273 MWh, and the peaked and averaged beam power of 950 kW and 851 kW, respectively. The maximum pitting damage depth is about 0.44 mm.

flow, was small (0.44 mm in the maximum). Additionally, the damage to the outer wall, the mercury boundary wall, was negligibly small, which is a promising result for the stable beam operation at 1 MW at the MLF. On September 13, the used mercury target vessel was replaced with a new one equipped with an improved bubble generator.

3. International workshop

Five researchers from the Neutron Source Section visited the Oak Ridge National Laboratory (ORNL) in the USA for the first time in 6 years. From March 19 to 21, 2024, an international collaboration workshop was held with the Spallation Neutron Source (SNS) of ORNL to discuss issues related to the neutron source system. Productive discussions were conducted on topics such as target vessel development and PIE tests, and the continuation of the collaboration was reaffirmed.

M. Harada[1], K. Sakai[1], and K. Haga[2]
[1]*Neutron Source Section, Materials and Life Science Division, J-PARC Center;* [2]*Materials and Life Science Division, J-PARC Center*

Improvement of Mercury and Gas Flow Rate in the Mercury Target Vessel #15

1. Introduction

In a mercury target system for a neutron source, pulsed proton beams repeatedly bombard the flowing mercury, which is confined in a stainless-steel vessel (target vessel (Fig. 1)). The bombardments of the proton beams cause pressure waves in the mercury and they induce cavitation erosion damage in the target vessel. The cavitation erosion damage is a factor determining the proton beam power and the lifetime of the target vessel. To mitigate the erosion damage, we developed a narrow channel structure [1] and a technique to inject the gas microbubbles into the flowing mercury by the swirl bubbler [2], as shown in Fig. 2, which can reduce the pressure waves inducing the cavitation erosion [3]. Thanks to these techniques, the neutron source continued its stable operation with averaged proton beam power of 795 kW in FY2023.

On the other hand, the spent targets are kept in a storage area, which takes space. Therefore, further reduction of the erosion damage is required to extend the lifetime of the target vessel and to reduce the generation frequency of spent target vessels. An effective way to increase the gas volume fraction of the gas microbubbles into the mercury is to mitigate the damage [3]. The severely damaged area is the beam window where the proton beam is injected, as shown in Fig. 1, because heat deposition and generated pressure waves are high. Since the injected gas bubbles rise due to buoyancy, it is assumed that the volume fraction of gas microbubbles near the beam window can be increased by moving the bubbler closer to the beam window. However, the space near the beam window of the target vessel is restricted, as shown in Fig. 1 (a). For this reason, the bubbler needs to be smaller. The bubbler can draw the gas to generate gas microbubbles by using pressure reduction caused by a swirl flow of mercury. The relationship between internal structure and performance of the bubbler is complicated. However, the performance of the bubbler, such as flow resistance, size of the generated microbubbles, and amount of drawn gas depends on the diameters of the inlet, D, and throat, De, the angle of swirl blades at exit, θ, and the mercury flow rate through the bubbler, V_{in} [2]. That is, as the bubbler becomes smaller, the flow resistance increases and the mercury flow rate decreases. These phenomena cause increases of temperature and thermal stresses in the mercury target vessel, generation of pressure in the mercury target system that exceeds the design value, and shortage of the drawn gas.

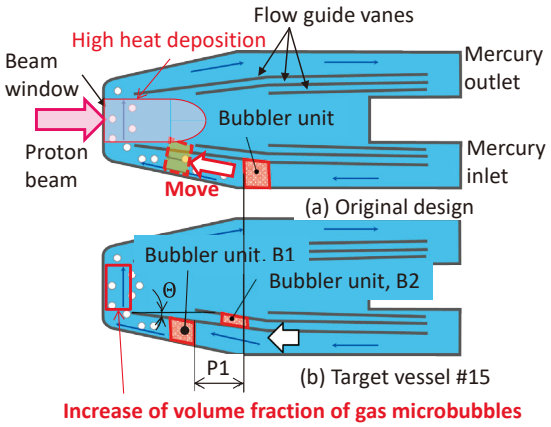

Figure 1. Schematic of the mercury target vessel: (a) original design, (b) Target vessel #15.

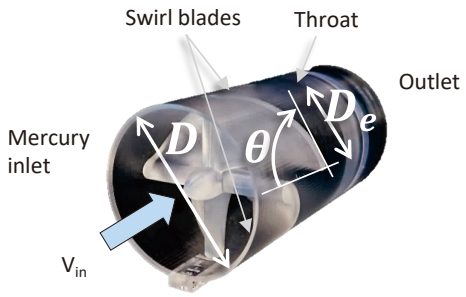

Figure 2. Swirl bubbler element.

Machine learning [4] was used to optimize the bubbler installation position and the internal structure of the bubbler with the aim of increasing the amount of the microbubbles near the beam window and reducing flow resistance in the bubbler and this optimized target vessel (Mercury target vessel #15) has been operated since November 2023.

2. Mercury target vessel in FY2023

From November 2022 to June 2023, to verify the effect of moving the bubbler closer to the beam window, a target vessel (Mercury target vessel #13) was used, in which the bubbler was moved 90 mm closer from the original target. In this position, the bubbler can be installed without changing the internal structure from the original one. The effect of moving the bubbler was confirmed, as shown in [5]. The Mercury target vessel #15, in which the bubbler was moved 240 mm closer from the original, was then replaced and used from November 2023.

3. Mercury and gas flow rates in Mercury target vessel #15

Mercury target vessel #15 (operated from 2023/11 to 2024/6) was expected to operate for 4000 hours at a proton beam power of 980 kW (25 Hz equivalent: The proton beams are delivered to the MR at regular time intervals, so the injection power into the MLF is around 850 kW).

The conditions for the Mercury target vessel to withstand these operating conditions are as follows.

(1) To keep temperature and thermal stress in the mercury target, mercury flow rate should be over 94% of it in Mercury target vessel #13.

(2) To suppress the cavitation erosion damage, the gas drawn into the bubble should be over 90% of it in Mercury target vessel #13.

To check whether the operation with Mercury target vessel #15 satisfied above conditions, the mercury flow conditions were investigated prior to the operation for users. The flow resistance inside the mercury target, including the bubbler, was high. The high flow resistance reduced the mercury flow rate, which was feared to increase the temperature of the mercury target vessel, as well as decrease the amount of the drawn gas into the bubbler. It is possible to increase the mercury flow rate by increasing the output of the mercury pumps, but doing so would increase the pressure in the system and exceed the design pressure of the mercury target system.

4. Countermeasure to increase mercury flow rate and amount of drawn gas

There was an urgent need to increase the mercury flow rate without exceeding the design pressure of the system. The reduction of the amount of mercury in the system decreases the static pressure in the target system and the output power of the mercury pumps could be increased to ensure the mercury flow rate without exceeding the design pressure. Figure 3 shows a schematic diagram of the mercury target system. Reducing the amount of mercury lowers the liquid level in a surge tank. Figure 4 shows mercury flow rate and the drawn gas rate (gas flow rate), which were normalized with the values of the Mercury target vessel #13 for various mercury levels. The output power of the pump was gradually increased until the design pressure of the target system was reached. As the pump output increases, the mercury flow rate and gas flow rate increase. As a result

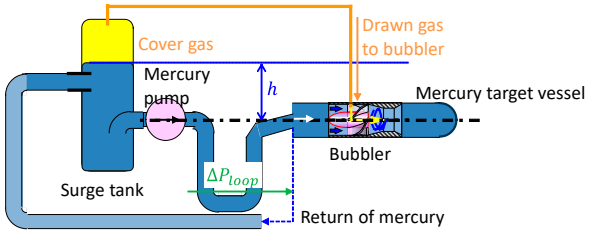

Figure 3. Schematic diagram of the mercury target system.

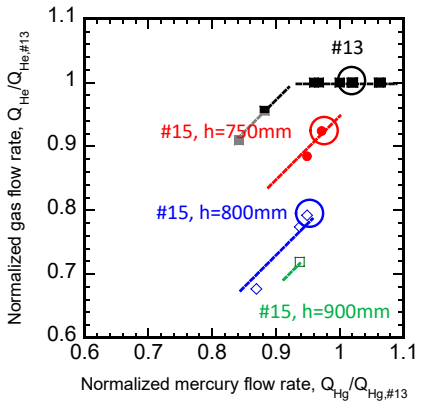

Figure 4. Mercury flow rate and the drawn gas rate (gas flow rate) for various mercury levels.

of decreasing the mercury level in the surge tank from 900 mm to 730 mm, the mercury flow rate and gas flow rate recovered to 97% and 90% of the Mercury target vessel #13's values, respectively. When the tank level is lower than 730 mm, the inlet pipe to the tank is higher than the tank liquid level, which may cause flow instability.

After that, the operation with Mercury target vessel #15 stabilized and continued until June 2024. After the operation, the erosion damage will be observed to confirm the effect of the new bubbler.

Recent studies have shown that flow resistance depends not only on the exit angle of the blades, but also on the angular gradient leading up to it [6]. In the future, we will consider a blade shape with low flow resistance and will increase the number of bubbles.

References

[1] T. Naoe et al., Mat. Sci. Forum, 1024 111 (2021).
[2] H. Kogawa et al., J. Nucl. Sci. Tech., 52 1461 (2015).
[3] H. Kogawa et al., J. Nucl. Sci. Tech., 54 733 (2017).
[4] H. Kogawa et al., JAEA-Tech., 2022-023 (2022).
[5] T. Naoe et al., MLF annual Report 2023, 2-3 (2024).
[6] Y. Nishi et al. Chem. Eng. Res. Des.212 457 (2024).

H. Kogawa, T. Wakui, and T. Naoe
Neutron Source Section, Materials and Life Science Division, J-PARC Center

Damage Inspection of Mercury Target Vessel #13

1. Introduction

In the MLF, liquid mercury is used as a spallation target material due to its advantages in cooling performance. The 316L stainless steel is filled with mercury, as the so-called target vessel, and the mercury is circulated for cooling with a heat exchanger during the operation. The target vessel has been severely damaged by pressure wave-induced cavitation erosion on the interior surface, in addition to the proton and neutron irradiation [1]. Cavitation damage mitigation techniques consisting of surface hardening to reduce surface deformation by cavitation impact, gas microbubble injection to suppress pressure waves which are a source of cavitation, and double-walled beam window structure to disturb the grow of the cavitation bubble are adopted and upgraded gradually. To demonstrate the effect of the above-mentioned techniques and reflect on the power lamp-up plan, the beam entrance portion of the target vessel is cut after the user operation prior to its periodical replacement [2].

2. Improvement of cutting conditions

Figure 1 shows the photograph of the cutting machine placed in front of the target vessel. There are two constraints for cutting the beam windows portion of the target vessel. One is that the target should be cut horizontally while being mounted on the target trolley to prevent the spill of the remaining mercury and water from the cutting portion. The other is the requirement of dry cutting to prevent release of tritium from the mercury side during cutting and the replacement work that follows [3].

Friction heating at the saw tip makes it difficult to dry cut. From FY2020, we have adopted molybdenum grease as a semi-dry lubricant in addition to AlCrN coating on the cutter surface to reduce the friction heating and increase the thermal resistance of the cutter. However, in FY2022, while cutting, the cutout specimen of the innermost wall of the target vessel dropped off inside the vessel and we could not extract the specimen. A cold cutting test using the beam window mockup was performed to investigate why the specimen dropped off and found that resuming cutting when the cutter is stuck due to overload causes a fallout from the cutter.

During the cutting process, the cutter feed/return is controlled at a constant rate. To reduce the risk of the cutter getting stuck, the cutting system was modified to monitor the motor current, and we added a refuge process for returning the cutter when the motor current increases beyond an arbitrary value. Furthermore, to definitely prevent dropping off of the specimen from the cutter, we have decided to adopt the center drill on the annular cutter. When cutting with a center drill, after the cutting is completed, there is the possibility for the highly radioactivated specimen to get stuck inside the cutter. The process of removing the cutout specimen from the cutter was carefully tested through the cold cutting tests. It is also concerning that the center of the cutout specimen where the region of interest for damage inspection is lost by the drill hole. We have decided to adjust the cutter position approximately 4 mm to the upstream side from the center in order to secure the severe damage potion, since the severe damage tends to be concentrated on the slightly downstream side from the center.

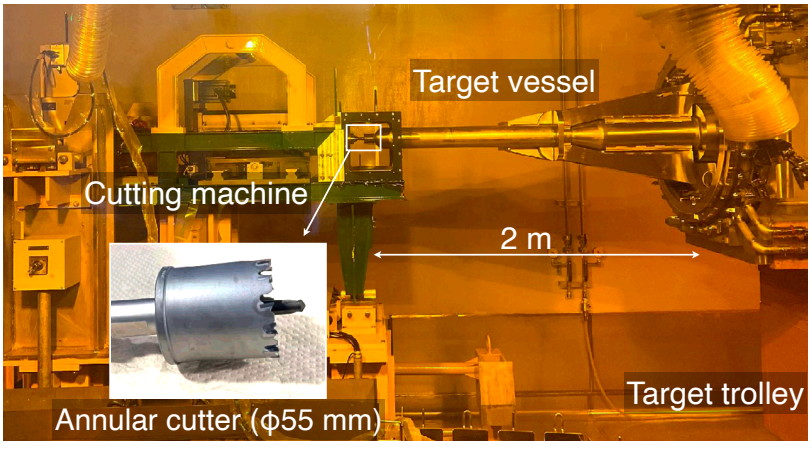

Figure 1. Photograph of the cutting machine for the target vessel.

3. Beam window cutting and damage inspection

Figure 2 shows the time history of the cutter position and motor current for the cutting of target vessel #13 operated up to 2273 MWh. As shown in the figure, the beam window portion of the target vessel consists of four layers, double-walled water shroud and double-walled mercury vessel. The double-walled mercury vessel consists of an outer and inner wall, and the gap between the outer/inner wall is designed to be 2 mm and to face high-speed mercury flow ~ 4 m/s, and the inner wall inside faces the bulks side mercury with a gas microbubble injection. Cutter was stopped twice at 9 mm where the end of first layer cutting, and stopped once at 25 mm where the end of third layer cutting. By resuming cutting, four layers of windows were cut successfully.

Cutout specimens were removed smoothly from the cutter, and specimens were cleaned by ultrasonic bath after splaying parts cleaner to remove grease, mercury and contaminated radioactive products.

Dose rates of the cutout specimens were measured using an Ionization chamber (C-110, Applied Engineering). The maximum dose rate of the cutout specimen was 197, 263, 264, and 523 Sv/h from outermost to innermost wall at contact, respectively. To quantitatively measure the erosion depth of the cutout specimen surface, the surface shape was traced using a silicone rubber replica (Repliset F-1, Struers) with a depth precision of 0.1 μm by remote handling, since the cutout specimen has a large dose rate, for detailed surface inspection using a digital microscope. Replicas were packed into transparent polystyrene box for contamination control and we observed in detail the damage depth by using a 3D profile measurement machine (Keyence, VR-3000).

4. Comparison between measured and predicted depths

Figure 3 shows the photographs and depth contour of the replica for the outer wall inside a faced narrow channel. It can be seen that the matt surface might be formed in fabrication by surface treatment. It is recognized that the machining and/or polishing surface in fabrication shown in A' and B' remain after operation in A and B. Cavitation erosion is not recognized on the inside of the outer wall and the reproducibility of results in the #10 and #11 target was confirmed. Figure 4 shows the results of analysis of the innermost wall that faced the bubbly mercury. A horizontal stripe pattern is recognized on the entire surface in the photograph. The stripe pattern may be caused by the cavitation erosion which is growing along with the machining and/or polishing lines, since the core of the cavitation bubble tends to be concentrated at the pit. In fact, it can be seen that the pits by the cavitation are distributed along with the stripe shapes, and localized erosion is recognized on the stripe lines in the high magnification depth contours C and D. The maximum erosion depth is 442 μm, and the depth is much shallower than that of the predicted depth of 1190 μm by empirical equation based on off-beam experiment and results of the previous damage inspection [4]. One possible reason for the difference between the measured and predicted damage depth is the effect of the gas microbubble injection, recently

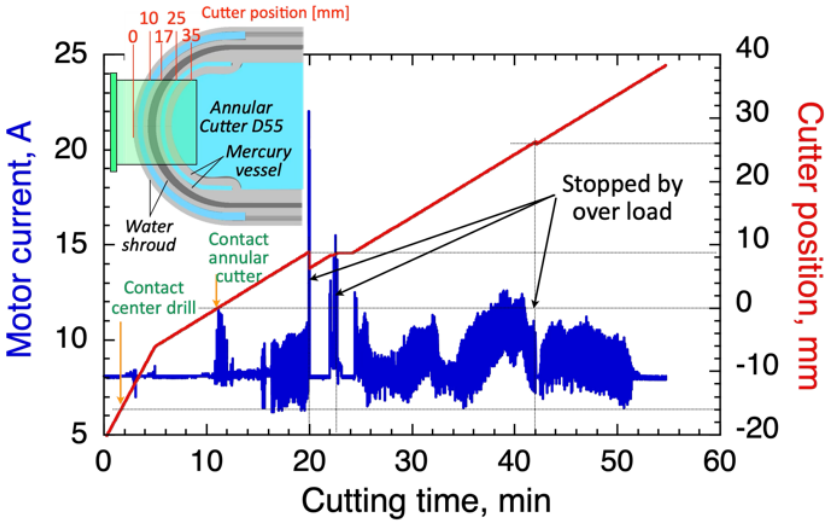

Figure 2. Time histories of the cutter position and motor current for the cutting of target vessel #13.

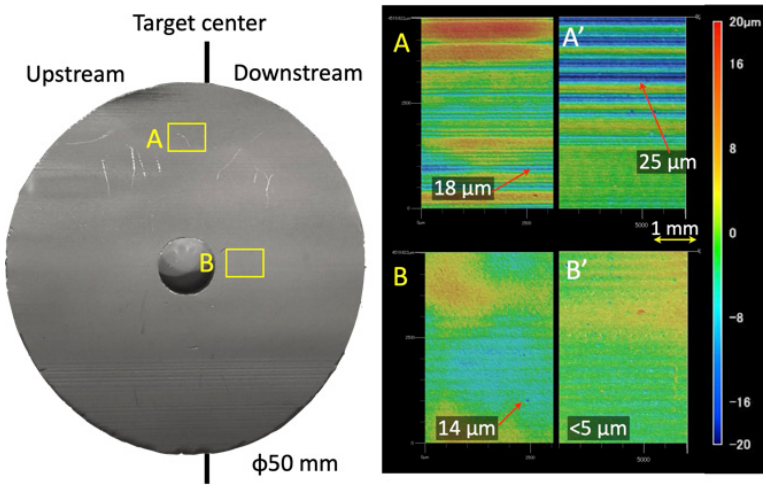

Figure 3. Photograph and depth contour of the replicated surface on the inside of the inner wall. Left and right contour were taken after operation and in fabrication, respectively.

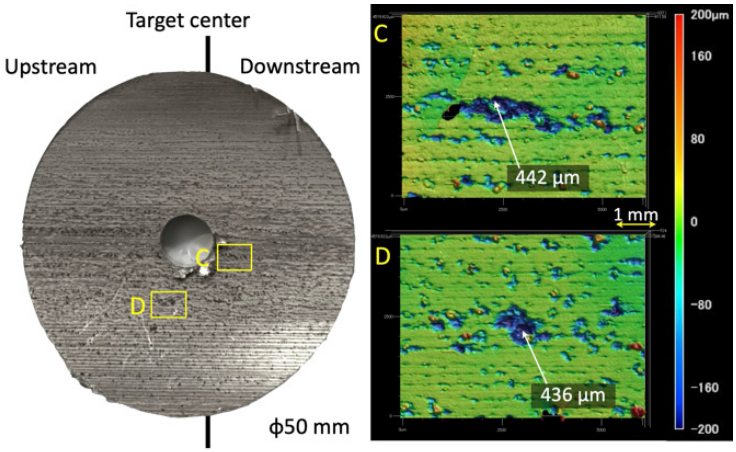

Figure 4. Photograph and depth contour of the replicated surface on the innermost wall.

improved local bubble void fraction around the beam window, which was not correctly reflected in the prediction procedure. Improvement of the empirical equation to increase the prediction precision and reflect the power ramp-up plan by accumulating damage data are our challenges for the future.

References

[1] T. Naoe, et al., Mat. Sci. Forum, **1024** 111 (2021).
[2] T. Naoe, et al., JAEA-Technol. 2022-018, (2022).
[3] T. Kai, et al., J. Phys. Conf. Ser. **1021** 012042 (2018).
[3] T. Naoe, et al., JAEA-Technol., 2023-022, (2023).
[4] T. Naoe, et al., J. Nucl. Mater. **468** 313 (2016).

T. Naoe, H. Kinoshita, T. Wakui, K. Saruta, and H. Kogawa
Neutron Source Section, Materials and Life Science Division, J-PARC Center

Irradiation Tests of Polarization-maintaining Fibers with a Pure Silica Core for Target Diagnostic System

1. Introduction

Optical fibers have a wide range of applications in the inspection of nuclear facilities from fiberscopes for visual testing to optical fiber sensors for structural health monitoring. In the MLF, optical fibers are used in the target diagnostic system [1].

For the spallation neutron source at the MLF, cavitation erosion is one of the most critical factors to limit the service life of a mercury target vessel and, in turn, a lot of research has been done to address this issue [2]. The target diagnostic system is one of those countermeasures against cavitation damage. Currently, the sound and vibration occurred on the target vessel are being monitored during in-service operation using a microphone and a laser Doppler vibrometer (LDV), respectively, and in the near future, anomalous behavior, including damage, will be diagnosed by applying statistical analysis to these measurements and operation parameters, such as the proton beam power.

A polarization-maintaining fiber (PMF) — a type of single-mode fiber (SMF) designed to maintain the polarization of light, a function that is essential to interferometers — is employed for transmission of the LDV's light into and out of the helium vessel, where the fiber is exposed to a radiation level estimated to be ~0.05 Gy/h for neutrons and ~0.01 Gy/h for gamma rays, at a proton beam power of 1 MW [3]. In general, radiation creates point defects called color centers related to dopants, such as germanium in the silica matrix through the process of ionization and displacement damage, leading to a reduction in transmittance, namely radiation induced attenuation (RIA). Figure 1 shows how RIA affects the optical power received with the LDV and consequently vibration measurement, in relation to the operation status of the target. Since the optical power level decreases linearly during the operation period, the SNR of vibration measurement deteriorates over time, resulting in a larger variation in the measurements of vibration velocity and eventually making it impossible to continue the measurement. With the increase in proton beam power, RIA has emerged as a significant problem in recent years.

A possible solution to this technical issue is to use a PMF with a pure silica core, which is known to have a low RIA because of the absence of dopants in the core [4]. However, regardless of whether the core is composed of pure silica or Ge-doped silica, PMFs have

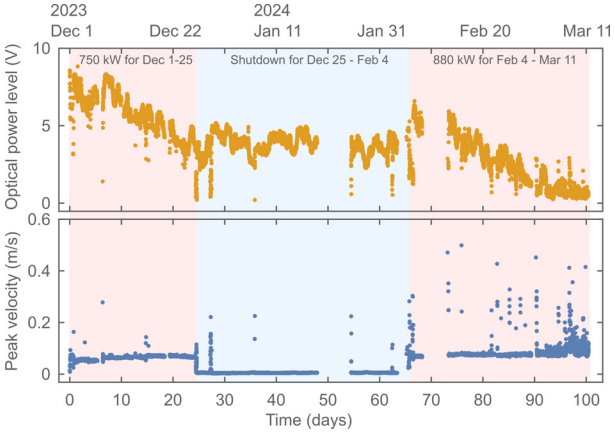

Figure 1. Change in the optical power level and the measured peak velocity of vibration during periods of operation (pink background) and shutdown (blue background).

stress rods typically made of borosilicate to preserve the polarization of light. Given that boron captures thermal neutrons, it is possible that the stress rods could be damaged, in which case the polarization-maintaining performance would be impaired, in addition to RIA.

We conducted neutron and gamma-ray irradiation tests to investigate the feasibility of PMFs with a pure silica core for the target diagnostic system. In this report some of the highlight data are presented.

2. Experiments

The optical fibers used in the experiments were PMFs and SMFs with a pure silica core (PSC), as well as those with a standard Ge-doped core. Each fiber was about 10 m long and coiled into 7.5 cm diameter loops with a 2 m long uncoiled part left from both ends of the loop. One end was connected to a light source that emits linearly polarized light at a wavelength of 633 nm and a power of 2 mW, and the other end was connected to a polarimeter for PSC-PMFs and standard PMFs and to a power meter for PSC-SMFs and standard SMFs. The polarization and the power of light transmitted in the fibers were measured in real time during irradiation and compared with each initial value at the beginning of irradiation to examine the effect of radiation on the RIA and polarization-maintaining function of the fibers.

The neutron irradiation experiments were performed at BL 10. The fibers were stacked at the center of the beam duct exit well within a 10 cm x 10 cm beam size. Two types of neutron spectra, fast neutrons and

white neutrons, were employed for irradiation. The irradiation time for both cases was about 20 hours. The neutron intensity was estimated using the spectral intensity of BL 10 [5] corrected with the proton beam power and the activation measurements of gold and aluminum foils that were irradiated simultaneously with the fibers. For gamma-ray irradiation, a Co-60 source from the National Institutes for Quantum Science and Technology was used. The coiled segments of the fibers, with the uncoiled parts shielded with lead blocks, were positioned at a distance of around 3 m from the center of the gamma-ray source and irradiated for about 166 hours. The dose of gamma irradiation was measured with alanine dosimeters placed with the coiled fibers.

3. Results

Figure 2 shows the transmittance of fibers irradiated with (a) white neutrons and (b) gamma rays. The absorbed dose is expressed in terms of dose uptake in silicon dioxide, which is the primary material of the fibers. In both cases, the transmittance of PMFs and SMFs decreases linearly with the increase of the absorbed dose, whereas that of PSC-PMF and PSC-SMFs remains at an almost constant value, indicating that the pure silica core fibers have greater tolerance to radiation than the standard Ge-doped core fibers. A similar tendency in transmittance was observed for the optical fibers subjected to fast neutrons.

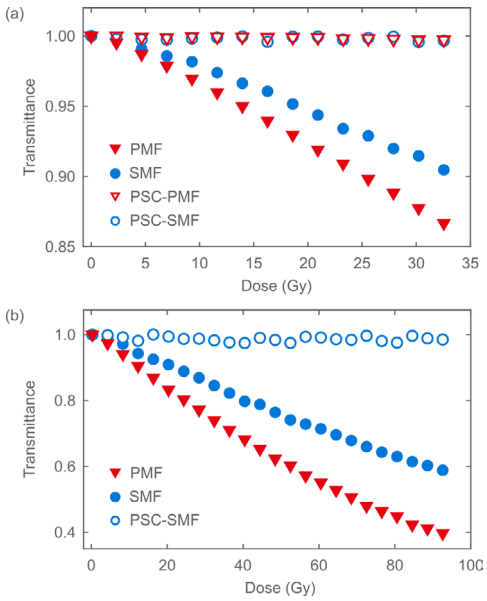

Figure 2. Transmittance of the fibers for (a) white-neutron irradiation and (b) gamma-ray irradiation.

With respect to the polarization-maintaining performance, the polarization state of light for both PSC-PMFs and standard PMFs remained stable throughout the course of irradiation and exhibited no evident dependence on the type of irradiation sources. At such low doses, the stress rods do not appear to be damaged to a degree that would result in a degradation of polarization-maintaining performance although further investigation, including elemental analysis of the stress rods, is necessary to confirm this.

4. Summary

The effect of neutron and gamma-ray irradiation on polarization-maintaining fibers with a pure silica core has been examined with respect to the transmittance and polarization-maintaining function in order to employ these fibers in the target diagnostic system. The irradiation tests demonstrate that there is no discernible degradation in the transmittance and polarization state of light when the absorbed dose reaches ~30 Gy for neutron irradiation and ~90 Gy for gamma-ray irradiation. This leads to the prediction that, in consideration of the estimated radiation level in the helium vessel, the use of a PSC-PMF will enable the target diagnostic system to operate for at least one month longer than would be possible with a standard PMF. Based on these results, a PSC-PMF was introduced as a replacement for the standard PMF in the target diagnostic system in the 2024 maintenance. We plan to evaluate the long-term radiation resistance of the PSC-PMF in the actual environment. Also, the vibration data can be taken for a longer period of time in the next operation, which we believe contributes to the safe and reliable operation of the target at a proton beam power of 1 MW.

References

[1] M. Teshigawara et al., J. Nucl. Mater. **398**, 238 (2010).
[2] H. Takada et al., Quantum Beam Sci. **1**, 8 (2017).
[3] M. Tamura and F. Maekawa, JAERI-Tech 2003-010 (2003).
[4] P. F. Kashaykin et al., J. Non-Cryst. Solids **508**, 26 (2019).
[5] M. Harada et al., Nucl. Instrum. Methods Phys. Res. A **1000**, 165252 (2021).

K. Saruta, T. Naoe, G. Ariyoshi, M. Teshigawara, Y. Yamaguchi, and M. Harada
Neutron Source Section, Materials and Life Science Division, J-PARC Center

Neutron Science

Neutron Science Section

1. User program

The continuously increasing electricity and fuel prices forced a reconsideration of the number of MLF operational days. The MLF was able to deliver an operation of 109.5 days in 2023, which was slightly shorter compared to previous years because of fire incidents. There were 277 and 289 applied proposals in the terms of 2023A and 2023B, respectively (BL03 and BL20 operated by Ibaraki Prefecture are not included). These numbers of proposals are almost comparable with previous years, and 122 out of 277 and 175 out of 289 were approved as general proposals. In addition to the general proposals, 5 long-term proposals were also assessed as mid-term evaluation, and all of them were accepted.

2. Instruments update

In collaboration with the Neutron Instrumentation Section, a large area detector is being developed to enhance the detection capabilities of SENJU (BL18), a single crystal diffractometer. This new detector features a detective area of 768 × 512 mm, which is six times larger than the previous model. The increased size will allow for more efficient data collection by covering a wider area during neutron scattering experiments. A "folding-fan" arrangement has been adopted, enabling a broad angular range of coverage, and a total of nine of these upgraded detectors are in production. The installation is planned to begin in the next 2024 fiscal year, marking a significant upgrade for SENJU's experimental capabilities.

3. Scientific achievements

In 2023, 256 scientific papers and 23 press releases came out from the neutron beamlines at the MLF. Those scientific achievements are widely spread in various fields of science, in particular the research of energy materials such like solid batteries, lithium-ion batteries, fuel cells, and so on can be one of mainstreams from the perspective of returning the research results to society.

In 2023, several groundbreaking results were achieved, particularly in the field of energy materials research, by taking advantage of the neutron probe. A team from the Tokyo Institute of Technology developed a solid electrolyte with the world's highest lithium-ion conductivity, and succeeded in achieving a high-capacity, high-performance all-solid-state battery [1]. The crystal structure of the newly developed material was investigated using neutron diffraction experiments at BL09 SPICA, and it was found that the conductivity of Li ions was enhanced by increasing the entropy. This research provides a new guideline for the design of smaller, more efficient all-solid-state batteries.

Toyota Central R&D Labs, Inc. developed a new method for observing the distribution and movement of water inside large fuel cells for vehicles at RADEN (BL22) [2]. By applying this method, it is expected that various developments in fuel cell research and development will be achieved, such as the optimization of fuel cell control methods, the planning and verification of material, and flow channel concepts.

These results have demonstrated the important role that advanced analytical techniques using neutrons play in the development of energy materials and have provided a solid foundation for the innovation of next-generation battery and fuel cell technologies.

4. Awards

The following awards were presented to the members of the Neutron Science Section in 2023.

(1) The Nishida Prize for Promotion of Geo- and Planetary Science, A. Sano-Furukawa, on "research on hydrogen in the Earth's materials at high pressure and temperature based on synchrotron X-ray and Neutron beams".

(2) Best Poster Award, The Japan Institute of Metals and Materials 2023 Fall Meeting, W. Mao and a member of TAKUMI (BL19), on "excellent combination of strength and ductility of an ultrafine-grained stainless steel at cryogenic temperatures studied by in situ neutron diffraction".

(3) Best Poster Award, The 24th International Collaboration of Advanced Neutron Sources (ICANS XXIV), M. Nirei, on "performance assessment of the cold-neutron disk-chopper spectrometer at J-PARC".

(4) Outstanding Reviewer Award in 2023, Acta Materialia and Scripta Materialia, W. Gong.

5. Other activities

SAKURA Mobility Programme:

To strengthen the scientific collaboration between Sweden and Japan, the Swedish Research Council (VR) decided to fund and launch SAKURA, a new mobility program focusing on neutron research and activities of European Spallation Source (ESS) and J-PARC in particular. Within the framework of this scientific exchange program, R. Kiyanagi, a member of the Neutron Science Section, visited ESS for two weeks. He discussed

Figure 1. Group photo of the ISSE School 2023 participants on October 24, 2023.

Figure 2. Group photo of the 7th Neutron and Muon School participants on December 22, 2023.

the upgrade of methodology on data analysis and computing.

ISSE School:

The MLF hosted the 4th International Training School on Sample Environment at Scattering Facilities (ISSE school 2023). This school focuses on developing basic sample environment (SE) skills for early career neutron and synchrotron facility staff (Fig. 1). Exchanging ideas and practical lectures on a wide range of SE at large scattering facility together with hands-on exercise can provide an excellent opportunity for communicating world-wide.

NEUWAVE-11:

Also, the MLF organized a series of workshops on neutron imaging (The 11th Workshop on Neutron Wavelength-Dependent Imaging) following the last Switzerland workshop in 2019. 90 participants enjoyed presentations and discussions on specific imaging topics including an MLF visit.

NM-School:

The 7th Neutron and Muon School was held in Tokai with the support of KEK IINAS-NX program for promoting career planning of young researchers (Fig. 2).

QBSF 2023:

The large conference, the Quantum Beam Science Festa in 2023 took place in-person for the first time in five years. 470 attendees who gathered in Mito presented many scientific and technical research results.

References

[1] Y. Li et al., Science **381** 50 (2023).
[2] W. Yoshimune et al., ACS Energy Lett. **8** 3485 (2023).

M. Nakamura[1], T. R. Yokoo[1,2], and A. Sano-Furukawa[1]
[1]Neutron Science Section, Materials and Life Science Division, J-PARC Center; [2]Institute of Materials Structure Science, KEK

BL01: 4D-Space Access Neutron Spectrometer 4SEASONS

1. Introduction and use trends

4SEASONS is a direct-geometry time-of-flight neutron spectrometer for thermal neutrons, and one of the Public Beamlines in the MLF [1]. In 2023, 19 General Use (GU) proposals, one New User Promotion (NUP) proposal, one Urgent Access (UA) proposal, one Long-Term proposal, and one Instrument Group Use proposal were approved. One reserved proposal was granted beamtime. Two Fast Track proposals were also approved but deferred to 2024 due to lack of beamtime. 88% of the GU, NUP, and UA proposals were submitted by international users. 78% of the submitted proposals were in the field of magnetism, while the rest targeted phonons and other atomic vibrations. 10 peer-reviewed papers were published.

2. Instrument upgrade

Detectors: We have been working on the introduction of new detector electronic modules (new NEUNET) that enable the pulse-width-and-height (PWH) limitation function [2]. Following the successful test described in last year's report, we purchased new NEUNET boards and performed on-beam tests. We placed a small piece of polyethylene at the sample position, and measured images of cadmium slits to see if the images appeared at the expected positions in the position-sensitive detectors. In the first measurement, using a prototype board, we found that the images appeared in the wrong positions. This was due to errors in the software and electronics on the board. After fixing the errors, we introduced 44 new NEUNET boards with the fixed design and performed the same on-beam test. The cadmium slit images appeared in the expected positions, confirming the integrity of the boards.

Sample Environment: 4SEASONS uses a top-loading (TL) refrigerator as its standard sample-environment device. It can provide temperatures up to 600 K in combination with a high-temperature sample stick (high-T stick). However, when using the high-T stick, we needed two temperature controllers (LakeShore 340 and 350) to power the heaters of the refrigerator and the stick, which made the operation complicated. We then modified the temperature control system of the refrigerator and the high-T stick to operate with one controller (LakeShore 336) and an external power supply. This modification made the control and interlock system simpler and the operation easier and safer.

In addition to the TL refrigerator, we recently introduced a bottom-loading (BL) GM refrigerator. This refrigerator has a radiation shield made of aluminum foil around the sample position. Unfortunately, the radiation shield scatters neutrons, which creates background. Figure 1(a) shows the intensity map as a function of the momentum (Q) and energy transfer (E) when a monochromatic neutron beam entered the refrigerator. The original radiation shield, which had a diameter of 254 mm, induced "dispersions" of the background. These "dispersions" were caused by the difference in the flight path between the sample and the radiation shield. Such background in the inelastic scattering region ($E \neq 0$) is troublesome in inelastic scattering experiments. We then replaced the radiation shield with one of a smaller diameter to make the dispersive background closer to the elastic scattering ($E = 0$). Figure 1(b) shows the intensity map with the new radiation shield with the new 98-mm-diameter shield. Scattering from the radiation

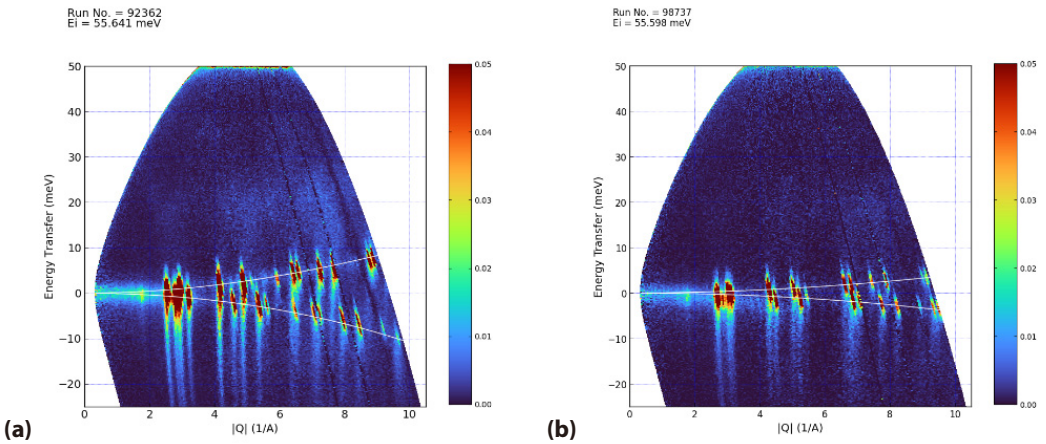

Figure 1. Intensity caused by the radiation shields of the bottom-loading type refrigerator when the diameter of the radiation shield was (a) 254 mm and (b) 98 mm. White lines are analytical calculations. The incident energy of the neutron beam was 55.6 meV.

shield is still observed, but its "dispersions" are much closer to the elastic scattering, as expected.

Vacuum system: The vacuum system for the 22 m^3 vacuum scattering chamber of 4SEASONS consists of a pair of roughing pumps, a turbo-molecular pump, a cryopump, and a set of air driers. As reported in last year's report, the vacuum system was greatly upgraded, which enabled automatic operation. This year we updated the vacuum system further: we added valves and gauges to the pipes of the air driers and the cooling water and updated the control panel accordingly. In addition, we modified the control system and now we can control it remotely through IROHA2. This modification enabled us to incorporate the operation of the vacuum system into the experiment procedure, and it made possible an automatic sequence, which includes evacuating the vacuum chamber, start of sample's cooling, and start of the measurement.

Remote control: 4SEASONS utilizes the IROHA2 software framework for remote control and logging the status of the devices. The web-based interface of IROHA2 enabled the automatic operation of the devices incorporated in the measurement sequences. This year, we newly adapted the power controller of the BL refrigerator, and the sliding system of the Fermi chopper to switch the white and monochromatic beams to IROHA2, in addition to the vacuum control system described above. The increase in the number of IROHA2-compatible devices makes the experiment and operation of the instrument easier. Conversely, it makes the web interface of IROHA2 complicated and creates difficulties in finding the necessary information. Then, we added a panel to the interface that summarizes the information critical for experiments (Fig. 2). This summary panel is so concise that it is highly visible on smartphones.

Acknowledgments

We thank R. Komine, H. Hasemi, H. Tanaka, K. Inoue, W. Kambara, K. Ohuchi, T. Morikawa, and Y. Ohe for their support and advice. The instrumentation works described here were supported by the engineers of the Neutron Science Section and the Technology Development Section of the MLF.

References

[1] R. Kajimoto et al., J. Phys. Soc. Jpn. **80**, SB025 (2011).
[2] S. Sato et al., J. Neutron Res. **24**, 427 (2022).

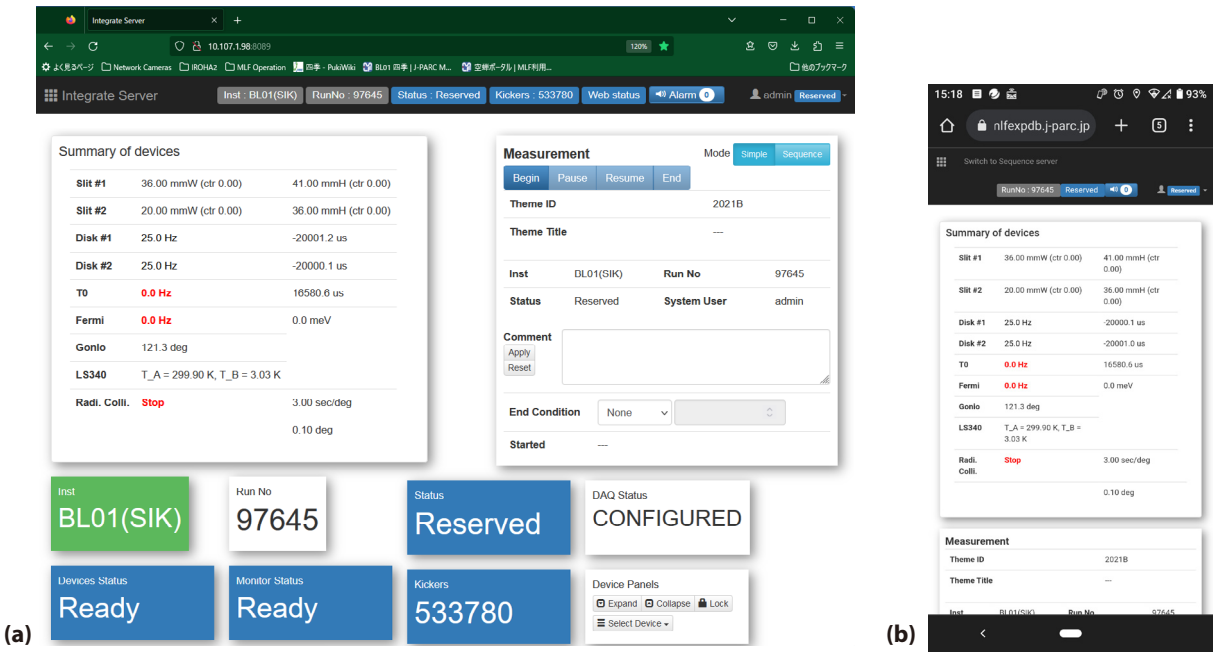

Figure 2. Screenshot of the web interface of IROHA2 of BL01 on (a) a PC and (b) a smartphone. The top-left panel in (a) and the top panel in (b) are the summary panels.

R. Kajimoto[1], M. Nakamura[1], K. Kamazawa[2], Y. Inamura[1], K. Iida[2], K. Ikeuchi[2,*], and M. Ishikado[2]
[1]*Neutron Science Section, Materials and Life Science Division, J-PARC Center;* [2]*Neutron Science and Technology Center, CROSS; *Present address: Institute of Materials Structure Science, KEK*

Current Status of BL02 DNA in 2023

1. Introduction

DNA is a TOF type Si crystal analyzer backscattering spectrometer installed at the neutron spallation source of the Japan Proton Accelerator Research Complex (J-PARC) [1, 2]. DNA uses a pulse-shaping chopper to extract pulsed neutrons with sharp time-structure from strong but broad ones of the coupled moderator, which achieves μeV-order energy resolution in wide energy transfers of the meV-order. Furthermore, the signal-to-noise ratio at DNA achieves ~10^5, which makes it possible to cover a variety of research fields with small scattering amplitudes or with small quantities of samples (of the order of milligrams).

The number of peer-reviewed papers from DNA in 2023 was 8, which is similar to the average of the last few years. One press release on the water dynamics in semiclathrate hydrate was issued. In addition, Dr. Md. Khalidur Rahman, who is in the doctor course of the Graduate University for Advanced Studies (SOKENDAI) at KEK successfully completed his degree in 2023 using DNA data.

2. User Program in the periods 2022B and 2023A

In 2023, 20 (2022B) and 21 (2023A) General Proposals (GP) were submitted to BL02. 7 GPs, including 1 New User Promotion (NUP), and 7 GPs including 1 NUP's were approved for 2022B and 2023A, respectively. The ratio of the approved beamtimes to the requested beamtimes was 29% for both 2022B and 2023A. The competition rate was high: 3.0 and 3.1 for 2022B and 2023A, respectively. Additionally, 2 reserved proposals were also conducted in 2022B.

Almost all the experiments were conducted, however, two proposals were carried over to 2023B due to fire accidents at the Main Ring and Hadron Facility in May and June of 2023, respectively. In addition, 3 General Proposals (Long Term Program) (hereafter LTP) and 1 JAEA Project proposal ran at BL02 in 2022B and 2023A.

3. Beamline activities

[Development of sample environment]

Solid state ionic conductors are one of the hottest research fields and there has been a recent increase in proposals to DNA. For some ionic conductors, observing QENS in the dynamic range of DNA (>1 μeV) requires relatively high sample temperatures of up to 1000°C, which is unreachable in the DNA's standard sample environment of a cryofurnace. To expand the temperature range for measurements at DNA, we developed a new compact high-temperature furnace with a maximum temperature of 1000°C. The schematic diagram and photo of the heater unit are shown in Fig. 1. The highest stable temperature eventually reached was 870°C. After the off-line test, the compact furnace was used for a long-term proposal of BL02.

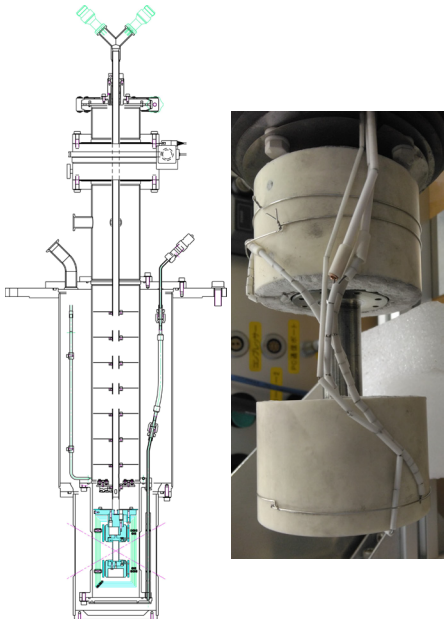

Figure 1. Design of the new compact high temperature furnace (left) and photo of the heater unit (right).

[Aging problem]

In 2021, we found out that some Gd-backcoated Si111 analyzers had cracked and were detached from the aluminum base due to oxidation of the Gd coating. The solution to the detachment problem was to change the neutron absorber sprayed on the back from Gd to Gd_2O_3. #12 bank (in 2021) and #10 & #13 banks (in 2022) of the Gd-backcoated Si111 analyzer mirrors have been replaced to Gd_2O_3-backcoated mirrors (Fig. 2). In 2023, three Si111 analyzer mirror banks (#6, #8, and #11) at scattering angles (2θ) of $31.5° < 2\theta < 40.5°$, $67.5° < 2\theta < 76.5°$, and $91.5° < 2\theta < 100.5°$ were successfully replaced to Gd_2O_3-backcoated mirrors. As for the Si311 mirrors shown in blue, Gd_2O_3 mirrors were installed, except for one bank around 90°. We will continue with the replacement of the remaining Gd-sprayed analyser mirrors.

In BL02, the detectors are located in the center of the scattering vacuum chamber, and a large number of relevant electrical cables are installed near the detectors. Recently, additives such as plasticizers and flame

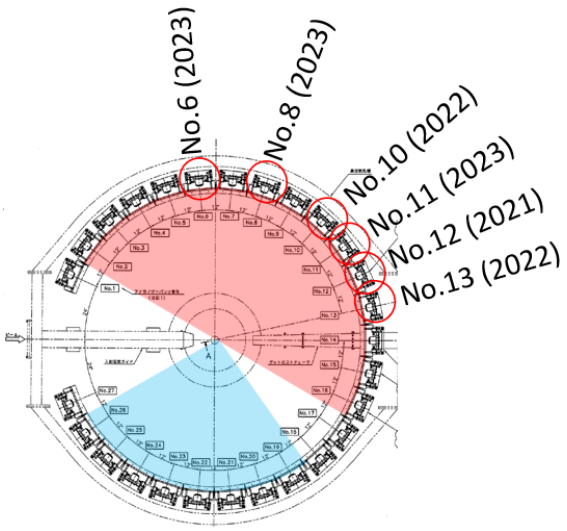

Figure 2. A bird view of DNA's analyzer bank. Si111 and Si311 analyzers were installed at the red and blue scattering area, respectively.

retardants in the cable sheaths installed in the vacuum chamber have been found to contaminate the vacuum chamber [3]. In poly(vinyl chloride) cables, once the plasticizers are lost, the cables have been found to stiffen, causing communication failures at the connectors, etc. For this reason, we replaced all cables placed in the detector (Fig. 3). BL02 has been in operation since 2008. In recent years, we have been dealing actively with various types of equipment issues caused by aging.

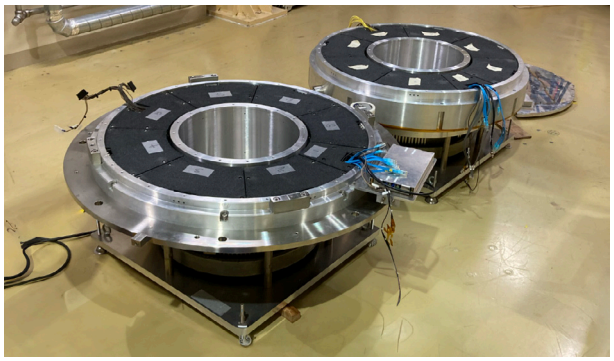

Figure 3. Detector units (top and bottom) installed in the vacuum scattering chamber. Various colors of cables, such as LAN-cable, signal cables, and power cables, are connected to the units.

4. Other activities

[Collaboration with ANSTO EMU group]

Dr. Nicolas de Souza, an instrumental scientist of the ANSTO EMU, visited [4] us again, and was able to conduct QENS experiments using BL02, which could not be performed in FY2019. ANSTO renewed the Memorandum of Understanding with J-PARC, operated by KEK and JAEA, broadening it to include its partner, CROSS [5]. Based on this, we can easily consult with each other on various issues related to the spectrometers, and our communications have become more fruitful over the years.

[Neutron & Muon school]

The NM School 2023 was held in December. Four participants, including two foreign students from Ghana and China, joined hands-on training at BL-02. They measured the water dynamics in Nafion® with different water content and analyzed the data.

5. Future plans

In addition to the aging problem of the Gd-backcoated Si111 analyzers, we found out that the N_2 monitor and ^{3}He detectors also showed deterioration due to changes in the CF_4 quench gas. We will tackle these issues by developing new N_2 monitor and ^{3}He detector without CF_4 quench gas. As for the sample environments, we plan to make a compact magnet which can fit into DNA's small space for sample environment (ϕ400) to cover magnetism with special focus on low energy excitations.

References

[1] Kaoru SHIBATA et. al., JPS Conference Proceedings, 8 (2015), 036022.
[2] Y. Kawakita et al., EPJ Web of Conferences 272 (2022) 02002.
[3] https://doi.org/10.5611/hamon.32.2_91
[4] https://mlfinfo.jp/_src/resource/PEPngy9XwF/MLF_AR_2019.pdf
[5] https://www.ansto.gov.au/news/renewed-agreement-japanese-research-organisations-to-bolster-cooperation-neutron-science-and

M. Matsuura[1], Y.Kawakita[2], T. Yamada[1], T. Tominaga[1], H. Tamatsukuri[2], K. Ohuchi[1], and H. Nakagawa[2,3]
[1]Neutron Science and Technology Center,CROSS; [2]Neutron Science Section, Materials and Life Science Division, J-PARC Center; [3]Materials Sciences Research Center, JAEA; [4]Technology Development Section, Materials and Life Science Division, J-PARC Center

Current Status of iBIX

1. Introduction

Neutron single-crystal diffraction is a powerful method for obtaining structural information, especially for light atoms. Because understanding the enzyme chemistry of proteins at the atomic level requires the visualization of hydrogen atoms at active sites and remote residues, co-factors, substrates, and water molecules, it is particularly important to obtain precise information on the positions of the hydrogen atoms in biological macro-molecules. The complementary use of neutron diffraction data, which includes more information on hydrogen atoms, and X-ray diffraction data, which includes more information on non-hydrogen atoms (such as C, O, N, and S etc.), allows us to obtain structural information on all atoms in the protein.

The IBARAKI Biological Crystal Diffractometer, the so-called iBIX, is a TOF neutron single crystal diffractometer to elucidate the hydrogen, protonation and hydration structure of biological macro-molecules, organic compounds and polymer samples [1]. Ibaraki University will relinquish its contract for the operation and maintenance of iBIX in the end of FY2022. From FY2023, CROSS has been contracted to manage the Ibaraki prefecture neutron beamline and is carrying out activities to promote its utilization. From FY2022, the neutron protein structure analysis with the iBIX is being supported by BINDS (Basis for Supporting Innovation Drug Discovery and Life Science Research). The specifications of iBIX are shown in Table 1.

Table1. Specifications of iBIX.

Moderator	Coupled
Wavelength of incident neutron	0.7 ~ 4.0 Å (1st frame) 4.0 ~ 8.0 Å (2nd frame)
Neutron intensity position just before chopper sample position	 2.7×10^9 n/s/cm^2/MW 2.9×10^8 n/s/cm^2/MW
L_1	40 m
L_2	491 mm
Solid angle of detectors	19.5 % for 4 π
Detector covered region	+15.5 ~ +168.5 deg.
Detector size	133 × 133 mm
Detectors pixel size	0.52 × 0.52 mm
No. of detectors	34
Sample environment	Gas flow type cooling system by N_2 gas (~100 K)
	Heating system for polymer sample (~600 K)
	Tensile loading system for polymer sample (~200 N, ~90 mm, 1~1000 μm/sec)

2. Current status

In FY2023, J-PARC was operated regularly at an accelerator power of 800 kW. We were able to collect a full data set of biological macromolecules for neutron structure analysis with around 2.0 Å resolution in less than 7 days by using the iBIX at the accelerator power of 800 kW. The typical sample size and the maximum unit cell size was 1.0 mm^3 and 135 × 135 × 135 Å^3 respectively. Recently, we have succeeded in data acquisition, reduction and analysis of a crystal sample with one unit cell length of around 190 Å (the remaining two axes were around 60 Å) using a newly developed integration method [2]. 2 test measurements for an industrial use proposal (applied from BINDS), 1 test measurement for a J-PARC proposal, 7 test measurements for a proposal of an innovative research project of the Ibaraki Neutron Beamline and 4 test measurements for a proposal of a leading research project of the Ibaraki Neutron Beamline were performed using the iBIX. And then, 7 proposals were moving on to the full data collection for neutron structure analysis.

3. Maintenance and development

Fifteen years have passed since the construction of iBIX began, but the incident neutron intensity has not been measured successfully, since it was measured at low power during the early stages of construction. In order to confirm the intensity of the incident neutrons when the accelerator power is stable at a high output of 800 kW (80% of the maximum operation), the intensity was measured at the sample position Fig. 1 and at the position after the iron collimator inside the biological

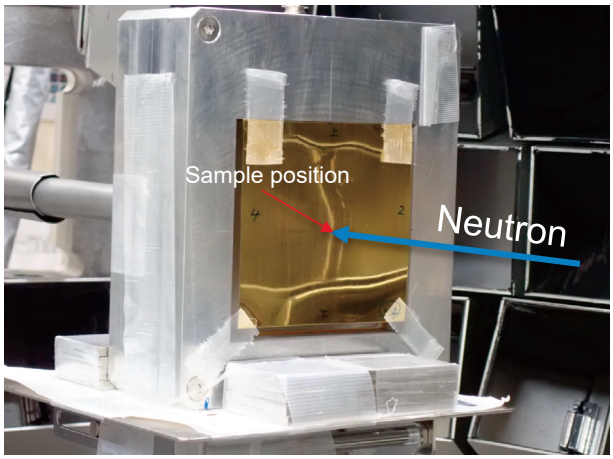

Figure 1. The gold foil irradiated with neutrons at the sample position.

shield (just before the chopper) using the gold foil method. The measurements were performed with the cooperation of Dr. Harada of the Neutron Source Section, MLF. The activation rate of the gold foil irradiated with neutrons at two points was measured, and the incident neutron flux value was calculated from the measured activation rate. To confirm the validity of these measured values, a simulation of the incident neutron intensity was carried out using a neutron ray-trace simulation software McStas for the same two points as the gold foil measurements. The measured values (Table 1) at both positions showed good agreement with the calculated values, confirming that the incident neutron intensity was transported to the sample position as planned even at a high output of 800 kW.

4. Future plans

Currently, we are working on accelerating and automating the data measurement, reduction and analysis, in order to shorten the time it takes to obtain experimental results. In anticipation of an automatic sample change and application for a new measurement method, a new 3-axis goniometer with an automatic sample centering function has been developed and installed on the iBIX diffractometer. In addition, we are considering automating the transfer of measurement data for users, further simplifying and automating data reduction, and developing a data analysis support GUI, to make the process from sample preparation to data analysis smoother and faster, leading to the acceleration of provision of results. Considering the promotion of future industrial use, we aim to expand the use of the iBIX to inorganic and organic compounds. Currently, with a view to further strengthening user support, we are planning to develop various sample environment devices and new measurement methods. We are also improving both hardware and software to meet the needs of in-situ measurement that takes advantage of the characteristics of pulsed neutrons.

References

[1] K. Kusaka, T. Hosoya, T. Yamada, K. Tomoyori, T. Ohhara, M. Katagiri, K. Kurihara, I. Tanaka and N. Niimura, J. Synchrotron Rad., **20** 994, (2013).

[2] K. Kusaka, T. Yokoyama, T. Yamada, N. Yano, I. Tanaka and M. Mizuguchi, Acta Cryst. **D76** 1050, (2020).

K. Kusaka, T. Sakakura, H. Sugiyama, and J. Suzuki
Neutron Industrial Application Promotion Center, CROSS

Circular Polarization Measurement for Neutron Capture Reactions in ANNRI (BL04)

1. Introduction

Circular polarization measurements of gamma ray emitted from neutron capture reactions of nuclei are one of the methods to determine the spin of the excited states of a nucleus. We installed in the Accurate Neutron-Nucleus Reaction Measurement Instrument (ANNRI) a newly developed gamma-ray polarimeter, which allows us to measure the circular polarization, and successfully measured the circular polarization in the pulsed neutron source for the first time. In this report, we briefly report on the gamma-ray polarimeter and the circular polarization measurement using the ^{32}S(n, γ)^{33}S reactions. The details of these activities have been published in Ref. [1].

2. Gamma-ray polarimeter

The circular polarization of gamma rays can be measured by the magnetic Compton scattering with polarized electrons. Therefore, the electromagnet shown in Fig. 1 was constructed as the gamma-ray polarimeter. Current of 4 A was applied to the coil, and the magnetization of the core material, permendur, could be saturated. The gamma rays were transmitted to the gamma-ray polarimeter, and the transmitted gamma-ray counts were different between the magnetization direction parallel and anti-parallel to the gamma-ray direction. The asymmetry was defined as

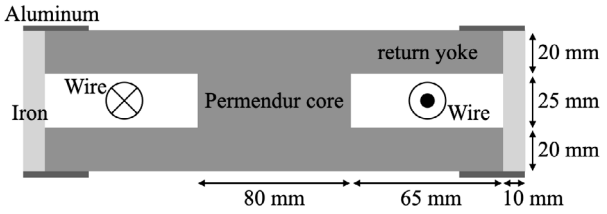

Figure 1. Schematic view of the polarimeter [1].

$$A = \frac{N_p - N_a}{N_p + N_a},$$

where N_p and N_a are the transmitted counts for each magnetization direction. The circular polarization can be obtained as

$$P_\gamma = \frac{A}{Q},$$

where Q is the polarization sensitivity.

The polarization sensitivity is defined as

$$Q = \frac{T_a - T_p}{T_a + T_p},$$

where T_p and T_a are the transmission of the circularly polarized gamma-ray for the magnetization direction parallel and anti-parallel to the gamma-ray direction, respectively. The polarization sensitivity could be calculated from the estimated magnetization in the core and the cross sections between gamma-rays and electrons and its obtained value was $Q = 1.89\%$.

3. Circular polarization measurements at ANNRI

As a demonstration of the circular polarization measurements in ANNRI, we measured ^{32}S(n, γ)^{33}S reactions. In the polarized neutron induced reaction, the emitted gamma-rays are circularly polarized depending on the spins of the initial, compound, and final states. In the sulfur case, the 5.4 MeV gamma-rays are 50% left (right)-handed circularly polarized when the neutron polarization direction is parallel (anti-parallel) to the gamma-ray emitted direction [2]. The polarization sensitivity was determined using this reaction.

Figure 2 shows the schematic view of the experimental setup. The HPGe detector was installed at a flight length of 21.5 m. The gamma-ray polarimeter was

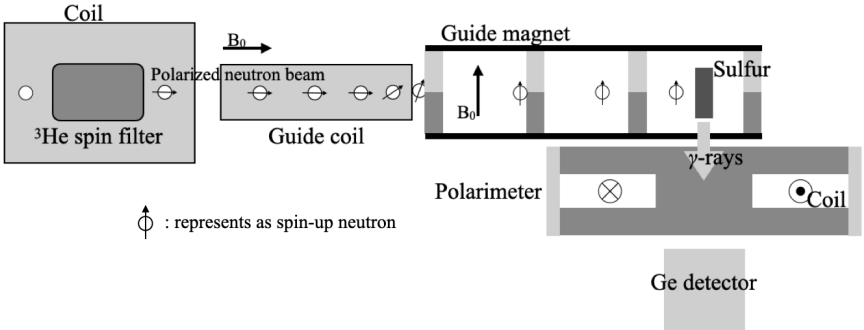

Figure 2. Schematic view of the experimental setup [2].

placed between the HPGe detector and the sulfur sample. Longitudinally polarized neutrons were produced using ^{3}He spin filter [3], and a guide magnet turned the polarization direction up (down). The neutron polarization direction was reversed every 30 minutes. The magnetization direction was fixed, and the circular polarization direction was changed by the neutron spin flip.

Figure 3 shows the obtained gamma-ray spectrum around 5.4 MeV (top) and the difference between neutron polarization direction up and down (bottom). A clear difference was observed, and the circular polarization measurements were performed successfully in the pulsed neutron source for the first time. The backgrounds were estimated by fitting with the 3rd-polynominal function, and the net-counts were deduced. The asymmetry was obtained from the net-counts, and the polarization sensitivity was determined to be $Q = (1.72 \pm 0.23)\%$.

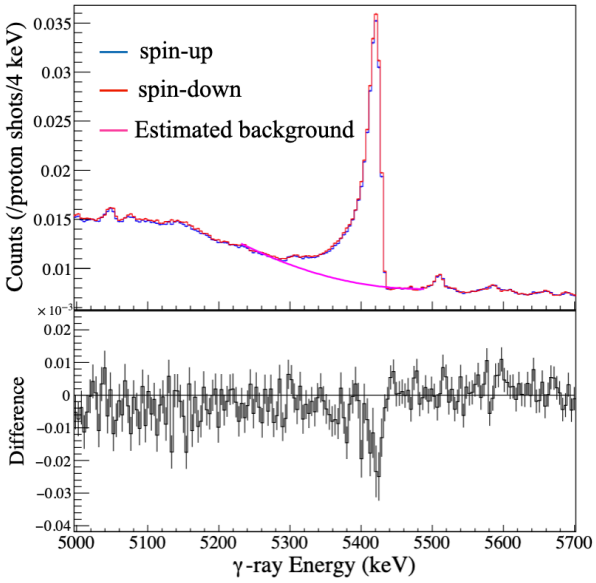

Figure 3. Gamma-ray spectrum (top) and difference between neutron polarization direction up and down (bottom).

4. Summary

It has been possible to measure the circular polarization of gamma rays from neutron capture reactions using a pulsed neutron source. Various experiments in nuclear physics using circular polarization of neutron capture reactions are expected to be performed at ANNRI in the future.

References

[1] S. Endo et al., Eur. Phys, J. A, **60** 166 (2024).
[2] L. C. Biedenharn, M. E. Rose, G. B. Arfken, Phys. Rev. **83** 683 (1951).
[3] T. Okudaira et al., Nucl. Instr. and Meth. A, **977** 164301 (2020).

Acknowledgements

The authors would like to thank the staff of beamline 04, ANNRI, for the maintenance of the germanium detectors. The neutron experiments at the MLF of J-PARC were performed under the user program (Proposals No. 2021B0385, 2022A0230, 2022B0187, 2023A0129). This work was partially supported by JSPS KAKENHI Grant Nos. JP19K21047, JP20K04007, JP20K14495, and JP21K04950.

S. Endo[1,2]
[1]*Nuclear Data Center, JAEA;* [2]*Neutron Science Section, Materials and Life Science Division, J-PARC Center*

Status of Fundamental Physics Beamline BL05 (NOP) in 2023

1. Introduction

Neutron Optics and Physics (NOP/ BL05) at the MLF in J-PARC is a beamline for studies in the field of fundamental physics. The beamline is divided at the upstream into three branches, the so-called Polarized, Unpolarized, and Low-Divergence branches, used in different experiments in a parallel way [1-2].

A neutron lifetime measurement is conducted at the Polarized beam branch with a spin flip chopper. Pulsed ultra-cold neutrons (UCNs) by a Doppler shifter are available at the Unpolarized beam branch. At the Low-Divergence beam branch, the search for an unknown intermediate force is performed by measuring neutron scattering with nano particles. The beamline is also used for R&D of optical elements and detectors.

2. Measurement of the neutron lifetime

The decay of neutrons is closely related to the mechanism of the synthesis of elements in the universe and to particle physics. The neutron lifetime has been measured in two ways: 1) by counting the incident neutrons and the protons from neutron beta decay (beam method) and 2) by storing UCNs in a container and determining the neutron lifetime according to the disappearing time (storage method). Currently, the lifetime determined via the former method is 888.0 ± 2.0 s, and that for the latter is 878.4 ± 0.5 s, with a difference of 9.5 s (4.6 σ) [3]. This discrepancy is called "neutron lifetime puzzle" and has remained unsolved for nearly 20 years. The smaller decays compared with the disappearance suggest that neutrons are lost owing to decay into dark matter or collisions with dark matter. In general, different methods are needed to validate the experimental results, as utilizing the same experimental methods may lead to the same mistakes. Using the polarization beam branch at NOP/BL05, an experiment was conducted via a different method, in which instead of protons, electrons were measured from the neutron beta decays. The first lifetime result was published in 2020 as 898 ± 10 (*stat.*) $^{+15}_{-18}$ (*syst.*) s, which is consistent with both the beam and bottle methods [4]. A spin-flip chopper (SFC), which shapes the neutron beam into bunches, was replaced with a larger one in 2020, and the intensity was increased by 3 times [5]. Commissioning began in 2021, and physics run for the neutron lifetime began after the SFC was tuned. The higher intensity of the neutron beam after the SFC upgrade, made it possible to achieve total statistics of 1.7 s. Analysis of the background estimation and the determination of efficiency are also in progress. After the evaluation of the systematic uncertainties is completed, we will publish the results in a paper.

The main source of systematic uncertainties is undefined background. To address this, we are developing a new apparatus for measuring the neutron lifetime (LiNA experiment [6] shown in Fig. 1), where a solenoid magnetic field of approximately 0.6 T is applied to the TPC to effectively discriminate β-decay events from other electron events, significantly improving the signal-to-noise (S/N) ratio.

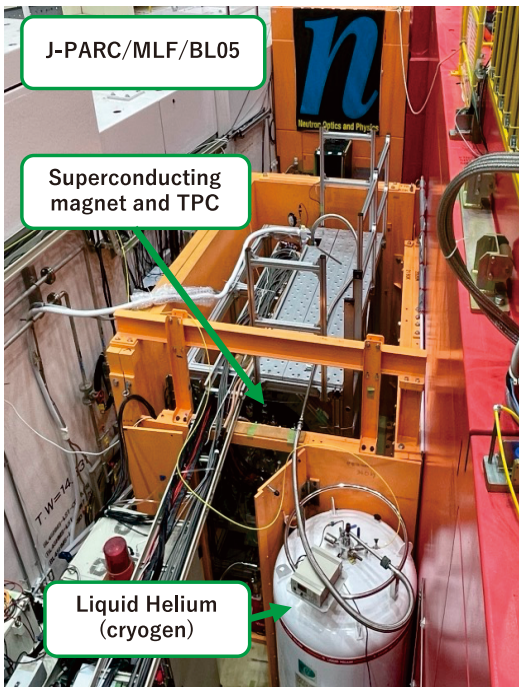

Figure 1. Photograph of the apparatus of the LiNA experiment set at the BL05 beamline.

Since 2020, a superconducting solenoid has been operational along the beamline, enhancing TPC performance as expected. We have installed and are commissioning the superconducting magnet. This approach not only enhances event identification but also reduces the measurement time by half, aiming for an uncertainty of 1 s because of the decreased environmental background.

3. Multilayer-type neutron interferometer

A neutron interferometer splits a single neutron's wave function into two paths, superimposing them to detect phase differences caused by path interactions.

It has been crucial in testing quantum mechanics, exploring gravitational effects on quantum particles, and measuring nuclear scattering lengths. Traditional silicon crystal interferometers, used since the 1970s, are limited by silicon ingot size and monochromatic neutron use.

We developed a new neutron interferometer using multilayer mirrors, capable of utilizing a wide range of neutron wavelengths with a pulsed neutron beam, significantly improving sensitivity. It features multilayer mirrors on a glass substrate with precise gaps for neutron superposition and is more tolerant to disturbances than the Si interferometers. The new device was demonstrated successfully at the low-divergence beam branch at BL05 [7] (Fig. 2).

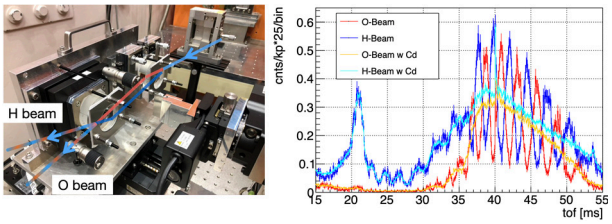

Figure 2. (Left) Interferometer setup at BL05 and (Right) the measured intensities of the H and O beams. When using pulsed neutrons, interference fringes appear in the TOF. The disappearance of these fringes when one path is obscured with Cd is clearly observed (orange & cyan) [9].

The beam width is 100 μm while the beam paths are 300 μm apart, so they are completely separated. When a certain material is inserted into a path, the phase changes depending on the refractive index of the material. This can be applied to measure the neutron scattering length of nuclei. Fujiie et al. have successfully demonstrated the measurements of the scattering lengths of some nuclei: Si, Al, Ti, V, and V-Ni alloy [7]. The values measured for Si, Al, and Ti agreed with those found in the literature, while V showed a disparity of 45% (Fig. 3). The Vanadium sample holders used in neutron scattering experiments have a significant impact.

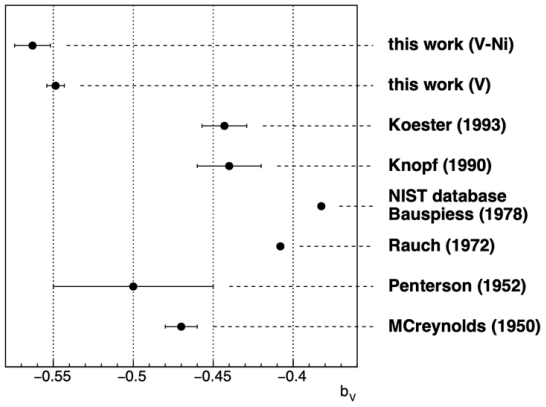

Figure 3. Scattering length of V. The value of V in this work is derived from measurements of the V sample, while V-Ni represents the scattering length of V as determined from measurements of the V-Ni alloy.

References

[1] K. Mishima et al., Nucl. Instruments Methods Phys. Res. Sect. A, vol. 600, no. 1 (2009) 342–345.
[2] K. Mishima, Hamon vol. 25, no. 2 (2015) 156–160.
[3] R.L. Workman et al., (Particle Data Group 2022), Prog. Theor. Exp. Phys. 2022, 083C01 (2022).
[4] K. Hirota et al., Prog. Theor. Exp. Phys. (2020) 123C02.
[5] K. Mishima et al., Prog. Theor. Exp. Phys. 2024, 093G01 (2024).
[6] N. Sumi et al., *Nucl. Instruments Methods Phys. Res. Sect. A*, 1045 (2023) 167586.
[7] T. Fujiie et al., Phys. Rev. Lett. **132**, 023402 (2024).

K. Mishima[1,2] on behalf of NOP collaboration
[1]*KMI, Nagoya University;* [2]*Institute of Materials Structure Science, KEK*

BL06: Commissioning Status of Village of Neutron Resonance Spin Echo Spectrometers (VIN ROSE)

1. Introduction

Kyoto University and The High Energy Accelerator Research Organization (KEK) have been collaborating on the construction of beamline BL06 since 2011. BL06 consists of two types of resonance neutron spin echo (NSE) spectrometers, which are a modulated intensity by zero effort (MIEZE) instrument and a neutron resonance spin echo (NRSE) instrument by branching the beam with two curved supermirror guide tubes [1]. The spectrometers are equipped with neutron resonance spin flippers (RSFs), which enabled us to downsize the instruments, and made it possible to place the two spectrometers very closely inside the radiation shielding [2].

The NSE technique is a variation of inelastic and quasi-elastic neutron spectroscopy [3]. Since the energy resolution in the energy transfer measurements is ideally decoupled with the energy spectrum of the incoming neutrons in the NSE technique, a moderately (typically 10 – 15%) monochromatic neutron beam can be acceptable. In addition, the intermediate scattering functions are directly derived by NSE, so that the method has been regarded to be suitable for investigation of slow relaxation dynamics in condensed matter, and high-intensity and high-energy-resolution NSE spectrometers have been developed and realized [4].

The user program at BL06 has started partially with the MIEZE spectrometer since the 2017B proposal round, while the NRSE spectrometer for fine-energy resolution is still under commissioning.

In this report, the status of the MIEZE and NRSE spectrometers at BL06 in FY2023 is summarized.

2. Commissioning status at BL06 in FY2023

In FY2023, the detectors at BL06 were updated by flat-panel PMT (FRP) systems [5] with a ^{6}Li-glass scintillator from the RPMT detector [6]. Figure 1 shows the FRP detectors in shading containers, which are for a single use and a 2 × 2 use. We are planning to install the FRP detectors to construct a multi-detector system for the MIEZE spectrometer, which will be able to enhance the efficiency of the measurements.

The achieved scientific highlight of BL06 is exploration of MIEZE signals from a thin monolayer with specular reflection, which is described in the following section in detail.

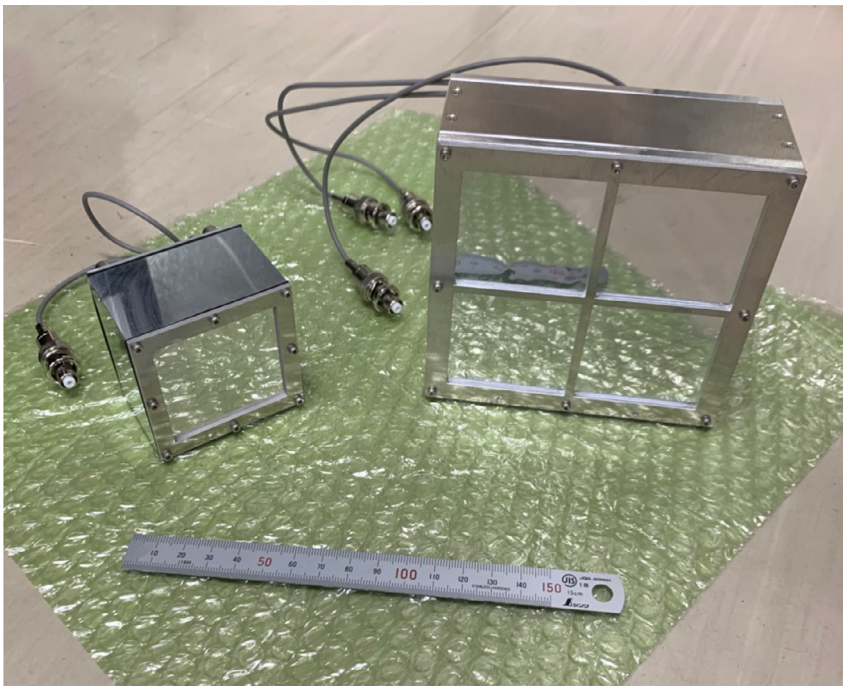

Figure 1. Picture of FRP detectors in shading containers for a single use (left) and a 2 × 2 use (right).

3. Exploration of specular reflection from a thin layer by MIEZE

In this study, a nickel carbon (NiC) monolayer deposited on a polished silicon block (50 mm × 50 mm, 10 mm in thickness) using an ion beam sputtering instrument was used. The applied MIEZE frequency ω_M was 10 kHz and the distance between the sample and the detector was 1.755 m. The neutron wavelength band was from 2.5 Å to 13.1 Å by operating a band chopper with 12.5 Hz while the accelerators were driven with 25 Hz repetition. The corresponding Fourier time τ observed in this study was from 3.6 ps to 236 ps.

Figure 2 shows the measured intermediate scattering functions $I(Q, \tau)/I(Q, 0)$ and the corresponding reflectivity as a function of momentum transfer Q. The reflectivity was evaluated with Parratt's recursive method. The solid curves in Fig. 1 represent the fitting result with the thickness of the monolayer D = 30.8 nm by fixing the surface and interface roughness to 0. Decay in $I(Q, \tau)/I(Q, 0)$is observed for the incident angle $\theta \geq 1.1^{\circ}$ resonantly. The most apparent decay can be observed around Q = 0.03 Å^{-1}, and other decay can be also observed at a larger incident angle θ and higher Q.

The combination of the time-of-flight (TOF) method and the MIEZE (TOF-MIEZE) technique possesses specific features in addition to the characteristics of the conventional NSE method [7]. For instance, since the Fourier time t is given by [7]

$$\tau = \frac{m_n^2}{h^2} \cdot f_M \cdot L_{sd} \cdot \lambda^3 \qquad (1)$$

with the mass of neutron m_n, Planck constant h, MIEZE frequency f_M, the distance between the sample and the detector L_{sd}, and the wavelength of neutron λ, the range of τ is independent from θ, while it becomes longer with larger θ at the same Q. In Fig. 3, the three-dimensional relationship between $I(Q, \tau)/I(Q, 0)$, Q, and τ is exhibited.

The resonant decay for the limited momentum transfer region Q^* in the observed intermediate scattering functions may reflect the process in inelastic scattering. By assuming the wavelength of the excited quasiparticle, λ_p, the λ_p is estimated at nearly 2/3 of the film thickness D with the relation of $Q^* = 2\pi/\lambda_p$, which corresponds to the stationary wave perpendicular to the surface. Further details will be described in Ref. [8].

4. Summary

In this report, the activities of BL06 VIN ROSE in FY2023 were summarized. The main achievement was introduced, i.e., specular reflection from a thin layer investigated by MIEZE. Resonant decay for limited momentum transfer region Q^* in the observed intermediate scattering functions was detected with different

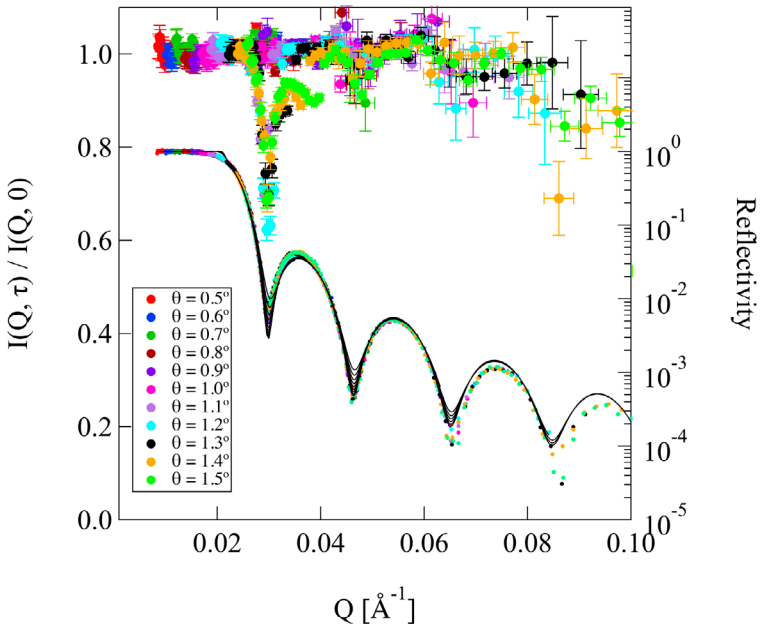

Figure 2. The normalized intermediate scattering functions $I(Q, \tau)/I(Q, 0)$ with different incident angles θ (the left ordinate) and the corresponding reflectivity (the right ordinate) as a function of Q are shown. The solid lines are the fitting results for reflectivity.

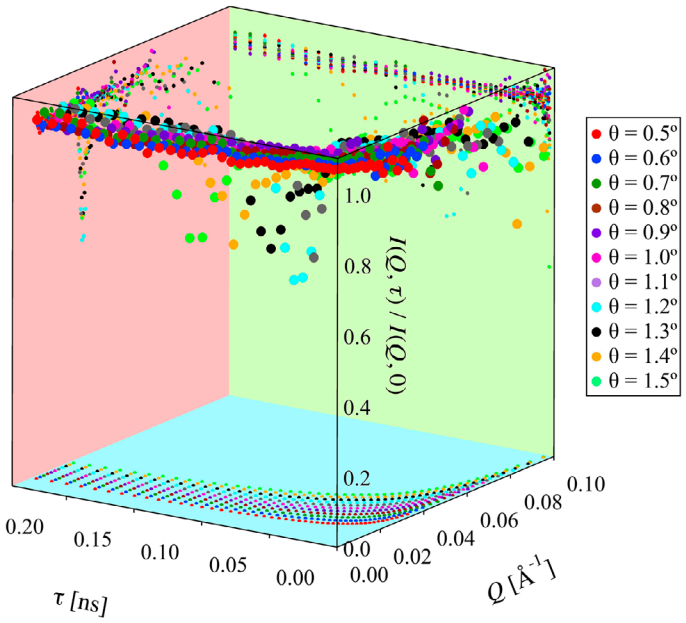

Figure 3. The three-dimensional normalized intermediate scattering functions $I(Q, \tau)/I(Q, 0)$ with different incident angles as a function of Q and Fourier time are shown.

incident angles, which relates the long stationary waves perpendicular to the surface. It had been thought that it would be very difficult to separate in-elastic or quasie-lastic neutron scattering components from a specular (elastic) neutron reflection due to the limitation of the scattering cross-section area in the reflection geometry. In these results, it was shown that the MIEZE method with fine angular resolution may be applied to observe inelastic neutron scattering in a specular neutron reflection, which will lead to the possibility to explore the dynamics of thin monolayers.

References

[1] M. Hino et al., *J. Nucl. Sci. Tech*, **54**, (2017) 1223.
[2] M. Hino et al., *Physics Procedia* **136-141**, (2013) 136.
[3] F. Mezei ed., *Neutron Spin Echo, Lecture Notes in Physics,* (Springer, Berlin) **128**, (1982).
[4] B. Farago et al., *Neutron News* **26**, (2015) 15.
[5] S. Sato, *Hamon* **27**, (2017) 8.
[6] K. Hirota, et al., *Phys. Chem. Chem. Phys*. **7** (2005) 1836.
[7] T. Oda, et al., *Phys. Rev. Appl*. **14**, 054032 (2020).
[8] H. Endo, et al., *Submitted*.

H. Endo[1,2], M. Hino[3], T. Oda[4], and H. Seto[1,2]
[1]*Neutron Science Division, Institute of Materials Structure Science, KEK;* [2]*Neutron Science Section, Materials and Life Science Division, J-PARC Center;* [3]*Institute for Integrated Radiation and Nuclear Science, Kyoto University;* [4]*The Institute for Solid State Physics, The University of Tokyo*

BL08: Remote Control of Vanadium High-Temperature Furnace

1. Introduction

The BL08 Super High Resolution Powder Diffractometer, SuperHRPD [1-2] has a vanadium high-temperature furnace (Fig. 1) as one of the sample environment instruments. Vanadium high-temperature furnaces reach a maximum temperature of 950°C in 4 hours from room temperature. The temperature is measured using a sheathed K thermocouple mounted near the sample. The measured temperature can be regarded as approximately the temperature of the sample. A sketch of the furnace is shown in Fig. 2. The vanadium high-temperature furnace consists of a vanadium heater and a radiation shield, which are kept in a vacuum chamber maintained at a vacuum lower than 10^{-3} Pa. The vanadium heater is heated by energizing and the sample space becomes hot by radiation heat. The radiation shield includes six layers, each of which consists of a stainless-steel frame with vanadium foil attached to it. The measured sample mounted on the tip of the sample stick is top-loaded and placed at the beam irradiation position. Vanadium high-temperature furnaces are high-demand sample environment instruments, with 1/4 of the proposals requesting their use. Meanwhile, it was only operated when a person was near the high-temperature furnace to avoid fire and other hazards. This report describes the measures taken to permit remote operation of the vanadium high-temperature furnace at J-PARC MLF.

Figure 1. Vanadium high-temperature furnace.

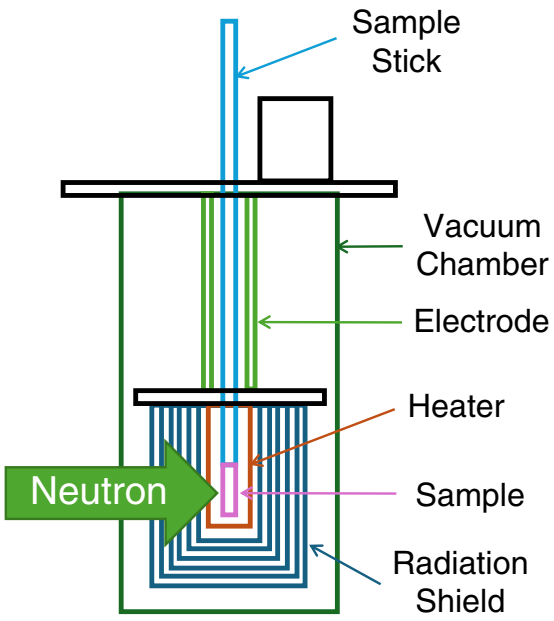

Figure 2. A sketch of Vanadium high-temperature furnace.

2. Steps to remote control

The vanadium high-temperature furnace of BL08 uses a control panel to monitor voltage, current, vacuum, temperature and cooling water, and if abnormal values are detected, the heater is automatically turned off and an alert of the problem is created by alarms and patrol lamps. In the past, at least one person was required to stay in the cabin at all times during the experiment, so that in case of danger, they could go to the side of the equipment at any time to stop the experiment. However, turning off the power supply by the interlock noted above is sufficient to prevent accidents. The human cost of constant monitoring is significant, yet the resulting benefits are minimal. In order to enable remote experiments in MLF, it is necessary to satisfy certain safety requirements. In particular, systems that can be monitored remotely, that check the well-being of the equipment, and that provide an environment where anyone can respond to emergencies are required.

Firstly, as part of the development of the remote monitoring system, an alert panel was installed to read signals from the control panel. The alert panel is supported by the software framework IROHA2 [3], which enables the real-time viewing of alerts and notifications from any machine

in the network (JLAN) via the web UI. Furthermore, software was developed in LabVIEW for the purpose of recording the data utilized in the experiments. This software enables the user to set and record temperatures. (Fig. 3)

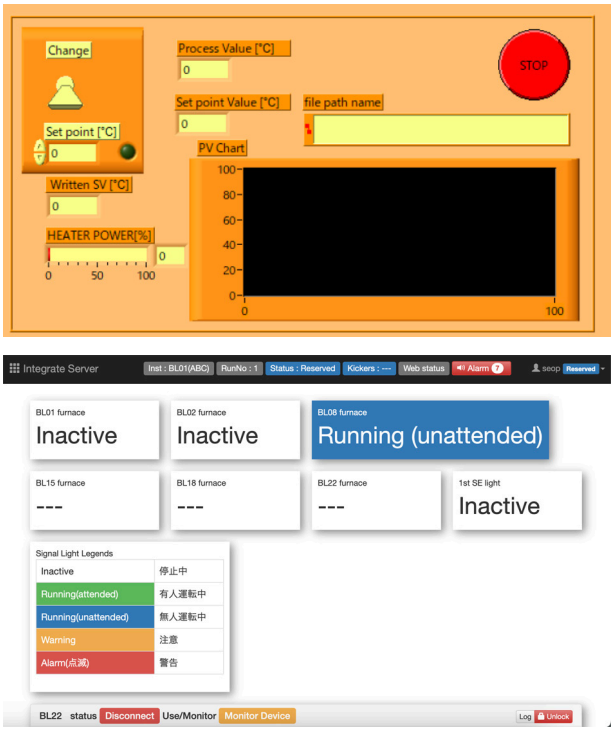

Figure 3. (a) Recording and control screens in LabVIEW. (b) Monitoring screen in IROHA2. The blue display indicates that the BL08 is in unmanned operation.

The next thing to consider is the security of the equipment. The vanadium high-temperature furnaces have been in operation since before 2009 and were checked and repaired in 2021. Heaters change their current and voltage values over time, so temperature rise tests are performed periodically to check the interlock criteria. In addition, regular maintenance and inspections of the furnace are also carried out to check the condition of the heating elements and so on. The user should always be asked to check the reaction of the sample at high temperatures and the reaction of the sample holder with the sample before using the sample in the experiment. And once the sample is in the furnace, it is always checked for continuity from the sample environment to the outside of the instrument. Immediately after start-up, the furnace is monitored until it has stabilized before remote control is switched on, with particular attention paid to checking the temperature range from room temperature to 300°C, where high temperature furnaces are not good and current and voltage values tend to be unstable.

For remote operation during the experiments, mainly at night, it was arranged to request the MLF monitoring room to periodically check on the operation from the IROHA2. In the event of an emergency, the monitoring room is directed to a prearranged response flow and the person in charge of the equipment is contacted. And we posted manuals on site so that if an alarm sounded, people could go to the side of the device to find out what to do.

The above steps have improved the safety of the equipment and these measures are being recognized by the MLF, allowing remote operation of the high-temperature furnace at BL08.

3. Summary

Steps to enable remote operation of the vanadium high-temperature furnace were presented. The safety of operating and experimenting with the equipment has been reviewed and improved, and policies also established. The situation, which used to be constantly monitored by the personnel, has improved as a result of these measures. In response to the shortage of personnel, which has been an issue at all sites in recent years, we intend to continue to improve the quality of the experimental environment by providing solutions from an operational and technical perspective.

References

[1] S. Torii, M. Yonemura, T. Y. S. Panca Putra, et al., J. Phys. Soc. Jpn., SB020 SB020-1-4 (2011).
[2] S. Torii, M. Yonemura, Y. Ishikawa, et al., J. Phys.: Conf. Ser., 502 012052 (2014).
[3] T. Nakatani, Y. Inamura, T. Ito and K. Moriyama, IROHA2: Standard instrument control software framework in MLF, J-PARC, NOBUGS 2016 Proceedings, **76** (2016).

S. Yamauchi[1,2], S. Torii[1,2], and K. Mori[1,2]
[1]*Neutron Science Section, Materials and Life Science Division, J-PARC Center;* [2]*Institute of Materials Structure Science, KEK*

Current Status of BL09 SPICA in FY2023

1. Introduction

The special environment powder diffractometer (SPICA) located at BL09 of J-PARC MLF was founded by the New Energy and Industrial Technology Development Organization (NEDO), together with the High Energy Accelerator Research Organization (KEK) and Kyoto University. In the NEDO projects (i.e., RISIN (FY2009 – 2015), RISING2 (FY2016 – 2020) [1], and RISING3 (in progress; FY2021 – 2025) [2]), SPICA is dedicated to structural investigations for the next-generation rechargeable batteries, as well as commercial lithium-ion batteries. SPICA was designed and developed to achieve a high resolution ($\Delta d/d$) of 0.08% with high intensity [3]. To realize the high $\Delta d/d$, SPICA has been situated at approximately 50 m from the neutron source system. SPICA focuses on neutron diffraction experiments under special environments, especially in charge-discharge operations (i.e., *operando* measurements). In addition, an annex building for SPICA (next to the 1st experimental hall of J-PARC MLF) was built to prepare samples for neutron diffraction experiments, assemble rechargeable batteries and conduct their charge-discharge evaluations before and/or after *operando* measurements. Currently, SPICA is widely used in various experiments, particularly in the field of battery science [4–10].

2. Specifications of SPICA

SPICA was installed at BL09, which has the thin side of a decoupled poisoned moderator with the shortest time resolution (or the shortest pulse at full width in half maximum (FWHM) region) of all MLF moderators. The neutron intensity on the thin side is weaker than that on the thick side (i.e., BL18, 19, and 20 in the 2nd experimental hall); however, the thin side has the advantage of a symmetrical peak profile, which can be used to extract strain information from the samples. The primary flight path from the moderator to the sample position (L_1) is 52 m, and the secondary flight path from the sample position to the detectors (L_2) is approximately 2 m, as shown in Fig. 1. An elliptical supermirror guide gradually changes the mirror coating from m = 3 to 6 toward the sample position, making it efficient to increase the number of neutrons at the sample position. SPICA utilizes 1568 ^{3}He gas-filled one-dimensional position-sensitive detectors (PSDs) with a diameter of 1/2 inch and an active length 0.60 m from a total of 0.67 m. The detector banks are formally grouped according to the scattering angle (2θ): backscattering bank ($150 \leq 2\theta \leq 175^{o}$), high-angle multi-purpose bank ($120 \leq 2\theta \leq 150^{o}$), 90-degree multi-purpose bank ($60 \leq 2\theta \leq 120°$), low-angle multi-purpose bank ($10 \leq 2\theta \leq 60^{o}$), and small-angle bank ($5 \leq 2\theta \leq 15°$). In particular, the detectors in the multi-purpose bank ($10 \leq 2\theta \leq 150°$) have been placed continually on a cylindrical locus approximately 2 m from the sample position. The $\Delta d/d$ value was evaluated for each bank: $\Delta d/d$ = 0.12% for the backscattering bank, $\Delta d/d$ = 0.47% for the 90-degree multi-purpose bank, and $\Delta d/d$ = 1.27% for the low-angle multipurpose bank. The chopper rotated at a frequency of 25 Hz, which was the same as the repetition rate of the proton beam injection. The natural bandwidth of the SPICA is 2.9 Å. Three single-disc choppers were used for bandwidth selection to prevent frame overlapping and operated with 25/4 to 25/1 Hz repetition to select bandwidths.

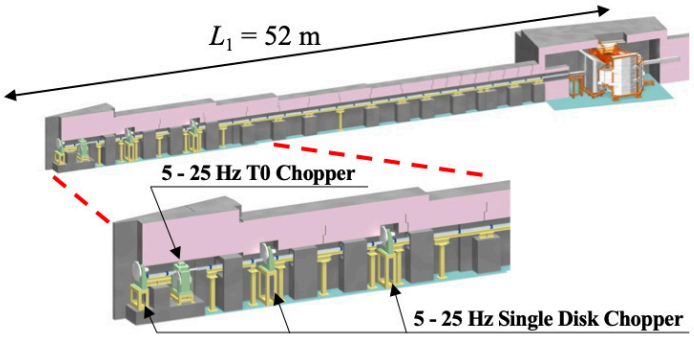

Figure 1. Layout of BL09 SPICA.

3. Visual inspection for supermirror guide

The preliminary visual inspection for the supermirror guide of SPICA was conducted during the summer, because the vacuum level of the supermirror guide has been gradually deteriorating over the past several years. The concrete blocks for radiation shielding around the end of the supermirror guide (in the BL09 annex building) were removed by MLF staff members. The work scenery of removing the concrete blocks is shown in Figs. 2, 3, and 4. This inspection did not find any defects in the supermirror guide. Next time, we will inspect further the supermirror guide located at the upper stream on the 1st experimental hall.

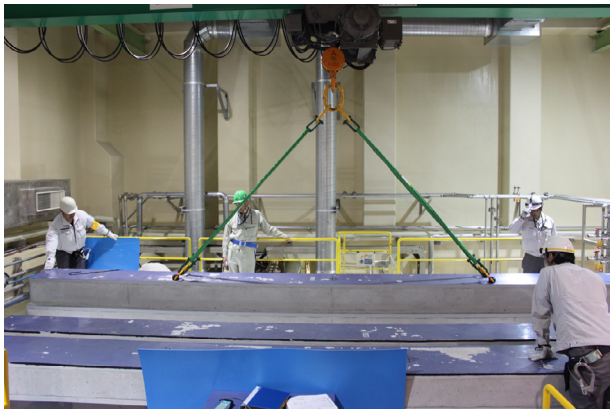

Figure 2. The work scenery of removing the concrete blocks for radiation shielding located at the top of the main body of SPICA.

Figure 3. The work scenery of removing the concrete blocks for radiation shielding around the end of the supermirror guide of SPICA.

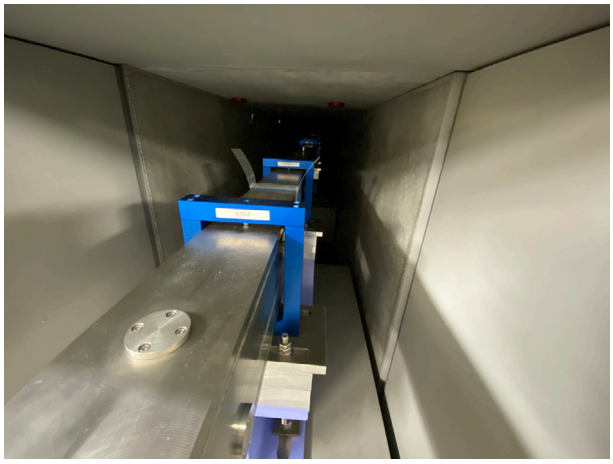

Figure 4. Partial view of the supermirror guide facing toward the decoupled poisoned moderator.

References

[1] https://www.rising.saci.kyoto-u.ac.jp/rising2/
[2] https://www.rising.saci.kyoto-u.ac.jp/en/
[3] M. Yonemura et al., J. Phys. Conf. Ser., **502** 012053 (2014).
[4] Y. Kato et al., Nat. Energy, **1** 16030 (2016).
[5] S. Taminato et al., Sci. Rep., **6** 28843 (2016).
[6] K. Mori et al., ACS Appl. Energy Mater., **3** 2873 (2020).
[7] K. Mori et al., ACS Appl. Energy Mater., **7** 7787 (2024).
[8] F. Takeiri et al., Nat. Mater., **21** 325 (2022).
[9] K. Kino et al., Appl. Phys. Express, **15** 027005 (2022).
[10] Y. Izumi et al., Adv. Energy Mater., **13** 2301993 (2023).

K. Mori[1,2], K. Namba[1], S. Song[1,2], T. Saito[1,2], and S. Torii[1,2]

[1]*Institute of Materials Structure Science, KEK;* [2]*Neutron Science Section, Materials and Life Science Division, J-PARC Center*

BL10: NOBORU

1. Introduction

We continue to study a temporal change in neutronic performance for the long-term stable neutron source operation under increasing the proton beam power up to 1 MW. This year, the proton beam power was kept at about 900 kW, but beamtime was significantly reduced due to two fire events in the accelerator area in 2023A and a minor trouble in the cryogenic hydrogen system in the MLF in 2023B. At NOBORU, sixteen general-use proposals, one long-term proposal and two project-use proposals were carried out.

We have conducted continuously fixed-point observations in the instrument-use beam time. The gold-foil activation method is usually used for measurement of thermal neutron intensity. However, the uniformity of the thermal neutron beam profile in the measurement caused problems in accurately deriving the beam intensity. This year we proposed and tested the large-size gold foil activation method to measure simultaneously both the thermal neutron beam profile and its intensity.

2. Experiment

Gold has a single isotope (Au-197) and good neutron absorption property, as shown in Fig. 1. Au-198 produced by the Au-197 (n, γ) Au-198 reaction is β-decay nuclide with 411.8 keV (96%) gamma-ray emission and its half-life is 2.69517 day. The gold-foil activation is a very simple method to measure neutron flux, which has been used for a long time [1]. Two measurements, with and without the cadmium cover, are necessary to distinguish the activation of resonance absorption, which appears at neutron energies above a few eV.

In the experiment at NOBORU, two large-size gold foils of 100 mm × 100 mm × 0.1mm were used. First, a bare gold foil was set behind a B_4C slit device (L_1 = 12.7 m) and irradiated for 17.5 minutes. Next, another gold foil with a 0.1 mm thick cadmium cover was set and irradiated for 24 minutes. Figure 2 shows the picture of the gold foil set behind the B_4C slit device.

In this experiment, the rotary collimator at L_1 = 8 m was set to "S" (10 × 10 mm^2 in hole size) and the insertion collimator "S" (20 × 20 mm^2 in hole size) was used at L_1 = 12.5 m. After irradiation, the activated gold foil was transferred to an imaging plate (BAS IP SR 2040 E) for gamma radiation for approximately 10 minutes. Figure 3 shows a picture of an imaging plate and the irradiated gold foil for gamma-ray transfer. The imaging plate was read by an imaging-plate reader (Typhoon FLA 7000). After that, the gold foil was measured with a High-purity Germanium radiation detector to obtain the absolute value of the irradiation dose.

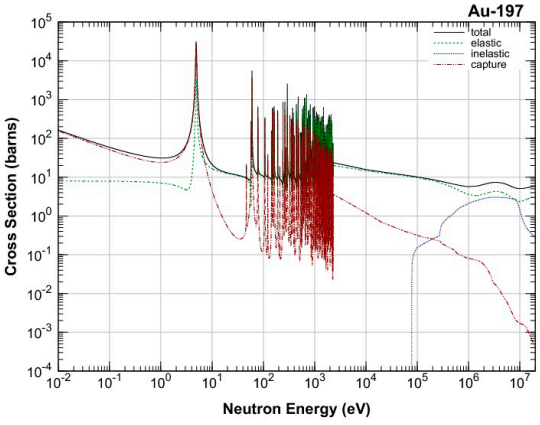

Figure 1. Cross section of Au-197.

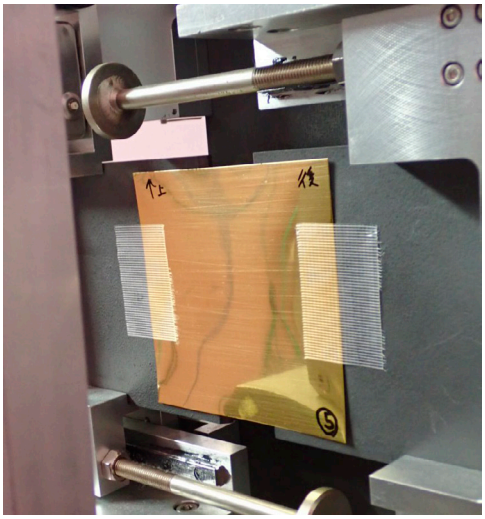

Figure 2. Picture of gold-foil setting.

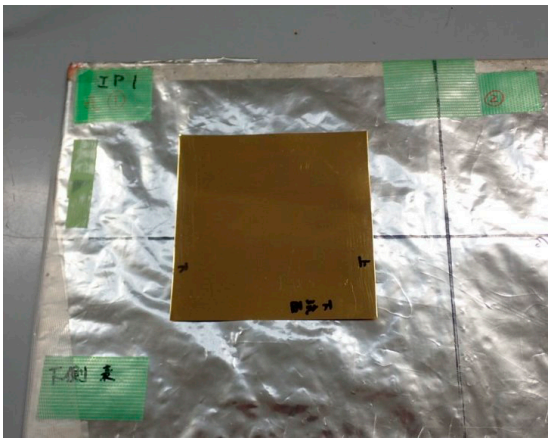

Figure 3. Picture of an imaging plate and the irradiated gold-foil for gamma-ray transfer.

3. Results

Figure 4 shows the neutron beam profile obtained with the imaging plate transferred from the irradiated gold foil. We confirmed that the neutron beam profile was almost uniform. The irradiated area retrieved from this data is 5.0 cm^2, which is slightly larger than the hole size of the insertion collimator.

Figure 5 shows the gamma-ray spectrum from the gold foil; using 111.5 burns obtained from other validation experiments performed at NOBORU as the effective cross section [2], the neutron flux equivalent to 1 MW was determined to be 3.6×10^6 $n/cm^2/s$.

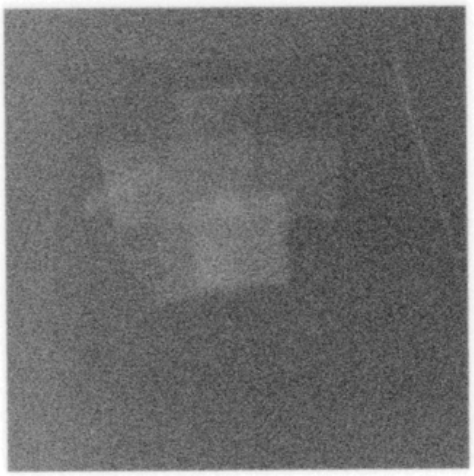

Figure 4. Beam profile on the imaging plate transferred from the irradiated gold foil.

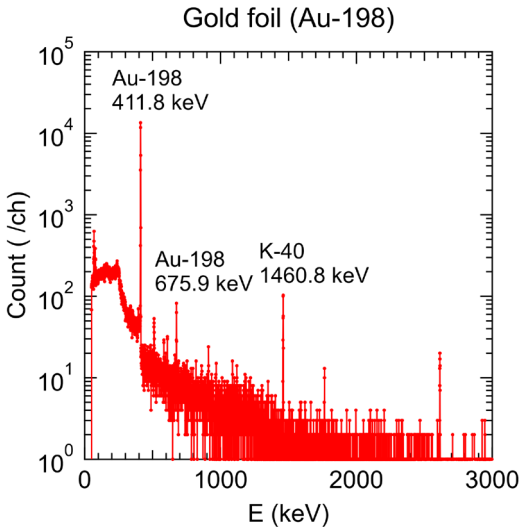

Figure 5. Gamma-ray spectrum of the irradiated gold foil.

4. Conclusion

We devised a large gold foil activation method and performed it at NOBORU. As a result, neutron beam profile and neutron intensity were obtained simultaneously with good accuracy. This new method was applied to neutron flux measurements for other neutron instruments and was also used to experimentally determine the efficiency of neutron monitor detectors.

References

[1] M. Harada et al., "Effect of proton beam profile and incident position on neutronic performance and structural integrity of a mercury target of the spallation neutron source at J-PARC, 2; Nuclear heat of mercury target and cold-thermal neutron intensity provided to neutron instrument", 2018 Fall Meeting of Atomic Energy Society of Japan.

[2] M. Harada et al., "Measurement of thermal neutron intensity and distribution using a large-area gold foil activation method at the J-PARC MLF", JSNS2023.

M. Harada and K. Oikawa
Neutron Science Section, Materials and Life Science Division, J-PARC Center

Developments at BL11 PLANET

1. Introduction

The developments during this year are explained below.

2. Replacement of deteriorated PSDs and their electronics

PLANET has a pair of 90-degree detector banks equipped with 320 PSDs. Since the start of their operation in 2013, PSDs and electronics have been deteriorating with time: two PSDs show too high intensity compared with the surrounding ones and seven PSDs show worse spatial resolution along the long direction. To fix these problems, we replaced the PSDs or PSD amplifier boards with new ones.

Figure 1 compares the detector map measured for the acrylic cylinder before and after the replacement. A strong vertical line caused by PSD degradation in the south bank disappeared and the top and bottom horizontal shadows by the Gd_2O_3 painted strings became sharp and homogeneous.

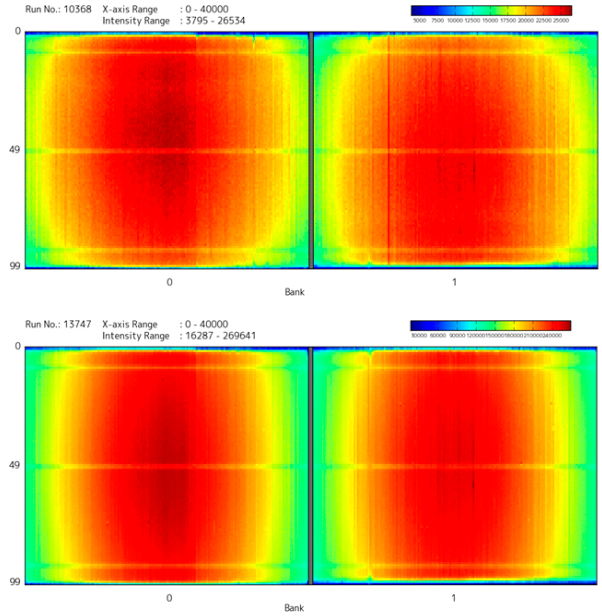

Figure 1. North (left) and South (right) detector maps of the acrylic cylinder before (top) and after (bot-tom) the replacement of PSDs or PSD amplifier boards.

3. Ar gas loading with a new load clamp

In the high-pressure powder diffraction experiments, the sample was normally compressed along with a liquid pressure medium (PTM) to avoid broadening of the sample Bragg peaks due to the internal stress and/or pressure inhomogeneity in the sample chamber. 4:1 methanol-ethanol mixture is normally used as PTM; however, it cannot be used for sample reactive with alcohol. In this case, liquid Ar is useful because it has low reactivity and prevents the emergence of strong Bragg peaks in the diffraction pattern [1].

So far, we have succeeded in cryogenically loading Ar in encapsulating gaskets for a Paris-Edinburgh cell using a load clamp based on the method invented by Klotz [2]. However, we had always encountered problems when retrieving the jig attached to the load clamp (see Fig. 2 left). To fix the problem, the top part of the load clamp was modified into a hexagon nut. With this modified cell, we tested Ar loading and confirmed the usefulness of the modification.

Figure 2. (Left) A modified load clamp and (right) an original load clamp with a jig to grab it with a handle bar. The screw to hold the load clamp is changed into a hexagon nut.

4. Development of remote-control systems

4.1 Remote screenshot of the control PC screen [3]

Data acquisition and device control are performed by the **Experimental Scheduler** software installed in the control PC. To monitor the experiment status from outside the facility, a system that takes screenshots of the control window, called **RemoShot**, has been devised and implemented at PLANET.

The **RemoShot** consists of a screenshot control server, a control PC, and cloud storage (Fig. 3). It is operated in the

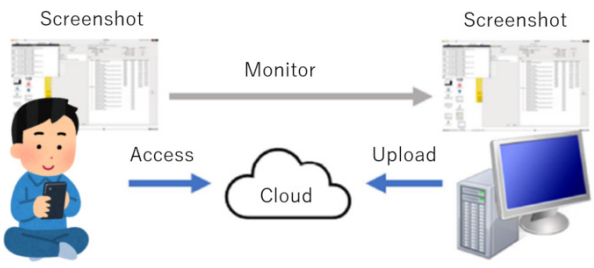

Figure 3. Architecture for users to get screen-shots of control PC at PLANET.

following sequence: i) the user launches **RemoShot** on the control PC at PLANET in advance; ii) The user requests capturing the screen from an external terminal, such as a smart phone or his own PC; iii) The screenshot control server accesses the control PC via SSH authentication, takes a screenshot, and saves the image to the cloud storage; iv) After authentication, users retrieve the screenshot from the cloud storage.

The **RemoShot** makes it possible for the users to remotely check the experiment status at any place, and notice unexpected command errors, beam stoppages, and blowouts if they happen.

4.2 Remote refrigerator compressor on/off system

A 4K-GM refrigerator (Iwatani, CryoMini) coupled with a compressor (Iwatani, CA112) is used in the low temperature experiments using a vanadium can for ambient pressure measurement or a piston cylinder cell for high-pressure measurements. The compressor must be turned off 4 hours prior to sample exchange to prevent frosting during the sample exchange. So far, the staff had to come to the MLF even at midnight for that purpose. In order to relieve the staff from such hassles, the compressor circuit was modified, and a remote compressor on/off command was implemented in the **Experimental Scheduler**.

The CA112 compressor did not have an external interface because it is a low-cost version of SA112, but it was found to be built-in when opening the front panel of the housing. Thus, holes were drilled in the rear panel and cables were connected to the internal circuit. Figure 4 shows how the system developed. The input signal for on/off control is distributed from a temperature controller (Lakeshore LS331) and the command to trigger the on/off is implemented in the **Experimental Scheduler**. The system works well and staffs are now relieved of their midnight duties.

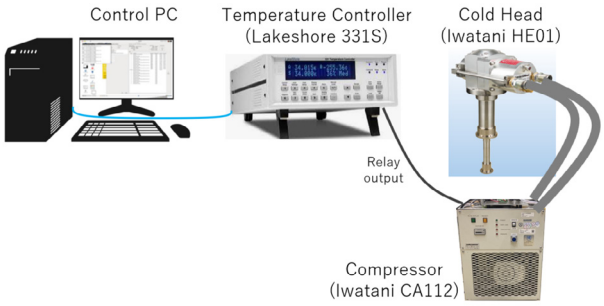

Figure 4. System configuration for remote ON/OFF control of compressors for 4K-GM refrigerator.

4.3 Enabled function to estimate the time to finish a batch job

The **Experimental scheduler** software originally has a function to estimate the time to finish batch jobs registered in advance. So far, this function has not been enabled because of poor coding of the source. This forced users to do the calculations by themselves, which sometimes caused mistakes in the planning of the experiment. To fix this problem, the existing function was enabled and additional functions were implemented (Fig. 5). The required time for one measurement depends on the criteria that determine when to stop each measurement. When the 'total exposure time' is selected, the time is directly estimated from the input time. If the 'kicker number' is selected, the required time is calculated from the accumulated kicker and the numbers of kicker per time that depends on the frame mode (i.e. single/double frame) employed in the measurement. In the new code, the flame mode being used is specified by putting 's' or 'd' character in the comment field. Additionally, the kicker per time changes with the distribution rate of the proton beam to the Main ring. Taking this into consideration, the estimated time is corrected by a factor written in the source code.

This function helps users to plan experiments more rigiorously and decrease the risk of missing data within the beamtime assigned to them.

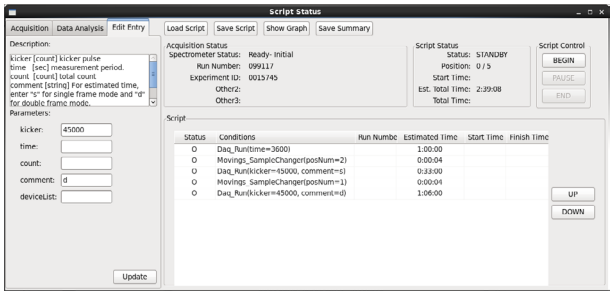

Figure 5. An example of the time estimation of the registered jobs by the Experimental Scheduler.

References

[1] T. Hattori *et al.*,High Press. Res. **40**, 325 (2020).
[2] S. Klotz, *Techniques in high pressure neutron scattering* (CRC Press, Boca Raton, 2013).
[3] N. Okazaki and T. Hattori, (in Japanese) CROSS Reports **1**, 1 (2023).

T. Hattori[1], A. Sano-Furukawa[1], S. Machida[2], J. Abe[2], Y. Sakai[2], and N. Okazaki[2]
[1]*Neutron Science Section, Materials and Life Science Division, J-PARC Center;* [2]*Neutron Science and Technology Center, CROSS*

High Resolution Chopper Spectrometer HRC

1. Introduction

The High Resolution Chopper Spectrometer (HRC) is being operated at BL12 in the MLF under the S-type project of IMSS, KEK, and the IRT project of ISSP, the University of Tokyo, in order to study dynamics in condensed matter. The activities of the HRC project in FY2023 are summarized in this report.

2. Instrumentation

A ^{3}He gas sorption type refrigerator, where the lowest temperature, 0.3 K, is maintained for 100 hours, was delivered in March 2023. The experiment control program YUI was modified to accommodate this refrigerator, and it is now open for the general user program. Sample environments (SEs) currently available on HRC are listed in Table 1 [1].

Table 1. Sample environments available on HRC. Cryofurnace is under commissioning. Pressure cell can be mounted in the standard sample cell.

Sample environment (SE)	Condition
GM refrigerator	T = 4 – 300 K
1K refrigerator	T = 0.6 – 300 K
^{3}He refrigerator	T = 0.3 – 300 K
Cryofurnace	T = 4 – 700 K
Superconducting magnet	$B \leq 5$ T, T = 0.3 – 300 K
Pressure cell	$P \leq 1.2$ GPa

A goniometer was manufactured for each SE, but the driver was made common due to space limitations in the control room. The motors used for the GM and 1 K refrigerators are no longer manufactured and are not compatible with the driver which was newly manufactured for the ^{3}He refrigerator. The motors for the GM and 1 K refrigerators were replaced by currently available ones. The cryofurnace uses another type of motor, thus the final form of the driver should be considered.

For YUI and the data visualization program HANA, the operating system (OS) was updated, and the basic software was replaced by Python3. The previous OS and Python2 will no longer be supported.

We have recognized noise signals in neutron intensities related to detector electronics for a long time. The pulse height distribution of the neutron counts in position sensitive detectors (PSDs) shows a minimum at h_0, as shown in Fig. 1(a). The pulse height is represented as $Q_1 + Q_2$ for each detected neutron, where Q_1 and Q_2 are electric charges detected at both ends of a PSD and the detection position is given by $Q_1/(Q_1 + Q_2)$. There is gamma ray noise in the pulse heights lower than h_0. This noise can be reduced by setting the lowest level of discrimination (LLD) so that data with pulse heights lower than LLD are not used in the data analysis. The noise was successfully reduced without reducing neutron intensities by setting LLD = 1.4 h_0 for all PSDs, as shown in the inelastic neutron scattering (INS) spectra from $CePtSi_3$ in Figs. 1(b) and 1(c).

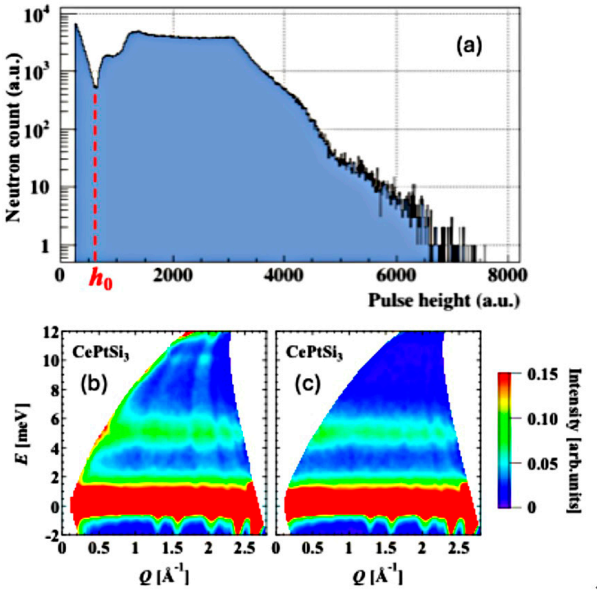

Figure 1. (a) Pulse height distribution of neutron counts in PSDs. INS spectra from a powder sample of $CePtSi_3$ with E_i = 13.3 meV, (b) with a smaller default value of LLD, and (c) with LLD = 1.4 h_0. Crystalline electric field excitations are observed at around 5 meV.

3. Scientific Results

Magnetic structures with multiple magnetic modulation wave vectors (q-vectors) have attracted great interest, since the discovery of magnetic skyrmion lattices in MnSi. Multi-q states are difficult to distinguish from multi-domain states of single-q orders. In order to address this issue, we investigated magnetic orders of an intermetallic compound $CeRh_2Si_2$ [2]. $CeRh_2Si_2$ exhibits antiferromagnetic transitions at T_{N1} = 36 K and T_{N2} = 25 K. The high-temperature phase (AF1) has a single-q order with a q-vector, q_1 = (1/2, 1/2, 0). Owing to the 4-fold symmetry of the crystal structure, the q-vector, q_1' = (1/2, –1/2, 0), is also allowed to appear in AF1. It is considered that q_1 and q_1' forms a multi-domain state. In the low-temperature phase (AF2), there are four q-vectors, (1/2, 1/2, 0), (1/2, –1/2, 0), (1/2, 1/2, 1/2) and (1/2, –1/2, 1/2). The neutron diffraction measurement was performed

under uniaxial stress at the triple-axis spectrometer PONTA installed in JRR-3. We revealed that AF1 has the single-*q* structure with the 2-fold rotational symmetry. In contrast, AF2 is stubborn in resisting in-plane uniaxial stress and the 4-fold rotational symmetry is recovered reflecting the multi-*q* state. We performed INS experiments on HRC at ambient pressure (Fig. 2) to determine the magnetic interactions. In AF2, the dispersion relations can be well reproduced by the linear spin-wave theory including the nearest and next-nearest exchange interactions, J_1 and J_2, and the uniaxial anisotropy D (solid lines in Figs. 2(e) and 2(f)). The fitting result indicates that J_1 and J_2 are dominant. However, J_1 and J_2 cannot lift the degeneracy of the single-*q* and multi-*q* states. We showed that the bilinear-biquadratic interaction, which is used to reproduce skyrmion lattice phase in $GdRu_2Si_2$, can lift the degeneracy and stabilize the multi-*q* phase.

Magnetic field control of magnon decay in a quantum antiferromagnet $RbFeCl_3$ was investigated, where the interaction between the magnon and two-magnon continuum is tuned by the field [3]. At low fields, where the interaction is small, the single magnon decay process is observed. At high fields, where the interaction exceeds a critical magnitude, the magnon is pushed downwards in energy and its lifetime increases. This study demonstrates that field control of quasiparticle decay is possible in the system where the two-quasiparticle continuum covers wide momentum-energy space. Details are described in a separate report in this issue.

Helimagnetic compounds $MnSi_{1-x}Ge_x$ show the three-dimensional multi-*q* orders referred to as hedgehog-antihedgehog spin lattice states, and also show a sign change in the Hall resistivity against the temperature. Spin fluctuations in $MnSi_{1-x}Ge_x$ with x = 0.6 and 0.8 were investigated using HRC and VIN ROSE [4]. A relation between the Hall resistivity and spin fluctuations was discussed. Details are described in a separate report in this issue.

INS experiments were performed on a helimagnet Ni_2InSbO_6, and well-defined spin-waves were observed below T_N = 76 K [5]. Using the linear spin-wave theory, the spectrum was reasonably reproduced with honeycomb spin layers coupled along the stacking axis (*c* axis). The proposed spin model reproduces the soliton lattice induced by a magnetic field applied perpendicular to the *c* axis.

A spin tube candidate $CsCrF_4$ exhibits a phase transition from a paramagnetic phase through an intermediate-temperature phase (IT) of a 120° structure to a low-temperature phase (LT) of another 120° structure. The INS spectra in $CsCrF_4$ observed in IT are surprisingly the same as those in LT, even though the magnetic structures in IT and LT are different [6]. No difference in the spectra indicates no change in the spin Hamiltonian, suggesting that the origin of the phase transition is a spin-entropy-driven mechanism.

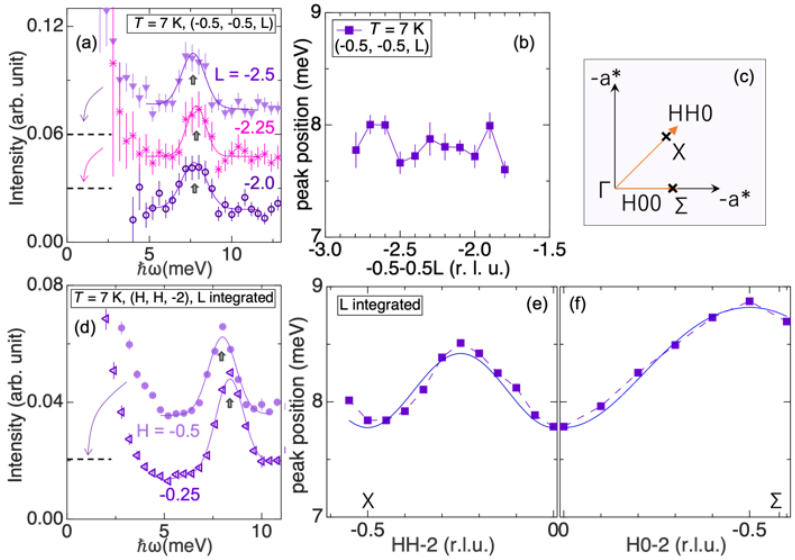

Figure 2. Magnetic excitation spectra and dispersion relation in AF2 of $CeRh_2Si_2$ (Reproduction from Ref. [2]).

References

[1] D. Ueta et al., JPS Conf. Proc. **41** 011008 (2024).

[2] H. Saito et al., Phys. Rev. B, **108** 094440 (2023).

[3] S. Hasegawa et al., Nat. Commun., **15** 125 (2024).

[4] S. Aji et al., Phys. Rev. B, **108** 054445 (2023).

[5] Z. Liu et al., Phys. Rev. B, **107** 064428 (2023).

[6] H. Kikuchi et al., Phys. Rev. B, **107** 184405 (2023).

S. Itoh[1,2], T. Masuda[3,2], D. Ueta[1,2], T. Nakajima[3], T. Yokoo[1,2], S. Asai[3], H. Saito[3], H. Kikuchi[3], D. Kawana[3], R. Sugiura[3], T. Asami[3], S. Aji[3], Z. Liu[3], M. Ozeki[3], S. Yamauchi[1,2], S. Torii[1,2], T. Seya[1,2], H. Ohshita[1,2], N. Kaneko[1,2], Y. Ihata[1], N. Yabe[1], and H. Tanino[1,2]

[1]*Materials and Life Science Division, J-PARC Center;* [2]*Institute of Materials Structure Science, KEK;* [3]*The Institute for Solid State Physics, The University of Tokyo*

BL14: AMATERAS

1. Introduction

AMATERAS is a cold-neutron disk-chopper spectrometer designed for studying the dynamical properties in atomic, molecular, and magnetic systems from cold to sub-thermal energy range with high efficiency and flexible resolution [1, 2]. It has been 15 years since AMATERAS was opened for the user program. During this time, we have continuously upgraded various instrument components while supporting the users' experiments. In FY2023, we relocated detectors, reduced background, commissioned a new cryogenic reactor, and evaluated beam flux and energy resolution. Furthermore, Dr. Pharit Piyawongwatthana, a postdoctoral researcher, joined the instrument group.

2. User program

In FY2023, 34 and 44 general proposals (short-term) were submitted to AMATERAS in the 2022A and 2022B rounds, respectively. 19 short-term proposals, including reserved and urgent proposals, and one project proposal were successfully conducted. Due to the delay in resuming the beam operation, some experiments were carried over. Statistics from the last four years show that 75% of the experiments performed were in the field of magnetism, 10% in thermoelectric materials and ionic conductors, and the rest in liquids, amorphous, soft matter, and biological materials. 11 peer-reviewed papers were published in 2023.

3. Instrument upgrades

The total number of detectors in the previous year was 286, covering a scattering angle (2θ) ranging from 3.4° to 117.5°. In the summer of 2023, 6 detectors were added and relocated. Currently, AMATERAS has 292 detectors, with angle ranges of $4.9° < 2\theta < 117.5°$ and $-15.1° < 2\theta < -4.9°$. The placement of the detectors on the negative side facilitates the observation of magnetic excitations appearing in a low Q region.

In 2021, we extended the supermirror guide tube by ~50 cm in the downstream section, between the monochromating chopper and the vacuum scattering chamber window. This extension led to the appearance of backgrounds at low scattering angles. To resolve this issue, the shielding of get lost tube was enhanced. Figure 1 shows Q-E intensity maps of a thin vanadium plate. Background appeared in the low Q region, indicated in the figure by magenta circles, and was suppressed by the shielding enhancement. However, the background has not yet been eliminated completely and further shielding of the get lost tube is planned.

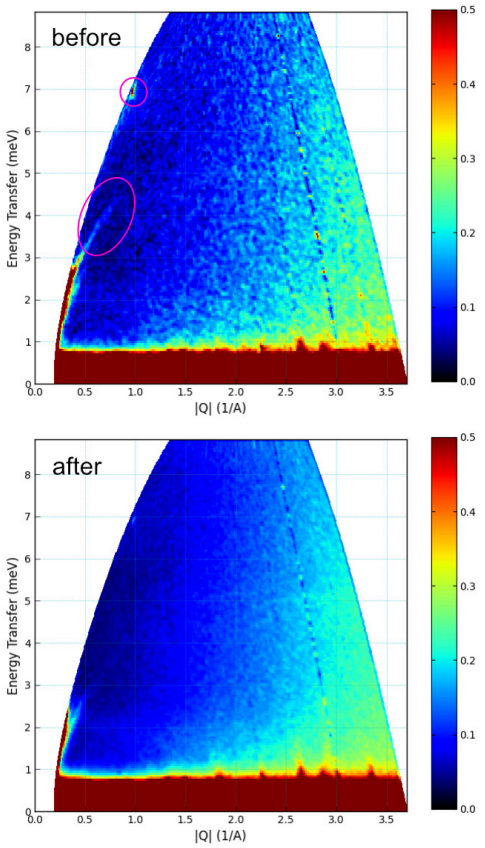

Figure 1. Q (horizontal) - E (vertical) intensity maps of a thin vanadium plate before and after the shielding enhancement of get lost tube. The data were taken with an incident energy (E_i) of 10.5 meV.

We commissioned a recently purchased ^{3}He top-loading cryofurnace (He3-TL) which is a cryogen-free system incorporating a pulse-tube cryocooler and the one-shot ^{3}He cooling system. This cryofurnace enables measurements at temperatures ranging from 0.3 K to ~700 K, using low-T, mid-T and high-T probes. Holding time at 0.3 K is about 3 days, but this is reduced to 1.5 – 2 days when the He3-TL is placed on AMATERAS. The reason for the reduced holding time is unknown. A further major problem is that the initial cooling and cooling from high temperatures to 0.3 K takes ~2 days. We intend to take steps to address these issues.

On-beam tests of the He3-TL were also carried out. As shown in Fig. 2, the background of the He3-TL is comparable with that of our bottom-loading closed cycle refrigerator (BLCCR), which has the lowest background among all available sample environments.

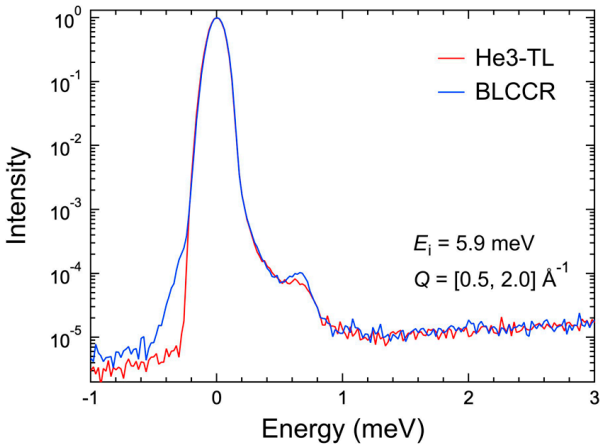

Figure 2. Energy profiles of the scattering intensity for the vanadium plate in the He3-TL and BLCCR, taken with E_i = 5.9 meV. The elastic scattering intensity is normalized to 1 for comparison.

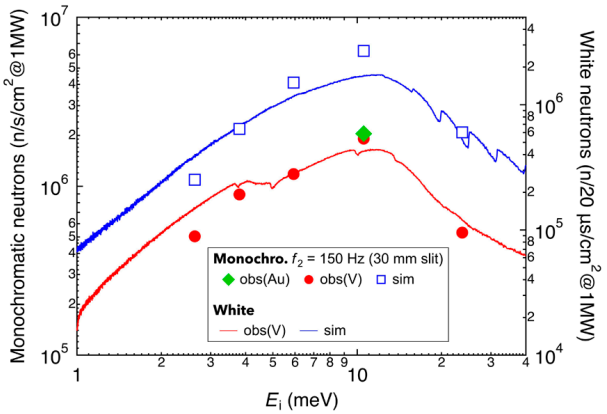

Figure 3. Measured and simulated flux of monochromatic and white neutrons at the sample position against E_i. The measured flux was evaluated using a gold (Au) foil and a vanadium (V) plate.

4. Neutron flux and energy resolution

We investigated neutron flux at a sample position and energy resolution under chopper conditions typically used in actual measurements (Fig. 3) [3]. The absolute flux was evaluated using gold foil and a Vanadium plate. The fluxes at E_i = 10.5 meV obtained from both measurements were almost the same, ~2 × 10^6 n/s/cm2@1 MW, which is comparable with that of other disk-chopper spectrometers in the world with high flux for similar energy resolution ($\Delta E/E_i$ = 6.5%). However, the simulated flux using McStas was approximately 3 – 4 times larger than the observed one, and the difference becomes more significant at higher E_is. The discrepancy could be due to the supermirror's performance being lower than nominal.

5. Future plans

We will achieve background reduction through further shielding of the get lost tube and cryofurnace. Shortly, the He3-TL will be used in actual user experiments. Replacement of the supermirror neutron guide tube is under consideration.

References

[1] K. Nakajima *et al.*, J. Phys. Soc. Jpn., **80**, SB028 (2011).
[2] K. Nakajima, RADIOISOTOPES, **66**, 101 (2017).
[3] M. Nirei *et al.*, J. Neutron Res., **26**, 75 (2024).

S. Ohira-Kawamura[1], M. Kofu[1], N. Murai[1], Y. Inamura[1], M. Nirei[1], P. Piyawongwatthana[1], D. Wakai[1,2], and K. Nakajima[3,1]
[1]Neutron Science Section, Materials and Life Science Division, J-PARC Center; [2]NAT Corporation; [3]Materials Sciences Research Center, JAEA

Current Status of Ultra-Small-Angle Scattering Measurements at BL15 TAIKAN

1. Introduction

The configuration of detectors at the small- and wide-angle neutron scattering instrument TAIKAN (BL15) [1] consists of a ^{3}He-gas position sensitive detector (PSD) installed at small, middle, high, and backward, and the resistor type photomultiplier tube (RPMT) [2] detector, as shown in Fig. 1. To perform ultra-small angle scattering measurements around q ≈ 5 × 10^{-4} at TAIKAN, the RPMT detector with a ZnS/^{6}LiF scintillator is used.

In this article, we report on the corrections for the neutron drop distance and rotation of the detector against the vertical direction, which are essential for performing ultra-small angle scattering measurements using the RPMT.

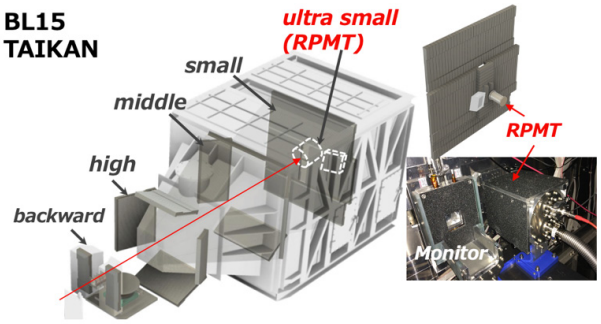

Figure 1. Detector layout at BL15 TAIKAN.

2. Correction of neutron drop distance

In ultra-small-angle scattering measurements at TAIKAN, the generated white neutrons from the neutron source arrive at the RPMT detector after passing through optical devices, such as collimators and slits. In addition, the range of wavelengths used in the TAIKAN is from about 1 to 15 Å (converted to velocity, from about 3955 m/s to 263 m/s, respectively), so the drop distance depends on the wavelength.

Figure 2 shows the results of the neutron drop distance, y as a function of wavelength for neutrons measured at TAIKAN. The results indicated that the y was longer for longer wavelengths than for shorter wavelengths. The y is described as $y = 1/2\, gt^2$ using the gravitational acceleration, g and the time of flight, t. The solid line is the fitting result using the equation described in Fig.2, where m_n and h are the neutron mass and Planck constant, respectively. As a result of the fitting, the flight distance, L was about 9.0 m. By taking these results into account, the correction for the wavelength dependence of the neutron drop distance was applied to the data reduction.

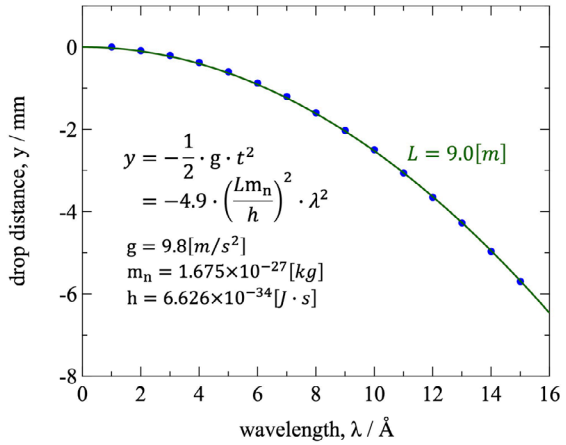

Figure 2. Neutron drop distance measured with RPMT as a function of wavelength.

3. Rotation correction of pixel position in RPMT

Since the detection area of the RPMT is a circular shape, it is, therefore, difficult to correctly install the detector position pixels (x, y) along the vertical direction in the vacuum scattering chamber of TAIKAN. In order to consider the rotation correction of the RPMT using the natural law of neutron vertical drop to gravity, the position of the direct beam center (x, y) for each wavelength is plotted in Fig. 3. The results revealed an alignment defect of about 3.3°. Based on these results, the correction for the pixel position (x, y) direction of the RPMT was implemented in the data reduction.

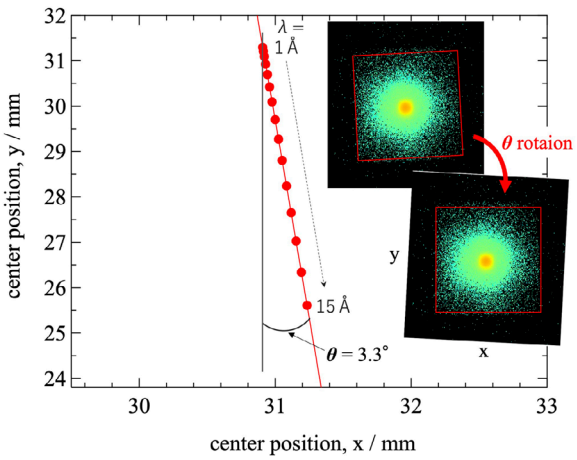

Figure 3. Rotational correction for the vertical direction in RPMT.

4. Example of measurement using RPMT

Figure 4 shows the measurement results of a spherical polystyrene powder with a diameter of 500 nm using PSD and RPMT at TAIKAN. The results demonstrated that $q_{min} = 4 \times 10^{-3}$ [Å^{-1}] could be measured using PSD and up to $q_{min} = 5 \times 10^{-4}$ [Å^{-1}] using RPMT. In particular, the RPMT data showed some oscillations of the particle correlation peak derived from the scattering function of the sphere, which could be measured with better resolution than the PSD data.

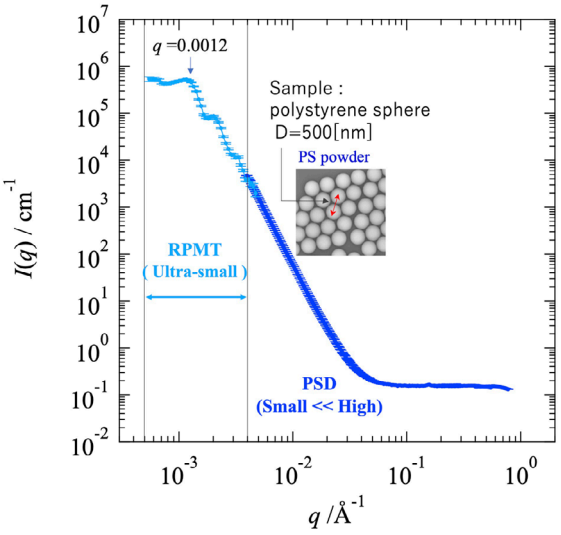

Figure 4. The measurement results of the polystyrene powder using RPMT and PSD.

5. Future plans

These two corrections are already integrated into the Utusemi [3] software system for data reduction and are also available for user experiments. We will continue to develop software for the reduction and analysis of measured data using TAIKAN.

In addition, since the photomultiplier (R3292) produced by Hamamatsu Photonics, which is used in the RPMT, has been discontinued since 2016, we have started to examine the introduction of a new high-resolution detector, the μ-NID detector [4].

References

[1] S. Takata, et al., JPS Conf. Proc., 8 036020 (2015).
[2] H. Iwase, et al., Physica B: Condensed Matter 551 (2018) 501–505.
[3] Y. Inamura, T. Nakatani, J. Suzuki, and J. Otomo, J. Phys. Soc. Jpn., 82 (2013) SA031.
[4] J. D. Parker et al., Nucl. Instr. and Meth. A 726, 155 (2013).

S. Takata[1], K. Hiroi[1], Y. Inamura[1], K. Ohishi[2], H. Iwase[2], Y. Kawamura[2], T. Morikawa[2], and M. Ueda[2]
[1]Neutron Science Section, Materials and Life Science Division, J-PARC Center; [2]Neutron Science and Technology Center, CROSS

Developments of Multi Incident-angle Neutron Reflectometry

1. Introduction

Neutron reflectometry (NR) is useful for investigating the structures of surfaces and buried interfaces. SOFIA is a horizontal-type neutron reflectometer constructed at BL16 of the MLF, J-PARC [1, 2]. Because of the high-flux beam of J-PARC, less than half an hour is required to obtain full Q-range data and only a few seconds for limited Q-range data for a sample with a diameter of 3 inches (76 mm). However, several hours are still required for a small sample such as 10 mm × 10 mm, which is the typical size of a sample used for X-ray reflectometry.

Currently, SOFIA employs a double-frame mode with a chopper rotation speed of 12.5 Hz (half of the neutron pulses generated at the source) to extend the Q-range using a wider wavelength band. This enables us to perform time-slicing measurements within a wider Q-region without incident-angle scans. However, the Q-region is still limited, even in the double-frame mode, owing to the limitation of the wavelength band, and the neutron flux is reduced by half because every other neutron pulse is cut by the chopper. To scan the entire Qz range without any angle scan and to enhance the time-slicing measurement ability with a short slicing time, SOFIA has been further upgraded since 2019. In this upgrade, multi-incident-angle neutron reflectometry (MI-NR) [3] will be applied, where two beams with different incident angles illuminate a sample and the two reflected beams are measured simultaneously by two individual detectors. Considering the merits and demerits of the double-frame mode mentioned above, we utilized a higher flux beam at 25 Hz for a higher incident angle and a wider wavelength beam at 12.5 Hz for a lower incident angle. Note that a longer exposure time is required for the measurement at a higher incident angle, i.e., a high Q_z range, because of the reduced reflectivity. Therefore, the reduction in the beam flux due to the double-frame mode at a lower incident angle has no effect on the total measurement time because it is limited by the statistics at a higher incident angle.

Because SOFIA is a running NR instrument for user experiments, we must maintain the performance of the conventional setup while upgrading the MI-NR setup. Therefore, the MI-NR setup was realized by modifying a conventional setup. Figure 1 shows the design of the optics used to achieve MI-NR. To obtain two beams with varying incident angles on a sample, one of the original beams with an incident angle of 2.22° is split into two by reflection with the top and bottom mirrors of a focusing guide. The two beams crudely form images at the virtual source slits and are transported by two pairs of precise focusing mirrors. At the sample position, the

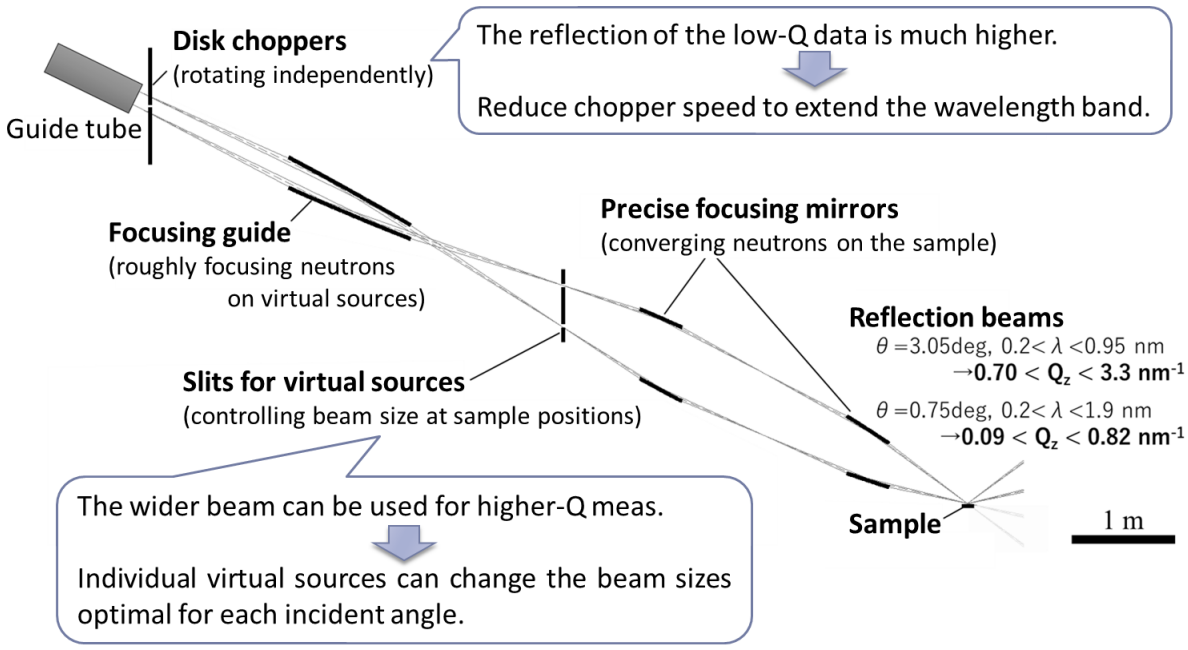

Figure 1. Design of optics for applying MI-NR at SOFIA.

two beams converge to a sample with incident angles against the horizontal surface of 0.75° and 3.05°, respectively. Moreover, users have the freedom to rotate their samples from a horizontal surface. The footprint sizes of the two beams on the sample are adjusted to the sample size by precisely adjusting the opening of the virtual-source slits, depending on the incident angle. The wavelength bands for the higher- and lower-angle beams are individually controlled by a double-disc chopper (DDC) to measure the double-frame and single-frame modes, respectively.

In this article, the concept and progress of the MI-NR upgrade and the upgrade of sample environments at SOFIA are reported.

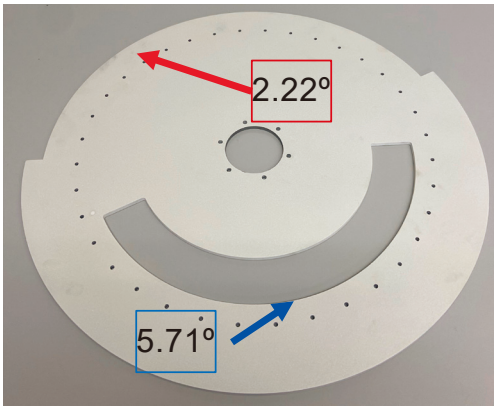

Figure 3. Disc with two openings for the 2.22º and 5.71º beams at the edge and the middle of the disc, respectively.

2. MI-NR

2.1 Beam transport optics

Beam transport optics composed of a focusing guide and DDC were installed at the exit of the guide in 2021 (Fig. 2). The incident beams from the chopper are separated into upper and lower beams by a separator, and the focusing guide tubes are irradiated as explained earlier.

Because two beams with different tilt angles (2.22° and 5.71°) are acceptable at SOFIA, the choppers have two windows: one at the edge to realize the MI-NR at the 2.22° beam, and the other at the middle of the disk to cut the beam with a tilt angle of 5.71° to illuminate the free-liquid surface with a high incident angle (Fig. 3). The high shielding performance was expected as follows: the transmission at 0.18 nm is 1.5×10^{-4} and is less than 10^{-5} above 0.2 nm.

The first chopper discs were fabricated from circular aluminum plates coated with Gd_2O_3 paint. However, the painting was peeled off owing to the centrifugal force. We then developed and installed new discs created from circular borated aluminum plates (B_4C 22 wt%, 4.5 mm thick). To achieve high shielding performance, the plates were coated with Gd paint (Gd_2O_3 40 wt%, 0.2 mm thick on both sides). The transmission was measured as 1.5×10^{-4} at 0.18 nm and less than 10^{-5} above 0.2 nm. The DDC with modified discs has been operational and utilized for double-frame mode NR measurements since November 2023.

A focusing guide was installed in the middle of

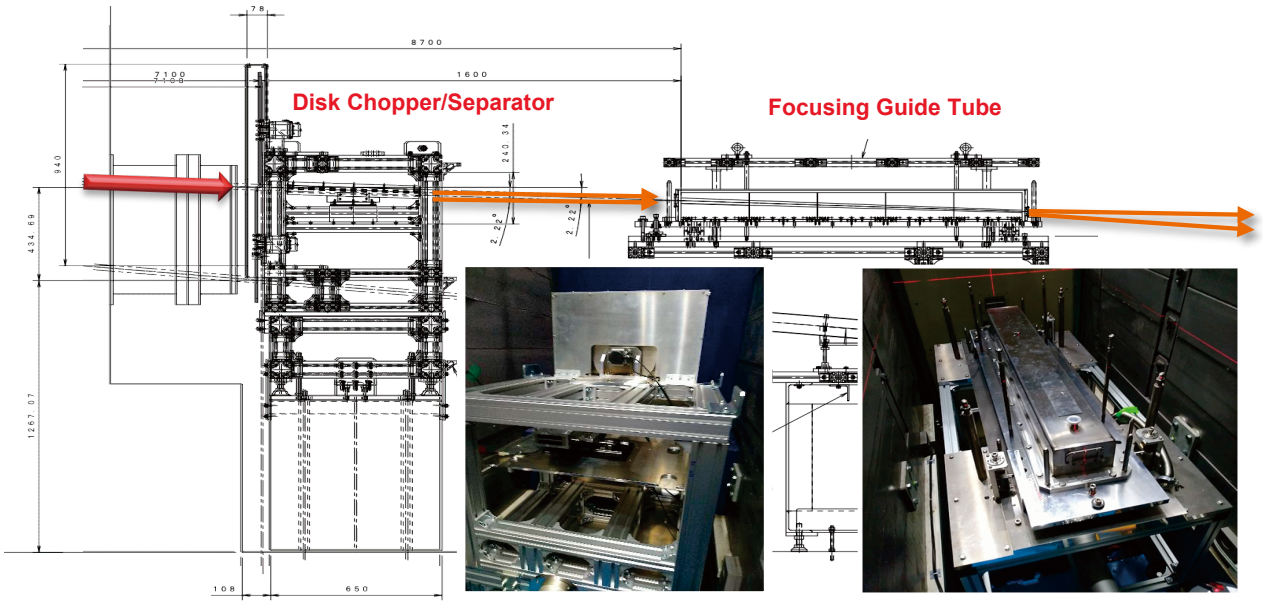

Figure 2. Beam transport optics of MI-NR setup consisting of the double disc chopper and focusing guide. The thick red arrow represents the original 2.22º beam. This upstream optics introduce separated beams to the virtual neutron sources.

the choppers and virtual sources to transport the two beams at the chopper position to the virtual sources 4500 mm from the choppers. The guide is 1300 mm in length and is equipped with $3Q_c$ supermirrors, in which the top and bottom shapes are ellipses with foci at the upper and lower halves of the beam at the chopper position and the lower and upper exits at the virtual sources, respectively. A separator was placed to avoid crosstalk between the two beams after the chopper, in which an iron plate was placed at the center to cut fast neutrons, and two $2.5Q_c$ supermirrors on glass were placed on the top and bottom sides of the iron plate to guide neutrons.

Figure 4 shows the beam profiles of the virtual neutron source. The distance between the upper and lower beams was 34 mm, which was almost equal to the designed value. Therefore, we can conclude that the guide tube construction is sufficiently precise.

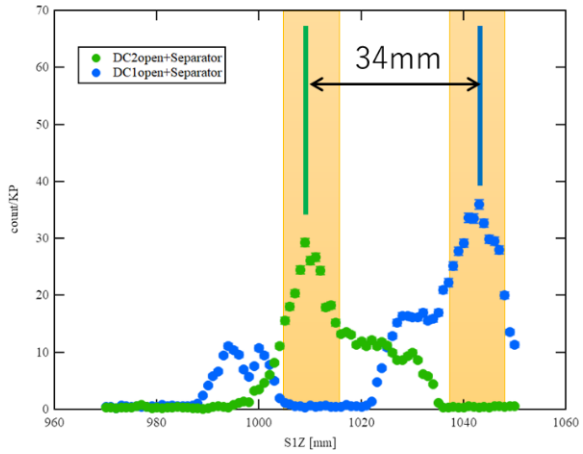

Figure 4. Observed beam profiles of the separated incident beams at the virtual neutron source.

2.2 Precise focusing mirrors

In 2022, a slit system with two apertures was installed to create virtual sources with optimized gaps depending on the incident angle and sample size. In addition, a set of precise focusing mirrors was installed to transport neutrons from virtual sources to the sample position with different incident angles.

The slits for the virtual neutron source were created from borosilicate glass with Gd_2O_3 painting and set parallel at a precision better than 25 μrad. All parts of the precise focusing mirrors were manufactured using ultra-precision cutting machines. Two sets of opposing mirrors were installed upstream and downstream of the beamline. The tilt errors of the mirrors were estimated to be between 30 and 50 μrad in FWHM using a laser interferometer.

Figure 5 shows the beam profiles at the sample position. A misalignment of 60 μm was observed, but the beam centers could be adjusted by tuning the virtual neutron source.

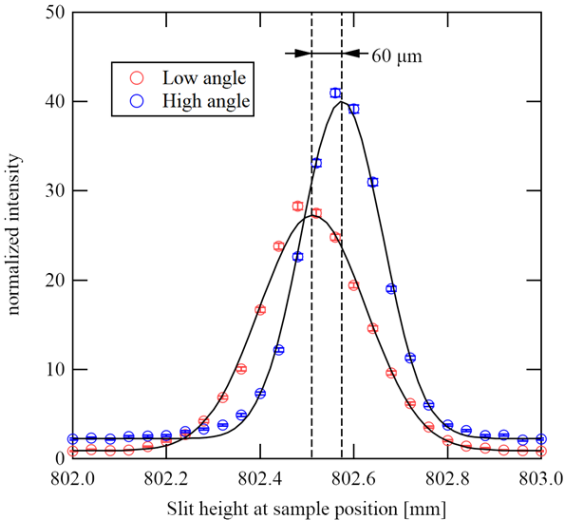

Figure 5. Observed beam profiles of the separated incident beams at the sample position.

2.3 Detectors

The former position-sensitive detector, the resistance division photomultiplier tube (RPMT) [4], with a ZnS/^{6}LiF scintillator detected neutrons using a cylindrical position-sensitive photomultiplier tube. However, the RPMT detector had a large dead area, making it geometrically impossible to measure two beams with incident angles differing by 2.3° at 1.3 m from the sample. The beam deviation at the detector position was 52 mm, and the two beams could not be measured by the two RPMT detectors at these centers. To address this problem, we evaluated a new detector utilizing a flat-panel multi-anode-type photomultiplier tube (FRP) [5, 6] with a detection area of 48 mm × 48 mm as a replacement for the RPMT detector. In 2020, two FRP detectors replaced the previous detectors. A significant advantage of this detector is that it requires only modifications to the existing data acquisition (DAQ) circuit.

As shown in Fig. 6 (left) (excerpt from [6]), the detection efficiency almost doubled. The spatial resolution of the FRP detector was approximately 0.6 mm at the center and 1 mm for the RPMT (see Fig. 6 (right) (excerpt from [6])). We also confirmed that these detectors can simultaneously measure two beams transported by an optical system. The position dependence of detection efficiency and spatial distortion were corrected based

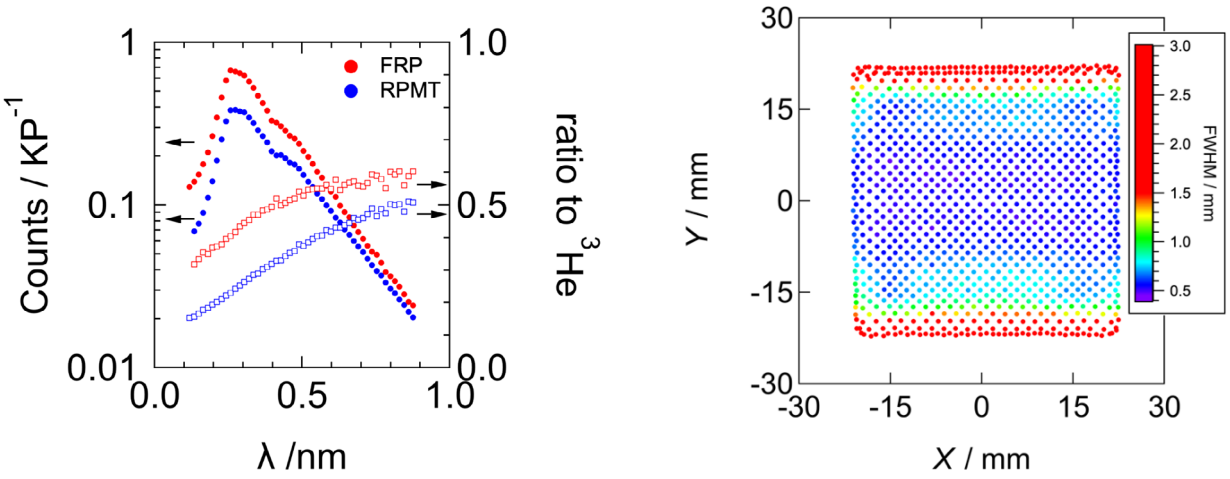

Figure 6. (Left) Comparison of the counting rates captured with the RPMT and FRP detectors depending on neutron wavelength [6]. (Right) Evaluated spatial resolution of the FRP detector depending on the position [6].

on the measured data.

2.4 Summary and future perspectives

The necessary items for achieving MI-NR were installed, and the alignment of all components was attempted. The focusing guide, DDC, the virtual-source slit system, and the FRP detector pair are operational. However, a set of precise focusing mirrors can be manufactured using a refined procedure and fixation. The installation and alignment of the new focusing mirrors will be attempted in FY2024, and the first MI-NR measurement with a sample will be tested.

References

[1] N. L. Yamada et al., Euro. Phys. J. Plus, 44 (2011) 9424.
[2] K. Mitamura et al., Polymer J., 45 (2013) 100.
[3] N. L. Yamada et al., J. Appl. Crystallogr., 53 (2020) 1462–1470.
[4] K. Hirota et al., Phys. Chem. Chem. Phys. 7 (2005) 1836–1838.
[5] S. Satoh, Plasma Fusion Res. 13 (2018) 3–6.
[6] F. Nemoto et al., Nucl. Instrum. Methods Phys. Res. Sect. A, 1040 (2022) 166988.

Masako Yamada[1,2], Norifumi L. Yamada[1,2], Fumiya Nemoto[3], Setsuo Sato[2], and Hideki Seto[1,2]
[1]Neutron Science Section, Materials and Life Science Division, J-PARC Center; [2]Institute of Materials Structure Science, KEK; [3]National Defense Academy

Current Status of SHARAKU: Polarized Neutron Reflectometer

1. Introduction

SHARAKU, installed at BL17 in Materials and Life Science Experiment Facility (MLF), is a neutron reflectometer with vertical sample geometry, which has been used to investigate nanometric structures in thin film samples [1, 2]. Since SHARAKU has a pair of a spin polarizer and a flipper for both of incident and reflected/scattered neutrons, it can be employed to analyze a magnetic structure of magnetic thin films using polarized neutron reflectivity (PNR) [3, 4]. Traditionally, SHARAKU has utilized a zero-dimensional (0D) ^{3}He tube detector to measure the neutron intensity reflected from sample films. This low-noise detector allows specular NR measurements of reflectivity as low as 10^{-7}, however, it cannot be used for an off-specular measurement. To overcome this limitation and expand SHARAKU's capabilities, the installation of a two-dimensional position-sensitive neutron detector became necessary. In recent years, we have made significant progress in developing divergent beams and position-sensitive data reduction techniques using a Multi-Wire Proportional Counter (MWPC) [5]. These advancements aim to substantially reduce measurement times while maintaining high data quality. With proton beam injection at 700 kW at the MLF, un-polarized measurements of typical 2″ diameter organic thin films can be completed within 2 hours per one condition. However, for magnetic thin films with dimensions of 15 mm × 15 mm, measurement times increase substantially. A single condition requires about 6 hours for 2-channel PNR, and about 9 hours for 4ch-PNR. This extended measurement time for magnetic samples poses a significant limitation on the throughput and efficiency of experiments. Addressing this issue is crucial for expanding the capabilities of SHARAKU in magnetic materials research and fully utilizing the potential of the PNR techniques. Therefore, we developed an application for angular divergence data reduction to PNR.

2. Data reduction system for specular NR profile measured by MWPC

The neutron beam has a finite divergence of an incident angle in the reflectometry measurement. The increase in the beam divergence, $\Delta\theta$ (shown in Fig. 1a), increases the intensity of the reflection signal. However, the 0D detector detects the sum intensity at the reflection angle range from $\theta - \Delta\theta/2$ to $\theta + \Delta\theta/2$, resulting in the decrease in the Q resolution of the obtained NR profile. On the other hand, the position sensitive detection by MWPC can resolve the divergence of the reflected neutron beam. Figure 1b shows the reflection intensity dependent on the reflection angle θ (X position) and the wavelength λ (time-of-flight: TOF) of the reflected neutron from 30 nm thin film of Permalloy on a silicon wafer at an incident angle of 1.6 degrees with a divergence, $\Delta\theta/\theta = 15.0\%$. This indicates that the reflected TOF profile is dependent on the reflection angle. In SHARAKU, a sample is mounted vertically; therefore, the neutron beam is spread in the X direction due to the large incident angle dispersion. The conversion from X-TOF vs intensity to momentum transfer Q space is done in the same way as in the article by Cubitt et al. [6]. For SHARAKU, the angular divergence correction is effective in the range of 1° to 4° angle of incidence. The reason for that is because the spatial resolution of the MWPC is insufficient for angles of less than 1°, and the aperture angle of MWPC is limited for angles of less than 4°.

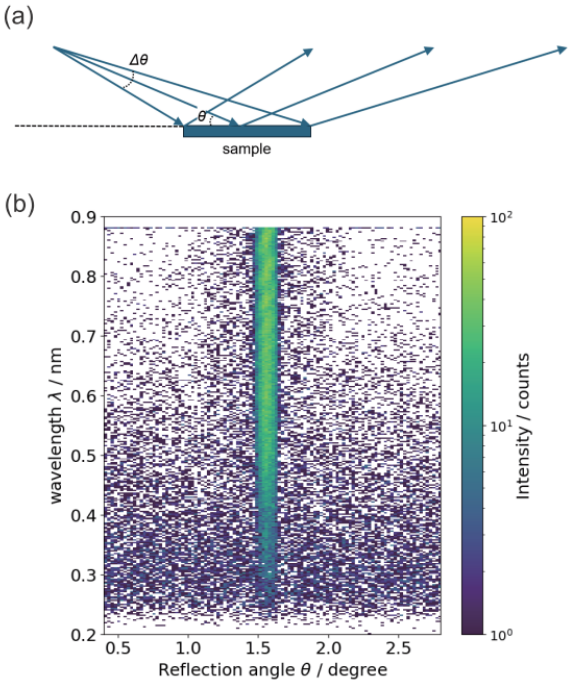

Figure 1. (a) Illustration of the reflection of a neutron beam at an incident angle θ and a divergence $\Delta\theta$, and (b) relation between the reflection angle θ (X position) and wavelength λ (TOF). Red dot lines show the extent of data processing.

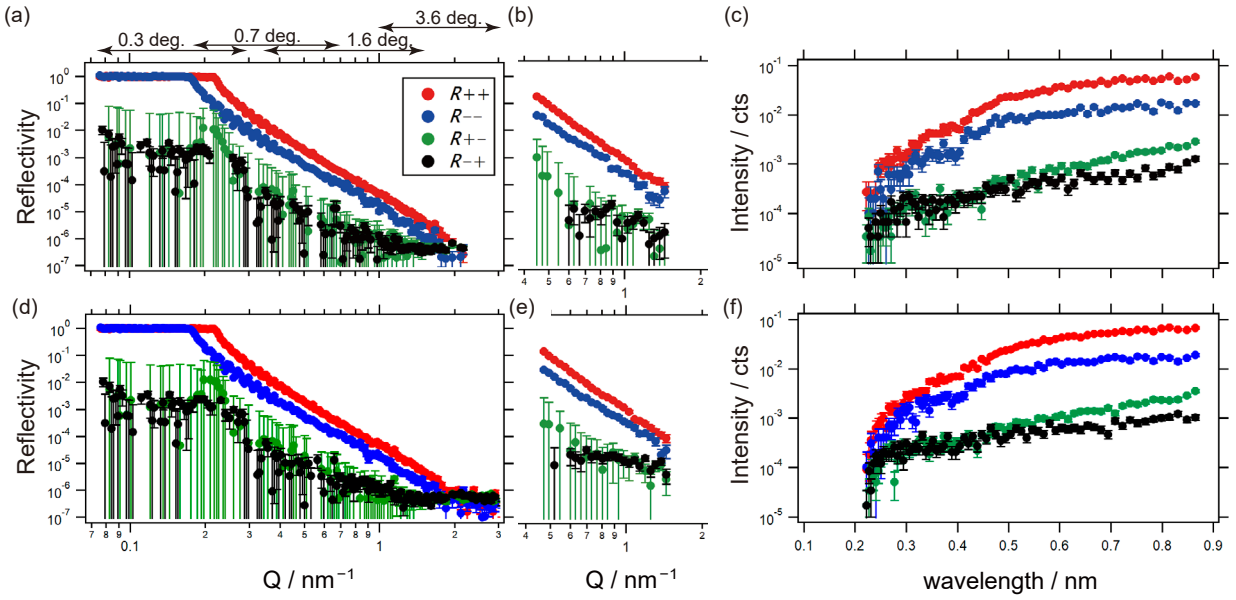

Figure 2. PNR measurement results for a 30 nm thick Permalloy magnetic thin film. (a)-(c) Conventional data processing with $\Delta\theta/\theta = 6.6\%$. (d)-(f) Data processing including angular divergence correction with $\Delta\theta/\theta = 15.0\%$.

3. Result

Figure 2 compares the PNR results processed with and without angular divergence correction. The high-Q region ($Q > 2$ nm^{-1}) in panel (d) shows improved data quality compared to panel (a). The reflectivity profile in panel (e) exhibits smaller error bars than panel (b), also indicating enhanced data quality. These improvements are attributed to the increased number of scattered neutrons processed in the measurement data with $\Delta\theta/\theta =$ 15.0%, as shown in panel (f) compared to panel (c). This results in a 1.2 times higher intensity for R+− in the TOF spectrum and a 1.1 times higher signal-to-noise ratio (S/N).

4. Summary

The angular divergence correction system developed for PNR measurements using MWPC has demonstrated significant improvements in data quality, particularly in the high-Q region. With an increased angular divergence of $\Delta\theta/\theta = 15.0\%$, we achieved a 1.2 times higher intensity for R+− in the TOF spectrum and a 1.1 times better signal-to-noise ratio compared to conventional measurements. This enhancement enables more efficient data collection at higher Q values while maintaining resolution. This improvement is particularly significant for magnetic thin film samples, where measurement times have traditionally been a limiting factor. The combination of MWPC detection and angular divergence correction provides two key advantages: enhanced Q resolution through precise position-sensitive detection, and reduced measurement times through increased neutron acceptance.

Future work will focus on validating this method across a broader range of sample types and experimental conditions. Based on the current results, we anticipate that this system will significantly improve the operational efficiency of SHARAKU, particularly for time-intensive measurements such as 4ch-PNR of magnetic thin films.

References

[1] K. Akutsu et al., *Applied Sciences* **12**, 1215 (2022).
[2] W. Yoshimune et al., *ACS Appl. Mater. Interfaces* **14**, 53744 (2022).
[3] R. Akiyama et al., *J. Phys. Chem. Lett.* **13**, 8228 (2022).
[4] S. Suturin, et al., *Materials Today Communications* **33**, 104412 (2022).
[5] H. Aoki et al., *MLF annual report* 102 (2017).
[6] R. Cubitt et al., *J Appl Crystallogr* **48**, 2006 (2015).

T. Hanashima[1], H. Aoki[2,3], S. Kasai[1], K. Akutsu[1], N. Miyata[1], K. Soyama[4], and D. Yamazaki[5]
[1]*Neutron Science and Technology Center, CROSS;* [2] *Neutron Science Section, Materials and Life Science Division, J-PARC Center;* [3]*Institute of Materials Structure Science, KEK;* [4]*Administration and Operations Support Division, J-PARC Center;* [5]*Neutron Instrumentation Section, Materials and Life Science Division, J-PARC Center*

Status of SENJU 2023

1. Introduction

SENJU is a TOF single-crystal neutron diffractometer designed for precise crystal and magnetic structure analyses under multiple extreme environments, such as low-temperature, high-pressure, and magnetic-field, as well as for taking diffraction intensities of small single crystals with a volume of less than 1.0 mm^3 down to 0.1 mm^3 [1]. Since the operation of SENJU started in 2012, our instrument group has carried out continuous commissioning and upgrades.

In 2023, we designed a 'fan-like detector arrangement' as a detector upgrading plan of SENJU, and updated a data-processing software, STARGazer-Online. In addition, we also report on the purposes of the instrument beam-time for SENJU.

2. Conceptual design of fan-like detector arrangement

The area detector is one of the most essential components of a single-crystal neutron diffractometer, and the evolution of the detector directly improves the performance of the diffractometer. In 2023, our SENJU group implemented a plan to upgrade the 36 area detectors arranged around the vacuum sample chamber of SENJU. Each of those area detectors has a 256 mm width and 256 mm height detective area. At SENJU, three detectors are stacked vertically to form one unit, and 12 of those units are lined up horizontally. In this upgrade plan, those 36 detectors will be replaced with nine area detectors whose detective area has a width of 512 mm and a height of 768 mm.

The main feature of these new area detectors is that the frame surrounding the detection surface is asymmetrical, with one frame being skinny (Fig. 1). This plan will attempt to eliminate the gap between the adjacent detectors by arranging them with these asymmetrical frames in such a way that they partially overlap. The present detector arrangement and the proposed new detector arrangement are shown in Fig. 2. We call the new detector arrangement a 'fan-shaped detector arrangement.'

In the present detector arrangement, there is a non-negligible gap around each detector (Fig. 2a). Therefore, not only the diffraction data corresponding to the gap region but also the data detected at the edge region of each detector cannot be used for analysis, which reduces diffraction measurement efficiency. In the new detector arrangement, the gap between the vertically stacked detectors is eliminated by the large area detectors, and

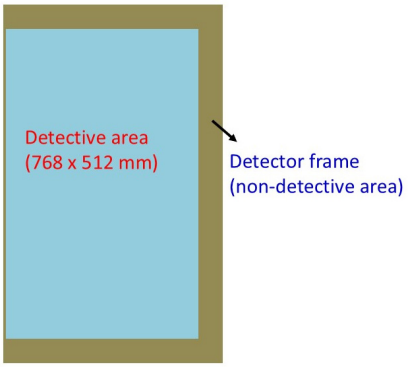

Figure 1. Conceptual design of the newly developed large area detector.

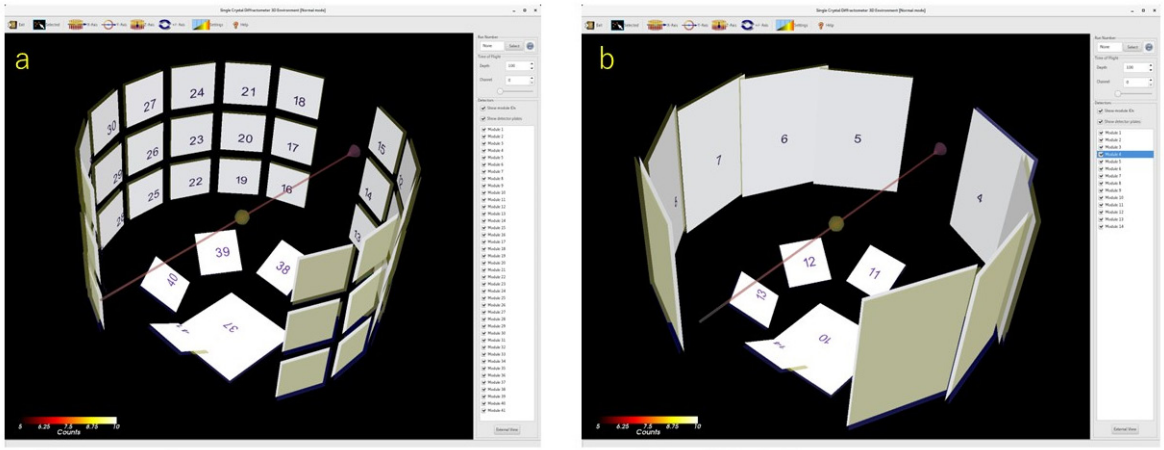

Figure 2. (a) Present detector arrangement of SENJU. (b) Concept of the 'fan-like' arrangement of the large area detectors.

the fan-shaped arrangement minimizes the gap between the adjacent detectors (Fig. 2b). Furthermore, if the data from the overlapping areas between the adjacent detectors can be processed appropriately, the gaps between the adjacent detectors can also be eliminated.

This detector upgrade project is now ongoing as a multi-year plan. The measurement efficiency of SENJU is expected to double with this upgrade.

3. Upgrading of STARGazer-Online

STARGazer-Online (SGO) is a remote data processing and data-visualization application for SENJU that works on web browsers such as Firefox, Chrome, and Safari. We have been continuously upgrading SGO to keep up with the latest scientific research.

In SENJU, the replacement of the present area detectors with larger ones is in progress. In FY2022, one area detector with a four times larger detection area than the conventional one was installed at the bottom of the sample chamber. In addition, over the next few years, nine area detectors with a six times larger detection area than the conventional one are scheduled to be installed. On the other hand, at SGO, the visualization of diffraction data by the newly installed large area detector was not possible because it could not visualize the diffraction data of area detectors with different detective area sizes and different pixel numbers simultaneously. Therefore, with the introduction of the large area detectors, we upgraded SGO to make the simultaneous visualization of the detectors with different detective area sizes possible. As a result of this upgrade, SGO can now correctly display diffraction data even when rectangular area detectors of any size and number of pixels are mixed.

4. Use of the instrument beam time

In 2023, the instrument beam time was used mainly for measurements of standard samples, and a vanadium-nickel alloy for calibration of the detector efficiency.

Reference

[1] T. Ohhara et al., J. Appl. Cryst., 49 120 (2016).

T.Ohhara[1], R. Kiyanagi[1], A. Nakao[2], K. Munakata[2], Y. Ishikawa[2], K. Moriyama[2], I. Tamura[3], K. Kaneko[1], T. Nakamura[4], K. Toh[4], K. Sakasai[4], and T. Hosoya[4,5]

[1]Neutron Science Section, Materials and Life Science Division, J-PARC Center; [2]Neutron Science and Technology Center, CROSS; [3]New Research Reactor Promotion Office, JAEA; [4]Neutron Instrumentation Section, Materials and Life Science Division, J-PARC Center; [5]Graduate School of Science and Engineering, Ibaraki University

Research Trends and Highlights in TAKUMI 2023

1. Introduction

TAKUMI is a neutron diffractometer dedicated for research in engineering materials sciences, installed at Beamline 19 in the MLF of J-PARC. TAKUMI has been used to conduct research on various materials at a high level and with great precision, from the fundamental stage to phases nearing practical application. This includes studies of microstructural evolutions during cooling and/or heating, deformation across a temperature range from 15 K to 1373 K in structural and functional materials, microstructural changes during thermo-mechanical processes, and residual stress scanning of engineering components — all yielding excellent results. These successes have been made possible by the high quality of diffraction patterns, enabling detailed analysis of Bragg peaks in neutron diffraction to reveal crucial structural information, such as internal stresses, phase conditions, dislocations, and texture. Additionally, a variety of sample environmental devices have been developed and employed to facilitate these experiments.

2. Research trends

The beam operation was stable throughout FY2023, and TAKUMI ran with minimal issues. This stability enabled us to conduct all accepted proposals, along with some reserved ones. Experiment statistics are categorized by experiment and material type (based on allocated beam time) and by principal investigator (PI) affiliation (based on proposal numbers), as shown in Fig. 1. The percentage of low-temperature loading experiments increased significantly to 60% from 42% in the previous fiscal year, indicating a shift in research trends at TAKUMI. There was also an increase in the studies of cryogenic deformation of high-entropy alloys, resulting in a rise in the percentage of other metals. Notably, studies involving irons and steels, as well as light metals, remained active. The number of proposals from overseas PIs slightly increased in FY2023, likely due to the performance of the MLF neutron source and the capabilities of the TAKUMI instrument. However, the number of proposals from industrial PIs remained low.

Thanks to our users and collaborators, 25 peer-reviewed original research papers, 1 review article, and 1 proceedings paper based on data from TAKUMI were published in 2023. Additionally, oral and poster presentations using TAKUMI data were delivered at numerous national and international conferences, workshops, and seminars. A press release was issued for a paper on magnesium alloys [3], which was subsequently featured in 4 newspapers. One peer-reviewed paper received the Sawamura Award from The Iron and Steel Institute of Japan, and three posters were awarded Best Poster for Young Scientists at the Japan Institute of Metals and Materials 2023 Autumn Meeting.

The publication statistics from TAKUMI (excluding oral and poster presentations) are categorized by experiment and material type, as shown in Fig. 2. Over 95% of the publications are based on *in situ* observation experiments, with room-temperature loading experiments accounting for 59%, making them the current majority. However, as low-temperature loading experiments have become the majority, as indicated in Fig. 1, publication trends may soon also shift towards low-temperature experiments. While publications based on experiments using irons and steels remain the majority, the use of light metals and other metals is expected to rise, reflecting the experimental distribution by material type shown in Fig. 1.

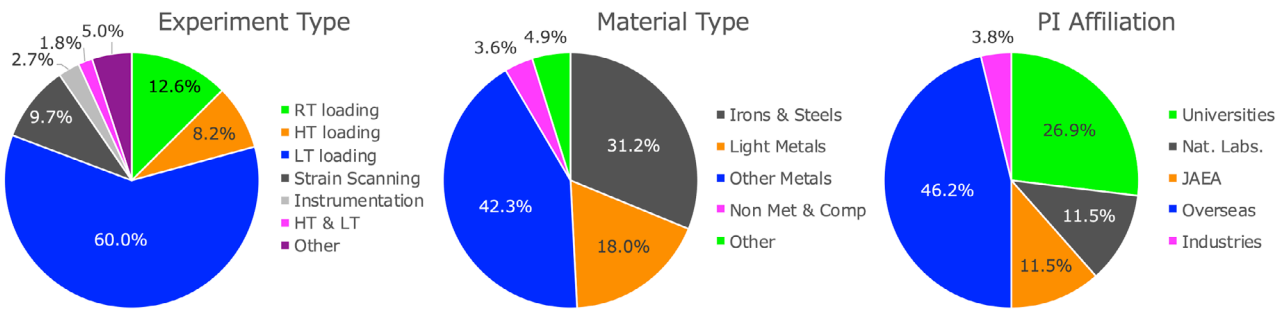

Figure 1. Experiment statistics for FY2023 categorized by experiment and material type (based on allocated beam time) and by principal investigator (PI) affiliation (based on proposal numbers).

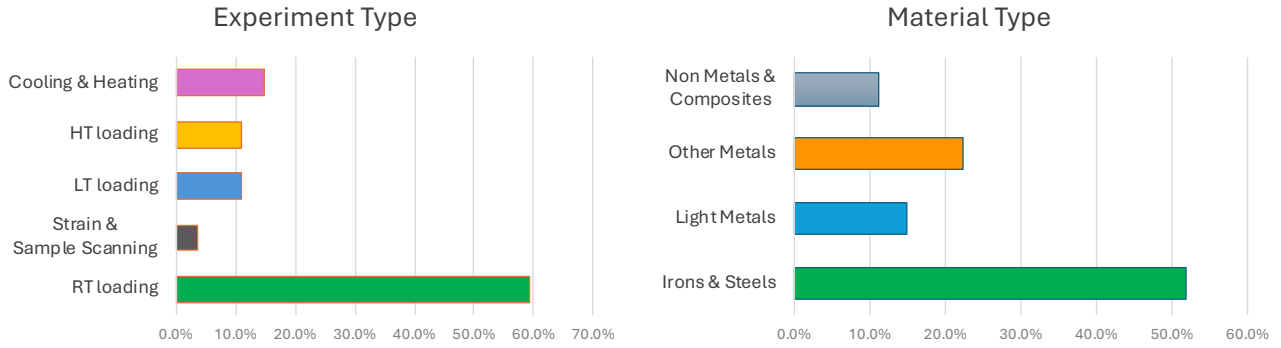

Figure 2. Publication (peer-reviewed original research papers, review articles, and proceedings) statistics for FY2023 categorized by experiment and material type.

3. Some highlights

Thanks to our users and collaborators, the scientific quality and practical relevance of the 2023 publications have been exceptionally high. However, due to limited space, only a few selected highlights are presented below.

"**Unexpected dynamic transformation from α phase to β phase in zirconium alloy revealed by in-situ neutron diffraction during high temperature deformation**", by B. Guo et al. [1]: Dynamic transformation from the alpha (HCP) to beta (BCC) phase in a zirconium alloy was revealed using *in situ* neutron diffraction during hot compression. This transformation was unexpectedly observed during isothermal compression at 900°C and 950°C (within the alpha + beta two-phase region) and strain rates of 0.01 s^{-1} and 0.001 s^{-1}, despite the equilibrium two-phase state being established prior to compression. The transformation was accompanied by the diffusion of Sn from the beta to the alpha phase, resulting in changes to lattice parameters and a distinctive microstructure in the alpha grains.

"**Lattice parameters of austenite and martensite during transformation for Fe–18Ni alloy investigated through in-situ neutron diffraction**", by W. Gong et al. [2]: *In situ* neutron diffraction combined with dilatometry measurements was conducted during martensitic transformation and subsequent cyclic tempering of an Fe–18Ni alloy. The phase strains, calculated from lattice parameter variations, showed a hydrostatic compressive strain in austenite and a tensile strain in martensite as the martensitic transformation progressed during continuous cooling or isothermal holding. However, the phase stresses in austenite and martensite, estimated from these strains, did not adhere to the stress balance law when dense crystal defects were present. Once these defects were removed through appropriate tempering, the stress balance law was restored. At the same time, the phase stresses in austenite and martensite reversed, revealing their true nature.

"**Strengthening of αMg and long-period stacking ordered phases in a Mg-Zn-Y alloy by hot-extrusion with low extrusion ratio**", by S. Harjo et al. [3]: In *in situ* neutron diffraction experiments, an as-cast sample and two hot-extruded $Mg_{97}Zn_1Y_2$ alloy samples with different extrusion ratios (R) were tested to study how microstructural changes in the HCP αMg matrix (soft phase) and LPSO phase (hard phase) affect mechanical properties. Hot extrusion enhanced the strength of both phases. At R = 5.0, partial dynamic recrystallization in α-Mg created a bimodal structure, improving yield strength due to dislocation accumulation, texture development, and grain refinement. However, at R =12.5, further recrystallization and grain growth reduced αMg yield strength but improved elongation. Meanwhile, LPSO strength increased with R, due to kink band formation and stronger texture. At R =12.5, the strength gain in LPSO offset the decrease in αMg, maintaining the alloy's high tensile strength.

"**High-density nanoprecipitates and phase reversion via maraging enable ultrastrong yet strain-hardenable medium-entropy alloy**", by H. Kwon et al. [4]: Maraging steels are known for ultrahigh strength and good fracture toughness due to their lath martensite structure with high-density nanoprecipitates. In this work, a novel Fe-based medium-entropy alloy ($Fe_{60}Co_{25}Ni_{10}Mo_5$ at.%) was designed, inspired by maraging steels. After a single-step 10-minute aging at 650°C, the alloy developed a lath martensite structure with a high density of $(Fe, Co, Ni)_7Mo_6$ nanoprecipitates and a reverted FCC phase, resulting in a yield strength exceeding 2 GPa. The alloy also achieved an ultimate tensile strength of ~2.2 GPa and 6% uniform ductility, benefiting from deformation-induced martensitic

transformation of the FCC phase.

"**Strong work-hardenable body-centered-cubic high-entropy alloys at cryogenic temperature**", by X. Wen et al. [5]: Body-centered cubic (BCC) metals and alloys are usually brittle with limited strain hardening capability at cryogenic temperatures due to the restricted dislocation nucleation and mobility. From *in situ* cryogenic loading neutron diffraction, it is found that decrease of the Nb content in the $TiZrHfNbTa_{0.2}$ high-entropy alloys (HEAs) can facilitate multiple deformation mechanisms, i.e., dislocation planar slip, strain-induced phase transformations and twinning, at the cryogenic temperature of 77 K due to the decreased phase stability. The $TiZrHfNb_{0.3}Ta_{0.2}$ HEA, notably, showed pronounced strain hardening capability and exceptionally high uniform elongation of about 25% with no sign of ductile-brittle transition.

References

[1] B. Guo et al., Acta Mater. **242**, 118427 (2023).
[2] W. Gong et al., Acta Mater. **250**, 118860 (2023).
[3] S. Harjo et al., Acta Mater. **255**, 119029 (2023).
[4] H. Kwon et al., Acta Mater. **248**, 118810 (2023).
[5] X. Wen et al., Scripta Mater. **231**, 115434 (2023).

S. Harjo[1], T. Kawasaki[1], W. Gong[1], T. Ito[1], and K. Aizawa[2]
[1]Neutron Science Section, Materials and Life Science Division, J-PARC Center; [2]Materials and Life Science Division, J-PARC Center

The Current Status of the Versatile Neutron Diffractometer, iMATERIA

1. Introduction

Ibaraki Prefecture, local government of Japan's area where the J-PARC sites are located, has decided to build a versatile neutron diffractometer (IBARAKI Materials Design Diffractometer, iMATERIA [1]) (fig. 1) to promote industrial applications for the neutron beam in J-PARC. iMATERIA is planned to be a high-throughput diffractometer that could be used by materials engineers and scientists in their materials development work, including chemical analytical instruments.

The applications of neutron diffraction in materials science are (1) to analyze the structure of newly developed materials, (2) to clarify the correlation between structures and properties (functions), and (3) to clarify the relation between structural changes and improvements of functions, especially for practical materials. A diffractometer with super high resolution is not required to achieve those goals. The match of features like intermediate resolution around $\Delta d/d = 0.15\%$, high intensity and wide d coverage is more important.

This diffractometer is designed to look at a decoupled-poisoned liquid hydrogen moderator (36 mm, off-centered) (BL20), and it has an incident flight path (L1) of 26.5 m, with three wavelength selection disk-choppers and straight neutron guides with a total length of 14.0 m. The instrumental parameters are listed in Table 1. There are four detector banks, including a low-angle and small-angle scattering detector bank. The angular coverage of each detector bank is also shown in Table 1. The

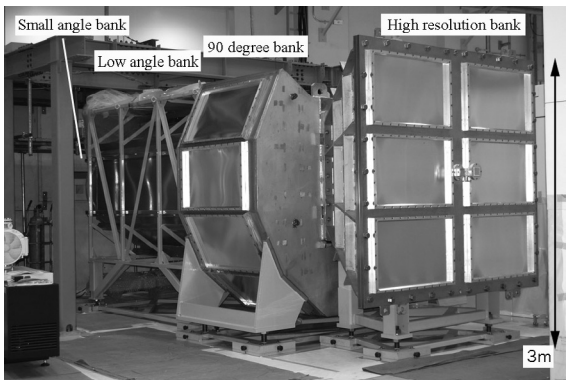

Figure 1. IBARAKI Materials Design Diffractometer, iMATERIA without detector for each bank and instrument shielding. The BS bank, 90-degree bank and low-angle bank can be seen from right to left. The small-angle detector bank, which is not shown in the picture, is situated in the low-angle vacuum chamber (left-hand side of the picture).

Table 1. Instrumental parameters of iMATERIA. L2 is the scattered flight path. The d-range (q-range) for each bank is the maximum value for 2-measurement mode.

L1	26.5 m	
Guide length		Total 14 m (3section)
Position of Disk choppers		7.5 m (double)
		11.25 m (single)
		18.75 m (single)
High	2θ	$150^\circ \le 2\theta \le 175$
Resolution	L2	2.0 – 2.3 m
Bank	d-range	$0.09 \le d\ (A^\circ) \le 5.0^\circ$
Special	2θ	$80^\circ \le 2\theta \le 100^\circ$
Environment	L2	1.5 m
Bank	d-range	$0.127 \le d\ (A^\circ) \le 7.2$
Low	2θ	$10^\circ \le 2\theta \le 40^\circ$
Angle	L2	1.2 – 4.5 m
Bank	d-range	$0.37 \le d\ (A^\circ) \le 58$
Small	2θ	$0.7^\circ \le 2\theta \le 5^\circ$
Angle	L2	4.5 m
Bank	q-range	$0.007 \le q\ (A^{\circ -1}) \le 0.6$

rotation speeds for the disk-choppers are the same, with a pulse repetition rate of 25 Hz for most applications (SF mode). In this case, the diffractometer covers $0.18 < d$ (Å) < 2.5 with $\Delta d/d = 0.16\%$ and covers $2.5 < d$ (Å) < 800 at three detector banks of 90-degree, low-angle and small-angle with a gradually changing resolution. When the speed of the wavelength selection disk-choppers is reduced to 12.5 Hz (DF mode), we can access a wider d-range, $0.18 < d$ (Å) < 5 with $\Delta d/d = 0.16\%$, and $5 < d$ (Å) < 800 with gradually changing resolution with doubled measurement time compared to the SF mode.

2. Current status

All of the four banks, high-resolution bank (BS bank), special environment bank (90-degree bank), low-angle bank and small-angle bank, are operational. It takes about 5 minutes (in DF mode) to obtain 'Rietveld-quality' data in the BS bank at 900 kW beam power for about 1 g of standard oxide samples.

Figure 2 shows a typical Rietveld refinement pattern for $LiCoO_2$ sample, cathode material for lithium-ion battery (LIB), at the BS bank by the multi-bank analysis function of Z-Rietveld software [2]. It takes 7 min in DF mode to collect the available Rietveld data, due to the high neutron absorption cross section for natural Li ($\sigma_s^{Nat} = 70$ barn).

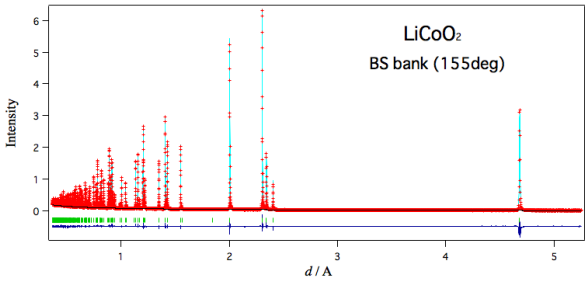

Figure 2. Rietveld refinement pattern for $LiCoO_2$ at the BS bank of iMATERIA.

3. Sample environments

The automatic sample changer is the most important sample environment for high-throughput experiments. Our automatic sample changer [3] consists of a sample storage, elevating system of two lines, two sets of pre-vacuum chambers and a sample sorting system. We can handle more than 600 samples continuously at room temperature (RT) without breaking the vacuum of the sample chamber.

The vanadium-furnace (~900°C), the gas flow furnace (~1000°C), and the 4K and 1K cryostats are ready for experiments.

The rapid heating/quenching furnace with automatic sample changer (RT – 1273 K with heating speed 10 K/s and cooling speed > 20 K/s) [4] and the universal deformation testing machine (max loading 50 kN with RT – 1273 K) [5] are available for texture measurements.

The in-operando charge and discharge measurement system for LIB with a sample changer is available in cylindrical, coin and laminated types of batteries.

4. Performance evaluation of local structure analysis

The pair distribution function $g(r)$ derived by Fourier transform of the static structure factor $S(Q)$ obtained from diffraction measurements can represent disordered atomic arrangements [6, 7]. Since the real-space resolution of $g(r)$ is proportional to the inverse of maximum value of the magnitude of the elastic scattering vector $Q = 4\pi\sin\theta/\lambda$ (2θ: scattering angle, λ: wavelength), iMATERIA, which can reach Q_{max} up to 90 $Å^{-1}$, is suitable for experiments to reveal local structures disrupted from crystal structures, as is the high intensity total scattering instrument NOVA. TiO_2 powder was used to evaluate the performance of local structure analysis.

Figure 3 shows the results refined by PDFgui [8]. The iMATERIA data was found to yield refinement results comparable to NOVA. In the future, it will be applied to experiments for industrial applications.

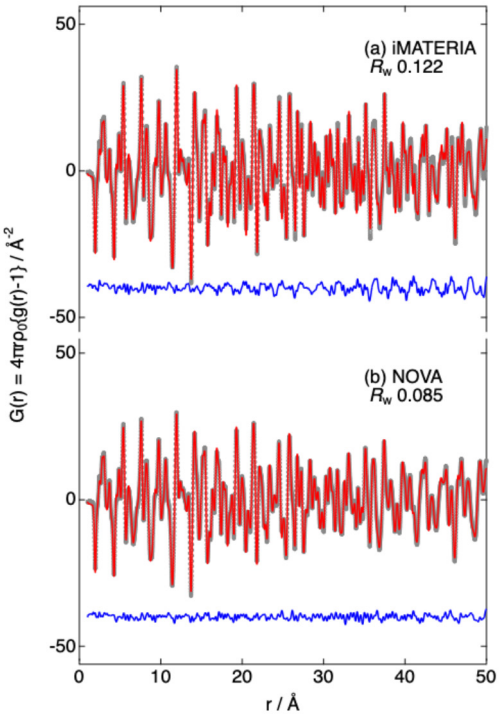

Figure 3. $G(r)$ and PDF analysis results of TiO_2 powder measured by (a) iMATERIA and (b) NOVA. The observed, calculated and difference patterns are indicated as gray circles, red and blue lines, respectively.

References

[1] T. Ishigaki, *et al.*, Nucl. Instr. Meth. Phys. Res. A 600 (2009) 189-191.
[2] R. Oishi, *et al.*, Nucl. Instr. Meth. Phys. Res. A 600 (2009) 94-96.
[3] A. Hoshikawa, *et al.*, J. Phys.: Conf. Ser. 251 (2010) 012083.
[4] Y. Onuki, *et al.*, Metall. Mat. Trans. A. 50 (2019) 4977-4986.
[5] Y. Onuki, *et al.*, Quantum Beam Sci., 4 (2020) 31.
[6] K. Ikeda *et al.*, J. Appl. Crystallogr. **55** 1631 (2022).
[7] K. Ikeda *et al.*, Nihon Kessho Gakkaishi **64** 174 (2022).
[8] C. L. Farrow *et al.*, J. Phys.: Condens. Matter **19** 335219 (2007).

T. Ishigaki
Neutron Industrial Application Promotion Center, CROSS

Status of the High Intensity Total Diffractometer (BL21, NOVA)

1. Introduction

Total scattering measurement is a powerful technique to analyze the structure of amorphous materials, such as liquids and glass, and uses a pair distribution function (PDF). The pair distribution function expresses the distance from one atom to another in a sample and is obtained by Fourier transform of the static structure factor *S(Q)*. Here, *Q* represents the magnitude of the scattering vector. NOVA is a neutron instrument for measuring high-precision *S(Q)* in a short measurement time. Furthermore, NOVA is the powder diffractometer with the highest neutron intensity in MLF, and its maximum instrumental resolution is $\Delta d/d$ ~0.35%. Here, *d* is the lattice spacing. At NOVA, material structural analysis is being carried out in various research fields, including amorphous materials, local disordered crystalline, and samples with magnetic structures with long lattice constants. Recently, a radial collimator (NOVARC) [1] has been introduced to reduce the background from the sample environment equipment, and measurement data with a good signal-to-noise ratio is obtained. In addition, in cooperation with the sample environment team at the MLF, the use of several types of common sample environment equipment, such as a 3-helium refrigerator, has begun [2]. One of the upgrade tasks at NOVA this year was the replacement of the Neutron Beam Monitor (NBM). An NBM is one of the important components for neutron experiments and its roles include providing the normalized parameters used to correct experimental data, as well as monitoring and diagnosing the characteristics of the neutron beam (neutron intensity, beam stability, beam profile, incident neutron wavelength distribution, etc.). This paper describes the operation of a nitrogen gas-filled neutron beam monitor (N_2-NBM) which is a new NBM at NOVA.

2. Operation of the N_2-NBM

NBMs that can operate stably in a high-intensity neutron environment, such as the MLF, are very limited due to various reasons, one of which is the pile-up of output signals. In fact, to normalize the neutron experimental data at many of the neutron beam lines at the MLF, the data of the number of protons that are incident on the neutron target are used, rather than the NBM data. The number of incident protons is measured using a current transformer (CT) installed on the proton beam line. In the CT, the induced current, which depends on the number of protons passing through the proton beam line, is read out as a signal. The CT data can be obtained by accessing the server maintained by the Neutron Source Section [3]. The number of incident protons is thought to be in good proportion to the number of neutrons incident on the neutron instrument, but this is not strictly appropriate as a normalization parameter because it does not reflect the effects of the physical processes (neutron production, slowing down (energy moderation), transportation, etc.) that occur after the neutrons have been incident on the neutron target. This problem will be solved by measuring the number of neutrons that reach the sample position of a neutron beam line using an NBM.

The N_2-NBM of NOVA was purchased from Canon Electron Tube & Devices Co. Ltd., and its operations began in June 2024. Neutron detection in the N_2-NBM is carried out by detecting the fast-charged particles emitted by the $^{14}N(n, p)^{14}C$ reaction. The reaction cross-section for the $^{14}N(n, p)^{14}C$ reaction with thermal neutrons of 1.8 Å is 1.94 b, which is 1/2763 of that of the commonly used $^{3}He(n, p)^{3}H$ reaction. Therefore, in situations where a thermal neutron efficiency of less than 10^{-5} is required, the N_2-NBM is one of the few practical neutron detectors available. The gas active area of the N_2-NBM is 65 × 65 mm, and the material of the incident window is A5083 alloy with a thickness of 1 mm. As a chamber gas, a mixture of Ar and N_2 is sealed in, with a filling pressure of 1.034 atm and 0.066 atm, respectively. The thickness of the chamber gas layer is 12 mm. The expected thermal neutron efficiency is 6.7×10^{-6}. The N_2-NBM has a multi-wire proportional chamber structure and works in the same way as a radiation gas proportional counter. Since multiple anode wires are grouped and read out, it is not possible to detect the neutron hit position. The N_2-NBM has a screw-fastened flange structure that maintains airtightness with an O-ring, which makes it possible to replace the filling gas and wire electrodes.

As shown in Fig. 1, the N_2-NBM was installed upstream of the vacuum chamber of NOVA to replace the existing neutron beam monitor using a gas electron multiplier [4]. The flight path from the neutron moderator in MLF BL21 to the N_2-NBM is 13.76 m, and the beam size at this position is 34.4 × 34.4 mm. The GateNET [5] was used to measure the signals output from the

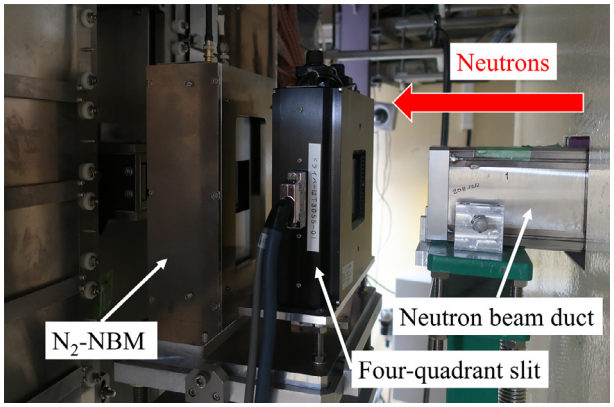

Figure 1. N_2-NBM installed in NOVA.

N_2-NBM. The neutron arrival time and pulse height were measured to derive the neutron wavelength distribution and perform nγ discrimination. In offline analysis, the amount of neutron irradiation is estimated, and this value can be applied as a normalization parameter. Figure 2 shows the trend in the number of incident protons and neutron flux in the neutron experiment in June 2024.

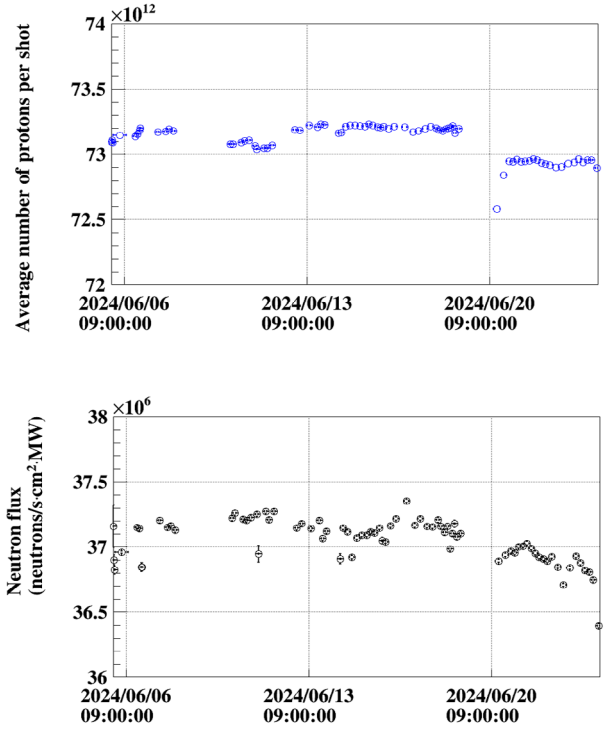

Figure 2. Trend in the number of incident protons and neutron flux.
The top is for the number of incident protons and the bottom is for the neutron flux.

The neutron flux is derived from the measured data for N_2-NBM. During the operation of J-PARC, the values of the number of incident protons and neutron flux were both stable. On the other hand, there are differences in the finer trends. In fact, as shown in Fig. 3, when the correlation between the two is taken, only a gentle positive correlation can be confirmed. The coefficient of variation Δ was given by σ/M, and the Δ values for the number of incident protons and neutron flux were 0.18% and 0.43%, respectively. Here, σ and M are the standard deviation and mean value of the distribution, respectively. The reason for the large Δ in that of the neutron flux may reflect the effects of the physical processes that occur after the proton beam is injected into the neutron target. From now on, we will continue to operate the N_2-NBM and verify that the N_2-NBM measurement data are useful as a normalization parameter.

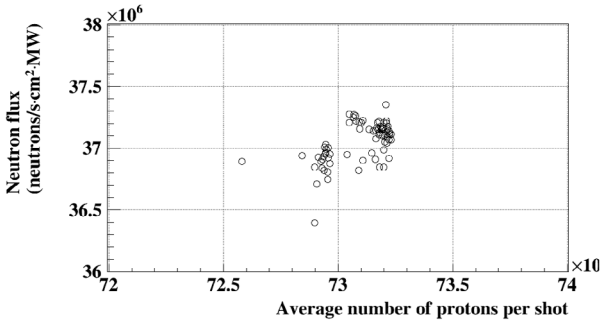

Figure 3. Correlation between the number of incident protons and neutron flux.

References

[1] M. Tsunoda, *et al.*, Nucl. Instr. and Meth. A **1055** (2023) 168484.
[2] T. Honda, *et al.*, MLF Annual Report 2021, **J-PARC 22-02** (2022) 120.
[3] M. Ooi and S. Meigo, JAERI-Tech **2005-025** (2005).
[4] H. Ohshita, *et al.*, JPS Conf. Proc. **8** (2015) 036019.
[5] S. Satoh, *et al.*, in proceedings of ICANS-XIX, conference proceedings ID IP132 (2010).

H. Ohshita[1,2], T. Honda[1,3,4], and T. Otomo[1,3,4]
[1]Institute of Materials Structure Science, KEK; [2]Neutron Instrumentation Section, Materials and Life Science Division, J-PARC Center; [3]Neutron Science Section, Materials and Life Science Division, J-PARC Center; [4]Department Materials Structure Science, The Graduate University for Advanced Studies, SOKENDAI

Current Status of the Energy-Resolved Neutron Imaging System RADEN

1. Introduction

RADEN, installed at beamline BL22 in the MLF of J-PARC, is a dedicated instrument for neutron imaging experiments using an intense short-pulse neutron beam. It offers a wide wavelength range ($\lambda < 8.8$Å) and excellent wavelength resolution ($\Delta d/d = 0.2\%$), making it particularly well-suited for energy-resolved neutron imaging [1]. In addition to conventional methods, RADEN supports advanced techniques such as Bragg-edge transmission (BET) imaging, neutron resonance absorption imaging, polarized neutron imaging, and phase contrast neutron imaging. This report provides an overview of the recent developments in the detectors used for energy-resolved imaging and highlights the applied research conducted at RADEN.

2. Development and operation of event-type neutron imaging detectors

The development and operation of event-type imaging detectors with high spatial and time resolution, as well as excellent radiation resistance, are continuously advancing at RADEN. The μNID (micro-pixel chamber (μPIC)-based Neutron Imaging Detector [2]) is one such energy-resolved neutron imaging detector developed in Japan, and its full-scale implementation at RADEN began in 2014. The μNID employs a time-projection chamber and fine-pitch, two-dimensional strip readout to track and analyze charged particles generated from neutron interactions in three dimensions. This enables high spatial resolution and strong gamma background rejection. Using ^{3}He gas as a neutron converter, the μNID achieves a detection efficiency of 26% for thermal neutrons, with a spatial resolution of 0.1 mm and a peak count rate of 44 kcps/cm^2 (global rate: 4.6 Mcps). It is mainly used for high-resolution measurements, such as polarized neutron imaging and phase contrast imaging.

To enhance count-rate performance, a new variant of the μNID, called the BμNID, was developed in recent years. The BμNID uses a ^{10}B thin film as a neutron converter, reducing event size and achieving a peak count rate of 100 kcps/cm^2 (global rate: 10 Mcps). Although the BμNID has lower spatial resolution (0.3 mm) and detection efficiency (5%) compared to the μNID, it provides significant advantages in applications that require high count rates, such as BET imaging. Introduced in 2021, the BμNID has been fully deployed for user experiments since February 2022, demonstrating consistent performance and increasing usage. Transmission images of a Gd test pattern obtained with both the μNID and BμNID are shown in Fig. 1 for reference.

Several updates have also been implemented to improve the usability of the μNID detectors. These improvements include real-time monitoring of measurement progress via an online log manager, the creation of analysis environments using Jupyter notebooks, and support for FITS-format data output to align with the file formats used by overseas facilities.

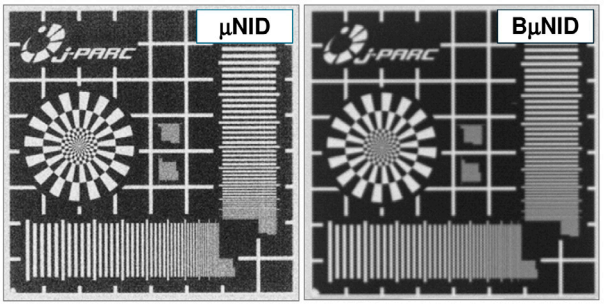

Figure 1. Transmission images of a Gd test pattern obtained by the μNID and BμNID detectors at RADEN.

3. Nondestructive analysis of crystallographic structures of a Japanese sword

At RADEN, nondestructive analysis of cultural assets with significant historical and cultural value is actively pursued. This report presents the latest research findings on Japanese swords [3].

Japanese swords are iconic steel artifacts that embody Japanese culture, with styles varying across different eras and regions. However, records of sword-making techniques before the Edo period are scarce, and many traditional methods have been lost over time. Understanding these ancient techniques is crucial for preserving their cultural value for future generations. Analyzing the internal crystallographic structures of swords from different periods and regions reveals their unique characteristics, contributing to a deeper understanding of the evolution of sword-making techniques. This study analyzed a 69.5 cm-long early Edo-period sword using BET imaging with the BμNID and neutron tomography (see Figs. 2 and 3). The sword bears the signature "Kiyomitsu," attributed to Kashu Fujiwara Kiyomitsu, a swordsmith from Kaga province (now southern Ishikawa prefecture).

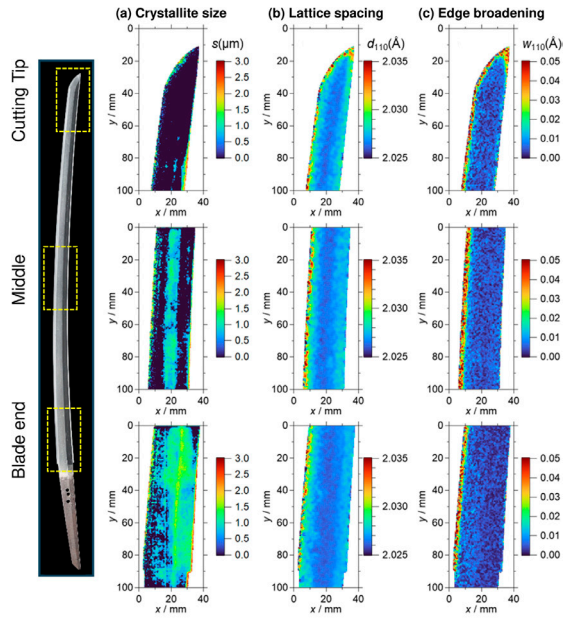

Figure 2. Two-dimensional mapping of (a) crystallite size s (μm), (b) lattice spacing d_{110} (Å), (c) edge broadening w_{110} (Å) of the (110) plane for Kiyomitsu.

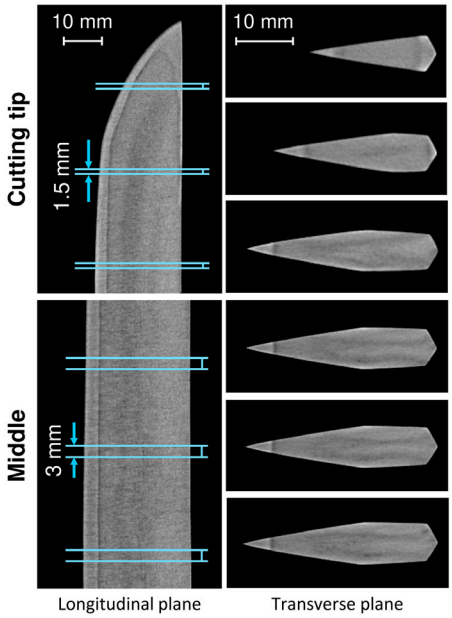

Figure 3. Cross-sectional tomograms of Kiyomitsu in the direction parallel (longitudinal) and perpendicular (transverse) to the blade.

BET imaging revealed uniformly distributed fine crystallites, about 0.5 μm or smaller, at the cutting tip, indicating a finely forged edge (Fig. 2a). In the middle section, a band-like region with 1 μm crystallites suggests the use of different steel types in a layered structure. Larger crystallites, measuring 1–2 μm, extend from the middle to the tang. Increased lattice spacing and edge broadening at the cutting edge (Figs. 2b and 2c) confirm the presence of a hardened martensite phase formed through quenching.

Tomography results (Fig. 3) align with the BET findings. A higher gray value, indicating lower neutron transmission, extends about 4 mm from the cutting edge, corresponding to the martensite phase. This martensite layer curves toward the back ridge, creating a distinct U-turn structure that reflects the swordsmith's technique. In the middle section, darker regions indicate structural variations or the use of steels with different properties, with the martensite phase extending linearly along the edge, as confirmed by transverse plane tomograms. The uneven contrast within the blade suggests a multilayered structure, likely composed of both softer and harder steels with varying carbon content. To enhance durability, the swordsmith likely combined these steel plates into a compound structure. While further studies are needed, the current findings suggest that Kiyomitsu features a complex layered structure.

4. Future plans

To enhance the spatial resolution and count rate of the μNID, we are developing new readout elements using MEMS processes, including one with a finer pitch and one utilizing three readout axes within the two-dimensional plane of the element. The finer pitch provides improved event localization for enhanced spatial resolution, while the additional information provided by the third readout axis enables better event separation and localization at high flux for improved rate performance. In our research on Japanese swords, we are accumulating data on various swords while introducing energy-selective tomography to evaluate its effectiveness. Additionally, to meet the diverse needs of academia and industry, we will continue advancing the development of devices, data analysis software, and imaging techniques.

References

[1] T. Shinohara et al., Rev. Sci. Instrum., **91** 043302 (2020).
[2] J.D. Parker et al., JPS Conf. Proc. **22** 011022 (2018).
[3] Y. Matsumoto et al., J. Archaeol. Sci.: Rep. **58** 104729 (2024).

Y. Matsumoto[1], J.D. Parker[1], T. Shinohara[2], T. Kai[2], Y. Tsuchikawa[2], Y.H. Su[2], K. Oikawa[2], H. Hayashida[1], Y. Nagai[1], and Y. Kiyanagi[3]
[1]*Neutron Science and Technology Center, CROSS;* [2]*Technology Development Section, Materials and Life Science Division, J-PARC Center;* [3]*Hokkaido University*

BL23: Polarized Neutron Spectrometer POLANO

1. Introduction

POLANO is a direct-geometry spectrometer with a capability of polarization analysis [1]. The third period of the S1-type KEK project began in 2019 and is planned to continue for five years. Over 30% of the beamtime has been allocated to general proposals, although it has only been used for unpolarized experiments. We invited international collaborators (ISIS and ANSTO), especially for conducting R&D and commissioning of polarization experiments. We also had a student from Italy as a contribution to the educational programs of J-PARC.

2. Instrument upgrade

Detectors: ^{3}He gas-filled position-sensitive neutron detector (PSD) is used in POLANO. As shown in Fig. 1 (a), POLANO has 24 sectors as a detector bank, and each sector can be equipped with 32 PSDs. In September 2023, the PSDs in sector 120U were relocated to sector 20L. At that time, the disabled detectors and preamplifiers were replaced. The so-called a-b-c parameters for tuning the specific positions between inter-detectors are the set of coefficients of charge disproportionation in the one-dimensional PSD. The parameters were determined according to a signal of polyethylene, passing through the surrounding three Cd-slits for each detector bank, and used to align the geometrical conditions for each detector's position. The results are shown in Fig. 1 (b), as an intensity distribution on the two-dimensional (2D) detector banks. The x- and y- axes represent PSD ID and p/L (p: position on the 1D tube), respectively. The algorithm for deriving the a-b-c parameters is useful, and we plan to develop software to automate its derivation in the future. Currently, 384 PSDs have been installed in 12 sectors. The angular ranges covered by a typical single sector are 18° and 17° in the horizontal and vertical directions, respectively.

Neutron Monitor: The gas-filled neutron beam monitor (NBM) is one of the few realistic neutron detectors used in scenarios in which an NBM with a thermal neutron efficiency lower than 10^{-5} is required to suppress the counting efficiency. We developed a new type of nitrogen-gas filled NBM. The monitor is generally essential for neutron measurements in order to count the number of incoming neutrons for data normalization and to determine the exact measurement of the device positions on the beamline. The newly developed nitrogen-gas detector was tested using POLANO. The NBM was placed on the beamline, and the distance from the moderator surface to the monitor was estimated as 16.32 m. A 40 mm × 40 mm SUS collimator and 35 mm × 35 mm B_4C collimator were installed upstream of the NBM, as shown in Fig. 2 (a). As an experimental result, Fig. 2 (b) shows the neutron intensity of the POLANO obtained using the NBM. The obtained results were comparable to our previous research [2], with a measured neutron flux of $(2.97 \pm 0.02) \times 10^8$ neutrons/s cm^2 MW (0.1 meV – 1 eV). The NBM was shown to be useful in intense pulsed neutron sources such as the MLF and is planned to be installed in other neutron beamlines at the MLF in the future.

Polarized ^{3}He spin filter: ^{3}He neutron spin filters (NSF) are now widely used in large-scale neutron facilities in the world for polarized neutron scattering measurements. Nuclear spins of ^{3}He gas can be polarized using a method called SEOP [3], and the state-of-the-art technology in SEOP can achieve a very high ^{3}He polarization, larger than 80%, in which 90% of the ^{3}He nuclear spins are aligned in the same direction, while 10% in the opposite. The *in situ* polarized ^{3}He NSF installed in POLANO makes the ^{3}He gas continuously spin-polarized to provide stable polarized beam [4]. In addition, an AFP NMR system [5] is implemented in the ^{3}He NSF to

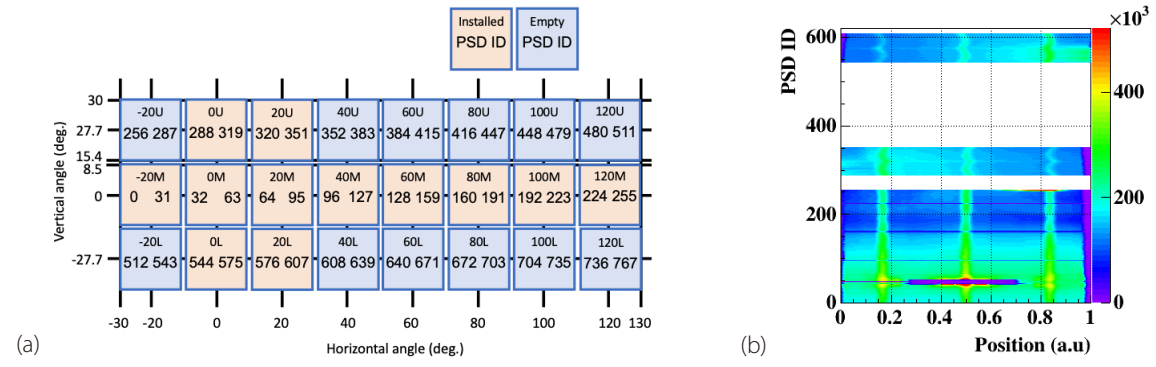

Figure 1. (a) Detector arrangement of POLANO. (b) 2D map of detection positions.

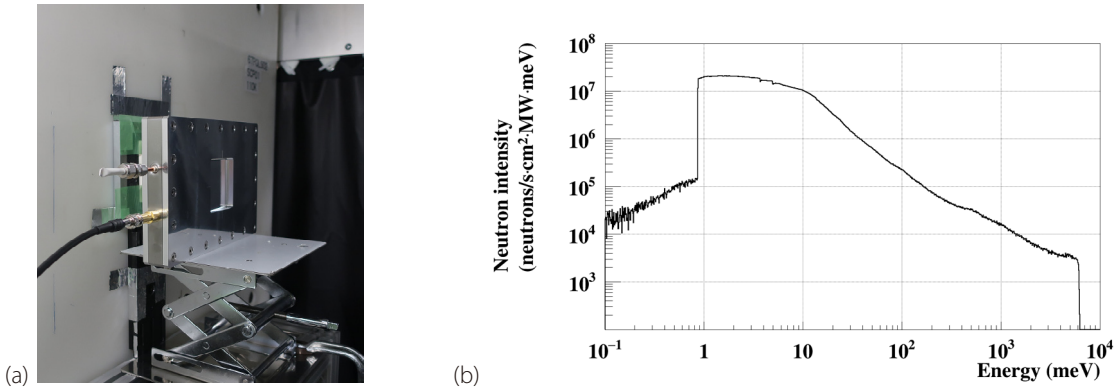

Figure 2. (a) The NBM, set at the upstream of the scattering chamber. (b) Neutron intensity distribution of the POLANO.

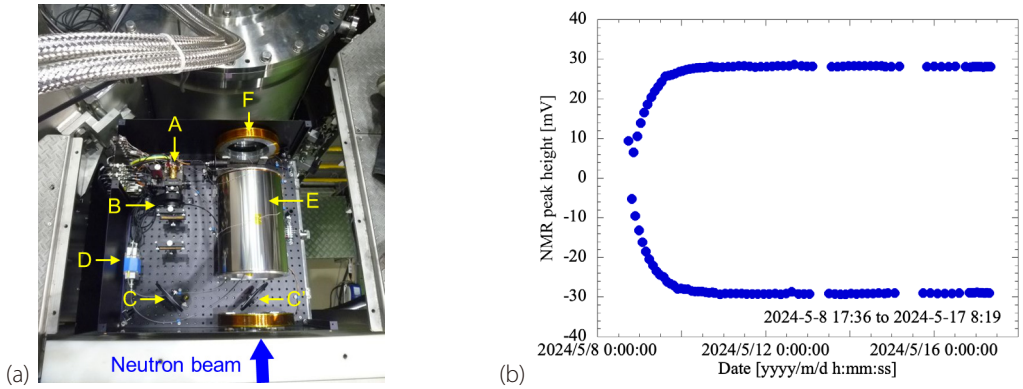

Figure 3. (a) In-situ polarized ^{3}He neutron spin filter in POLANO. A: Laser diode array. B: Optical components, chirped VBG, quarter-wave plate, lenses. C & C': mirrors. D: Low-noise amplifier for AFP NMR. E: Magnetically shielded solenoid, E: Neutron guide coil. For safety, these components are placed compactly in a laser shield box 60 cm wide, 60 cm long, and 25 cm high. (b) ^{3}He polarization during the commissioning runs from May 16 to June 6, 2024. Positive values correspond to spin-up, and negative ones to spin-down.

reverse the neutron spins. Figure 3 (a) shows the ^{3}He NSF equipped with a high-power laser with various optical elements, a non-magnetic electrical heater [6], a magnetically shielded solenoid, and an RF coil for AFP NMR. Figure 3 (b) shows the ^{3}He polarization measured using AFP NMR during the commissioning runs. At the beginning of each run, the ^{3}He gas was polarized using SEOP with a build-up time constant of approximately 6 hours. After saturation was achieved, the ^{3}He polarization was maintained constant for days with no disruptions until the system was shut down. We confirmed the feasibility by several tests, and no problems were encountered.

Future plans

Now we are getting to the starting line for polarization commissioning. It would be our first time conducting real tuning of the set of polarization devices in the MLF. Many things require further development and even the refurbishing will take significant time and costs. We are planning to conduct an operational test with all current polarization setup and take the first polarized data of polarized neutron inelastic signal.

References

[1] T. Yokoo et al., J. Phys. Soc. Jpn. **82**, SA035 (2013).
[2] S. Itoh, KEK Progress Report **2022-6** (2023) 46.
[3] T. R. Gentile et al., Rev. Mod. Phys. **89** (2017) 045004.
[4] T. Ino, et al., J. Phys. Conf. Ser. **711** (2016) 012011.
[5] T. Ino, JPS Conf. Proc. **22** (2018) 011015.
[6] T. Ino et al., Rev. Sci. Inst. **87** (2016) 115108.

T. R. Yokoo[1,2], S. Itoh[1,2], K. Ikeuchi[1,2], N. Kaneko[1], D. Ueta[1,2], S. Yamauchi[1], and H. Ohshita[1]
[1]*Institute of Materials Structure Science, KEK;* [2]*Neutron Science Section, Materials and Life Science Division, J-PARC Center*

Real-Time Data Storage and Display Module for Time-of-Flight Neutron Measurement

1. Introduction

Experiments using time-of-flight (TOF) measurements with pulsed neutrons are conducted at the Materials and Life Science Experimental Facility (MLF) of the Japan Proton Accelerator Research Complex (J-PARC). The MLF has 21 experimental instruments, and various neutron scattering experiments using 25 Hz pulsed neutrons are performed [1]. Users of the facility can choose various incident and scattered neutron energies by using the TOF measurements.

We have developed a gas-based two-dimensional (2D) neutron detector system with real-time position data output for in situ TOF measurements [2]. During the development phase of the detector, we used a data acquisition system with many features because we needed to measure various parameters of the detector system. Because of its many features, this acquisition system has the disadvantage of being complicated to operate and its operating speed is slow due to the heavy load on the processor. However, it is not necessary to have a multifunctional data acquisition system to measure pulsed neutron scattering experimental data at the TOF experimental facility. Therefore, a fast, simple, and user-friendly module was developed that acquires 2D neutron position data in real time and displays the minimum necessary data. Here, we also made an effort to further improve the operating speed by limiting the features.

2. Developed module

We have developed a data display and storage module for the time-of-flight measurement of neutrons. Figure 1 shows an image of the developed module; the module was fabricated with a single-width VME, as the VME standard is widely used at the MLF. As signal inputs, a 68-pin connector is mounted at the bottom of the module to input 2D position data from the detector and an ERA.00 connector to input T0 signals from the facility. Outputs from the module include a USB (Universal Serial Bus) connector for data storage and an HDMI (High-Definition Multimedia Interface) connector for screen display. Both USB and HDMI connectors are used because they are widely used for storage devices and monitors. A thumbwheel switch for determining the measurement time is located at the top of the module, and the module is started/stopped using the on/off switch in the middle of the module. The user only needs to determine the measuring time and start/stop the module, making it simple and easy to understand even for beginners.

The image of the data output from the HDMI is shown in Fig. 2. A large two-dimensional image is displayed, with the Y-axis and X-axis projections to the right and below the two-dimensional image, respectively. The figure shows that the neutron spot beam is irradiated near the center of the two-dimensional detector. The bottom right graph shows the TOF of the two-dimensional data. In this figure, strong counts can be

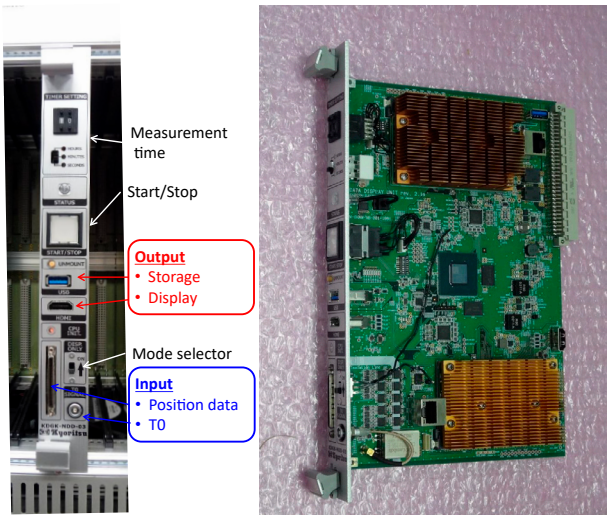

Figure 1. Front (left) and side (right) views of the module. The module was fabricated according to the one-unit VME standard.

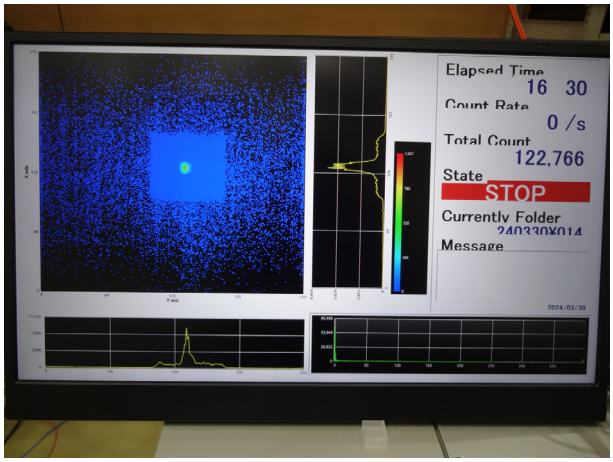

Figure 2. Display image on the monitor measured at BL10 (the refresh rate of the displayed image was 800 ms).

seen at TOFs below 1 μs. On the right side, simplified data are shown; elapsed time, count rate, total counts, detector status, folders to be stored and messages.

The frequency of the pulsed neutrons at the MLF is 25 Hz, so T0 signals at 40 ms intervals are constantly supplied to the module from the experimental facility. The TOF is calculated in the developed module using the received T0 signal and the 2D position data from the 2D detector. There are two operating modes on the module: standard mode and simple display mode. In the standard mode, experimental data are stored and displayed, while in the simplified display mode, only the measurement results are displayed on the monitor. The simple display mode is useful for testing the operation of neutron detectors and for adjusting the neutron beam in irradiation facilities.

3. Operation test

Performance tests of the developed module were conducted. The operating speed was verified using test pulses that simulate the signals output from a two-dimensional detector. The test pulse generator was specially developed to output 16-bit XY coordinate data.

The time response of each mode of the module was verified using a double-pulse test signal with different time intervals. Figure 3 shows the dependency of counting loss in the measured signals on the time interval of double pulse. It can be seen that the counting loss increases as the time interval decreases. No counting loss was observed at time intervals of more than 1 μs and 0.6 μs in standard and simple display modes, respectively.

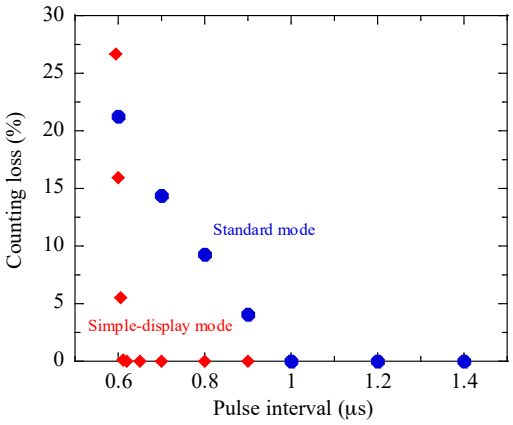

Figure 3. Counting loss in the measurement signal as a function of the time interval of double pulses.

The counting rate capability was measured using continuous test pulses. Figure 4 shows the dependency of counting loss in the measured signals on the frequency of a continuous test pulse. It can be seen that the counting loss increases as the frequency of the continuous pulses increases. No counting loss was observed for time intervals of less than 1 MHz and 1.6 MHz in standard and simple display modes, respectively.

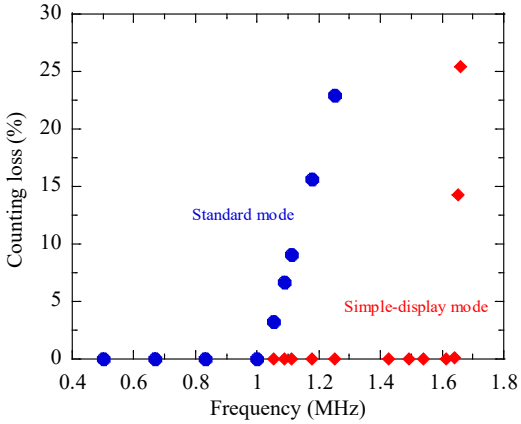

Figure 4. Counting loss of the measurement signal as a function of continuous pulse frequency.

4. Summary

We have developed a module for neutron scattering experiments that stores and displays neutron position data from a two-dimensional neutron detector system in real time. The module has the capability to store the incident neutron position coordinates with TOF and display 2D images and TOF spectra in real time. Operational tests using double pulses with various time intervals showed that the standard mode and simple display mode can discriminate input signals with a time interval of 1 μs and 0.6 μs, respectively. Operational tests using continuous pulses of various frequencies showed that the standard mode and simple display mode can measure continuous pulses with a frequency of 1.0 MHz and 1.6 MHz, respectively. As a result, the simple display mode was found to operate faster than the standard mode.

References

[1] J-PARC | Japan Proton Accelerator Research Complex, https://j-parc.jp/c/en/index.html.

[2] K. Toh et al., Nucl. Instr. Meth. A **726**, 169 (2013).

K. Toh, T. Nakamura, and K. Sakasai

Neutron Instrumentation Section, Materials and Life Science Division, J-PARC Center

Sample Environment

1. Activities in JFY2023

Table 1 summarizes the frequency of the experiments in which the MLF sample environment equipment was used in JFY2023. The 7T superconducting magnet and the humidity control system were frequently used throughout the beam operation period in JFY2023.

Table 1. Frequency of the experiments in which the MLF sample environment equipment was used in JFY2023.

Name of equipment	No. of experiments
7 T superconducting magnet	19
^{4}He cryostat	3
^{3}He cryostat	9
Dilution refrigerator	6
Gifford-McMahon (GM) cryostat	2
GM cryofurnace	1
Nb furnace	1
LED light source	2
Raman spectrometer	2
Humidity control system	26
Pulsed magnet system	3

2. Feasibility study of remote liquid He transfer system

So far, the neutron beam time is consumed while liquid He is re-filled in the tank of the superconducting magnet. It takes minimum an hour and maximum 4 hours to complete the operation, depending on the experimental conditions. To re-fill the tank with liquid He, a liquid He transfer tube should be inserted in both the liquid He tank and the liquid He supply vessel by opening the shielding hutch (Fig. 1(a)). The neutron beam is off while the shielding hutch is open. To reduce the beam time loss, we tried to improve the liquid He filling system, and performed a feasibility test to find the optimum conditions. In the improved new system, the He transfer tube keeps being inserted as shown in Fig. 1(b). In the system, the shielding hutch is closed, and the neutron beam can be on while liquid He is being re-filled. Also, one can operate the liquid He filling remotely, outside from the hutch. However, there is one concern with the new system due to the evaporation of the liquid He in the tank caused by the warm He gas in the transfer tube. The warm He gas exits until the tube is cooled down to the temperature of the liquid He in the process of the liquid He transfer. To minimize the amount of evaporation of the liquid He in the tank during the liquid He transfer, liquid He must be transferred very slowly. After conducting several test experiments (Fig. 2), we found the optimum flow rate to fully cool down the tube, which was about 30 minutes at 0.5 psi pressure. The new system is feasible under the optimum condition.

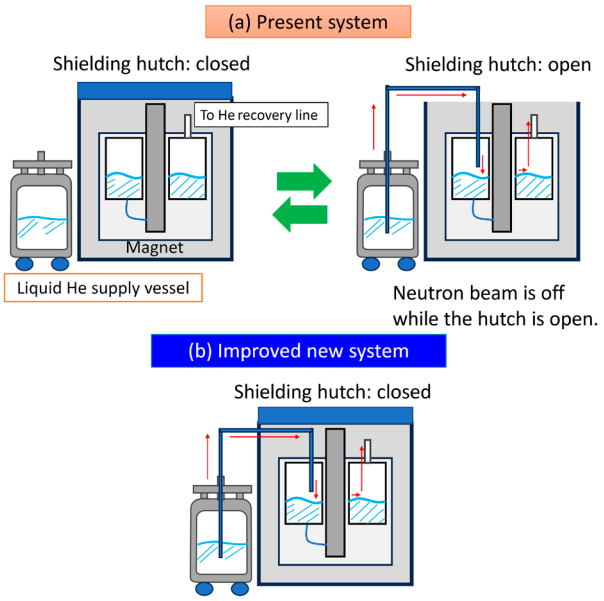

Figure 1. Liquid He transfer system for the 7 T magnet.

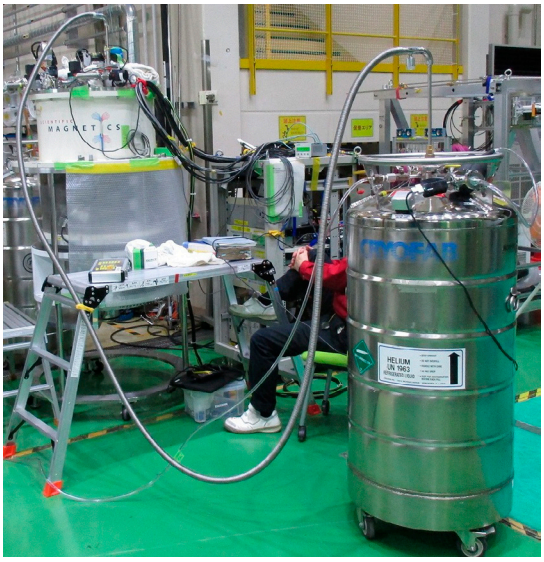

Figure 2. Remote liquid He transfer system in the test experiment.

3. Pulsed magnet

A new longer pulsed magnet system was developed in collaboration with Dr. Kohama and Dr. Nakajima of the University of Tokyo. Figure 3 shows a photograph of the longer pulsed magnet system. The maximum

Figure 3. The longer pulsed magnet system.

magnetic field is approximately 15 T. The opening angle is ± 30°. Longer pulses over 100 ms can be generated by using electric double-layer capacitors (EDLC) while the shorter pulses approximately a few milliseconds can be generated by using the conventional polypropylene capacitors. The EDLC bank consists of a series connection of 120 EDLC cells and has a total capacitance of 30 F (Nippon Chemi-Con). Maximum charged voltage is 300 V. A wide range of the reciprocal space is covered due to the wide opening of the magnet and a wide range of the neutron wavelength at the time-of-flight scattering instrument of the MLF. To demonstrate the availability of the new pulsed magnet system, the field-induced magnetic phases in the triangular lattice antiferromagnets $CuFe_{1-x}Ga_xO_2$ (x = 0 – 0.035) was investigated [1].

4. ISSE Training School 2023

The International Society for Sample Environment (ISSE) holds the international training school every two years, for the engineers, technicians, and scientists, especially for the beginners at the SE team in neutron and synchrotron facilities. In October 22-26, 2023, the 4th ISSE Training School was held in Tokai, Japan (Fig. 4). The MLF SE team hosted this school in cooperation with the staff members of JRR-3. The MLF staff and some invited lecturers from both Japan and abroad gave lectures in various topics, such as high and low temperatures, high pressure, vacuum, humidity control system, basics of neutron and X-ray experiments, and so on. We also carried out five hands-on training courses, which were cryogenic techniques, high-temperatures furnaces, high-pressure techniques, soft matter experiments, and pulsed magnet systems. 18 participants gathered in Tokai from 11 neutron and synchrotron facilities of the world and enjoyed these programs and communications.

Reference

[1] T. Nakajima *et al.*, Phys. Rev. Research. 6, 023109 (2024).

Figure 4. Group photo at the ISSE Training School 2023.

Y. Sakaguchi[1], R. Takahashi[2], M. Ishikado[1], S. Zhang[1], Y. Yamauchi[3], S. Ishimaru[3], H. Arima-Osonoi[1], S. Takata[2,4], Y. Su[2], T. Morikawa[1], K. Ohuchi[1], S. Yamauchi[4,5], S. Ohira-Kawamura[2,4], M. Watanabe[2], and T. Oku[2]

[1]Neutron Science and Technology Center, CROSS; [2]Technology Development Section, Materials and Life Science Division, J-PARC Center; [3]NAT Corporation; [4]Neutron Science Section, Materials and Life Science Division, J-PARC Center; [5]Institute of Materials Structure Science, High Energy Accelerator Research Organization (KEK)

Activities for Data Management at MLF

1. Introduction

Several policy developments on "Open Science" have recently been implemented in Japan to promote open access to scientific research data [1]. These policies have led to the launch of various projects aimed at developing platforms for open science, particularly for managing and publishing research data [2]. In this context, J-PARC's Materials and Life Science Facility (MLF) has been encouraged to align with the policies by adopting these platforms. Additionally, the MLF plans to offer data search and remote access services, enabling users to access experimental data for analysis from outside of J-PARC, although this implementation has not yet been achieved.

To support these goals, it is essential not only to gather neutron scattering data but also to collect and organize metadata that describes the data themselves. This metadata, which includes the user's name, proposal number, sample name, and experimental details on the instrument, is important for ensuring effective data usage and interpretation. Currently, this information is managed across different systems in the MLF, complicating the integration process. Therefore, to unify this diverse information as one metadata, we must review each existing system and establish a framework to add metadata flow between systems.

2. Outline of developments

We now plan to enhance the flow of metadata and neutron measurement data by upgrading the current systems, as illustrated in Fig. 1. To support this plan, we have developed an improved sample database that collects sample and user information from the Users Office support system. Additionally, we have upgraded the instrument control system (IROHA2) to combine user and sample information with neutron measurement data, including details such as sample environment device status, enabling this information to be treated as metadata for each measurement. Furthermore, we have enhanced the common storage system to store this metadata and measurement data for long-term research preservation, with the expectation that these stored data will be published and used across various fields in the future.

3. Sample Database

The Sample Database is responsible for managing samples at the MLF and providing sample and user information to external systems operated on the instrument side, such as IROHA2. The new system was developed from scratch to promote open data and data utilization, improve the efficiency of sample and safety management tasks, and address the issues present in the existing system. The main functions of the new system are as follows:

- Sample storage management
- Sample safety management
- Integration with the Users Office support system
- Provision of sample and user information to external systems

In storage management, the system centrally manages the storage status of samples brought into the facility by users. Additionally, at the MLF, chemical safety reviews are conducted on samples before they are brought into the facility, from the perspective of safety management. This system supports chemical safety review tasks and issues the review results as a risk assessment sheet.

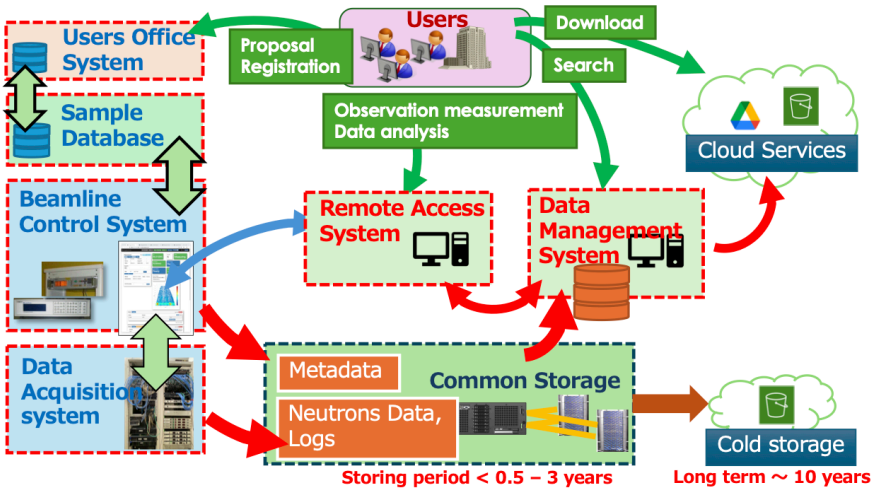

Figure 1. The structure of a metadata flow using updated systems in the MLF, J-PARC.

Sample and user information is obtained through API-based system integration, where information registered by users in the Users Office support system is retrieved. This linkage enables seamless, one-stop handling of tasks from sample registration by users to safety review. Furthermore, the API for providing sample and user information allows external systems, such as IROHA2, to utilize this information for generating metadata. By offering this information, the Sample Database supports the generation of metadata within external systems, enabling the integration and utilization of metadata across the infrastructure at the MLF.

4. IROHA2

The instrument control software framework IROHA2 [3, 4] is used to control instruments and measurements in neutron and muon experiments at the J-PARC MLF. IROHA2 consists of four elements.

1) Device control server sends commands to the experimental devices and monitors their status.
2) Instrument management server manages the configuration of the devices used for the experiment and controls the measurements using the data acquisition system.
3) Sequence management server controls the automatic measurements.
4) Integrated control server collects information from the other servers and centrally controls devices and automatic measurements.

The instrument management server generates the metadata about the measurement and records the time series data of the device status during the measurement. The metadata includes the details of the measurement, such as the measurement ID, start and end date of the measurement, the composition of the devices and their settings. Moreover, the instrument management server can retrieve user and sample information from the Users Office support system via an intermediate database, subsequently adding it to the metadata. We plan to implement a function to the instrument management server to retrieve the sample information from the new sample database.

5. Common storage

The MLF has prepared a common storage system on premises to store only raw data produced by the data acquisition system and measurement log data from the instrument control system. These stored data should be managed by the MLF and kept for several years. On the other hand, the management of processed data, called secondary data, is left to the users.

This storage system is located in the J-PARC research building and is connected to the PCs at the beamlines in the MLF experimental hall via a high-speed, redundant network. This system allows all beamlines to write data at a speed of 400 MB/s. or faster. This system was built five years ago with an initial capacity of 0.3 PB and currently has expanded to 1.0 PB. As per the usage policy of this storage, the MLF will store active data, defined as data created within the past one to three years. However, this capacity is insufficient to keep all the raw data produced by all the beamlines in the MLF for a long period. Therefore, the MLF plans to move older data to a cold storage, utilizing both cloud and on-premises hardware. Currently, more than 8 beamlines are connected directly to this system.

6. Future plans

As part of our future vision, the MLF must continue to develop systems for the utilization and application of stored data. Initially, we need a database system to manage the collected metadata. This database, working as a catalog, enables the MLF users to not only access their own data but also to search for and reference information from past experiments. The catalog function will be especially valuable in a remote access environment, where users can download or analyze their measured data. We have already begun designing the overall structure of the system, including the metadata catalog and data publishing system. These services have been planned to be completed by 2028. In the longer term, although we still have manpower problems, we would like to start a new project to collaborate with several existing platforms to align with the "Open Science" policy.

References

[1] https://www8.cao.go.jp/cstp/english/index.html
[2] https://rcos.nii.ac.jp/en/service/
[3] T. Nakatani et al., JPS Conf. Proc., **8** 03613 (2015).
[4] T. Nakatani et al., Proceedings of NOBUGS2016, 76 (2016).

Y. Inamura[1], K. Moriyama[2], H. Hasemi[3], and N. Okazaki[2]
[1]Neutron Science Section, Materials and Life Science Division, J-PARC Center; [2]Neutron Science and Technology Center, CROSS; [3]Technology Development Section, Materials and Life Science Division, J-PARC Center

Muon Science

Muon Section

1. Overview

The fire incidents in certain facilities in J-PARC stopped the MLF operation. Review and modification were conducted on all devices in the Muon Facility to prevent future trouble of a similar nature. In addition, the MLF has been operating since the release of the first beam in 2008, and measures to handle the deterioration had to be considered. The MLF continues to improve its robustness to ensure the stable and safe operation of the high-power beams. This article focuses on these measures.

2. Muon target monitor

The monitor system of the rotating target for detecting abnormalities and obtaining the signs of long-term wearing in the rotating target is under development. The torque of the rotating motor driver was analyzed to derive the intrinsic frequencies of the target wheel (0.25 Hz) and the bearing (0.1 and 0.15 Hz) in the rotational parts, as shown in Fig. 1. It is required to detect a change in the frequency data, eliminate the trivial effect like temperature dependence, and to classify its characteristics. For this purpose, the spectral centroid method was adopted, in which the gravity center of the FFT spectrum was calculated to detect easily a change in the data. This method was confirmed to detect abnormal vibrations (1.5 – 2.5 Hz) due to the force applied externally in the off-beam test. The off-beam data indicate a typical pattern and its slow changes. This could correlate with the wear of the bearings and could be applied to predict their remaining life.

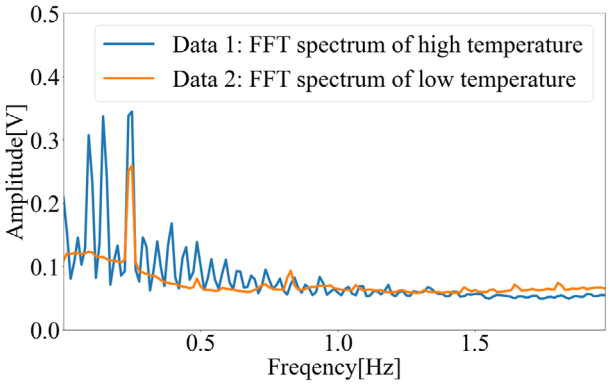

Figure 1. Typical FFT spectra.

3. Magnet power-supply monitor

The measures applied to prevent future fire incidents were determined as follows: (1) hardware inspection with a suitable periodicity (annual) and (2) installing a new monitoring system to detect signs of the power supply (PS) anomalies by monitoring current and voltage deviations. MUSE has 82 PSs for beamline magnets: 71 for constant-current ones, 9 for superconducting ones, and 2 for kicker magnets. Each of them has different interlocks. Figure 2 shows a scheme for controlling the PS by the EPICS program. When a user or staff inputs a PS operation command or current setting value on EPICS, the information is transmitted to the PS. The read-back information, including the output current, voltage value, and interlock status is returned to the program. In the modified monitoring system, the EPICS issues a command to turn off the power supply when a current deviation error is detected in the PS and creates an alert on the program. The new monitoring system was tested on 4 representative PSs in the 2024A period. The test was successful, and thus the system will be implemented in the remaining constant-current PSs in the next maintenance period. The monitoring systems of the PS for super-conducting magnets and kicker magnets are being developed.

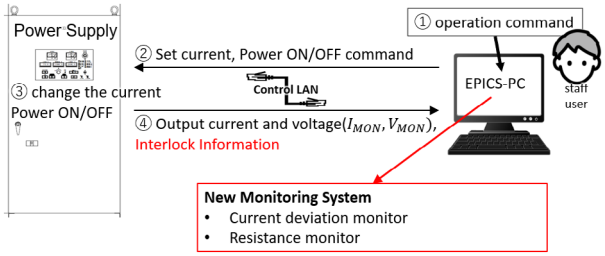

Figure 2. Schematic of the power supply and the control program.

4. Transparent material for the Lyman-α laser

Materials that exhibit high transmittance in the UV wavelength region are generally those composed of light elements. Fluoride is used as optical windows for the VUV region because oxides show strong optical absorption. Especially LiF, MgF_2, and CaF_2 are widely used as UV windows, since CaF_2 has very low transmittance at Lyman-α wavelength. MgF_2 and LiF are candidates for our application. MgF_2 has been used because it is a birefringent material and the information about its refractive index at Lyman-α wavelength is insufficient which made its use questionable. With the increase in Lyman-α light intensity due to the upgrade of the U-line laser system, the disadvantages of the observed degradation in the LiF window became serious, and it was decided to use a MgF_2 window. The MgF_2 window

showed higher transmittance than LiF over the entire 120 – 300 nm range and 1.5 times higher transmittance at the Lyman-α wavelength, as shown in Fig. 3. Based on these results, the LiF window was replaced by an MgF_2 one, and the intensity of the available Lyman-α light for ultra-slow muon generation was measured. The Lyman-α light intensity was enhanced from 5 μJ to 8 μJ. The MgF_2 does not form a color center even when irradiated with strong Lyman-α light, so the transmittance shows no degradation and can be used for a long period.

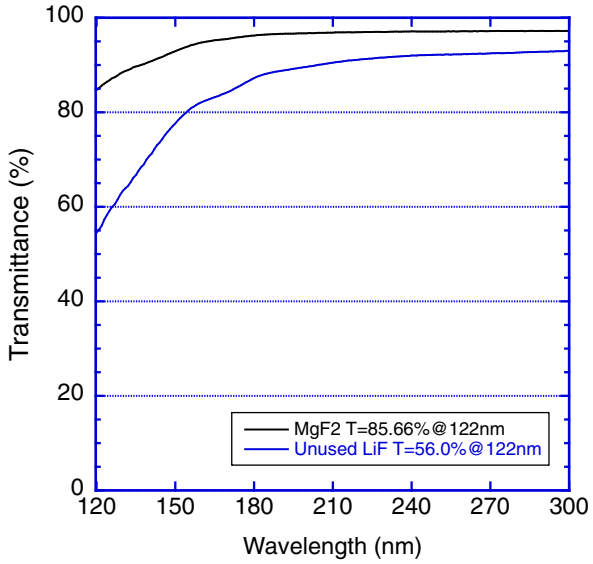

Figure 3. Transmission spectra of the LiF and MgF_2 window in VUV to UV region. The blue line is the non-irradiated LiF window, and the black line is the MgF_2 window.

5. Present status of the S line

In 2022, gate valve SGV1, located upstream of the S line, had a problem with Kapton foil, which separates the vacuum between the primary and secondary beamlines, getting stuck in it. The gate valve was replaced in 2022, but some parts of the Kapton fragments remained in the beamline. The work was carried out in July 2023 to recover this debris and to check whether any other Kapton debris remained. The mechanical strength of the recovered Kapton fragments will be checked. On the other hand, to prevent problems with the installed Kapton foil, a viewport and mirror were mounted downstream where the foil could be watched. This enables observation and checking during the beam operation using a web camera.

The kicker, the most important device for the simultaneous operation of the S1 and S2 areas, began to fail frequently around the start of full-time operation of the S2 area in the 2022B term. The failures were caused by the breaking of the Si MOS-FETs used in the Marx high voltage circuit, and aging degradation of the device is suspected. Each time a failure occurs, the Si MOS-FET is transplanted from a spare board and repaired. However, the device itself has already been discontinued, and thus we decided to employ SiC MOS-FETs. In April 2023, a Marx power supply unit replaced by a SiC MOS-FET was checked in the MLF. Comparing the generated voltage waveforms with the old Marx power supply unit, it was confirmed that there were no problems with the rise time and flat top time width, as shown in Fig. 4. Though the SiC MOS-FETs show a slightly faster turn-off time, no problems occurred when the old and new Marx power supply units were operated together. The new Marx power supply will be replaced with the old one in April 2024, and a long-term operation test is planned.

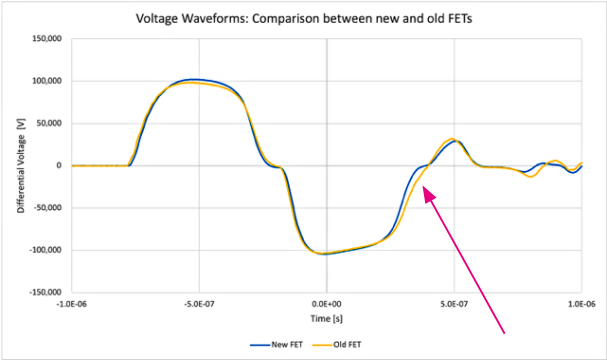

Figure 4. Comparison of high voltage waveforms between the new and old Marx circuits. The blue curve shows the waveform on the new SiC MOS-FET, and the yellow one is the old Si MOS-FET. The arrow indicates a slight difference around the turn-off time.

N. Kawamura
Muon Science Section, Materials and Life Science Division, J-PARC Center

Status of the Ultra-Slow Muon Beamline and Progress in FY2023

1. Introduction

The muon spin rotation/relaxation/resonance (μSR) technique, which utilizes muons as a highly sensitive local magnetic probe, is a unique method in materials science. μSR has been widely applied to the study of magnetic materials, super- conductors, and semiconductors. Muon beams in accelerator facilities are obtained from the decay of charged pions, typically possessing kinetic energies exceeding several MeV. Surface muons, which originate from pions that decay near the surface of the muon production target, have an energy of 4 MeV and an almost complete spin polarization. These are employed in various experiments, including μSR. To stop surface muons in a material, a thickness of at least sub-millimeter is required, and their stopping depth profile extends throughout the bulk. Thus, using surface muon beams for studying thin films and interfaces within materials is challenging. At J-PARC MUSE, the practical use of μSR using ultra-slow muons (USM) generated by laser ionization of thermal muonium is being pursued. Muonium is generated by irradiating a positive muon beam onto materials, such as hotmetal or room-temperature silica. Muonium atoms in a vacuum can be excited and dissociated using laser lights at wavelengths of 122 nm and 355 nm to generate thermal muons. In the U1 experimental area of MLF, USMs are focused and accelerated using an electrostatic lens, then transported to the U1A and U1B experimental areas. The U1A area facilitates a muon spin spectrometer for μSR experiments using USM, while a prototype of a transmission muon microscope is placed in the U1B area. A paper presenting the facility overview and providing an update on its recent activities was published in 2023 [1].

2. Present status and tasks

USM possesses excellent characteristics, such as low energy, small emittance, and high time resolution. However, to proceed with practical applications requiring high statistics, it is necessary to improve the beam flux. The key tasks for this improvement include (1) optimizing the surface muon beam transport, (2) increasing the muonium conversion efficiency, (3) enhancing the pulse energy of the ionization laser, and (4) improving the extraction and transport efficiency. In FY2023, the focus was placed on task (4).

3. Progress in FY2023

The extraction efficiency of ultra-slow muons (USM) is greatly influenced by the transport path from their generation to the pre-acceleration extraction stage. Since the trajectory of low-energy muons is sensitive to environmental magnetic fields, maintaining a clean magnetic field environment in the USM generation area is crucial. Previously, only correction coils for the beam extraction direction (*z*-axis) were installed in the USM generation area, which was insufficient for correcting the magnetic field near the generation target. To address this, new correction coils were added along the *x*- and *y*- axes, and a zero-field correction was performed. Figure 1 shows photographs of the correction coils and the results of the zero-field correction. Before the correction, there was a residual field close to seven Gauss, but the three-axis correction coils reduced this to the milligauss order.

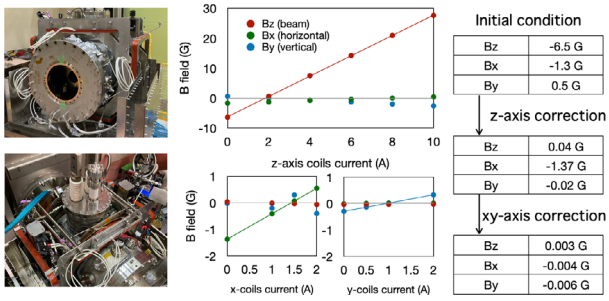

Figure 1. Zero-field correction coils: (Left) Photos of the coils installed in the USM generation chamber. (Middle) The relationship between the current flowing through the correction coils and the resulting magnetic field. (Right) The results of the zero-field correction. The majority of the residual magnetic field originates from the leakage field of the focusing solenoid in the Super-Omega surface muon beamline. Additionally, the surrounding magnetic materials and openings in the magnetic shielding contribute to a spatially non-uniform distribution. The correction coils can reduce these magnetic fields to the milligauss level.

At the intermediate focus point of the transport optics system, a beam monitor using a microchannel plate (MCP) has been installed. These detectors play a crucial role in exploring the transport parameters to the experimental area. Last year, one of these monitors was upgraded to a position-sensitive detector using a delay line detector (DLD). This upgrade significantly improved

the efficiency of the transport studies. This year, the detectors at the U1A/B branch point were also updated to DLDs. By using these beam profile monitors in combination, it became possible to study the USM transport parameters while considering the tilt of the central trajectory, leading to improved downstream trans- port efficiency. A typical profile image is shown in Fig. 2.

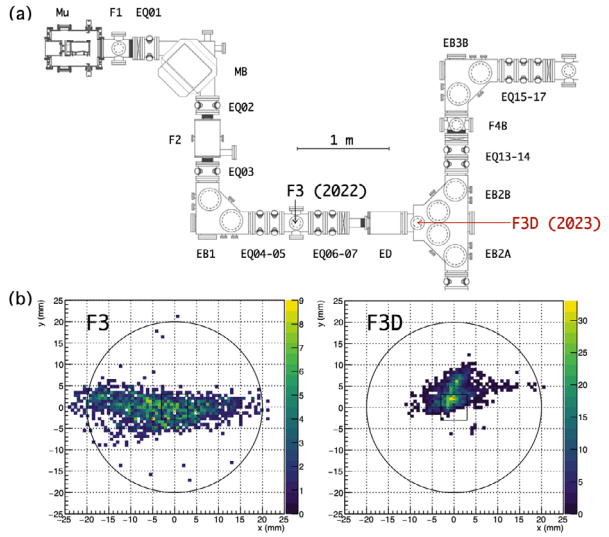

Figure 2. Beam profile monitor upgrade: (a) A plan view of the ultra-slow muon beamline. In FY2022, an MCP-DLD was added at the F3 location, and this fiscal year, another one was added at the F3D location. (b) A typical result of beam profile measurements. By measuring profiles at both the F3 and F3D locations, it has become possible to quickly establish a beam trajectory that can be smoothly transported downstream.

In previous beam studies, the agreement between experimental results and Monte Carlo simulations, which considered the field map, was limited. In the FY2023 studies, simulations were conducted under more realistic initial conditions. Additionally, the upgrade of the monitors improved the quality of the experimental data, allowing for better reproduction of experimental results in the simulations. Figure 3 shows a comparison of the experimental data and simulations investigating the changes in beam width by varying the voltage of the electrostatic quadrupole in the transport optics. Some of the results were presented at the IPAC2024 conference [2].

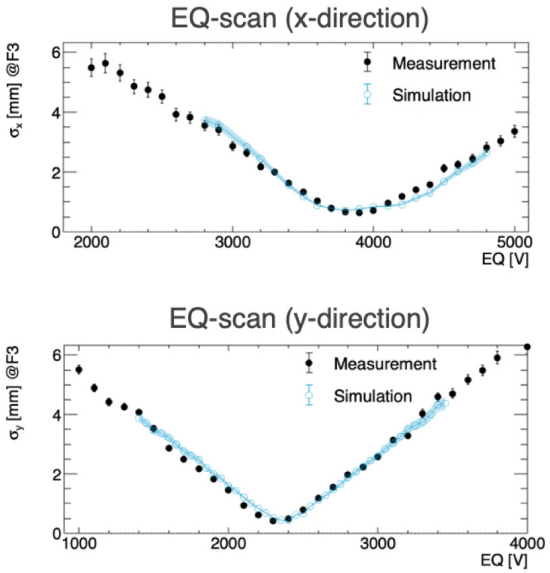

Figure 3. Comparison of experimental and simulation results of the Q-scan at the intermediate focusing point F3: The change in the beam profile width as a function of EQ voltage allows for the evaluation of the beam trajectory's position and momentum spread. The experimental data showed good agreement with Monte-Carlo simulations. Achieving this consistency in simulating the beam trajectory has enabled the quantitative assessment of losses and emittance growth along the transport path, thereby improving the understanding of the transport optics.

4. Summary and prospects

In FY2023, there were various advancements in the extraction and transport of USMs. The zero-field correction in the USM generation chamber and the upgrade of beam monitors improved the understanding of the beam trajectories and enhanced transport efficiency. The better agreement between experimental data and simulations concerning the beam transport system established a solid foundation for optimizing the transport optics.

References

[1] S. Kanda *et al.*, J. Phys.: Conf. Ser. 2462 012030 (2023).
[2] Y. Nakazawa *et al.*, in Proc. IPAC'24, Nashville, TN, May 2024, pp. 2933-2936. doi:10.18429/JACoW-IPAC2024-THAN2

S. Kanda[1], Y. Hoshikawa[1], Y. Ikedo[1], Y. Nakazawa[2], Y. Oishi[1], and K. Shimomura[1]
[1]*Muon Science Laboratory, Institute of Materials Structure Science, KEK;* [2]*Nishina Center, RIKEN*

Status of the U1A Spectrometer and Progress in FY2023

1. Introduction

The use of ultra-slow muons (USM) in muon spin rotation/relaxation/resonance (μSR) allows for the study of magnetism and superconductivity in thin films and at interfaces within materials. Additionally, because the time origin and spread of measurements are redefined through the laser ionization of muonium, USM offers significantly higher time resolution compared to conventional pulsed muon beams. To capitalize on these features and implement USM-μSR practically, commissioning of the USM beam and muon spin spectrometer has been carried out in the MUSE U1A experimental area.

2. Present status and tasks

Recently, a proof-of-principle experiment using a multi-layered thin-film test sample has been conducted [1]. As the final step towards practical application, we have begun comprehensive scientific measurements that include sample cooling, magnetic field application, and control of implantation energy.

3. Progress in FY2023

The muon implantation energy in the U1A spectrometer is controlled by a high-voltage stage that elevates the entire spectrometer. The voltages of the USM extraction electrode and the stage can be set independently, allowing for the reduction of implantation energy uncertainty by accurately evaluating the relative potential between these components. To calibrate the implantation energy, we measured the voltages of the extraction electrode and the spectrometer stage using a common high-voltage probe. The results are shown in Fig. 1. The probe's output was recorded as an analog wave-form on an oscilloscope and analyzed, including the energy spread due to noise. The study found that the spread in beam extraction and deceleration voltages was approximately 26 V at 1σ. This level of energy spread is acceptable when investigating thin films with thicknesses exceeding 10 nm or structures within materials of similar scale.

The beam profile at the sample position within the spectrometer is measured using a monitor that combines a microchannel plate (MCP) and a delay line detector (DLD). By accurately measuring the relative positioning of this MCP-DLD and the sample cryostat, it is possible to irradiate small samples with a narrow USM beam precisely. A thermal shield for the sample holder,

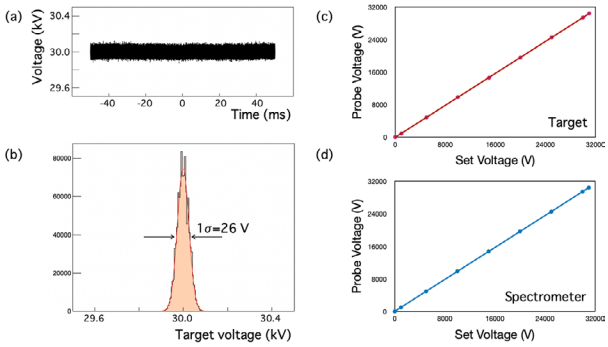

Figure 1. Beam implantation energy calibration: (a) An analog voltage waveform measured using a high-voltage probe attached to the target busbar.; (b) Voltage distribution sampled at a rate of 10 MHz over a measurement period of 100 milliseconds; (c) Relationship between measured and set extraction voltages; (d) Similar plot for measured and set voltages at the spectrometer.

featuring a grid-patterned opening, was fabricated, and a position calibration of the MCP-DLD was performed. The results are shown in Fig. 2.

The positron detector of the spectrometer consists of a scintillation detector with two layers— inner and outer—read out by silicon photomultipliers (SiPM). By requiring an inner-outer coincidence in the data analysis, noise floor due to the dark counts of the SiPM can be suppressed, and positrons originating from the sample position can be selectively observed. The data analysis program of the spectrometer has been updated to evaluate the event-selection efficiency and time resolution.

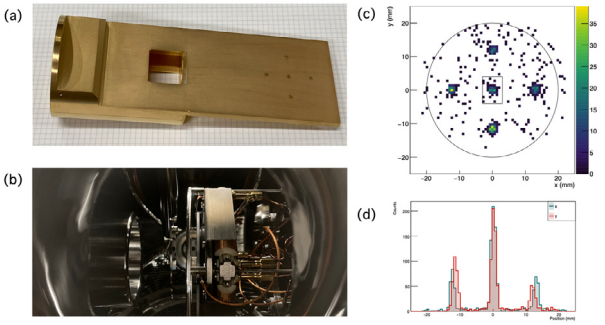

Figure 2. Beam spot calibration at the spectrometer's sample position: (a) Thermal shield with grid-patterned openings; (b) Setup in the spectrometer chamber; (c) Measured beam profile; (d) The *x* and *y* projections of the profile. The beam profile was measured using the MCP-DLD, with peaks corresponding to the positions of the openings in the thermal shield. The result ensures an accurate alignment between the beam profile monitor and the sample holder.

Figure 3 shows a hit pattern analysis on the detector module, where the approximate trajectory of positrons passing through the inner and outer layers can be estimated. This helps improve the signal-to-noise (*S*/*N*) ratio in μSR measurements. The segmentation of the detector was designed with consideration for the positron multiplicity induced by the pulsed USM beam. So far, the detector has not exhibited significant pulse pileup, so the detector's rate tolerance is sufficient. However, finer segmentation that allows for positron track reconstruction is expected to enhance the *S*/*N* ratio even further. Figure 4 shows the distribution of the time differences between inner and outer coincidence hits after event selection, providing information on the time resolution of the detector. The time resolution of the spectrometer was evaluated to be about 2 ns at 1 σ. Since the time spread of the beam is also at a similar level, the focus will now be on improving the spectrometer's time response characteristics to enhance the time resolution of measurements. The time spectrum obtained by the USM spectrometer consists of sharp peaks from prompt positrons (reflecting the double-pulse structure of the primary proton beam), background events from surface muon decay positrons, and signals from the USM decay positrons. Background events from surface muons dilute the asymmetry of the USM decay positrons, necessitating a sufficient signal-to-background (*S*/*B*) ratio. The *S*/*B* ratio, which varies depending on the detector's position,

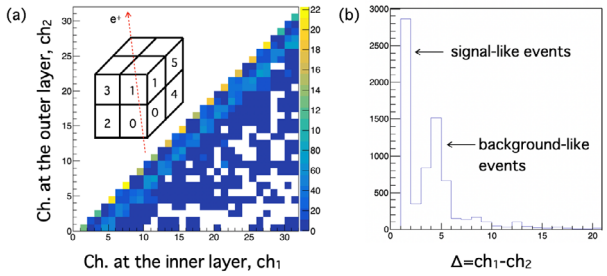

Figure 3. Hit pattern analysis of the spectrometer: (a) Correlation of hit positions in the inner/outer detectors and conceptual diagram of the detector's channel assignment; (b) Separation of signal and background events using hit pattern information. The positrons originating from USM stopped in the sample are localized at a hit channel difference of $\Delta = 1$ between the inner and outer detectors. In contrast, background events, originating from USM that stopped upstream in the beam duct, are distributed around $\Delta \sim 4$.

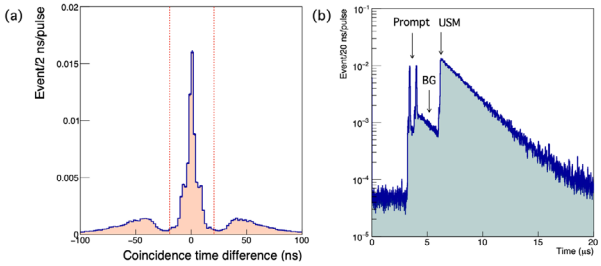

Figure 4. Time resolution and time spectrum of the spectrometer: (a) Time difference distribution between inner-outer coincidence hits; (b) Positron time spectrum with an event selection requiring the coincidence time difference less than 20 ns and the channel difference Δ equals to 1.

ranges from approximately 10 to 20. This is enough to ensure that background events do not pose a significant concern for asymmetry analysis.

The data obtained from the initial scientific campaign is currently under analysis and will be reported in a separate paper. Additionally, as a pilot user experiment using the U1A spectrometer, students participating in the 7th Neutron and Muon School conducted measurements on test samples [2]. This demonstration allowed the students to experience the entire process of USM-μSR, serving as a test case for future user experiments.

4. Summary and prospects

In FY2023, we focused on achieving the first scientific results while conducting various studies to understand the systematic effects unique to USM-μSR. Calibration of implantation energy and beam spot were crucial steps for obtaining reliable results. The performance evaluation of the spectrometer helped determine the types of measurements that were feasible with U1A and identified the necessary upgrades.

As the first user experiment, hands-on training was conducted during the Neutron Muon School, providing valuable experience for future practical experiments. Moving forward, the primary goal is to achieve the initial scientific results, while simultaneously working on upgrading the spectrometer and beam quality.

References

[1] S. Kanda *et al.*, J. Phys.: Conf. Ser. 2462 012030 (2023).
[2] https://www2.kek.jp/imss/eng/news/ 2024/topics/0603nms2023/

S. Kanda[1], Y. Ikedo[1], W. Higemoto[2], and T. U. Ito[2]
[1]*Muon Science Laboratory, Institute of Materials Structure Science, KEK;* [2]*Advanced Science Research Center, JAEA*

3NBT Buffer Tank Pressure Gauge Monitor Update

1. Introduction

Since the muon target on the 3NBT proton transport beamline was replaced by a rotating target, the amount of gas generated during vacuum evacuation near the muon target has been increased, and this gas includes tritium. For radiation safety, the exhaust gas from the vacuum system is temporarily stored in the buffer tank and released after the radioactivity is measured [1].

In order to confirm the safety of the buffer tank pressure and other vacuum exhaust functions near the muon target, the pressure gauge of the buffer tank installed in the control room of 3NBT downstream is routinely monitored on daily basis. In order to be able to monitor this status in the MLF control room, a monitoring system was developed with the co-operation of Mr. M. Ooi and Mr. A. Akutsu of the Japan Atomic Energy Agency (JAEA).

In this section, the monitoring of the buffer tank pressure and vacuum around the muon target will be introduced.

2. The vacuum equipment around the muon target

The devices that need to be monitored in the MLF control room are as follows:

- The vacuum gauge controller for the inter-midterm exhaust
- TK1 vacuum gauge controller
- TK2 vacuum gauge controller
- The control panel for the inter-midterm exhaust vacuum pump

These devices are installed in the control room of 3NBT downstream. Figure 1 shows these vacuum gauges.

Figure 1. The vacuum gauge controller installed in the control room of 3NBT downstream.
(Left: for inter-midterm exhaust, middle: for TK1, right: for TK2)

These vacuum gauge controllers have analog voltage outputs for vacuum values and are connected to the vacuum control system of the 3NBT proton transport line. Each vacuum value that is obtained by the vacuum control system of the 3NBT proton transport line, is sent to the control PC for 3NBT in the MLF control room and displayed in the control window. Figure 2 shows a control window displaying these vacuum values.

Figure 2. The monitor window of the vacuum system near the muon target.

In the MLF control room, there is a PC that displays images of the muon areas from the web camera connected to J-LAN, and the image of the control panel for the inter-midterm exhaust vacuum pump is added to this PC. Figure 3 shows the PC screen for displaying web camera images.

Figure 3. The PC for displaying the muon areas (left) and the display of the control panel for the inter-midterm exhaust vacuum pump (right).

3. Acknowledgements

We are grateful to Mr. M. Ooi and Mr. A. Akutsu for their full co-operation in this works.

Reference

[1] (Eds.) M. Teshigawara, M. Nakamura et al., Current Status and Upgrading Strategies of J-PARC Materials and Life Science Experimental Facility (MLF) and Related Components, JAEA-Technology 2021-022, pp. 104-105.

Y. Kobayashi[1,2], S. Matoba[1,2], Y. Ikedo[1,2], A. Koda[1,2], and N. Kawamura[1,2]
[1]Muon Science Laboratory, Institute of Materials Structure Science, KEK; [2]Muon Science Section, Materials and Life Science Division, J-PARC Center

Present Status of the S-line

The S line is a beamline mainly dedicated to surface muons in experimental hall No.1, with two experimental areas, S1 and S2, where a double-pulse muon beam can be delivered simultaneously as a single pulse to each area by using a kicker device.

In March 2022, the gate valve SGV1, located upstream of the S line, had a problem with Kapton foil, which separates the vacuum section between the primary and secondary beamline sides, getting stuck in it. The gate valve was replaced in May 2022, the details of which have been reported previously, but the Kapton fragments that got stuck in the beam blocker SBB1 were not recovered and remained in the beam duct.

In July 2023, work was carried out to recover the debris and to check whether any other Kapton debris remained upstream of the blocker. As with the SGV1 replacement work in 2022, a greenhouse was set up, and the work procedures and radiation protection at the MLF Division's safety review meeting were carefully discussed. The actual work went very smoothly and the recovery of Kapton stuck in the blocker was successfully completed. It was also confirmed that there were no Kapton fragments left upstream of the blocker.

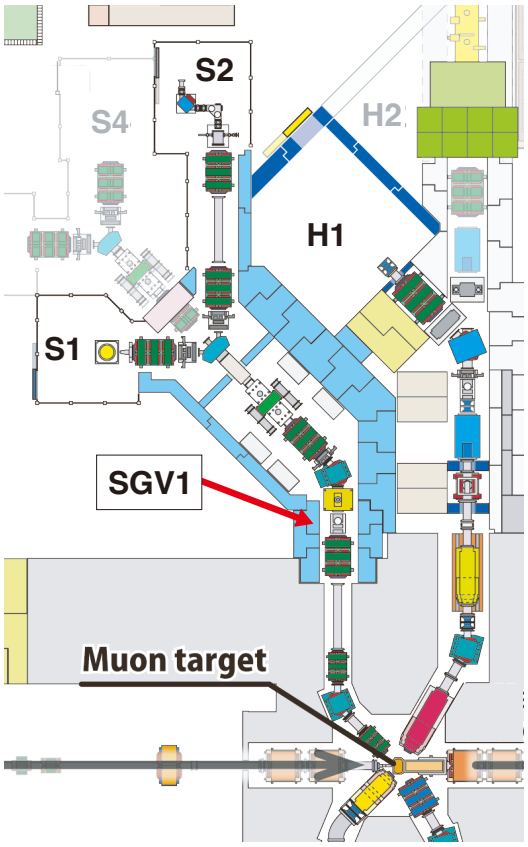

Figure 1. Layout of S line and location of SGV1.

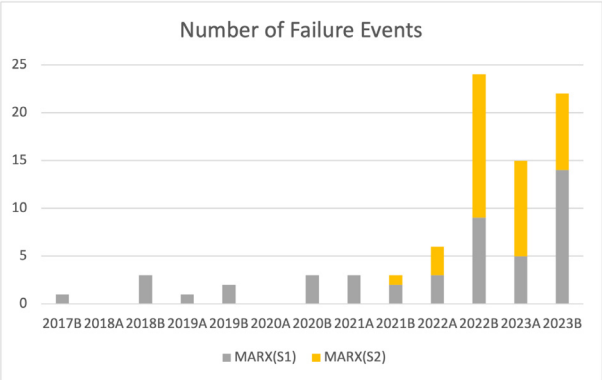

Figure 2. Number of MARX board failures that occurred during each operating period (as of Feb. 19, 2023). Gray and yellow bars represent the number of failures in the circuit that kicks the beam toward S1 (S2), respectively.

In carrying out this work, the experimental hall had to be declared a Radiation Controlled Area, Class 1, and the change of category was delayed until the completion of this work, when it would normally have been changed to Class 2 in the summer shutdown period. The entire MLF, including the Neutron Science Section, cooperated in this matter. The mechanical strength of the Kapton fragments recovered during this work and those recovered during the 2022 work will be checked in the future. On the other hand, to ensure that there are no problems with the Kapton foil in the beamline, a viewport and mirror were mounted in the SB2 beam duct for observation. This can be observed and checked at any time during beam operation using a web camera.

The kicker, the most important device for the simultaneous operation of the S1 and S2 areas, began to fail frequently around the start of full-time operation of the S2 area in the 2022B term, as shown in Fig. 2. The cause of the failures is due to the breaking of the Si MOS-FETs (IXYS DE475-102N21A) used in the Marx high voltage circuit, and aging degradation of the device is suspected. Each time a failure occurs, the Si MOS-FET was transplanted from a spare board and repaired, but as the device itself has already been discontinued, it is necessary to decide on the next countermeasure as soon as possible. We discussed with the manufacturer and attempted to replace the device with a SiC MOS-FET (GeneSiC G3R20MT12K).

In April 2023, a Marx power supply unit replaced by a SiC MOS-FET was brought to the MLF to check its operation. Comparing the generated voltage waveforms with those of the old Marx power supply unit, it was

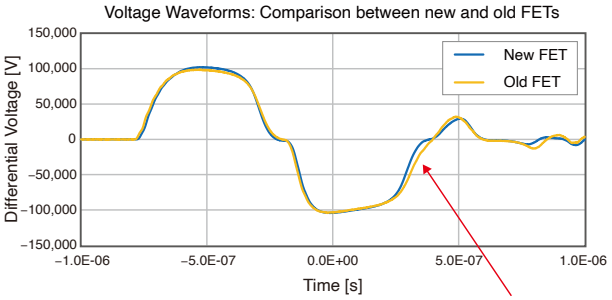

Figure 3. Comparison of obtained high voltage waveforms between the new and old Marx circuits. The blue curve shows the waveform on new SiC MOS-FET and the yellow curve shows that on Old MOS-FET, respectively. The arrow indicates a slight difference seen around the turn-off time.

confirmed that there were no problems with the rise time and flat top time width. As shown in Fig. 3, the SiC MOS-FETs were found to show slightly faster turn-off time, but no problems were found when the old and new Marx power supply units were operated together. The new Marx power supply will be replaced with the old one in April 2024, and it is planned to confirm that there are no problems in the long-term continuous operation.

A. Koda, T. Yuasa, J.G. Nakamura, S. Nishimura, and P. Strasser
Muon Science Laboratory, Institute of Materials Structure Science, KEK

Muon-Cyclotron Development in the U1B area

The world's first muon-cyclotron has been constructed at the U1B area (Fig. 1). The muon-cyclotron accelerates the 30 keV ultraslow muon beam to 5 MeV for the transmission muon microscope (TμM), which is now under construction. The TμM will visualize thick objects (>10 μm) in nanometer resolution, especially it will allow us to visualize both electric and magnetic fields distribution in thick objects. The acceleration to 5 MeV gives the muon beam a deep-penetration power.

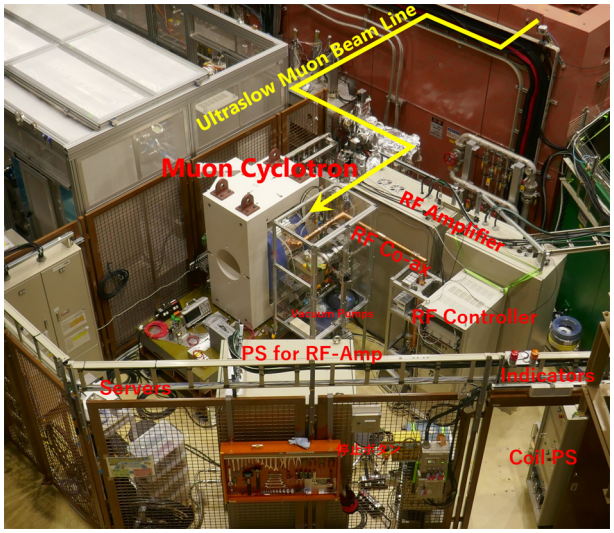

Figure 1. The 5 MeV muon-cyclotron system completed at the U1B area. The RF amplifier provides RF of 108 MHz/20 kW to the cyclotron through the RF coaxial tube. The installation of the RF controller is temporary, the main column of the TμM will be installed into the place of the RF controller. The Ultraslow muon beam enters the cyclotron from its rear, and the accelerated muon beam is ejected diagonally upward and is bended down to the TμM by a magnet.

The muon beam should have quite a small emittance and ultra-high stability of the beam energy, to observe images with high special resolution and with high sensitivity for electromagnetic field. The ultraslow muon beam, which is created by beam cooling using dissociations of muonium and has very fine emittance and ultra-low energy spreads, should be accelerated while maintaining these properties. The flat-top acceleration technique is adopted to keep these properties of the ultraslow muon beam. The flat top cyclotron is realized by installing the 3-times frequency (324 MHz) acceleration cavity in addition to the fundamental frequency (108 MHz) cavities (Fig. 2).

The RF controller (Fig. 3) for the cyclotron has been improved at this fiscal year. Driving of the RF-amplifier and detection of the RF in the cyclotron are fully controlled by FPGA, thorough complex RF-mixers controlled by DACs and detections by ADCs. Both continuous wave and pulsed wave operations are available. Any operation-mode is selected by a software directive.

The beam acceleration experiments officially started at 24/Jun/2024.

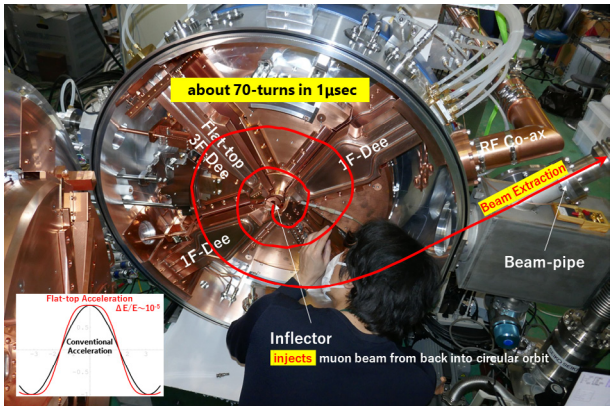

Figure 2. The internal structure of the muon-cyclotron. The ultraslow muon beam is injected into the center and accelerated by the two 1F Dee cavities driven by 108 MHz/20 kW RF-power. The 3F Dee cavity, which is driven by 324 MHz RF-power, forms the acceleration into flat-top shape.

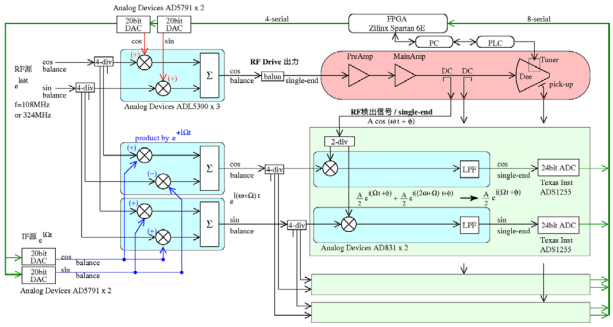

Figure 3. Block diagram of the RF-control system.

References

[1] Y.Nagatani, Y.Miyake, Isotope News, Vol 773. 31-36 (2021).

[2] Y.Nagatani, K.Shimomura, Journal of the Crystallographic Society of Japan, Vol 65. 33-41 (2023).

Y. Nagatani[1], T. Yamazaki[1], J. Ohnishi[2], A. Goto[1], T. Yuasa[1], Y. Nakazawa[2], T. Adachi[1], and Y. Ikedo[1]

[1]Muon Science Laboratory, Institute of Materials Structure Science, KEK; [2]Nishina Center, RIKEN

The Progress of the Laser System for Ultra-Slow Muon Generation

1. Introduction

Ultra-slow Muon Spin Rotation / Relaxation / Resonance (USμSR) for measurering the material properties in thin films and surface/interface has recently begun at J-PARC [1]. The only method to generate the Ultra-slow muon, with a narrow momentum range below ~0.2 eV, is through laser photoionization of thermal muonium (Mu). This method requires intense coherent Lyman-α light (122.09 nm) and 355 nm light due to the large Muonium evaporated volume (70 mm × 40 mm × a few mm). So far, we have constructed an all-solid-state laser system, which has highly stabilized wavelength and output pulse energy, and achieved the generation of Lyman-α light pulses exceeding 20 μJ through subsequent wavelength conversions [2]. We have been working on the enhancement of the irradiated light intensity, not only by increasing the output power of the laser amplifier, but also by efficient transport after the generation of the Lyman-α. This fiscal year, we introduced a new optical window at the Lyman-α generating gascell to enhance the transmittance.

2. Degradation of window transmittance

In order to generate an intense Lyman-α light, 212 nm and 820 nm pulses from an all-solid-state laser system are spatiotemporally superimposed and focused into a gas cell. The light-matter-interaction nonlinear process of two-photon resonance four-wave mixing in Krypton gas can generates Lyman-α light. The generated Lyman-α light is transmitted through a window separating the gas and ultrahigh vacuum and is reflected by a mirror pair for the ultra-slow muon generation region. A schematic of the apparatus for the generation and the transportation of Lyman-α light to the production of the ultra-slow muons is shown in Fig. 1. A LiF window with the shortest cut-off wavelength material has been used as the window so far. However, when LiF is irradiated with intense Lyman-α light, the ionization of fluorine in the crystal forms an F center (color center), causes light absorption in the vacuum ultraviolet and ultraviolet wavelength bands, which significantly reduces the intensity of the Lyman-α light that directly contributes to the yield of the ultra-slow muons. To minimize this problem, we introduced a window position translating device to avoid color centers [3]. However, this method, which consumes expensive windows, will become unsustainable in the future when the Lyman-α light intensity is enhanced as planned. We therefore decided to reconsider the window material. In preparation for this, we introduced an instrument (Bunkokeiki Co., Ltd, KV-201) that can quantitatively measure the transmittance of the window in off-beamline environment. The transmission spectra of non-irradiate and Lyman-α irradiated LiF windows were measured. The measured window has a dimension of ø70 mm with 6° wedge (4 mm in minimum thickness and 11.3 mm in maximum thickness). Both measurements were carried out at an area with almost the same thickness (7.0 mm). The transmission spectrum is shown in Fig. 2. Obviously, a red shift in a cut-off wavelength and a strong broad absorption centered on 250 nm has appeared for the irradiated LiF window.

3. Transparent material for Lyman-α

Materials that exhibit high transmittance in the UV wavelength region are generally those composed of light elements. Fluoride is used as optical windows for VUV region because the oxides show strong optical

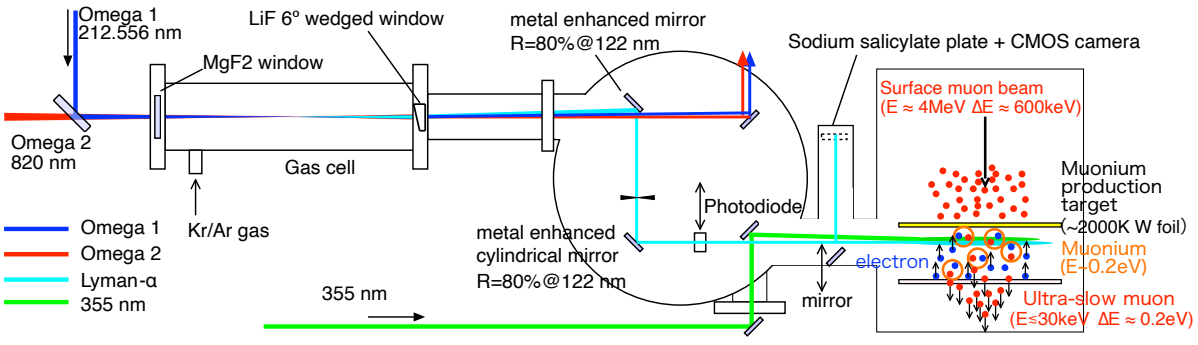

Figure 1. Schematic of Lyman-α generation and ultra-slow muon generation setup. The Lyman-α light is generated in the middle of Kr/Ar mixture filled gas cell, transported through the window, and reflected by a pair of mirrors to the muonium evaporated region.

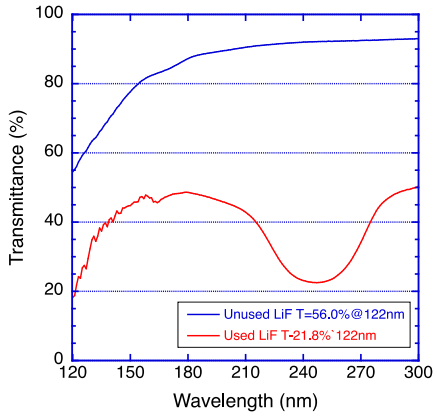

Figure 2. Transmission spectra of the LiF window in VUV to UV region. The bule line is the non-irradiated window and the red line is the Lyman-α beam irradiated.

absorption. Especially LiF, MgF_2 and CaF_2 are widely used as UV windows. Since CaF_2 is known to have very low transmittance at Lyman-α wavelengths, MgF_2 and LiF are candidates for our application. We were hesitant to use MgF_2 because it is a birefringent material and little is known about its refractive index at Lyman-α wavelengths [4]. With the increase in Lyman-α light intensity due to the upgrade of the all-solid-state laser system, the disadvantages of LiF described above became too great a problem, and it was decided to use an MgF_2 window. The MgF_2 window with the same shape as the LiF window was prepared and its transmission spectrum measured (see in Fig. 3). The MgF_2 window showed higher transmittance than LiF over the entire 120 – 300 nm. 1.5 times higher transmittance was obtained at the Lyman-α wavelength. Based on these results, the LiF window was replaced by an MgF_2 window and Lyman-α generation was carried out to measure the intensity of the available Lyman-α light for ultra-slow muon generation. The measured Lyman-α light intensity was enhanced from 5 μJ to 8 μJ. The MgF_2 does not form a color center even when irradiated with strong Lyman-α light, so the transmittance does not degrade and can be used for a long period of time without any translational manipulation of the window position.

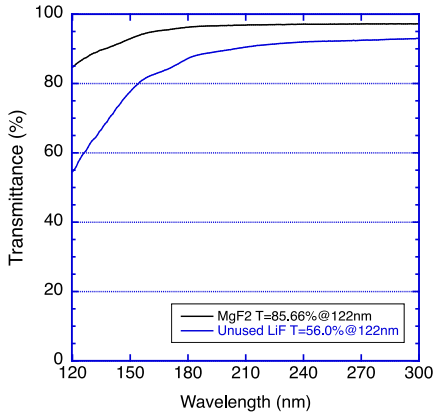

Figure 3. Transmission spectra of LiF and MgF_2 window in VUV to UV region. The bule line is the non-irradiated LiF window and the black line is the MgF_2 window.

4. Summary

The improvement of the intensity from the Lyman-α light source for ultra-slow muon generation is ongoing. The degradation of the transmittance of the LiF window was a major problem. We reconsidered the alternative transparent window materials and studied an MgF_2 window instead of LiF windows. The MgF_2 window showed 1.5 times higher transmittance at Lyman-α wavelength than the LiF window. The MgF_2 window was applied to high-intensity Lyman-α light and the amount of light contributing to ultra-low muon generation was successfully increased from 5 μJ to 8 μJ. Furthermore, it was found that there was no decrease in transmittance even after prolonged exposure to high-intensity Lyman-α light. Lyman-α intensity of >20 μJ will be expected after the improvement of the transmittance of the window reported here, in addition to the enhancement of the solid-state laser power by the power amplifier, which is described in the previous report [5].

Translated with DeepL.com (free version)

Acknowledgement

This work was done with Mr. K. Umeda and Prof. S. Nakamura.

References

[1] S. Kanda *et al.*, J. Phys. Conf. Ser. 2462(1), 012030 (2023).
[2] Y. Oishi *et al.*, J. Phys. Conf. Ser. 2462(1), 012026 (2023).
[3] KEK-MSL Report2021, 21 (2023). https://lib-extopc.kek.jp/preprints/PDF/2022/2223/2223007.pdf
[4] Refractive index database https://refractiveindex.info/?shelf=main&book=MgF2&page=Li-o.
[5] KEK-MSL Report2022, 19 (2024). https://lib-extopc.kek.jp/preprints/PDF/2023/2323/2323008.pdf

Y. Oishi[1,2]
[1]*Muon Science Laboratory, Institute of Materials Structure Science, KEK;* [2]*Muon Science Section, Materials and Life Science Division, J-PARC Center*

Muon Rotating Target

Developing monitor of the rotating target

The muon target has been operating normally since the replacement of the rotating parts in last year's maintenance. Although the Machine Protection System (MPS) has been updated by changing the threshold value of the torque signal, we further consider early detection of anomalies and life prediction of rotating parts is necessary.

We performed FFT analysis of torque signal data obtained from a rotating motor driver, and confirmed the fundamental frequency of the rotating target (0.25 Hz) and the bearing (0.1 and 0.15 Hz) of the rotational parts from FFT spectra (Fig. 1). We found that the bearing rotation frequency appears irregularly, and its frequency increases significantly during beam operation (Fig. 2). However, these vibrations were also observed in the data before the replacement, and since the system is operating normally, they are not abnormal. It is important to know and classify the characteristics of these data to confirm the changes in the data. To classify a large amount of data, we used the spectral centroid method. The method is very effective in detecting anomalies by calculating the center of gravity of the spectrum from the obtained FFT spectrum, thereby making it possible to easily confirm data changes. Using this method, we found that anomalous vibrations (1.5 – 2.5 Hz) are caused by external influences and tend to occur on maintenance days when the beam is off. Those external influences are currently under investigation.

We attempted to confirm the gradual change in vibration only from the data obtained during beam off without anomalous vibrations. The basic statistics of the data obtained during beam shutdown indicate that there is a certain pattern in the torque and this pattern changes slowly (Fig. 3). We believe that it correlates with the degree of wear of the bearings because there is a correlation between the basic statistics and the FFT spectrum of the data obtained. Currently, we are developing a system which can predict the bearing lifetime using an off-line muon target while continuing the analysis of the torque data of the muon target in operation.

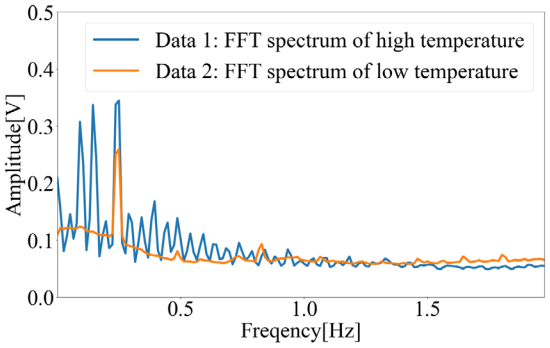

Figure 1. The FFT spectrum depends on temperature and torque of the rotating target.

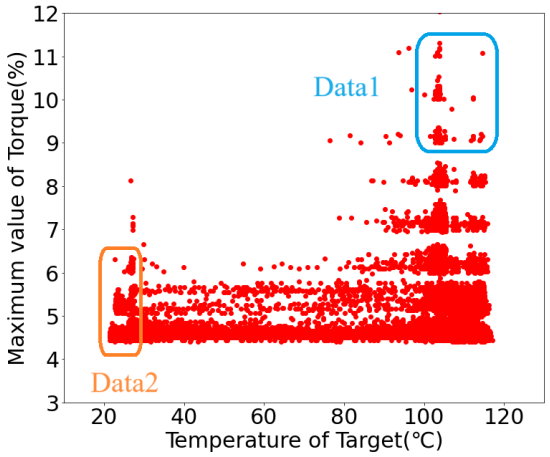

Figure 2. Correlation between maximum torque and temperature.

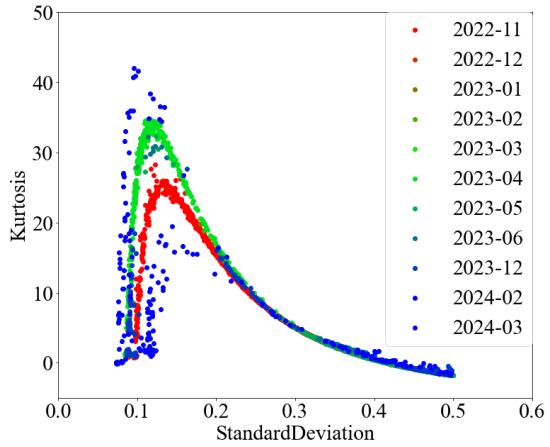

Figure 3. The pattern of torque signal during beam off and without anomalous vibrations.

H. Sunagawa[1,2], S. Matoba[1,2], and N. Kawamura[1,2]

[1]Muon Science Laboratory, Institute of Materials Structure Science, KEK; [2]Muon Science Section, Materials and Life Science Division, J-PARC Center

Development of the D2 (Muonic X-ray Element Analysis) Instrument and Sample Environment

The D2 experimental area provides various momentum of decay muons with a large space of about 4 m × 4.5 m, allowing users to bring in their own equipment or chambers needed to realize their experiments. This has led to the publications of remarkable results in several fundamental physics experiments [1-2] and elemental analysis [3-4] in FY2023.

Two of the KEK long-term S1 projects led by Prof. Miyake (KEK) and Prof. Takahashi (The University of Tokyo) have conducted experiments at the D2, providing fruitful results and publications. These include an attempt of CT imaging technique of muonic x-rays for analysis on archaeological samples using CdTe detectors [3] and an experiment with transport of slow muons for μCF [5].

We have also an ongoing KEK long-term S2 project led by Dr. Umegaki (KEK) to achieve an imaging technique of muonic x-rays from lithium using Si pixel detectors and SOI imagers [6-7]. A system equipped with two Si double stripe detectors has been installed especially for this theme.

A new program of "Integration of arts and sciences (Bunri-yugo)" has started for 2023B. At the PAC meeting, a proposal submitted by Prof. Shimomura was approved. In 2023FY, golden ancient coins [4], golden crafted accessories for swords and parts of the statue of Shachihoko (a dolphin like imaginary creature) once placed on the roof of the Nagoya Castle were analyzed with standard curves of muonic x-rays from gold, silver, and copper. Beam profile and the momentum bite at low momentum were studied in the program as well.

In FY2023, we had 7 experiment themes, including two of the P-type proposals conducted at the D2 experimental area mostly using negative decay muons [8]. Their theme was elemental analysis of muonic x-rays, soft error, Atomic Physics with TES detectors, μCF, and nuclear capture:

[2023A0090] Development of non-destructive isotopic analysis method for lead by muon induced gamma-ray measurement

[2023B0285] Non-destructive isotopic analysis for lead by muon induced gamma-ray measurement

[2023B0307(P)] Study of the time correlation of neutrons emitted by nuclear muon capture

[2023A0324] Depth profiling of gradient composition in diode-type CdTe X-ray detector by position sensitive muonic atom spectroscopy (2)

[2023B0036] High-precision spectroscopy of muonic x-rays using 50 and 130 keV superconducting TES calorimeter

[2023B0238] Search for 2-alpha emission from nuclear muon capture reaction on Ni, Zn and Ca isotopes

[2023B0254(P)] Measurement of the material dependence of the Doppler broadening effect of gamma-rays induced by muon capture.

In the Prof. Miyake's S1 project, we developed a sample chamber to install germanium (Ge) semiconductor detectors. Then, the sample chamber, which is called hemispherical chamber, will be available to any user of the D2. The hemispherical chamber has been designed by Dr. M. Tampo to install nine Ge detectors to measure muonic x-rays. We have finally completed the installation of nine Ge detectors for low energy to the hemispherical chamber for elemental analysis (Fig. 1).

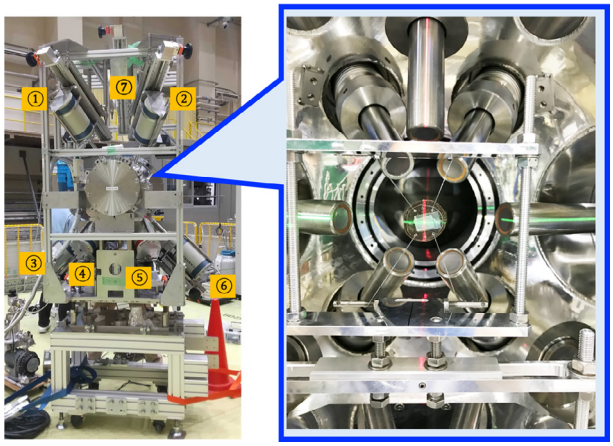

Figure 1. The system with the hemispherical chamber and 9 Ge detectors to detect muonic x-rays for elemental analysis.

We have made progress in the D2 experimental area in FY2023 in the development of software to analyze data instantly during measurements of muonic x-rays. The software enables us to calibrate the energy of nine detectors in the chamber (up to 16 detectors), and to obtain total count of all data from the nine detectors. It helps when you need to know whether the statistics in the measurement are high enough. The software was upgraded by Mr. Y. Ishikake and Mr. S. Doiuchi.

Other than elemental analysis, the hemispherical chamber was also used for experiments, which additionally enabled us to observe muonic x-rays at the same

time. Particularly, for investigation of errors caused by muons in an SRAM, the depth to analyze can be confirmed by measuring muonic x-rays during irradiation of muons, as reported before. The research attempted to find the momentum dependence of rate of error occurrences by irradiation of muons in semiconductor devices. In that sense, the hemispherical chamber has been a standard one with a measuring system of muonic x-rays.

Acknowledgments

The development of the software that we showed here was conducted as a part of "integration of arts and sciences" research program promoted by the KEK IMSS MSL and a part of Dr. Miyake's S1 project. It was also supported by the JSPS Grant-in-Aid for Scientific Research on Innovative Areas "Toward new frontiers: Encounter and synergy of state-of-the-art astronomical detectors and exotic quantum beams". The authors appreciate the cooperation of Mr. Shogo Doiuchi, Dr. Akiko Hashimoto, Mr. Yudai Ishikake, Dr. Amba Datt Pant, Dr. Soshi Takeshita, Dr. Patrick Strasser and other members of the Negative Muon Group. The design and production of the hemispherical chamber and the detector addition were managed with great diligence by Dr. Tampo.

References

[1] T. Okumura et al., "Proof-of-Principle Experiment for Testing Strong-Field Quantum Electrodynamics with Exotic Atoms: High precision X-Ray Spectroscopy of Muonic Neon" Phys. Reb. Lett. 130 (2023) 173001 (1-7).
[2] P. Strasser et al., "Improved Measurements of Muonic Helium Ground-State Hyperfine Structure at a Near-Zero Magnetic Field", Phys. Rev. Lett. 131 (2023) 253003(1-6).
[3] I-H. Chiu et al., "Non-destructive elemental analysis of lunar meteorites using a negative muon beam", Meteorite. Planet. Sci. 58 (2023)1333-1344.
[4] M. Tampo et al., Interact. 245 39(1-9) (2024).
[5] Y. Nagatani et al., JPS meeting, 2023, Sendai, 17pA102-3.
[6] R. Nishimura et al., JPS meeting, 2023, Sendai, 17pA102-7.
[7] K. Magata et al., JPS meeting, 2023, Sendai, 17pA102-6.
[8] S. Takeshita et al., Interact. 245 38(1-15) (2024).

I. Umegaki and M. Tampo
Muon Science Laboratory, Institute of Materials Structure Science, KEK

Development of Sample Environment at the S1 Area – Cryostat Lifter, Aluminum Platform, AC Current Meter –

At the S1 area, about 40 user experiments are conducted every year and most of them take 2 or 3 days of beamtime. Half of the experiments are conducted with a minicryo or microstat, a small cryostat using liquid helium as a cryogen, while about 16% of the experiments are done with a helium-3 (^{3}He) cryostat [1, 2].

Figure 1 shows the ratio of sample environments (ratios counted in days) used during the 2023A and B beamtime conducted in the S1 area.

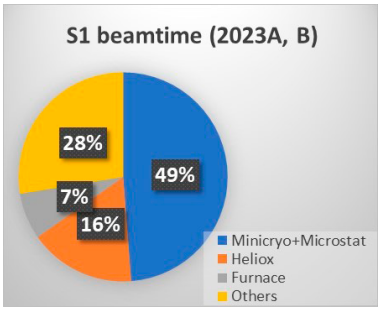

Figure 1. S1 beamtime ratio.

The installation of vertical cryostats, including the ^{3}He cryostat, requires access to the spectrometer from the top. To improve the convenience and safety of this access, we installed an aluminum platform (Fig. 2). A new cryostat lifter was also installed on the S1 spectrometer. The lifter allows the vertical cryostat to be relocated to the standby position without crane operation (Fig. 3).

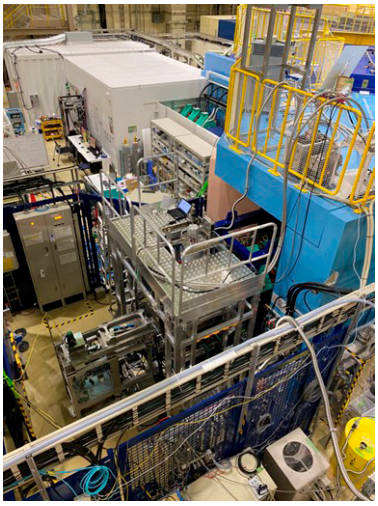

Figure 2. Aluminum platform.

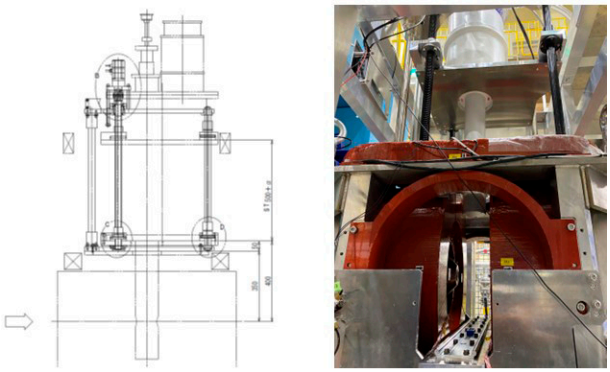

Figure 3. Cryostat lifter (left) and moving the cryostat to a standby position with the lifter (right).

In addition, we previously reported on the reorganization of electrical systems in order to separate the power lines used in the sample environment and the power lines for the vacuum pumps in the beamline [3]. In this context, we have additionally installed a new AC current meter on the electrical distribution board (Fig. 4) so that we can check the amount of electrical power used in each power line at the S1 area.

Figure 4. New AC current meter.

References

[1] J. G. Nakamura et al., JPS Conf. Proc. 14 011007(1-6) (2024).
[2] J. G. Nakamura et al., KEK Progress Report 2019-3 KEK-MSL REPORT 2018 23-24 (2019).
[3] J. G. Nakamura et al., KEK Progress Report 2022-7 KEK-MSL REPORT 2021 24-25 (2022).

J. G. Nakamura[1,2], S. Nishimura[1,2], H. Li[1], H. Osawa[1], A. Koda[1,2], and R. Kadono[1,2]
[1]Muon Science Laboratory, Institute of Materials Structure Science, KEK; [2]Muon Science Section, Materials and Life Science Division, J-PARC Center

Present Status of the H-line

The H-line is a high-intensity muon beamline for general use [1-3]. It is located in the east experimental hall #1 of the MLF and has two experimental areas named H1 and H2 area. Various experimental studies utilizing high-intensity pulsed muons of the H-line are performed and planned. At the H1 area, precise measurements of the hyperfine structure of muonium (MuSEUM experiment [4]) and search for μ-e conversion (DeeMe experiment [5]) are ongoing. The H2 area is an experimental area to produce ultra-slow muons (USMs) and re-accelerate them up to 4 MeV, and its beamline construction is underway. The H2 area will be extended further to produce a novel low-emittance muon beam by accelerating muons up to 212 MeV using linear accelerators. The low-emittance muon beam is a key technology for the J-PARC muon g-2/EDM experiment [6] and a transmission muon microscope (TμM). To install long linear accelerators, a new experimental building has to be built on the east side of the MLF, and its design is in the final stage. There were many upgrades over the past year, and this report describes the major ones.

One of the major upgrades of the H-line is the installation of a DC separator, which is necessary to eliminate positrons/electrons backgrounds from a muon beam by applying crossed electric and magnetic fields and selecting particle velocity. The gap, width, and length of its electrodes are 300, 500, and 750 mm, respectively. The expected e/μ separation power for surface muon beams is shown in Fig. 1.

Since FY2021, there has been a problem with the rated currents of the power supplies of the capture solenoids (HS1-1, 2, 3) being much lower than their specifications. This problem seriously reduced beam intensity at high momentum, but it was resolved at last by tuning the parameters of the control circuits. The rated currents before and after tuning are summarized in Table 1.

In the H1 area, an MRI magnet was installed for the MuSEUM experiment. The magnet is a superconducting solenoid cooled by liquid helium. A liquid helium recovery line and an oxygen monitor were installed in the H1 area, and then the MRI magnet was installed and aligned. It was successfully excited up to 1.7 T without any serious effects of the leakage field on surrounding apparatuses, such as vacuum pumps, gauges, and so on. Figure 2 shows the MRI magnets installed in the H1 area. To prevent the magnetic field from leaking out of the H1 area, 3~6 mm steel plates are attached to the wall of the H1 area.

The beamline construction to obtain surface muon beams with design intensity (10^8 μ^+/s) at the H2 area has advanced. Vacuum apparatuses, such as beam ducts, gate valves, pumps, gauges, and so on, were installed, and their control cables were wired. In addition, a fire alarm, lights, and air conditioners were installed in the H2 area because the H2 area is a closed space enclosed by radiation shield blocks.

The detailed design of a new solenoid (HS4) with ϕ610 mm aperture and a new quadrupole triplet (HS4) with ϕ400 mm aperture has been completed. These

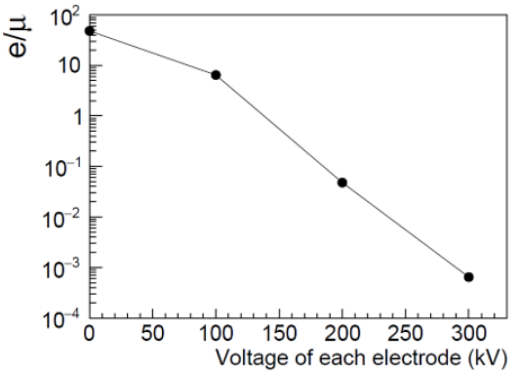

Figure 1. Simulated e/μ separation power of the DC separator for the surface muon beam as a function of the voltage applied to each electrode.

Table 1. Status of the maximum currents of the power supplies of the capture solenoids (HS1-1, 2, 3)

	Current in FY 2021 (A)	Before tuning (A)	After tuning (A)
HS1-1	1500	2500	2500
HS1-2	1500	2200	2500
HS1-3	900	2100	2400

Figure 2. The MRI magnet installed in the H1 area.

magnets are final focusing magnets before the H2 area and their design was optimized by calculating magnetic fields using Opera-3D and checking beam optics using G4beamline. Figure 3 shows the magnetic field of HQ456 in vertical (y) direction along the beam (z) axis at x =100 mm and y = 0 mm, after optimizing the pole shapes. The fabrication of HS4 and HQ456 has already begun and their installation is scheduled for FY2024.

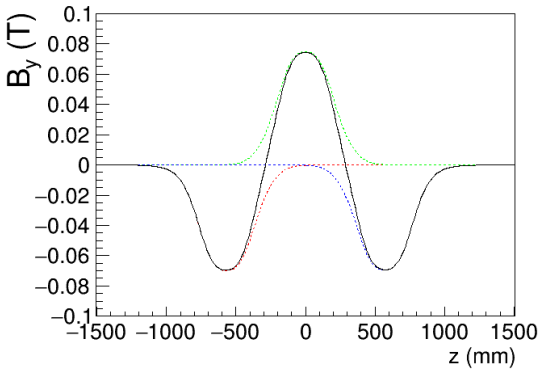

Figure 3. Magnetic field of HQ456 in vertical (y) direction along the beam (z) axis at x = 100 mm and y = 0 mm, after optimizing the pole shapes.

In addition, a laser room was constructed beside the H2 area as shown on Fig. 4. The laser room will be used to produce ultra-slow muons in the H2 area by laser ionization of muoniums. The laser room achieved ISO 6 (Class 1000) cleanliness. The stability of the room temperature can be controlled at less than ± 0.2 °C. A platform to place power supplies of linear accelerators to be installed in the H2 area was also constructed above the laser room.

We report on the present status and recent updates of the H-line. In the core part of the H-line, the DC

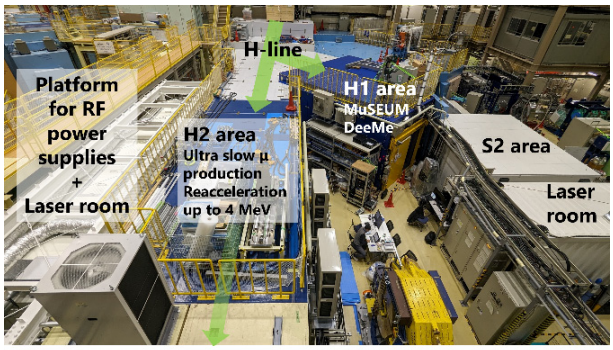

Figure 4. Picture of the H-line. A laser room and a platform for RF power supplies are located beside the H2 area.

separator was installed, and the problem of the capture solenoids was fixed. The preparation of the MuSEUM experiment has advanced, and its first result in the H1 area is expected in FY2024. The construction to produce USMs in the H2 area has also made progress. The first milestone at the H2 area is the surface muon beam with design intensity in FY2024, after which we will proceed to USM production and their re-acceleration.

References

[1] N. Kawamura, *et al.*, Prog. Theor. Exp. Phys. **2018** (2018) 113G01.
[2] T. Yamazaki, *et al.*, EPJ Web of Conferences **282**, 01016 (2023).
[3] T. Yamazaki and N. Kawamura, KEK-MSL Report 2021, pp. 26-27.
[4] K. Shimomura, AIP conf. proc. **1382** (2011) 245.
[5] H. Natori, *et al.*, Nucl. Phys. B (Proc. Suppl.) **248-250** (2014) 52-57.
[6] T. Mibe, *et al.*, Chin. Phys. C **34** (2010) 745.

T. Yamazaki[1,2] and N. Kawamura[1,2]
[1]Muon Science Section, Materials and Life Science Division, J-PARC Center; [2]Muon Science Laboratory, High-Energy Accelerator Research Organization (KEK-IMSS)

Muon Beamline Magnets and Power Supplies Update – Status of Monitoring System of Power Supply –

1. Introduction

On June 22, 2023, a fire occurred in the Hadron Facility because of increased contact resistance in a power supply polarity changer. Figure 1 shows the trend graph of the output current and voltage just before the fire. As shown in the figure, suddenly, the output current decreased, and the output voltage increased. Immediately after that, the output current returned to its original current value but with an increased voltage for a constant- current power supply. That process generated more heat than normal and led to the fire.

Since this event could have been prevented if there had been an interlock to monitor the sudden fluctuation of current and voltage, a new monitoring system was installed at J-PARC.

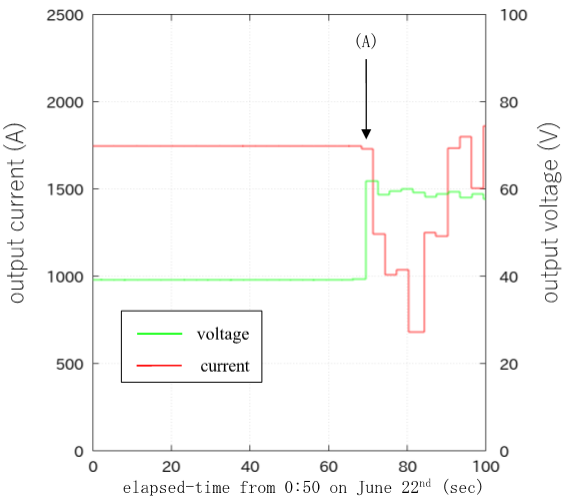

Figure 1. Trend graph of the power supply current and voltage (graph from the J-PARC fire report).

2. Description of each power supply interlock in MUSE

MUSE has 82 power supplies in total, which are categorized into 3 groups: 71 constant-current power supplies, 9 superconducting magnet power supplies, and 2 kicker magnet power supplies.

Interlocks for the constant-current power supplies can be divided into two categories. One is a "heavy fault", an interlock related to an anomaly of the power supply itself, and other abnormal stops. The other is a "light fault" due to external anomalies (magnet overheating, low magnet cooling water) or a current deviation error. In the case of external anomalies, the power supply immediately stops. However, in the case of current deviation error, the operation is continued and automatically restored when the deviation anomaly returns to normal.

There are two ways to power off superconducting magnet power supplies: "fast down" and "slow down". "Fast down" is triggered by output anomalies, heat, or quench and immediately stops the power supply. On the other hand, "slow down" is triggered by cooling water anomalies and power supply fan failure and stops the power supply while gradually lowering the current.

Kicker magnet power supplies have three operating modes: preheat phase (LV-on), ready-to-run phase (HV-on), and in operation (TRIG-on). LV-off is a critical interlock that turns LV (low voltage) off due to excessive voltage and current, low cooling water, or heat-related anomalies. HV-off is a safety interlock that turns HV (high voltage) off due to a thyratron misfire or anomaly in charging voltage and current. However, HV cannot be turned back on until the preheat phase (LV-on) is completed.

When excessive voltage and current, low cooling water, or heat-related anomalies occur, the power supply is turned off via the LV interlock. On the other hand, when a thyratron misfires or an anomaly in charging voltage and current occurs, the power supply turns off only HV via HV interlock but without turning off LV (LV-off).

3. Overview of the monitoring system

Measures taken in response to the fire in the Hadron Facility include hardware inspection with a suitable periodicity (annual) and installing a new monitoring system to detect signs of power supply anomalies by monitoring current and voltage deviations.

Figure 2 shows the relationship between the power supply and the control program (EPICS). When a user or staff inputs a power supply operation command or current setting value from the EPICS-PC, the information is transmitted to the power supply, which then operates as commanded. The information about the output current, voltage value, and interlock status is then transmitted to the EPICS-PC. In the newly added monitoring system, the EPICS-PC issues a command to turn off the power supply when a current deviation error is detected on the power supply and reported.

The current deviation error is one of the power

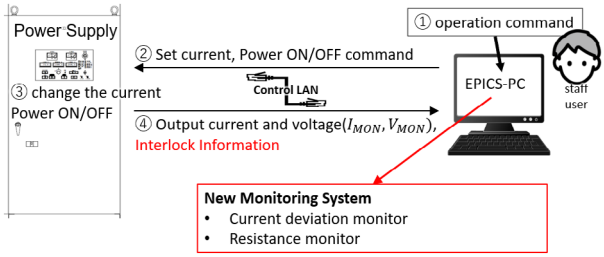

Figure 2. Relationship between the power supply and the control program.

supply's interlocks. However, the operation is continuing at the moment because it was introduced to check the stability of the output current. Since constant-current power supplies do not have an interlock to monitor voltage deviation, we considered a policy whereby voltage monitoring could indirectly detect voltage anomalies by monitoring the magnet resistance.

4. Current deviation monitor

Figures 3 and 4 show the current EPICS-PC and new monitoring system screens, respectively. The new monitoring system automatically turns off the power supply in the event of a current deviation error. We have conducted test runs with four power supplies (DB1, DQ5, DQ6, and DQ7) as representative units and confirmed that this monitoring system can be operated without any problems. Therefore, we plan to introduce this system to all constant-current power supplies.

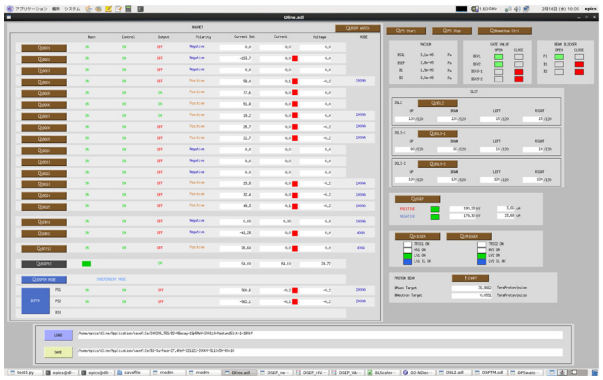

Figure 3. EPICS-PC screen.

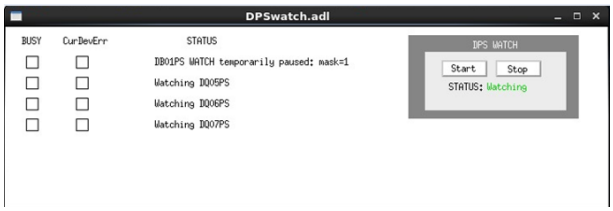

Figure 4. New monitoring system screen.

5. Magnet resistance monitor

We considered monitoring the magnet resistance by measuring the output current and voltage, and consequently decided on the threshold of the magnet resistance from calculated values. As with the current deviation monitoring system, we have conducted a trial run with several representative units and confirmed that this monitoring system can be operated without any problems.

6. Summary

We tested the new monitoring system on four representative units. The test runs were successful, so we will install this system on all constant-current power supplies. In the summer of 2024, we also plan to change the threshold of the D-Kicker power supply and install a current deviation detection function on the D-line superconducting magnet power supply (DSOL).

T. Yuasa[1,2], H. Fujimori[1,2], T. U. Ito[2,3], and N. Kawamura[1,2]

[1]Muon Science Laboratory, Institute of Materials Structure Science, KEK; [2]Muon Science Section, Materials and Life Science Division, J-PARC Center; [3]Advances Science Research Center, JAEA

Beam Commissioning at D1 Area and Other Progress

1. Introduction

The D line of the MLF MUSE has a long superconducting solenoid, which can provide positive and negative decay muons from a few MeV/c to 120 MeV/c in addition to surface muons. The primary proton beam energy of MLF is as high as 3 GeV, resulting in a high negative muon yield. Thanks to the recent increase in beam power, negative muon beams with the world's highest intensity are available. Using this high-intensity negative muon beam, various experimental applications have been developed, such as nondestructive elemental analysis using negative muon characteristic X-rays and negative muon spin rotation/relaxation. In this report, we report on the status of the beam commissioning at the D line.

2. Negative muon beam commissioning at D1

Negative muons exhibit different lifetime curves depending on the captured element. Therefore, to improve the signal-to-noise (S/N) ratio, it is important to eliminate components other than the sample, such as the sample holder, as much as possible. Fundamentally, it is crucial to reduce the number of negative muons stopping in areas other than the sample. Currently, the negative muon beam in the D1 area has a spread of approximately σ ~15 mm, which is larger than general measurement samples. Hence, a smaller beam is required.

To achieve beam convergence at the sample position, a mask with 15 mm diameter aperture was placed at the sample position of the D1 spectrometer, and detectors were installed downstream of it for beamline tuning (Fig. 1). A muon detector (upstream) and an electron detector (downstream) were placed downstream of the mask, and the electromagnets were optimized to maximize the intensity at the muon detector.

The beam axis dependency of the beam profile obtained by the tuning at 40 MeV/c is shown in Fig. 2. Before tuning, the spread was approximately 15 mm in both horizontal and vertical directions, but after tuning, it was reduced to about 10 mm. Additionally, the divergence angles in the beam axis direction significantly improved from approximately 170 mrad (vertical) and 200 mrad (horizontal) to 34(2) mrad (vertical) and 47(4) mrad (horizontal).

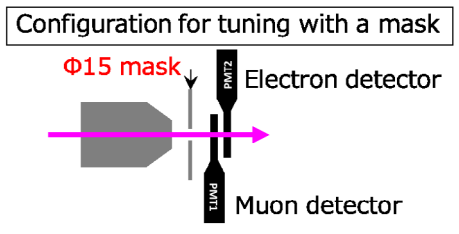

Figure 1. Configuration for tuning with a mask.

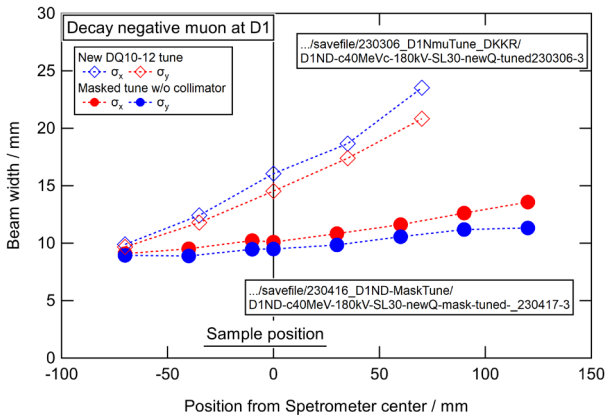

Figure 2. Beam divergence of 40 MeV/c negative muon measured at the D1 spectrometer.

3. Additional supported data format for μSR

The data formats for μSR spectra provided by MUSE have included msr, bin, ral, and root formats. Among these, the ral format was developed by ISIS, but its support has already been discontinued. To address this issue, with the cooperation of F. Pratt from ISIS who stayed at J-PARC under the KEK Visiting Researcher Program in FY2023, we have introduced a new conversion program for the nexus format (Fig. 3). The nexus file includes metadata such as sample environment logs, making it convenient for more detailed monitoring of the sample environment during measurements.

The data flow is as follows: The DAQ program collects hit timing information from the detectors and creates an event data file in edb format. Based on the event data read from this edb file, coincidence event data between paired detectors are generated, which are then restructured into histograms for each detector pair

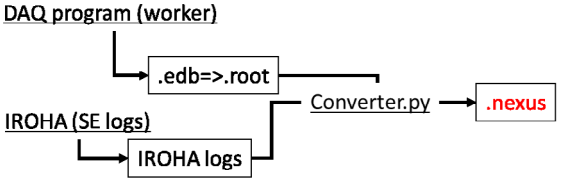

Figure 3. Overview diagram of nexus file creation.

and saved in root format. Simultaneously, the software framework IROHA, which controls various sample environment devices and the DAQ program, records the log data of the sample environment (temperature, magnetic field, etc.) in a log file. This log file and the aforementioned root format data are integrated by Converter.py to generate a nexus file.

4. Summary

We conducted tuning using a mask to improve the performance of the negative muon beam in the D1 area. As a result, we successfully reduced the beam divergence and obtained a smaller beam size. Additionally, we introduced a program for generating nexus files.

S. Takeshita[1,2], P. Strasser[1,2], A. Koda[1,2], W. Higemoto[2,3], I. Umegaki[1,2], M. Tampo[1,2], S. Doiuchi[1,2], A. Hashimoto[1,2], N. Kawamura[1,2], and K. Shimomura[1,2]

[1]Muon Science Laboratory, Institute of Materials Structure Science, KEK; [2]Muon Science Section, Materials and Life Science Division, J-PARC Center; [3]Advanced Science Research Center, Sector of Nuclear Science Research, JAEA

MLF Safety

Research Safety

1. Radiation safety

Radiological license upgrade and radioactivity of a sample

The applications for radiological license upgrades in FY2023 were not planned because they were not an urgent matter.

On the other hand, as the neutron intensity into the neutron instruments increases, the radioactivity of a sample after irradiation generally also increases. Based on our experience, the radioactive nuclides that are likely to remain are shown in Table 1. When an experiment plan is considered in advance, it is recommended that the materials listed in Table 1 are avoided or are reduced.

Table 1

Nuclide	Half life	Main reaction	Sample characteristics
P-32	14.26 d	P-31 (n, γ)	Biological
S-35	87.51 d	S-34 (n, γ)	Biological
K-42	12.36 h	K-41 (n, γ)	Biological
Mn-54	312.1 d	Mn-54 (n, p)	Metal, a bit long lifetime
Mn-56	2.579 h	Mn-55 (n, γ)	Metal
Co-60	5.271 y	Co-59 (n, γ)	Metal, long lifetime
Ag-110 m	249.8 d	Ag-109 (n, γ)	Metal, a bit long lifetime
Ta-182	114.4 d	Ta-181 (n, γ)	Metal, a bit long lifetime
Au-198	2.695 d	Au-197 (n, γ)	Electronic components

2. Chemical safety

The total number of chemical substances brought into the facility in FY2023 slightly increased compared to the previous year as shown in Fig. 1. This trend likely reflects the enhanced neutron beam intensity at the neutron scattering experiment facility and the maturation of the facility, which has enabled a broader range of experiments.

While there were no significant changes in the types of substances, a notable trend was the continued prevalence of battery-related samples and hydrogen storage alloys. Additionally, the use of flammable gases, such as methane and ethane, remained high.

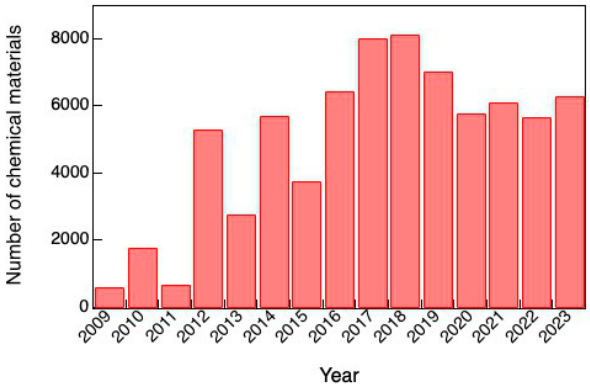

Figure 1. Trend of the amount of user-brought chemical materials for chemical safety check from the start of the MLF operation to the last year.

3. Crane safety

The number of crane operations throughout FY2023 showed little change compared to the previous year, reflecting the facility's stable operational schedule (Fig. 2).

The in-house staff's usage of cranes increased by approximately 20% compared to FY2022. This rise was attributed to the enhanced neutron beam intensity and the facility's maturation, which have enabled a greater number of experiments. On the other hand, the number of crane operations by contractors remained largely unchanged from the previous year.

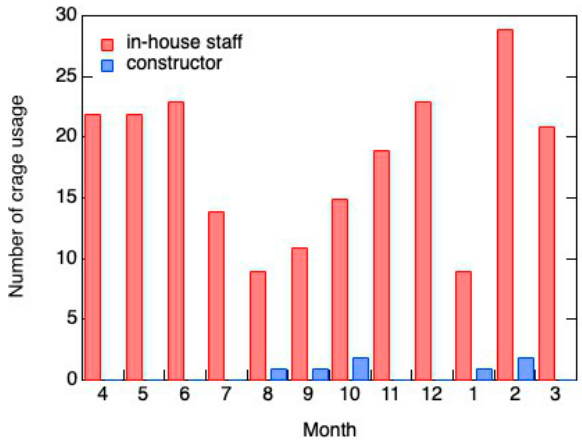

Figure 2. Trend of the total crane usage in one year.

M. Harada[1], T. Ito[1], H. Tajima[1], N. Hashimoto[2], Y. Watanabe[2], H. Tanaka[2], W. Kambara[2], H. Inoue[2], T. Oku[2], K. Suzuya[3], N. Kawamura[4], Y. Sakaguchi[5], R. Takahashi[2], and Y. Yamaguchi[5]

[1]Neutron Source Section, Materials and Life Science Division, J-PARC Center, [2]Technology Development Section, Materials and Life Science Division, J-PARC Center, [3]Neutron Science Section, Materials and Life Science Division, J-PARC Center, [4]Muon Science Section, Materials and Life Science Division, J-PARC Center, [5]Neutron Science and Technology Center, CROSS

MLF Operations in 2023

Beam Operation Status at the MLF

1. Overall

In Japanese Fiscal Year (JFY) 2023, the beam operation at the MLF started on April 1, 2023, and ended on March 31, 2024. Despite the slight influence of the pandemic and the steeply raised electrical fees, the operation was conducted almost as planned.

Figure 1 shows the records of the beam power and availability. In JFY2023, the beam operation started with a power of 822 kW with a double-bunch beam. After April 7, the beam power increased from 822 kW to 850 kW, achieving our goal of beam power of 1 MW for 25 Hz, excluding the duty loss of 12% due to beam sharing to the Main Ring (MR), with a repetition of 1.36 seconds.

J-PARC had two fire accidents in JFY2023 before the summer outage. The first fire accident occurred in the power supply for the MR magnets on April 25, causing the beam to stop entirely in J-PARC from April 26 to May 13. The second accident happened on June 22; the beam operation stopped from June 22 to 27 due to a fire accident in another power supply for the Hadron experimental facility (HD).

On June 2, the beam power was reduced to 800 kW because the cooling water capacity was insufficient to cool the RCS RF cavity due to the high external temperature and humid weather. The beam power was further reduced to 750 kW on June 8 since the hot weather outside continued.

During the summer outage, the spent neutron production target #13 was replaced with a new target #16. During the replacement, no significant problem was found on the target. Since our precise inspection found no severe damage on target #13, we decided to continue with the 850-kW beam after the outage. The proton beam window (PBW) #4, placed before the target to separate the high-vacuum of the accelerator and the helium-filled target vessel, was replaced with PBW #5. The PBW #4 had been used for 3 years. The exchange of PBW was completed without any trouble.

The beam period of 2023A was switched to 2023B on November 21, 2023. During the control system test at the MLF, hydrogen gas was released to the outside due to an error in the cryogenic control system, and it took 9 days to fix the problem. After restarting the beam operation, a target test was conducted. Although the new target #16 was redesigned to mitigate the pitting erosion on the vessel's surface more than the previous ones, the helium gas bubbler introduced to the target did not have an adequate flow rate for unknown reasons. After resuming the beam operation, the flow rate improved gradually. In February 2024, the beam power was resumed at 800 kW.

Because the MLF's air conditioning system was replaced in January 2024, the beam operation stopped

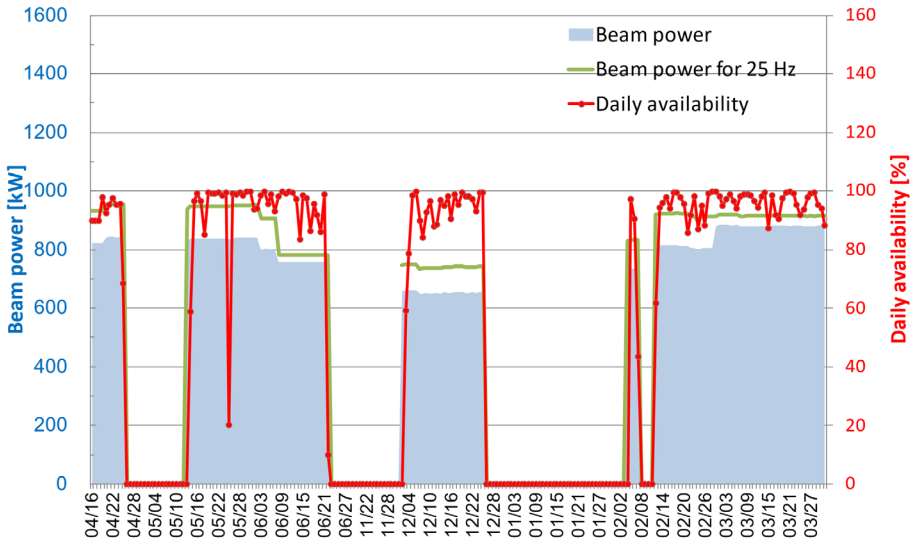

Figure 1. Beam power trend (blue line) at the MLF, beam power for the 25 Hz operation (green line,) i.e., beam power per shot and including the loss of duty for MR delivery, and availability per day (red line).

Table 1. Run cycle, scheduled time, actual beam time, and availability.

Run cycle	Duration	Scheduled time (h)	Beam time (h)	Availability (%)
90	April 16 – June 27	1,536	991	64.5
91	November 21 – March 31	1,920	1,480	77.1
2023A	April 16 – June 27	1,536	991	64.5
2023B	November 21 – March 31	1,920	1,480	77.1
Overall	April 16 – March 31	3,456	2,471	71.5

Table 2. Events that stopped the beam with a duration longer than 3 hours.

Stop date	Cause of beam stop	Stop duration for each event
April 25	Fire incident of power supply for MR	19 days
May 25	Water leakage of RCS RF	12 hours
June 17	LINAC RF	3 hours
June 22	Fire incident of power supply for HD	6 days
November 21	Cryo system of the MLF	9 days
December 4	Cooling water of target station at the MLF	4 hours
December 8	Cooling water of target station at the MLF	4 hours
February 7	Mortor of cooling water pump of RCS	6 days
February 24	Power supply malfunction of 3NBT	3 hours
March 15	Charge exchange foil at RCS	3 hours

in January and resumed on February 5. However, a failure of the cooling water pump for RCS on February 7 stopped the beam operation for nine days.

Table 1 shows the scheduled time and availability in JFY 2023. As shown in the table, beam operation with 64.5% availability was achieved up to June 27 for 2023A. Eventually, the overall availability in JFY 2023 was 71.5%. Because of the two fire accidents and the malfunction of the cryogenic system, the availability has been worse than ever.

The beam operation was stopped on several occasions due to minor failures. Table 2 summarizes the typical causes of a beam stop lasting longer than 3 hours and describes them below.

2. Causes of the beam stop

LINAC:

During JFY2023, there were no shortages of water flow for the magnet at LINAC, which had been the main reason for beam stops before JFY2019. In JFY2023, there were a few failures related to LINAC RF.

3 GeV Rapid Cycling Synchrotron (RCS):

Due to the pump's failure to supply water, restarting the operation in February took a long time. For all available cavities, the resuming time tends to be shorter because tuning is applied before the cavity malfunctions. The charge exchange foil used to accumulate the beam in the ring had malfunctioned. With access to the tunnel, the foil was exchanged.

MLF and 3 GeV beam transport (3NBT)

After the summer outage, the water loop systems for cooling the mercury target vessel and the proton beam window at the MLF failed twice. The gas caused failures in the water loop, exceeding the allowable pressure at the surge tanks. These failures occurred after last year's outage.

The 3NBT quadrupole magnet (QB1) power supply failed. Without this magnet, the beam optics were tuned, minimizing the interruption's duration.

S. Meigo
Neutron Source Section, Materials and Life Science Division, J-PARC Center

Users at the MLF

The MLF beam operation for FY2023 started on April 1 and the beam power increased to 850 kW on April 7 which corresponds to a goal power of 1 MW operation of J-PARC, excluding the duty loss of beam sharing to the Main Ring. After June 2, the beam power was gradually reduced to 750 kW because the cooling power of the RF cavity of RCS was insufficient. Due to two fire accidents and malfunction of the cryogenic system of the neutron source, the beam operation of MLF stopped in April 26 – May 13, June 22 – 27 and November 21 – 30. Resulting overall availability in JFY2023 was 71.5% which was worse than ever.

The total number of users of MLF in FY2023 was 732, a gradual recovery from the impact of the travel restrictions due to COVID-19 continues. The trend for the number of users at neutron and muon facilities since the start of the operations in FY2008 is summarized in Table 1 and Fig. 1.

Table 1. The number of domestic and foreign users by fiscal year.

	FY2008		FY2009		FY2010		FY2011		FY2012		FY2013		FY2014		FY2015	
	Domestic Users	Foreign Users	Domestic Users	Foreign Users	Domestic Users	Foreign Users	Domestic Users	Foreign Users	Domestic Users	Foreign Users	Domestic Users	Foreign Users	Domestic Users	Foreign Users	Domestic Users	Foreign Users
Neutron	107		317		476		259		708		449		824		559	
	95	12	303	14	432	44	238	21	628	80	399	50	711	113	476	83
Muon	18		40		50		23		56		61		91		69	
	18	0	38	2	42	8	21	2	46	10	50	11	78	13	59	10

	FY2016		FY2017		FY2018		FY2019		FY2020		FY2021		FY2022		FY2023	
	Domestic Users	Foreign Users	Domestic Users	Foreign Users	Domestic Users	Foreign Users	Domestic Users	Foreign Users	Domestic Users	Foreign Users	Domestic Users	Foreign Users	Domestic Users	Foreign Users	Domestic Users	Foreign Users
Neutron	852		927		965		940		489		307		406		451	
	744	108	742	185	789	176	827	113	448	41	257	50	296	110	333	118
Muon	99		179		161		138		92		117		238		281	
	83	16	149	30	146	15	127	11	88	4	112	5	203	35	242	39

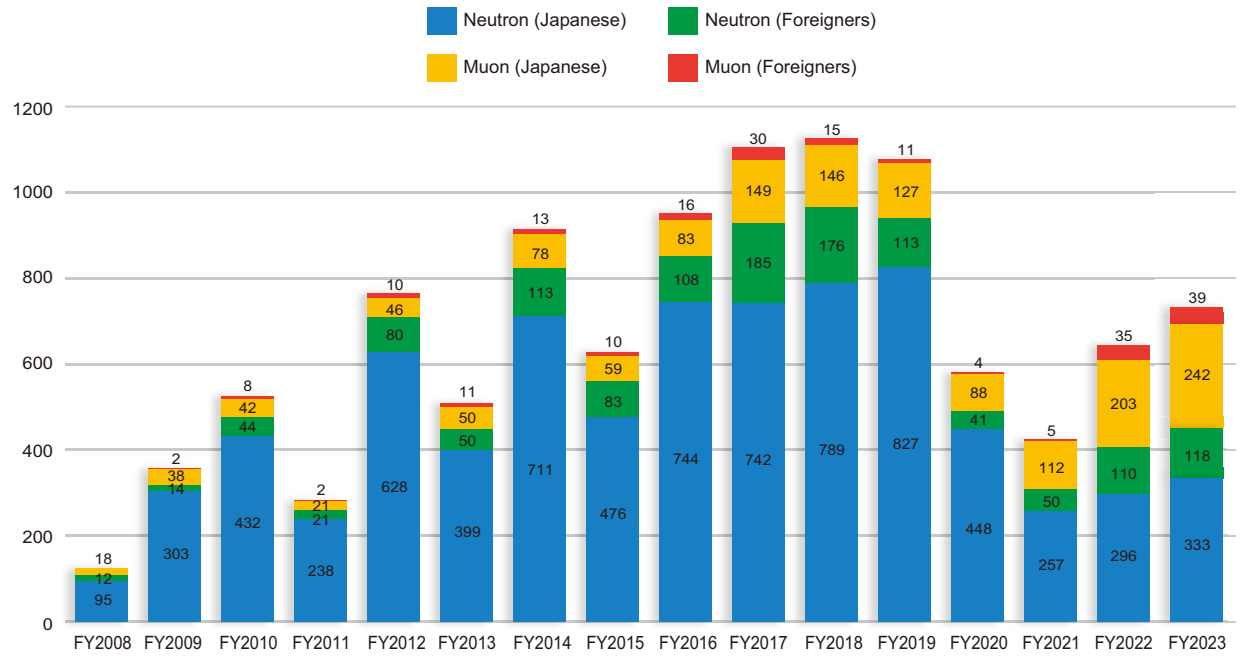

Figure 1. The number of domestic and foreign users by fiscal year.

MLF Proposals Summary – FY2023

Table 1. Number of Proposals by Beamline.

Beam-line	Instrument	2023A		2023B		Full Year			
		Submitted	Approved	Submitted	Approved	Submitted		Approved	
		GU	GU	GU	GU	PU/S	IU	PU/S	IU
BL01	4D-Space Access Neutron Spectrometer - ***4SEASONS***	22(1)	8(1)	29(0)	15(0)	0	1	0	1
BL02	Biomolecular Dynamics Spectrometer - ***DNA***	22(1)	7(1)	18(1)	16(1)	2	1	2	2
BL03	IBARAKI Biological Crystal Diffractometer - ***iBIX*** (100-β)‡	1	1	0	0	0	0	0	0
	(β)†	2	2	1	1	17※	0	16※	0
BL04	Accurate Neutron-Nucleus Reaction Measurement Instrument - ***ANNRI***	5	3	5	3	2	1	2	1
BL05	Neutron Optics and Physics - ***NOP***	4	4	10	7	1	0	1	0
BL06	Village of Neutron Resonance Spin Echo Spectrometers - ***VIN ROSE***	5	2	2	1	2	0	2	0
BL08	Super High Resolution Powder Diffractometer - ***SuperHRPD***	9	6	7	6	1	0	1	0
BL09	Special Environment Neutron Powder Diffractometer - ***SPICA***	3	3	4	4	1	0	1	0
BL10	NeutrOn Beam-line for Observation and Research Use - ***NOBORU***	10	8	11	10	2	1	2	1
BL11	High-Pressure Neutron Diffractometer - ***PLANET***	13(0)	8(0)	9(0)	8(0)	0	2	0	2
BL12	High Resolution Chopper Spectrometer - ***HRC***	5	3	13	8	1	0	1	0
BL14	Cold-Neutron Disk-Chopper Spectrometer - ***AMATERAS***	34	6	44	12	1	1	1	1
BL15	Small and Wide Angle Neutron Scattering Instrument - ***TAIKAN***	28(1)	8(1)	23(1)	17(1)	2	4	2	4
BL16	Soft Interface Analyzer - ***SOFIA***	17	10	18	8	1	1	1	1
BL17	Polarized Neutron Reflectometer - ***SHARAKU***	13(1)	11(1)	16(1)	16(1)	3	3	3	3
BL18	Extreme Environment Single Crystal Neutron Diffractometer - ***SENJU***	23(0)	8(0)	17(0)	10(0)	1	1	1	1
BL19	Engineering Materials Diffractometer - ***TAKUMI***	31	7	26	10	2	1	2	1
BL20	IBARAKI Materials Design Diffractometer - ***iMATERIA*** (100-β)‡	3	3	5	5	0	0	0	0
	(β)‡	28	28	24	24	12	0	12	0
BL21	High Intensity Total Diffractometer - ***NOVA***	15	12	26	13	1	0	1	0
BL22	Energy Resolved Neutron Imaging System - ***RADEN***	17(0)	8(0)	18(2)	18(2)	0	1	0	1
BL23	Polarization Analysis Neutron Spectrometer - ***POLANO***	3	2	3	3	1	0	1	0
D1	Muon Spectrometer for Materials and Life Science Experiments - ***D1***	11(0)	5(0)	16(3)	6(1)	0	1	0	1
D2	Muon Spectrometer for Basic Science Experiments - ***D2***	5(1)	2(0)	8(2)	5(2)	3	1	3	1
S1	General purpose μSR spectrometer - ***ARTEMIS***	25(0)	15(0)	38(0)	21(0)	1	1	1	1
S2	Muonium Laser Physics Apparatus - ***S2***	0(0)	0(0)	0(0)	0(0)	0	1	0	1
U1A	Ultra Slow Muon Microscope - ***U1A***	0	0	0	0	0	1	0	1
U1B	Transmission Muon Microscope - ***U1B***	0	0	0	0	0	0	0	0
H1	High-intensity Muon Beam for General Use - ***H1***	0	0	0	0	0	1	0	1
Total		**354**	**180**	**391**	**247**	**49**	**23**	**48**	**23**

GU : General Use **PU** : Project Use or Ibaraki Pref. Project Use **S** : S-type Proposals **IU** : Instrument Group Use

† : Ibaraki Pref. Exclusive Use Beamtime (β = 80% in FY2022) **‡** : J-PARC Center General Use Beamtime (100-β = 20% in FY2022)

( ) : Proposal Numbers under the New User Promotion (BL01, BL02, BL11, BL15, BL17, BL18, BL22) or P-type proposals (D1,D2, S1) in GU

※ **:** Operations period is held twice per year (for each of the A and B periods), with only the yearly total shown above.

The actual total number of proposals in each beamline named in the table does not match the number shown in the "Total" cell, because some proposals are submitted or approved across multiple beamlines.

Table 2. Number of Long-Term Proposals by Fiscal Year.

Application FY	Submitted	Approved
2021	0	0
2022	5	4
2023	0	0

No Long-Term Proposals were called for FY2021 and FY2023.

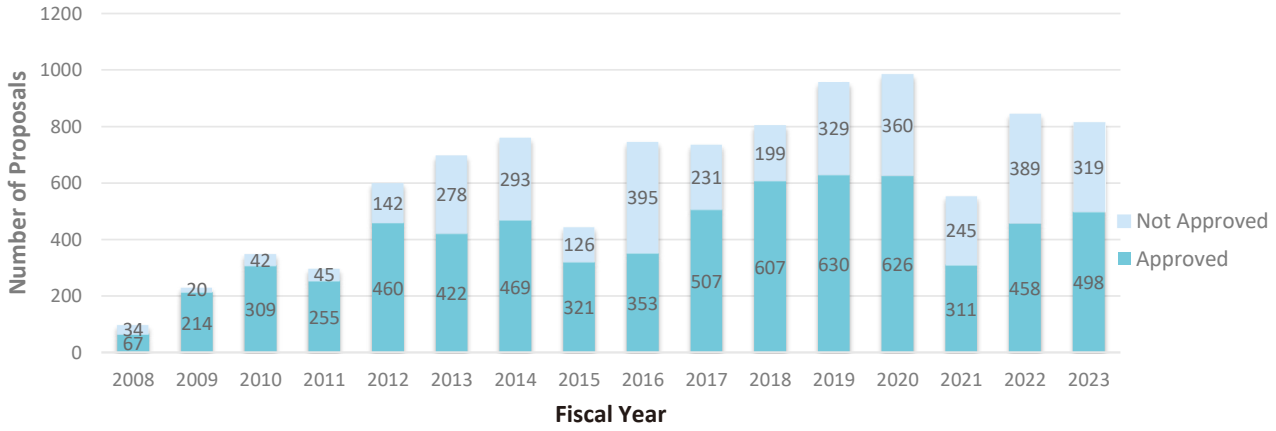

Figure 1. Number of MLF Proposals over Time.

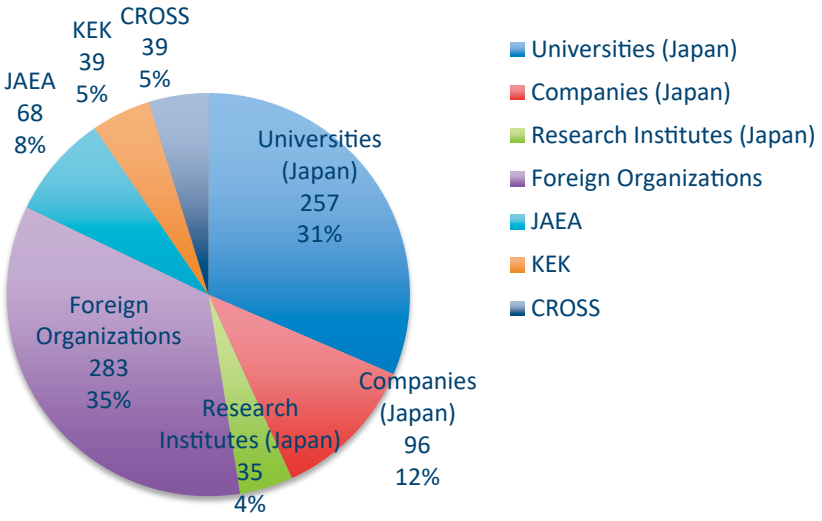

Figure 2. Origin of Submitted Proposals by Affiliation - FY2023.

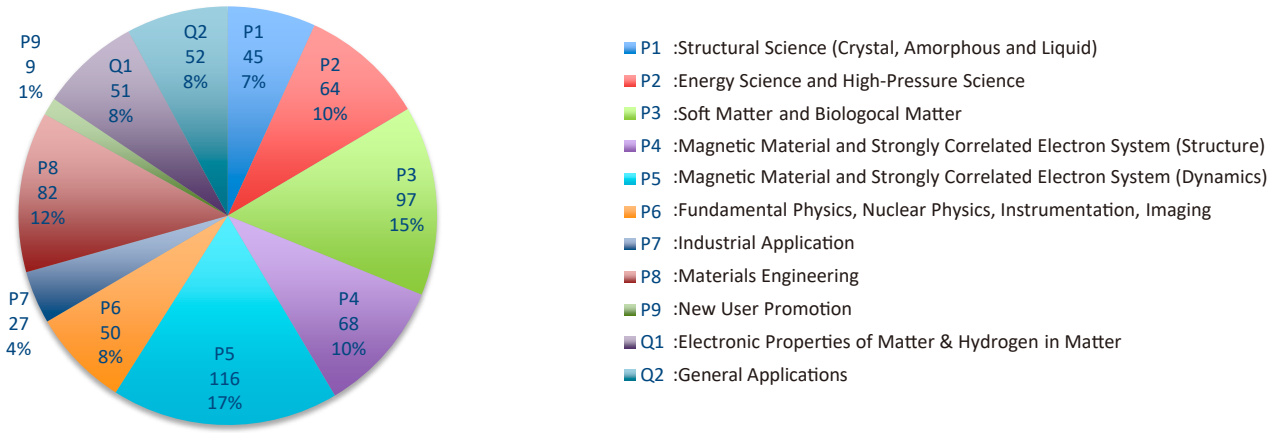

Figure 3. Submitted Proposals by Sub-committee/Expert Panel – FY2023.

MLF Division Staff 2023

*: additional duties

Toshiya Otomo (Head)
Hiroshi Takada (Deputy Head)
Koichiro Shimomura (Deputy Head)
Yukinobu Kawakita (Deputy Head)
Masaaki Sugiyama (Invited Researcher)

Kazuya Aizawa
Eiichi Wakai
Kyoko Aizawa
Kenji Nakajima *

Neutron Source Section

*: additional duties

<JAEA>

Katsuhiro Haga (Leader)
Kenji Sakai (Sub-Leader)
Makoto Teshigawara
Masahide Harada
Tomokazu Aso
Hiroyuki Kogawa
Hidetaka Kinoshita
Takashi Wakui
Takashi Naoe
Koichi Saruta
Masakazu Seki
Shiho Masuda
Gen Ariyoshi
Hideki Muto
Shigeto Tanaka
Yoshinori Kikuchi
Toshiyuki Yasuhara
Masakazu Nakamura
Takahiro Tajima
Akiyoshi Futakawa
Taku Ito
Aya Suzuki
Shizuka Yoshinari
Rie Nemoto
Shin-ichiro Meigo *
Tetsuya Kai *
Kenichi Oikawa *
Shoichi Hasegawa *
Hiroyuki Uehara *
Motoki Ooi *
Yuji Yamaguchi *
Shoya Suda *
Midori Yamamoto *

Neutron Science Section

*: additional duties

<JAEA>

Mitsutaka Nakamura (Leader)
Asami Sano (Sub-Leader)
Ryoichi Kajimoto
Takanori Hattori
Stefanus Harjo
Kenichi Oikawa
Takashi Ohhara
Takenao Shinohara
Hiroyuki Aoki
Tetsuya Kai
Seiko Kawamura
Shinichi Takata
Ryoji Kiyanagi
Yasuhiro Inamura
Maiko Kofu
Wu Gong
Kosuke Hiroi
Naoki Murai
Yusuke Tsuchikawa
Hiromu Tamatsukuri
Kentaro Suzuya
Wenqi Mao
Masami Nirei
Pharit Piyawongwatthana
Tatsuya Ito
Fangzhou Song
Shingo Takahashi
Tatsuya Kikuchi
Masashi Harada
Hiroshi Nozaki
Takeshi Harada
Hideaki Isozaki
Keiichi Inoue
Sakai Motonobu
Motohiro Aizawa
Hiroko Uchiki
Keiko Nemoto
Naoko Shimizu
Koji Kaneko *
Hiroshi Nakagawa *
Atsushi Moriai *
Satoshi Morooka *
Atsushi Kimura *
Shoji Nakamura *
Shunsuke Endo *
Yosuke Toh *
Mariko Segawa *
Masahide Harada *
Masao Watanabe *
Dai Yamazaki *
Takuro Kawasaki *

<KEK>

Testuya Yokoo (Sub-Leader)
Shinichi Ito
Hideki Seto
Toshiya Otomo *
Kazuhiro Mori
Hitoshi Endo
Takashi Ino
Takashi Honda
Taichi Ueta
Masako Yamada
Naokatsu Kaneko
Shuki Torii
Kaoru Taketani
Sara Yamauchi
Hiroyuki Aoki *
Asami Sano *
Kenji Mishima
Takashi Saito
Kazuhiko Ikeuchi
Nur Ika Puji Ayu
Seungyub Song
Yuki Hirota
Ginga Kitahara
Go Ichikawa
Norifumi Yamada
Hidetoshi Oshita *
Tomohiro Seya *
Setsuo Sato *

Technology Development Section

*: additional duties

<JAEA>

Takayuki Oku (Leader)
Kazuyoshi Tatsumi (Sub-Leader)
Masao Watanabe
Yuhua Su
Ryota Komine
Hiroyuki Hasemi
Chie Shibazaki
Takashi Oda
Takayuki Nishiyama
Takuya Okudaira
The Dang Vu
Shusuke Takada
Satoru Fujiwara
Motoyasu Adachi
Wataru Kambara
Yoko Watanabe
Hideaki Takahashi
Ryuta Takahashi
Nirimichi Hashimoto
Hiromichi Tanaka
Hiroyuki Asai
Ariga Asuko
Kenji Sakai *
Tetsuya Kai *
Hiroyuki Kogawa *
Motoki Ooi *
Kentaro Suzuya *
Mitsutaka Nakamura *
Shinichi Takata *
Tatsuya Nakamura *
Yasuhiro Inamura *
Masahide Harada *
Tomokazu Aso *
Seiko Kawamura *

<KEK>

Testuya Yokoo *
Shuki Torii *
Takashi Ino *
Naokatsu Kaneko *
Kaoru Taketani *
Naritoshi Kawamura *
Hiroshi Fujimori *

Neutron Instrumentation Section

*: additional duties

<JAEA>

Tatsuya Nakamura (Leader)
Kentaro Toh (Sub-Leader)
Dai Yamazaki
Ryuji Maruyama
Kaoru Sakasai
Masahiro Tobe
Yukio Hishinuma
Takaaki Hosoya
Hiroki Kajihara
Aoi Yanagi
Masumi Ebine *

<KEK>

Hidetoshi Oshita
Tomohiro Seya
Setsuo Sato

Muon Science Section

*: additional duties

<KEK>

Naritoshi Kawamura (Leader)	Yutaka Ikedo	Shoichiro Nishimura
Akihiro Koda (Sub-Leader)	Yasuo Kobayashi	Natsuki Teshima
Koichiro Shimomura *	Jumpei Nakamura	Eric Michael Kenney II
Patrick Strasser	Shiro Matoba	Ryosuke Kadono
Soshi Takeshita	Takahiro Yuasa	Hiroshi Fujimori
Takayuki Yamazaki	Hikaru Sunagawa	Tsutomu Mibe *
Sohtaro Kanda	Yu Oishi	Shusei Kamioka *
Izumi Umegaki	Yukinori Nagatani	Masato Kimura *

<JAEA>

Wataru Higemoto *	Takashi Ito *	Masayoshi Fujihala *

CROSS Staff 2023

Neutron Science and Technology Center

Director Mitsuhiro Shibayama

Science Coordinators

Shamoto Shinichi
Jun Sugiyama
Matahiro Komuro
Midori Kamimura

Research & Development Division

*: additional duties

Mastato Matsuura (Head)
Kazuki Ohishi (Deputy Head)

<BL01 Group>
Kazuya Kamazawa (Leader)
Kazuki Iida (Sub-Leader)
Kazuhiko Ikeuchi

<BL02 Group>
Takeshi Yamada (Leader)
Taiki Tominaga
Masato Matsuura *

<BL11 Group>
Kenichi Funakoshi * (Leader)
Shinichi Machida (Sub-Leader)
Jun Abe

<BL15 Group>
Kazuki Ohishi (Leader)
Hiroki Iwase
Yukihiko Kawamura

<BL17 Group>
Masato Matsuura * (Leader)
Kazuhiro Akutsu (Sub-Leader)
Takayasu Hanashima
Noboru Miyata *

<BL18 Group>
Akiko Nakao (Leader)
Koji Munakata
Yoshihisa Ishikawa

<BL22 Group>
Hirotoshi Hayashida (Leader)
Joseph Don Parker
Yoshihiro Matsumoto

<Technical Support Group>
Kazuki Ohishi * (Leader)
Nobuo Okazaki (Leader)
Toshiaki Morikawa (Sub-Leader)
Hiroshi Arima
Motoyuki Ishikado
Misaki Ueda
Keiichi Ohuchi
Yoshimasa Ohe
Hiroshi Kira
Masae Sahara
Shuoyuan Zhang
Koji Kiriyama *
Yoshifumi Sakaguchi *
Satoshi Kasai
Yuuki Nagai
Kentaro Moriyama
Takayoshi Ito *

Safety Division

*: additional duties

Mitsuhiro Shibayama * (Head)
Koji Kiriyama (Leader)
Yoshifumi Sakaguchi (Leader)
Tazuko Mizusawa *
Masae Sahara *

Utilization Promotion Division

*: additional duties

Takashi Noma (Head)
Kenich Funakoshi (Deputy Head)
Takayoshi Ito (Leader)
Toshiki Asai (Leader)
Miho Igarashi
Taeko Ishikawa
Tomoko Ishikawa
Maya Endo
Kaoru Ohuchi
Emi Goto
Hideyuki Niitsuma
Tazuko Mizusawa
Nobuo Okazaki *

Administration Division

*: additional duties

Takashi Hikita (Head)
Seiya Konishi * (Deputy Head)
Junichi Sato * (Leader)
Rei Ito (Leader)
Mami Uchida
Tomoko Sakuma
Mutsumi Shiraishi
Hiromi Watanabe
Shinobu Matsumoto *
Maiko Kawata *

Industrial Collaboration Promotion Division

*: additional duties

Mitsuhiro Shibayama * (Head)
Kazuki Mita (Deputy Head)
Noboru Miyata (Leader)
Jun Abe *
Hiroki Iwase *
Yoshihiro Matsumoto *
Seiya Konishi *
Kazuki Mita *
Takeshi Yamada *

Neutron Industrial Application Promotion Center

Director Jun-ichi Suzuki

<User Promotion Group> *: additional duties

Jun-ichi Suzuki * (Leader)
Mamoru Sato (Science Coordinator)
Tetsuroh Minemura (Science Coordinator)
Shiho Tanaka
Rika Oonuki

<BL03 Group> *: additional duties

Katsuhiro Kusaka (Leader)
Terutoshi Sakakura
Haruki Sugiyama
Mamoru Sato *

<BL20 Group> *: additional duties, †: cross appointment

Kazutaka Ikeda (Leader)
Toru Ishigaki
Takafumi Hawai
Tetsuroh Minemura *
Satoshi Koizumi †
Shigeo Sato †
Yohei Noda †
Tomoki Maeda †

<BL Technical Group> *: additional duties

Jun-ichi Suzuki * (Leader)
Shinju Shibata
Junichi Yasuda
Masatoshi Nakamura

Proposals Review System, Committees and Meetings

Proposal Review System

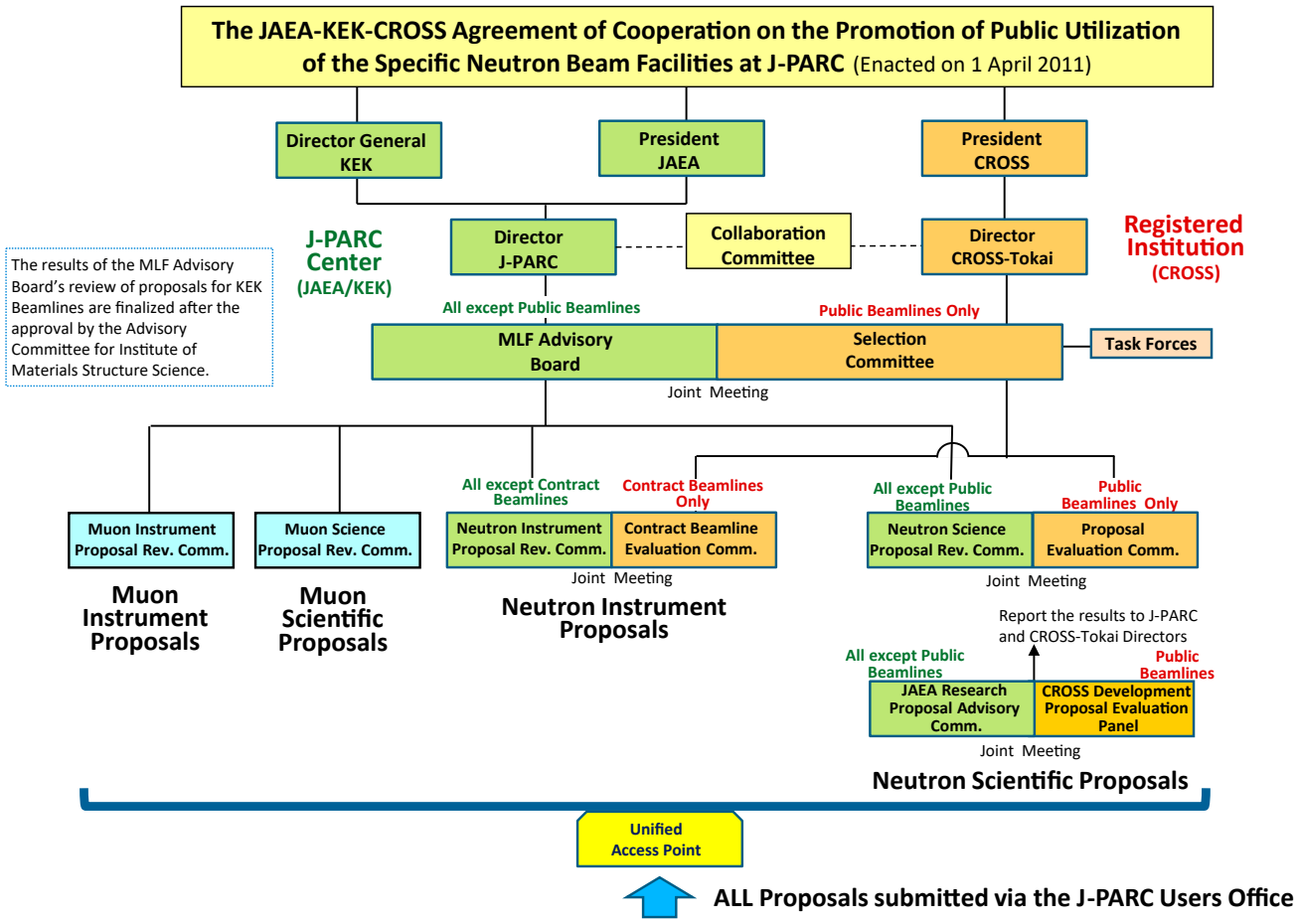

Figure 1. Proposals Review System Framework.

Materials and Life Science Facility Advisory Board

Tadashi Adachi	Sophia University
Taka-hisa Arima (Chair)	The University of Tokyo/RIKEN
Katsuhiro Haga	Japan Atomic Energy Agency
Masahiro Hino	Kyoto University
Kohzo Ito	The University of Tokyo / Research Center for Strategic Materials
Shinichi Itoh	High Energy Accelerator Research Organization
Hiroyuki Kagi	The University of Tokyo
Takashi Kamiyama	High Energy Accelerator Research Organization
Yukinobu Kawakita	Japan Atomic Energy Agency
Naritoshi Kawamura	High Energy Accelerator Research Organization
Shigeru Kimura	Japan Synchrotron Radiation Research Institute
Hiroyuki Kishimoto	Sumitomo Rubber Industries, LTD.
Masato Matsuura	Comprehensive Research Organization for Science and Society
Kenji Nakajima	Japan Atomic Energy Agency
Mitsutaka Nakamura	Japan Atomic Energy Agency
Kenji Ohoyama	Ibaraki University
Yoshie Otake	RIKEN
Toshiya Otomo	High Energy Accelerator Research Organization
Koichiro Shimomura	High Energy Accelerator Research Organization
Yoko Sugawara	Kitasato University
Mikihito Takenaka	Institute for Chemical Research, Kyoto University
Isao Watanabe	RIKEN
Osamu Yamamuro	The University of Tokyo

Term: through March 31, 2025

Neutron Science Proposal Review Committee

Hiroshi Abe	National Defense Academy of Japan
Mitsuhiro Hirai	Gunma University
Shinich Itoh	High Energy Accelerator Research Organization
Yukinobu Kawakita	Japan Atomic Energy Agency
Naritoshi Kawamura	High Energy Accelerator Research Organization
Masaaki Kitaguchi	Nagoya University
Takatsugu Masuda	The University of Tokyo
Koichi Mayumi	The University of Tokyo
Kenji Nakajima	Japan Atomic Energy Agency
Toshiya Otomo	High Energy Accelerator Research Organization
Taku Sato	Tohoku University
Toshiyuki Takamuku	Saga University
Noriyuki Tsuchida	University of Hyogo
Satoshi Tsutsui	Japan Synchrotron Radiation Research Institute
Osamu Yamamuro (chair)	The University of Tokyo

Term: through September 30, 2023

Muon Science Proposal Review Committee

Tadashi Adachi	Sophia University
Kenta Amemiya	High Energy Accelerator Research Organization
Hidehito Asaoka	Japan Atomic Energy Agency
Katsuyuki Fukutani	The University of Tokyo
Wataru Higemoto	Japan Atomic Energy Agency
Adrian Hillier	Rutherford Appleton Laboratory
Hiromi Iinuma	Ibaraki University
Katsuya Inoue	Hiroshima University
Shinichi Itoh	High Energy Accelerator Research Organization
Ryosuke Kadono	High Energy Accelerator Research Organization
Yukinobu Kawakita	Japan Atomic Energy Agency
Naritoshi Kawamura	High Energy Accelerator Research Organization
Yasushi Kino	Tohoku University
Akihiro Koda	High Energy Accelerator Research Organization
Kenya Kubo (chair)	International Christian University
Roderick Macrae	Marian University
Kenji Mishima	High Energy Accelerator Research Organization
Takehito Nakano	Ibaraki University
Seiko Ohira-Kawamura	Japan Atomic Energy Agency
Chihiro Ohmori	High Energy Accelerator Research Organization

Toshiya Otomo	High Energy Accelerator Research Organization
Hideki Seto	High Energy Accelerator Research Organization
Tatsushi Shima	Osaka University
Koichiro Shimomura	High Energy Accelerator Research Organization
Takashi Suemasu	University of Tsukuba
Yoko Sugawara	Kitasato University
Toshiyuki Takayanagi	Saitama University

Term: through March 31, 2023

Selection Committee

Tadashi Adachi	Sophia University
Taka-hisa Arima (Chair)	The University of Tokyo / RIKEN
Masahiro Hino	Kyoto University
Kohzo Ito	The University of Tokyo / Research Center for Strategic Materials
Hiroyuki Kagi	The University of Tokyo
Takashi Kamiyama	High Energy Accelerator Research Organization
Shigeru Kimura	Japan Synchrotron Radiation Research Institute
Hiroyuki Kishimoto	Sumitomo Rubber Industries, LTD.
Kenji Ohoyama	Ibaraki University
Yoshie Otake	RIKEN
Yoko Sugawara	Kitasato University
Mikihito Takenaka	Institute for Chemical Research, Kyoto University
Isao Watanabe	RIKEN
Osamu Yamamuro	The University of Tokyo

Term: through March 31, 2025

Proposal Evaluation Committee

Hiroshi Abe	National Defense Academy of Japan
Mitsuhiro Hirai	Gunma University
Masaaki Kitaguchi	Nagoya University
Takatsugu Masuda	The University of Tokyo
Koichi Mayumi	The University of Tokyo
Toshiya Otomo	High Energy Accelerator Research Organization
Taku Sato	Tohoku University
Toshiyuki Takamuku	Saga University
Noriyuki Tsuchida	University of Hyogo
Satoshi Tsutsui	Japan Synchrotron Radiation Research Institute
Osamu Yamamuro (chair)	The University of Tokyo

Term: through September 30, 2023

Neutron Advisory Committee (NAC)

NAC convened on 19 and 20 February 2024.

Taka-hisa Arima	The University of Tokyo
Christiane Alba-Simionesco	Laboratoire Léon Brillouin
Bertrand Blau	Paul Scherrer Institut
Michael Dayton	Oak Ridge National Laboratory
Phillip King	Rutherford Appleton Laboratory
Toyohiko Kinoshita	Japan Synchrotron Radiation Research Institute
Guenter Muhrer	European Spallation Source
Yoshie Otake	RIKEN
Sungil Park	Korea Atomic Energy Research Institute
Jamie Schulz (chair)	Australian Nuclear Science and Technology Organization
Jon Taylor	European Spallation Source

Muon Advisory Committee (MAC)

MAC convened on 21 and 22 February 2024.

Thomas Prokscha (chair)	Paul Scherrer Institut
Hiroshi Amitsuka	Hokkaido University
Klaus Kirch	ETH Zurich and Paul Scherrer Institut
Kenji Kojima	TRIUMF
Kenya Kubo	International Christian University
Andrew Macfarlane	The University of British Columbia
Martin Månsson	KTH Royal Institute of Technology
Nori Aoi	Osaka University
Tadayuki Takahashi	The University of Tokyo

Workshops, Conferences, Seminars and Schools in 2023

Conferences held jointly by J-PARC MLF and CROSS

2023 Meeting on J-PARC MLF Industrial Use
13-14 Jul. 2023, Akihabara Convention Hall, Tokyo, Online

Photo of 2023 Meeting on J-PARC MLF Industrial Use
(photo courtesy of CROSS)

2023 Workshop on Neutron Imaging
31 Aug.-1 Sep. 2023, Shimbashi Business Forum, Tokyo, Online

2023 年度中性子実験技術基礎講習会（レベル 1 講習会）
26 Jun. 2023, Online

4th ISSE Training School in Tokai
22-26 Oct. 2023, J-PARC Center, Tokai

Photo of ISSE Training School
(photo courtesy of CROSS)

2023 年度中性子実験技術基礎講習会（レベル 1 講習会）
26 Jun. 2023, Online

2023 Z-Code Beginner Level Training Course
10 Aug. -20 Sep. 2023, On-demand

11th Workshop on Neutron Wavelength-Dependent Imaging (NEUWAVE-11)
22-26 Oct. 2023, Miraikan, Tokyo

Photo of NEUWAVE-11
(photo courtesy of CROSS)

2023 Z-Code Intermediate level Training Course
6 Dec. 2023-29 Feb. 2024, On-demand

2023 Quantum Beam Science Festa (The 15th MLF Symposium and the 41st PF Symposium)
5-7 Mar. 2024, Mito City Civic Center, Mito

Photo of Quantum Beam Science Festa
(photo courtesy of IMSS, KEK)

Conferences held by KEK

第 8 回文理融合シンポジウム“量子ビームで歴史を探る ー加速器が紡ぐ文理融合の地平ー”
2-3 Nov. 2023, National Museum of Nature and Science, Ueno, Online

Photo of 文理融合シンポジウム
(photo courtesy of KEK)

Workshops held by KEK

Annual Muon Achievement Report Meeting 2022
26-27 Jul. 2023, KEK Tokai Campus, Tokai

Photo of Annual Muon Achievement Report Meeting 2022
(photo courtesy of KEK)

物構研コロキウム
“ 中性子散乱によるスピントロニクスへの挑戦 ”
31 Jul. 2023, Online

CIQuS 研究会
“ 量子ビームを用いた食品科学 ”
8 Mar. 2024, Mito City Civic Center

CIQuS 研究会
“ マルチプローブ、マルチスケールで見る金属材料の破壊メカニズム ”
8 Mar. 2024, Mito City Civic Center

Workshops and Seminars held by CROSS and other organizations

第 89 回 Spring-8 先端利用技術ワークショップ / 第 4 回放射光・中性子連携利用研究会 / 第 2 回量子ビームを用いた構造材料研究会
26 Apr. 2023, Online

8th Joint Workshop for Complementary Use of Synchrotron Radiation and Neutrons
“ 粉末回折測定研修会 ”
20 Jul., 20 Nov., 2023, 26 Feb. 2024, JRR-3, IBARAKI Quantum Beam Research Center, J-PARC MLF, Tokai

9th Joint Workshop for Complementary Use of Synchrotron Radiation and Neutrons
“ 小角散乱測定研修会 ”
3 Aug., 21 Nov. 2023, IBARAKI Quantum Beam Research Center, JRR-3, Tokai

9th Symposium on the Collaborative Use of Large Research Institutions and the Super Computer
4 Sep. 2023, Akihabara UDX, Tokyo

CBI 研究機構 量子構造生命科学研究所 中性子産業利用推進協議会 生物・生体材料研究会 合同シンポジウム “Beyond Academic Drug Discovery ～若手研究者による牽引～ ”
11 Sep. 2023, Online

第 1 回 小角散乱 < 実験デザイン解析 > 研究会
15 Sep. 2023, Hokkaido University, Online

The 27th CROSSroads Workshop
“ 中性子・ミュオンによるオペランド測定のエネルギー材料への展開 ”
30 Oct. 2023, IBARAKI Quantum Beam Research Center, Online

Photo of 27th CROSSroads Workshop
(photo courtesy of CROSS)

小型中性子施設活用研究会　2023 年度研究会・見学会
“ 小型中性子施設の産業利用の最前線について学ぶ ”
13-14 Dec. 2023, National Institute of Advanced Industrial Science and Technology, Tsukuba, Online

The 28th CROSSroads Workshop
“ 高圧中性子実験の物性研究への展開 ”
11 Jan. 2024, IBARAKI Quantum Beam Research Center, Online

Photo of 28th CROSSroads Workshop
(photo courtesy of CROSS)

2023 Workshop on Magnetic Materials
24 Jan. 2024, Tohoku University, Online

Workshop on Organic materials and Polymers
“ 中性子と軟 X 線を用いた有機・高分子材料解析 ”
1 Feb. 2024, Online

CBI 研究機構 量子構造生命科学研究所 中性子産業利用推進協議会 生物・生体材料研究会 合同シンポジウム
“Synergies between Cryo-EM and other technologies in Pharma”
16 Feb. 2024, Online

ものづくり基盤研究会
“ ー回折・散乱法を中心とした材料強度における課題解決に向けた評価技術ー ”
26 Feb. 2024, Online

2023 Workshop on Liquids and Amorphous Materials
9 Mar. 2024, KEK, Mito City Civic Center, Mito

Workshop on Battery Materials
19 Mar. 2024, Kokukaikan Business Forum, Tokyo

Workshops and Seminars held by Ibaraki Neutron Beamline and other organizations

2023 1st Workshop on iBIX
29 Sep. 2023, Online

2023 2nd Workshop on iBIX
8 Dec. 2023, IBARAKI Quantum Beam Research Center, Tokai, Online

2023 年度中性子構造生物学研究会「動的構造生物学」
22 Mar. 2024, Online

第 5 回量子ビーム材料解析セミナー（令和 5 年度 iMATERIA 研究会）
28 Mar. 2024, Tohoku University, Sendai, Online

第 1 回 量子線リサイクル研究会（令和 5 年度 iMATERIA 研究会）
29 Mar. 2024, Essam Kanda Hall, Tokyo, Online

Schools in 2022

Hello Science from J-PARC
“Neutrons Reveal Microscopic ‘Movement’ of Materials”
26 Apr. 2023, IBARAKI Quantum Beam Research Center, Tokai, Online

Hello Science from J-PARC
“Various Imaging with Muons”
22 Dec. 2023, IBARAKI Quantum Beam Research Center, Tokai, Online

Photo of Hello Science from J-PARC
(photo courtesy of J-PARC)

KEK-IINAS School The 7th Neutron and Muon School
18-22 Dec. 2023, J-PARC Center, Tokai

Photo of Neutron and Muon School
(photo courtesy of CROSS)

Award List

CSJ BCSJ Award
Experimental determination of relationship between intramolecular bond lengths and their stretching vibrational frequencies of N,N-dimethylformamide and Acetonitrile Molecules in the Liquid State
Y. Kameda, Y. Amo, T. Usuki, H. Watanabe, Y. Umebayashi, K. Ikeda, T. Honda, T. Otomo (2024-03-15)

The Iron and Steel Institute of Japan, The Best Year's Paper Award, Sawamura Award
Hierarchical Deformation Heterogeneity during Lüders Band Propagation in an Fe-5Mn-0.1C Medium Mn Steel Clarified through in situ Scanning Electron Microscopy
M. Koyama, T. Yamashita, S. Morooka, Z. Yang, R. S. Varanasi, T. Hojo, T. Kawasaki, S. Harjo (2024-03-13)

Graduate School of Science Awards for Master's studies, Utokyo
H. Kobayashi (2024-03-12)

The JSNS Young Researcher Prize
中性子散乱による液晶性ソフトマターの構造形成に関する研究
F. Nemoto (2024-03-08)

2023 Quantum Beam Science Festa Student Award
Spin dynamics in easy-plane antiferromagnet $CsFeCl_3$ in magnetic fieldsSpin dynamics in easy-plane antiferromagnet $CsFeCl_3$ in magnetic fields
Z. Wei (2024-03-06)

Acta Materialia and Scripta Materialia Outstanding Reviewer Award
Acta/Scripta Materialia's Outstanding Reviewers in 2023
W. Gong (2024-03)

The 29th Outstanding Paper Award of the Physical Society of Japan
Unique Helical Magnetic Order and Field-Induced Phase in Trillium Lattice Antiferromagnet EuPtS
K. Kaneko, M. D. Frontzek, M. Matsuda, A. Nakao, K. Munakata, T. Ohhara, M. Kakihana, Y. Haga, M. Hedo, T. Nakama, Y. Ōnuki (2024-01-22)

Student Presentation Award of the Physical Society of Japan
μSR study on single-component molecular crystal $Au(dexbdt)_2$ with canted antiferromagnetism
R. Tadano (2023-10-23)

Student Presentation Award of the Physical Society of Japan
A challenge of observing hydrogen in metals using white neuron holography
Y. Tomimatsu (2023-10-14)

The Iron and Steel Institute of Japan, The Best Year's Paper Award, Sawamura Award
Hierarchical Deformation Heterogeneity during Lüders Band Propagation in an Fe-5Mn-0.1C Medium Mn Steel Clarified through in situ Scanning Electron Microscopy
M. Koyama, T. Yamashita, S. Morooka, Z. Yang, R. S. Varanasi, T. Hojo, T. Kawasaki, S. Harjo (2023-09-29)

The Japan Institute of Metals and Materials, The Metals Best Poster Award
Excellent combination of strength and ductility of an ultrafine-grained stainless steel at cryogenic temperatures studied by in situ neutron diffraction
M. Wenqi, S. Gao, W. Gong, T. Kawasaki, S. Harjo (2023-09-20)

The Japan Institute of Metals and Materials, The Metals Best Poster Award
Mg/LPSO複相合金における組織と引張変形挙動の相関
K. Yamamoto, M. Sugita, T. Tokunaga, K. Hagihara, T. Mayama, M. Yamasaki, S. Harjo, W. Gong (2023-09-20)

The Japan Institute of Metals and Materials, The Metals Best Poster Award
Cu-Al-Mn合金における極低温弾性熱量効果の直接測定
S. Xu, Y. Song, T. Ito, T. Kawasaki, X. Xu, T. Omori, S. Harjo, W. Gong, R. Kainuma (2023-09-20)

Award of the Japan Society for Analytical Chemistry 2023
有機分子の溶存構造に関するミクロからメゾスコピックレベルにおける分析法の開発
T. Takamuku (2023-09-14)

JOCS Oleomaterial Division Oleo Material Award
Elucidation of structural changes through drying process for polyether modified silicone vesicle systems by using Rheo-SANS & NR
M. Uyama (2023-09-07)

JSEM 学会賞（論文賞）
Effect of Pulsed Laser Irradiation on the Micro-plastic Behavior of Radiation Shielding Lead Glasses
T. Wakui (2023-08-30)

日本食品工学会第 24 回年次大会 優秀発表賞
水分活性変化による最近の活動停止ー再開とガラスー ラバー転移
K. Kawai, T. Sogabe, H. Nakagawa, T. Yamada, S. Koseki (2023-08-28)

JpGU Nishida Prize for Promotion of Geo- and Planetary Science
Research on hydrogen in the Earth's materials at high pressure and temperature based on synchrotron X-ray and Neutron beams
A. Sano-Furukawa (2023-05-25)

The Award of the Society of Polymer Science, Japan (2022)
表面及び界面における高分子鎖の熱運動特性
K. Tanaka (2023-05-25)

Award for Encouragement of Research in Polymer Science; The Society of Polymer Science, Japan (2022)
高分子側鎖による表面物性および構造制御
T. Matsumoto (2023-05-25)

BCSJ: The Bulletin of the Chemical Society of Japan
CSJ: The Chemical Society of Japan
JOCS: Japan Oil Chemists' Society
JpGU: Japan Geoscience Union
JSEM: The Japanese Society for Experimental Mechanics
JSNS: The Japanese Society for Neutron Science
Utokyo: The University of Tokyo

MLF Publication 2023

1 K. Ohishi, D. Igarashi, R. Tatara, I. Umegaki, J. G. Nakamura, A. Koda, M. Månsson, S. Komaba, J. Sugiyama
Ion Dynamics in P2-Na_xCoO_2 Detected with Operando Muon Spin Rotation and Relaxation
ACS Appl. Energy Mater., **6** 8111–8119 (2023).

2 Y. Idemoto, K. Shima, C. Ishibashi, N. Ishida, N. Kitamura
Rate Dependence of the Average Crystal Structure and Electronic Structure of $0.5Li_2MnO_3$ –$0.5LiMn_{10/24}Ni_{7/24}Co_{7/24}O_2$ for a Lithium-Ion Battery Positive Electrode Material in Steady State
ACS Appl. Energy Mater., **6** 8327–8335 (2023).

3 M. Harada, H. Kadoura, S. Takata, H. Iwase, S. Kajiya, T. Suzuki, N. Hasegawa, A. Shinohara, S. Kato
Equation Elucidating the Catalyst-Layer Proton Conductivity in a Polymer Electrolyte Fuel Cell Based on the Ionomer Distribution Determined Using Small-Angle Neutron Scattering
ACS Appl. Mater. Interfaces, **15** 42594–42602 (2023).

4 T. Kämäräinen, K. Kadota, H. Arima-Osonoi, H. Uchiyama, Y. Tozuka
Tailoring the Self-Assembly of Steviol Glycoside Nanocarriers with Steroidal Amphiphiles
ACS Biomater. Sci. Eng., **9** 5747–5760 (2023).

5 S. Misaki, H. Ariga-Miwa, T. U. Ito, T. Yoshida, S. Hasegawa, Y. Nakamura, S. Tokutake, M. Takabatake, K. Shimomura, W.-J. Chun, Y. Manaka, K. Motokura
Pd Nanoparticles on the Outer Surface of Microporous Aluminosilicates for the Direct Alkylation of Benzenes Using Alkanes
ACS Catal., **13** 12281–12287 (2023).

6 T. Murakawa, K. Kurihara, M. Shoji, N. Yano, K. Kusaka, Y. Kawano, M. Suzuki, Y. Shigeta, T. Yano, M. Adachi, K. Tanizawa, T. Okajima
Neutron Crystallography of a Semiquinone Radical Intermediate of Copper Amine Oxidase Reveals a Substrate-Assisted Conformational Change of the Peptidyl Quinone Cofactor
ACS Catal., **13** 12403–12413 (2023).

7 T. Osawa, S. Nagasawa, K. Ninomiya, T. Takahashi, T. Nakamura, T. Wada, A. Taniguchi, I. Umegaki, K. M. Kubo, K. Terada, I.-H. Chiu, S. Takeda, M. Katsuragawa, T. Minami, S. Watanabe, T. Azuma, K. Mizumoto, G. Yoshida, S. Takeshita, M. Tampo, K. Shimomura, Y. Miyake
Development of Nondestructive Elemental Analysis System for Hayabusa2 Samples Using Muonic X-Rays
ACS Earth Space Chem., **7** 699–711 (2023).

8 W. Yoshimune, Y. Higuchi, A. Kato, S. Hibi, S. Yamaguchi, Y. Matsumoto, H. Hayashida, H. Nozaki, T. Shinohara, S. Kato
3D Water Management in Polymer Electrolyte Fuel Cells toward Fuel Cell Electric Vehicles
ACS Energy Lett., **8** 3485–3487 (2023).

9 K. Yamashita, K. Nakayama, K. Komatsu, T. Ohhara, K. Munakata, T. Hattori, A. Sano-Furukawa, H. Kagi
The Hydrogen-Bond Network in Sodium Chloride Tridecahydrate: Analogy with Ice VI
Acta Crystallogr. Sect. B Struct. Sci. Cryst. Eng. Mater., **79** 414–426 (2023).

10 T.-N. Lam, H.-H. Chin, X. Zhang, R. Feng, H. Wang, C.-Y. Chiang, S. Y. Lee, T. Kawasaki, S. Harjo, P. K. Liaw, A.-C. Yeh, T.-F. Chung, E.-W. Huang
Tensile Overload-Induced Texture Effects on the Fatigue Resistance of a CoCrFeMnNi High-Entropy Alloy
Acta Mater., **245** 118585 (2023).

11 W. Woo, Y. S. Kim, H. B. Chae, S. Y. Lee, J. S. Jeong, C. M. Lee, J. W. Won, Y. S. Na, T. Kawasaki, S. Harjo, K. An
Competitive Strengthening between Dislocation Slip and Twinning in Cast-Wrought and Additively Manufactured CrCoNi Medium Entropy Alloys
Acta Mater., **246** 118699 (2023).

12 H. Kwon, P. Sathiyamoorthi, M. K. Gangaraju, A. Zargaran, J. Wang, Y.-U. Heo, S. Harjo, W. Gong, B.-J. Lee, H. S. Kim
High-Density Nanoprecipitates and Phase Reversion via Maraging Enable Ultrastrong yet Strain-Hardenable Medium-Entropy Alloy
Acta Mater., **248** 118810 (2023).

13 W. Gong, S. Harjo, Y. Tomota, S. Morooka, T. Kawasaki, A. Shibata, N. Tsuji
Lattice Parameters of Austenite and Martensite during Transformation for Fe–18Ni Alloy Investigated through In-Situ Neutron Diffraction
Acta Mater., **250** 118860 (2023).

14 S. Harjo, W. Gong, K. Aizawa, T. Kawasaki, M. Yamasaki
Strengthening of aMg and Long-Period Stacking Ordered Phases in a Mg-Zn-Y Alloy by Hot-Extrusion with Low Extrusion Ratio
Acta Mater., **255** 119029 (2023).

15 W. Mao, S. Gao, W. Gong, Y. Bai, S. Harjo, M.-H. Park, A. Shibata, N. Tsuji
Quantitatively Evaluating Respective Contribution of Austenite and Deformation-Induced Martensite to Flow Stress, Plastic Strain, and Strain Hardening Rate in Tensile Deformed TRIP Steel
Acta Mater., **256** 119139 (2023).

16 Y. Izumi, F. Takeiri, K. Okamoto, T. Saito, T. Kamiyama, A. Kuwabara, G. Kobayashi
Electropositive Metal Doping into Lanthanum Hydride for H^- Conducting Solid Electrolyte Use at Room Temperature
Adv. Energy Mater., **13** 2301993 (2023).

17 H. Zhou, J. Izumi, S. Asano, K. Ito, K. Watanabe, K. Suzuki, F. Nemoto, N. L. Yamada, K. Aso, Y. Oshima, R. Kanno, M. Hirayama
Fast Lithium Intercalation Mechanism on Surface-Modified Cathodes for Lithium-Ion Batteries
Adv. Energy Mater., **13** 2302402 (2023).

18 X. Liu, J.-K. Han, Y. Onuki, Y. O. Kuzminova, S. A. Evlashin, M. Kawasaki, K.-D. Liss
In Situ Neutron Diffraction Investigating Microstructure and Texture Evolution upon Heating of Nanostructured CoCrFeNi High-Entropy Alloy
Adv. Eng. Mater., **25** 2201256 (2023).

19 H. Yaguchi, D. Morikawa, T. Saito, K. Tsuda, M. Yashima
High Oxide-Ion Conductivity through the Interstitial Oxygen Site in Sillén Oxychlorides
Adv. Funct. Mater., **33** 2214082 (2023).

20 K. Kubota, T. Asari, S. Komaba
Impact of Ti and Zn Dual-Substitution in P2 Type $Na_{2/3}Ni_{1/3}Mn_{2/3}O_2$ on Ni–Mn and Na-Vacancy Ordering and Electrochemical Properties
Adv. Mater., **35** 2300714 (2023).

21 J. Nakayama, H. Zhou, J. Izumi, K. Watanabe, K. Suzuki, F. Nemoto, N. L. Yamada, R. Kanno, M. Hirayama
Electrical Double Layer Formation at Intercalation Cathode–Organic Electrolyte Interfaces During Initial Lithium-Ion Battery Reactions
Adv. Mater. Interfaces, **11** 2300780 (2023).

22 H. Asai, M. Shibata, M. Takenaka, S. Takata, K. Hiroi, M. Ouchi, T. Terashima
Micelle-crosslinked Hydrogels with Stretchable, Self-healing, and Selectively Adhesive Properties: Random Copolymers Work as Dynamic yet Self-sorting Domains
Aggregate, **4** e316 (2023).

23 T. Sato, H. Takabayashi
Effect of Si/Al Addition on Magnetic Properties of Fe-Co Alloy
AIP Adv., **13** 035306 (2023).

24 C. Shito, H. Kagi, S. Kakizawa, K. Aoki, K. Komatsu, R. Iizuka-Oku, J. Abe, H. Saitoh, A. Sano-Furukawa, T. Hattori
Hydrogen Occupation and Hydrogen-Induced Volume Expansion in $Fe_{0.9}Ni_{0.1}D_x$ at High P-T Conditions
Am. Mineral., **108** 659–666 (2023).

25 Y. Miyagi, J. Jiang, K. Ohishi, Y. Kawamura, J. Suzuki, D. R. Alshalawi, J. Campo, Y. Kousaka, Y. Togawa
Presence of a Chiral Soliton Lattice in the Chiral Helimagnet $MnTa_3S_6$
APL Mater., **11** 101105 (2023).

26 Y. Wang, W. Gong, T. Kawasaki, S. Harjo, K. Zhang, Z. Zhang, B. Li
In Situ Neutron Diffraction Study on the Deformation Behavior of the Plastic Inorganic Semiconductor Ag_2S
Appl. Phys. Lett., **123** 011903 (2023).

27 J. Shimada, A. Tani, T. Yamada, T. Sugahara, T. Hirai, T. Okuchi
Quasi-Elastic Neutron Scattering Studies on Fast Dynamics of Water Molecules in Tetra-n-Butylammonium Bromide Semiclathrate Hydrate
Appl. Phys. Lett., **123** 044104 (2023).

28 H. Yamamoto, H.-C. Wu, A. Miyake, M. Tokunaga, A. Suzuki, T. Honda, H. Kimura
Magnetic Field-Induced Phase Transition in Ilmenite-Type $CoVO_3$
Appl. Phys. Lett., **123** 132404 (2023).

29 Y. Hirota, T. Tominaga, T. Kawabata, Y. Kawakita, Y. Matsuo
Differences in Water Dynamics between the Hydrated Chitin and Hydrated Chitosan Determined by Quasi-Elastic Neutron Scattering
Bioengineering, **10** 622 (2023).

30 E. Saiki, H. Iwase, Y. Horikawa, T. Shikata
Structure and Conformation of Hydroxypropylmethyl Cellulose with a Wide Range of Molar Masses in Aqueous Solution—Effects of Hydroxypropyl Group Addition
Biomacromolecules, **24** 4199–4207 (2023).

31 Y. Hanazono, Y. Hirano, T. Tamada, K. Miki
Description of Peptide Bond Planarity from High-Resolution Neutron Crystallography
Biophys. Physicobiology, **20** e200035 (2023).

32 S. Ito, H. Akama, K. M. Kojima, I. McKenzie, K. Kuwahata, M. Tachikawa
Muon Spin Rotation (μSR) for Characterizing Radical Addition to C=S in Xanthene-9-Thione and Thioxanthene-9-Thione
Bull. Chem. Soc. Jpn., **96** 461–464 (2023).

33 S. Takagi, K. Shimoda, J. Haruyama, H. Kiuchi, K. Okazaki, T. Fukunaga, Z. Ogumi, T. Abe
Operando Structural Analysis of Phase Transition of Graphite Electrode during Li De-Intercalation Process Using Neutron and Synchrotron Radiation X-Ray Diffraction
Carbon, **215** 118414 (2023).

34 T. Xia, T. Yoshii, K. Nomura, K. Wakabayashi, Z.-Z. Pan, T. Ishii, H. Tanaka, T. Mashio, J. Miyawaki, T. Otomo, K. Ikeda, Y. Sato, M. Terauchi, T. Kyotani, H. Nishihara
Chemistry of Zipping Reactions in Mesoporous Carbon Consisting of Minimally Stacked Graphene Layers
Chem. Sci., **14** 8448–8457 (2023).

35 T. Hiromoto, K. Nishikawa, S. Inoue, H. Ogata, Y. Hori, K. Kusaka, Y. Hirano, K. Kurihara, Y. Shigeta, T. Tamada, Y. Higuchi
New Insights into the Oxidation Process from Neutron and X-Ray Crystal Structures of an O_2-Sensitive [NiFe]-Hydrogenase
Chem. Sci., **14** 9306–9315 (2023).

36 M. Akamatsu, K. Sakai, H. Sakai
Dynamic Control of Interfacial Properties and Self-Assembly with Photoirradiation
Chem. Lett., **52** 573–581 (2023).

37 S. Yamagishi, T. Hayashida, R. Misawa, K. Kimura, M. Hagihala, T. Murata, S. Hirose, T. Kimura
Ferroaxial Transitions in Glaserite-Type Compounds: Database Screening, Phonon Calculations, and Experimental Verification
Chem. Mater., **35** 747–754 (2023).

38 Y. Cao, H. Zhou, S. Khmelevskyi, K. Lin, M. Avdeev, C.-W. Wang, B. Wang, F. Hu, K. Kato, T. Hattori, J. Abe, K. Ohara, S. Kawaguchi, Q. Li, M. Fukuda, T. Nishikubo, K. Lee, T. Koike, Q. Liu, J. Miao, J. Deng, B. Shen, M. Azuma, X. Xing
Pressure-Modulated Magnetism and Negative Thermal Expansion in the Ho_2Fe_{17} Intermetallic Compound
Chem. Mater., **35** 3249–3255 (2023).

39 Y. Cao, T. Matsukawa, A. Gibbs, M. Avdeev, C.-W. Wang, H. Wu, Q. Huang, K. Ohoyama, T. Ishigaki, H. Zhou, Q. Li, J. Miao, K. Lin, X. Xing
Quantified Zero Thermal Expansion in Magnetic R_2Fe_{17}-Based Intermetallic Compounds (R = Rare Earth)
Chem. Mater., **35** 4549–4555 (2023).

40 K. Ogawa, H. Suzuki, A. Walsh, R. Abe
Orbital Engineering in Sillén–Aurivillius Phase Bismuth Oxyiodide Photocatalysts through Interlayer Interactions
Chem. Mater., **35** 5532–5540 (2023).

41 Y. Sakuda, T. Murakami, M. Avdeev, K. Fujii, Y. Yasui, J. R. Hester, M. Hagihala, Y. Ikeda, Y. Nambu, M. Yashima
Dimer-Mediated Cooperative Mechanism of Ultrafast-Ion Conduction in Hexagonal Perovskite-Related Oxides
Chem. Mater., **35** 9774–9788 (2023).

42 A. Zhang, K. Deng, J. Sheng, P. Liu, S. Kumar, K. Shimada, Z. Jiang, Z. Liu, D. Shen, J. Li, J. Ren, L. Wang, L. Zhou, Y. Ishikawa, T. Ohhara, Q. Zhang, G. McIntyre, D. Yu, E. Liu, L. Wu, C. Chen, Q. Liu
Chiral Dirac Fermion in a Collinear Antiferromagnet
Chin. Phys. Lett., **40** 126101 (2023).

43 M. Harada, S. Kajiya, T. Mitsuoka, S. Takata, H. Iwase, H. Aoki
Scattering Investigations into the Structures of Polymer-Electrolyte-Fuel-Cell Catalyst Layers Exhibiting Robust Performance against Varying Water Fractions of Catalyst Ink Solvents
Colloids Surf. Physicochem. Eng. Asp., **665** 131183 (2023).

44 H. Nakao, M. Nagao, T. Yamada, K. Imamura, K. Nozaki, K. Ikeda, M. Nakano
Impact of Transmembrane Peptides on Individual Lipid Motions and Collective Dynamics of Lipid Bilayers
Colloids Surf. B Biointerfaces, **228** 113396 (2023).

45 N. Terada, H. Mamiya, H. Saito, T. Nakajima, T. D. Yamamoto, K. Terashima, H. Takeya, O. Sakai, S. Itoh, Y. Takano, M. Hase, H. Kitazawa
Crystal Electric Field Level Scheme Leading to Giant Magnetocaloric Effect for Hydrogen Liquefaction
Commun. Mater., **4** 13 (2023).

46 R. Morikawa, T. Murakami, K. Fujii, M. Avdeev, Y. Ikeda, Y. Nambu, M. Yashima
High Proton Conduction in Ba_2LuAlO_5 with Highly Oxygen-Deficient Layers
Commun. Mater., **4** 42 (2023).

47 E. Nocerino, S. Kobayashi, C. Witteveen, O. K. Forslund, N. Matsubara, C. Tang, T. Matsukawa, A. Hoshikawa, A. Koda, K. Yoshimura, I. Umegaki, Y. Sassa, F. O. Von Rohr, V. Pomjakushin, J. H. Brewer, J. Sugiyama, M. Månsson
Competition between Magnetic Interactions and Structural Instabilities Leading to Itinerant Frustration in the Triangular Lattice Antiferromagnet $LiCrSe_2$
Commun. Mater., **4** 81 (2023).

48 G. Sala, M. B. Stone, G. B. Halász, M. D. Lumsden, A. F. May, D. M. Pajerowski, S. Ohira-Kawamura, K. Kaneko, D. G. Mazzone, G. Simutis, J. Lass, Y. Kato, S.-H. Do, J. Y. Y. Lin, A. D. Christianson
Field-Tuned Quantum Renormalization of Spin Dynamics in the Honeycomb Lattice Heisenberg Antiferromagnet $YbCl_3$
Commun. Phys., **6** 234 (2023).

49 S. Shamoto, H. Yamauchi, K. Iida, K. Ikeuchi, A. E. Hall, Y.-S. Chen, M. K. Lee, G. Balakrishnan, L.-J. Chang
Spiral Spin Cluster in the Hyperkagome Antiferromagnet Mn_3RhSi
Commun. Phys., **6** 248 (2023).

50 I. E. Golub, M. Heere, V. Gounaris, X. Li, T. Steenhaut, J. Wang, K. Robeyns, H.-W. Li, I. Dovgaliuk, K. Ikeda, G. Hautier, Y. Filinchuk
Structural Insight into the Magnesium Borohydride – Ethylenediamine Solid-State Mg-Ion Electrolyte System
Dalton Trans., **52** 2404–2411 (2023).

51 E. M. Germany, N. Thewasano, K. Imai, Y. Maruno, R. S. Bamert, C. J. Stubenrauch, R. A. Dunstan, Y. Ding, Y. Nakajima, X. Lai, C. T. Webb, K. Hidaka, K. S. Tan, H. Shen, T. Lithgow, T. Shiota
Dual Recognition of Multiple Signals in Bacterial Outer Membrane Proteins Enhances Assembly and Maintains Membrane Integrity
eLife, **12** RP90274 (2023).

52 E. M. Germany, N. Thewasano, K. Imai, Y. Maruno, R. S. Bamert, C. J. Stubenrauch, R. A. Dunstan, Y. Ding, Y. Nakajima, X. Lai, C. T. Webb, K. Hidaka, K. S. Tan, H.-H. Shen, T. Lithgow, T. Shiota,
Simultaneous Recognition of Multiple Signals in Bacterial Outer Membrane Proteins Enhance Assembly and Maintain Membrane Integrity
eLife, **12** RP90274 (2023).

53 H. Yamada, K. Ohara, S. Hiroi, A. Sakuda, K. Ikeda, T. Ohkubo, K. Nakada, H. Tsukasaki, H. Nakajima, L. Temleitner, L. Pusztai, S. Ariga, A. Matsuo, J. Ding, T. Nakano, T. Kimura, R. Kobayashi, T. Usuki, S. Tahara, K. Amezawa, Y. Tateyama, S. Mori, A. Hayashi
Lithium Ion Transport Environment by Molecular Vibrations in Ion-Conducting Glasses
ENERGY Environ. Mater., **7** e12612 (2024).

54 T. Saito, R. Motokawa, T. Ohkubo, D. Miura, T. Kumada
Heterogeneous Aggregation of Humic Acids Studied by Small-Angle Neutron and X-Ray Scattering
Environ. Sci. Technol., **57** 9802–9810 (2023).

55 S. Endo, A. Kimura, S. Nakamura, O. Iwamoto, N. Iwamoto, G. Rovira
Covariance of Resonance Parameters Ascribed to Systematic Uncertainties in Experiments
EPJ Web Conf., **281** 00012 (2023).

56 T. Katabuchi, O. Iwamoto, J. Hori, A. Kimura, N. Iwamoto, S. Nakamura, G. Rovira, S. Endo, Y. Shibahara, K. Terada, Y. Kodama, H. Nakano, Y. Sato, S. Matsuura
Fast-Neutron Capture Cross Section Data Measurement of Minor Actinides for Development of Nuclear Transmutation Systems
EPJ Web Conf., **281** 00014 (2023).

57 S. Kunieda, S. Endo, A. Kimura
Updates to the AMUR Code for R-Matrix Analyses on Heavy Nuclei
EPJ Web Conf., **281** 00017 (2023).

58 A. Kimura, S. Nakamura, S. Endo
Uncertainty Estimation in Neutron TOF Measurements with ANNRI
EPJ Web Conf., **281** 00025 (2023).

59 T. Yamazaki, Kawamura Naritoshi, K. Shimomura, Y. Miyake, Y. Oishi, T. Adachi, P. Strasser, A. Koda, H. Fujimori, T. Yuasa, Y. Ikedo, Y. Kobayashi, K. Sasaki, T. Mibe, T. Ushizawa, Y. Higashino, D. Nagao, M. Aoki, K. Hase, S. Kaneko, R. Tagawa, T. Uematsu, Y. Seiya, S. Uetake, T. Masuda, H. Tada, S. Sugiyama, K. Suzuki
New Beamlines and Future Prospects of the J-PARC Muon Facility
EPJ Web Conf., **282** 01016 (2023).

60 Y. Kodama, T. Katabuchi, G. Rovira, A. Kimura, S. Nakamura, S. Endo, H. Nakano, Y. Sato, J. Hori, Y. Shibahara, K. Terada
Measurements of the Neutron Capture Cross Section of Am-243 with the ANNRI Beamline, MLF/J-PARC
EPJ Web Conf., **284** 01024 (2023).

61 H. Nakano, T. Katabuchi, K. Terada, A. Kimura, S. Nakamura, S. Endo, G. Rovira, Y. Kodama
Neutron Capture Cross Section Measurement and Resonance Analysis of ^{107}Pd Using ANNRI at MLF/J-PARC
EPJ Web Conf., **284** 01032 (2023).

62 G. Rovira, A. Kimura, S. Nakamura, S. Endo, O. Iwamoto, N. Iwamoto, T. Katabuchi, Y. Kodama, H. Nakano, J. Hori, Y. Shibahara, T. Kazushi
Neutron Filtering System for Neutron Capture Cross Section Measurement at the ANNRI Beamline of MLF/J-PARC
EPJ Web Conf., **284** 06007 (2023).

63 K. Akutsu-Suyama, M. Ueda, M. Shibayama, K. Ishii, N. Nishi
Effective Synthesis of Deuterated N-Octylamine and Its Analogues
EPJ Web Conf., **286** 01004 (2023).

64 S. Endo, S. Kawamura, T. Okudaira, H. Yoshikawa, G. Rovira, A. Kimura, S. Nakamura, O. Iwamoto, N. Iwamoto
Measurements of Neutron Total and Capture Cross Sections of ^{139}La and Evaluation of Resonance Parameters
Eur. Phys. J. A, **59** 288 (2023).

65 H. Mamiya, Y. Oba, N. Terada, K. Hiroi, T. Shinohara
Polarized Neutron Transmission Spectroscopy on Carbon Steel
IEEE Trans. Magn., **59** 1–5 (2023).

66 H. Iwashita, R. Kiuchi, Y. Hiroshima, Y. Okugawa, T. Sebe, M. Takeda, H. Sato, T. Kamiyama, M. Furusaka, Y. Kiyanagi
Energy-Resolved SEU Cross Section From 10-meV to 800-MeV Neutrons by Time-of-Flight Measurement
IEEE Trans. Nucl. Sci., **70** 216–221 (2023).

67 H. Ubukata, D. Kato, S. Kitade, T. Broux, C. Tassel, D. Schnieders, R. Dronskowski, H. Kageyama
Structural Transformation in LnHS (Ln = La, Nd, Gd, and Er) with Coordination Change between an S-Centered Octahedron and a Trigonal Prism
Inorg. Chem., **62** 6696–6703 (2023).

68 M. Minohara, Y. Dobashi, N. Kikuchi, S. Suzuki, A. Samizo, T. Honda, K. Nishio, Y. Aiura
Control of Hole Density in Russellite Bi_2WO_6 via Intentional Chemical Doping
Inorg. Chem., **62** 8940–8947 (2023).

69 Y. Su, K. Oikawa, T. Shinohara, T. Kai, T. Horino, O. Idohara, Y. Misaka, Y. Tomota
Residual Stress Relaxation by Bending Fatigue in Induction-Hardened Gear Studied by Neutron Bragg Edge Transmission Imaging and X-Ray Diffraction
Int. J. Fatigue, **174** 107729 (2023).

70 T. Yamashita, S. Harjo, T. Kawasaki, S. Morooka, W. Gong, H. Fujii,

Y. Tomota
Martensitic Transformation Behavior of Fe–Ni–C Alloys Monitored by In-Situ Neutron Diffraction during Cryogenic Cooling
ISIJ Int., **64** 192–201 (2024).

71 A. Yasue, K. Kobayashi, M. Yoshioka, T. Noma, K. Okuno, S. Tanaka, Y. Hirata, T. Oh-oka, Y. Kimura, T. Nagai, T. Shobu, Y. Nishio, M. Kanematsu
Evaluation of Bond Repair Effect for Ultra-High-Strength Concrete Specimens by Neutron Diffraction Method
J. Adv. Concr. Technol., **21** 337–350 (2023).

72 P. Thirathipviwat, Y. Onuki, K. Umemura, S. Sato
Microstructure, Dislocation Density and Microhardness of 1 %C-Doped CoCrFeNi Complex Concentrated Alloys during Isochronal Annealing
J. Alloys Compd., **930** 167504 (2023).

73 M. R. Joo, J. H. Jeon, J. G. Jeon, S. J. Lee, K. M. Choi, T. W. Oh, J. W. Lee, S. E. Shin, H. J. Choi, H. Kang, J. H. Shin, K. Ikeda, D. H. Bae
High-Ductility Aluminium Alloys Including Small Sub-Grains with Wide Low Angle Boundary
J. Alloys Compd., **934** 167868 (2023).

74 K. Chu, B. Wang, Q. Li, Y. Onuki, F. Ren
Grain Size Effect on the Temperature-Dependence of Elastic Modulus of Nanocrystalline NiTi
J. Alloys Compd., **934** 167907 (2023).

75 T. Kurumaji, M. Gen, S. Kitou, K. Ikeuchi, M. Nakamura, A. Ikeda, T. Arima
Single Crystal Growths and Magnetic Properties of Hexagonal Polar Semimetals RAuGe (R = Y, Gd–Tm, and Lu)
J. Alloys Compd., **947** 169475 (2023).

76 Y. Onuki, K. Masaoka, S. Sato
Ductile Behavior Assisted by Continuous Dynamic Recrystallization during High-Temperature Deformation of Calcium-Added Magnesium Alloy AZX612
J. Alloys Compd., **962** 171147 (2023).

77 A. Morimura, S. Kamiyama, N. Hayashi, H. Yamamoto, I. Yamada
High-Pressure Syntheses, Crystal Structures, and Magnetic Properties of Novel Quadruple Perovskite Oxides $LaMn_3Ru_2Mn_2O_{12}$ and $LaMn_3Ru_2Fe_2O_{12}$
J. Alloys Compd., **968** 172263 (2023).

78 H. Iwase, M. Akamatsu, Y. Inamura, Y. Sakaguchi, T. Morikawa, S. Kasai, K. Oh-uchi, K. Kobayashi, H. Sakai
New Measurement System Based on Small-Angle Neutron Scattering for Structural Analysis of Light-Responsive Materials
J. Appl. Crystallogr., **56** 110–115 (2023).

79 F. Malamud, J. R. Santisteban, M. A. Vicente Alvarez, M. Busi, E. Polatidis, M. Strobl
An Optimized Single-Crystal to Polycrystal Model of the Neutron Transmission of Textured Polycrystalline Materials
J. Appl. Crystallogr., **56** 143–154 (2023).

80 M.-M. Schiavone, D. H. Lamparelli, C. Daniel, M. Golla, Y. Zhao, H. Iwase, H. Arima-Osonoi, S. Takata, L. Szentmiklosi, B. Maroti, J. Allgaier, A. Radulescu
Extended Q -Range Small-Angle Neutron Scattering to Understand the Morphology of Proton-Exchange Membranes: The Case of the Functionalized Syndiotactic-Polystyrene Model System
J. Appl. Crystallogr., **56** 947–960 (2023).

81 Y. Noda, S. Koizumi, T. Maeda, T. Inada, A. Ishihara
Water Distribution in Human Hair Microstructure Elucidated by Spin Contrast Variation Small-Angle Neutron Scattering
J. Appl. Crystallogr., **56** 1015–1031 (2023).

82 H. Shishido, T. D. Vu, K. Aizawa, K. M. Kojima, T. Koyama, K. Oikawa, M. Harada, T. Oku, K. Soyama, S. Miyajima, M. Hidaka, S. Y. Suzuki, M. M. Tanaka, S. Kawamata, T. Ishida
Orientation Mapping of $YbSn_3$ Single Crystals Based on Bragg-Dip Analysis Using a Delay-Line Superconducting Sensor
J. Appl. Crystallogr., **56** 1108–1113 (2023).

83 H. Arima-Osonoi, S. Takata, S. Kasai, K. Ohuchi, T. Morikawa, N. Miyata, T. Miyazaki, H. Aoki, H. Iwase, K. Hiroi, M. Ogura, T. Kikuchi, H. Takashina, T. Sakayori
Development of a D_2O/H_2O Vapor Generator for Contrast-Variation Neutron Scattering
J. Appl. Crystallogr., **56** 1802–1812 (2023).

84 A. Muneem, J. Yoshida, H. Ekawa, M. Hino, K. Hirota, G. Ichikawa, A. Kasagi, M. Kitaguchi, N. Muto, K. Mishima, J.-U. Nabi, M. Nakagawa, N. Naganawa, T. R. Saito
Investigation of Neutron Imaging Applications Using Fine-Grained Nuclear Emulsion
J. Appl. Phys., **133** 054902 (2023).

85 K. Cho, T. Kamiyama, Y. Horibe, S. Park
Weak Trimer Distortion and Planar Spin Configuration in Hexagonal $Lu_{0.6}In_{0.4}FeO_3$
J. Appl. Phys., **133** 194103 (2023).

86 M. Hiraishi, A. Koda, H. Okabe, R. Kadono, K. A. Dagnall, J. J. Choi, S.-H. Lee
Photo-Excited Charge Carrier Lifetime Enhanced by Slow Cation Molecular Dynamics in Lead Iodide Perovskite $FAPbI_3$
J. Appl. Phys., **134** 055106 (2023).

87 T. Joutsuka, R. Nanasawa, K. Igarashi, K. Horie, M. Sugishima, Y. Hagiwara, K. Wada, K. Fukuyama, N. Yano, S. Mori, A. Ostermann, K. Kusaka, M. Unno
Neutron Crystallography and Quantum Chemical Analysis of Bilin Reductase PcyA Mutants Reveal Substrate and Catalytic Residue Protonation States
J. Biol. Chem., **299** 102763 (2023).

88 T. Okuyama, R. Suzuki, M. Kubo, T. Tsukada, E. Shoji, H. Fukuyama
Comparison of Phase Separation Structures between Undercooled Cu–Fe and Cu–Co Alloys Solidified Under a Static Magnetic Field
J. Chem. Eng. Jpn., **56** 2211117 (2023).

89 S. Hashimoto, S. Yamaguchi, M. Harada, K. Nakajima, T. Kikuchi, K. Ohishi
Anomalous Behavior of Liquid Molecules near Solid Nanoparticles: Novel Interpretation on Thermal Conductivity Enhancement in Nanofluids
J. Colloid Interface Sci., **638** 475–486 (2023).

90 S. Abeykoon, C. Howard, S. Dominijanni, L. Eberhard, A. Kurnosov, D. J. Frost, T. B. Ballaran, H. Terasaki, T. Sakamaki, A. Suzuki, E. Ohtani, A. Sano-Furukawa, J. Abe
Deuterium Content and Site Occupancy in Iron Sulfide at High Pressure and Temperature Determined Using In Situ Neutron Diffraction Measurements
J. Geophys. Res. Solid Earth, **128** e2023JB026710 (2023).

91 S. Kobayashi, E. Nomura, M. Chiba, Y. Kawamura, K. Ohishi, K. Hiroi, J. Suzuki
Polarized Neutron Scattering Study of Hollow Fe_3O_4 Submicron Spherical Particles
J. Magn. Magn. Mater., **569** 170410 (2023).

92 A. Matsushita, N. Tsuchida, E. Ishimaru, N. Hirakawa, W. Gong, S. Harjo
Effects of Loading Direction on the Anisotropic Tensile Properties of Duplex Stainless Steels Based on Phase Strains Obtained by In Situ Neutron Diffraction Experiments
J. Mater. Eng. Perform., **33** 6352–6361 (2024).

93 T. Yokoyama, K. Kusaka, M. Mizuguchi, Y. Nabeshima, S. Fujiwara

Resveratrol Derivatives Inhibit Transthyretin Fibrillization: Structural Insights into the Interactions between Resveratrol Derivatives and Transthyretin
J. Med. Chem., **66** 15511–15523 (2023).

94 Y. Kameda, Y. Amo, T. Usuki, Y. Umebayashi, H. Watanabe, K. Ikeda, T. Otomo
Direct Determination of Intramolecular Structure of D_2O in the First Hydration Shell of Ni^{2+}
J. Mol. Liq., **382** 121927 (2023).

95 T. Kikuchi, Y. Kawakita, K. Nakajima, S. Ohira-Kawamura, Y. Inamura
Overall Picture and Details of Diffusion Dynamics for Liquid Benzene by Quasielastic Neutron Scattering and Mode Distribution Analysis
J. Mol. Liq., **385** 121868 (2023).

96 H. Abe, F. Nemoto, K. Hiroi, S. Takata
Nanoconfined Water in Ionic Liquid and Lyotropic Ionic Liquid Crystals by Small- and Wide-Angle X-Ray and Neutron Scattering: 1-Decyl-3-Methylimidazolium Nitrate
J. Mol. Liq., **386** 122551 (2023).

97 G. Wang, Y. Zhou, T. Yamaguchi, K. Yoshida, K. Ikeda, K. Chai, Z. Liu, Z. Wu
Atomic Insights into the Heterogeneity and the Interface Interactions of Nanoconfined Aqueous Electrolyte Solution
J. Mol. Liq., **388** 122746 (2023).

98 R. Toyoda, K. Usui, T. Hirota, K. Kimura, Y. Onodera, M. R. Cicconi, R. Belli, M. Brehl, J. Lubauer, U. Lohbauer, H. Tajiri, K. Ikeda, T. Hayakawa, D. De Ligny, S. Kohara, K. Hayashi
Atomic Structure of ZrO_2-Doped Li_2O–SiO_2-Based Multi-Component Glasses Revealed by Molecular Dynamics–Reverse Monte Carlo Modeling
J. Non-Cryst. Solids, **616** 122472 (2023).

99 G. Rovira, A. Kimura, S. Nakamura, S. Endo, O. Iwamoto, N. Iwamoto, T. Katabuchi, Y. Kodama, H. Nakano, Y. Sato
^{241}Am Neutron Capture Cross Section Measurement Using the NaI(Tl) Spectrometer of the ANNRI Beamline of J-PARC
J. Nucl. Sci. Technol., **61** 459–477 (2024).

100 M. Akamatsu
Inner and Interfacial Environmental Nanoarchitectonics of Supramolecular Assemblies Formed by Amphiphiles: From Emergence to Application
J. Oleo Sci., **72** 105–116 (2023).

101 Y. Kameda, Y. Amo, T. Usuki, K. Ikeda, T. Honda, T. Otomo
Direct Determination of the Relationship between the Intramolecular Oxygen–Hydrogen Bond Length and Its Stretching Vibrational Frequency of the Methanol Molecule in the Liquid State
J. Phys. Chem. B, **127** 7758–7763 (2023).

102 M. Nakada
Low-Temperature Behaviors, Cold Crystallization, and Glass Transition in Poly(vinylpyrrolidone) Aqueous Solution
J. Phys. Chem. B, **127** 10556–10563 (2023).

103 K. Mori, S. Torii, K. Iwase, T. Abe, T. Fukunaga
Effects of Mixed Phases on Electrical Conductivities for $(CeF_3)_{1-m}(CaF_2)_m$ Fast-Fluoride-Ion-Conducting Solid Electrolytes
J. Phys. Chem. C, **127** 59–68 (2023).

104 A. Kitajou, S. Hiroi, K. Ohara, K. Ikeda, T. Nanami, S. Muto
Cathode Properties of x LiF–$LiCrO_2$ Composites (x = 0–1.5) Prepared by Dry Ball-Milling Method for Lithium Ion Batteries
J. Phys. Chem. C, **127** 2866–2874 (2023).

105 K. Ikeda, T. Kimura, K. Ohara, T. Sato, H. Ohshita, A. Sakuda, A. Hayashi
Vacancies Introduced during the Crystallization Process of the Glass-Ceramics Superionic Conductor, Na_3PS_4, Investigated by Neutron Total Scattering and Reverse Monte Carlo Method
J. Phys. Chem. C, **127** 6199–6206 (2023).

106 Y. Fujita, T. Kimura, M. Deguchi, K. Motohashi, A. Sakuda, M. Tatsumisago, H. Tsukasaki, S. Mori, K. Ikeda, K. Ohara, N. Kuwata, K. Amezawa, A. Hayashi
Structural Investigation of Li_2O–LiI Amorphous Solid Electrolytes
J. Phys. Chem. C, **127** 14687–14693 (2023).

107 Z. Jing, Y. Zhou, T. Yamaguchi, K. Yoshida, K. Ikeda, K. Ohara, G. Wang
Hydration of Alkali Metal and Halide Ions from Static and Dynamic Viewpoints
J. Phys. Chem. Lett., **14** 6270–6277 (2023).

108 T. Kumada, H. Nakagawa, D. Miura, Y. Sekine, R. Motokawa, K. Hiroi, Y. Inamura, T. Oku, K. Ohishi, T. Morikawa, Y. Kawamura, K. Kawai
Polarized Neutrons Observed Nanometer-Thick Crystalline Ice Plates in Frozen Glucose Solution
J. Phys. Chem. Lett., **14** 7638–7643 (2023).

109 H. Kobayashi, K. Komatsu, H. Ito, S. Machida, T. Hattori, H. Kagi
Slightly Hydrogen-Ordered State of Ice IV Evidenced by In Situ Neutron Diffraction
J. Phys. Chem. Lett., **14** 10664–10669 (2023).

110 J. G. Nakamura, Y. Kawakita, H. Okabe, B. Li, K. Shimomura, T. Suemasu
Short-Range Spin Order in Paramagnetic $AgCrSe_2$
J. Phys. Chem. Solids, **175** 111199 (2023).

111 R. Kadono, M. Hiraishi, H. Okabe, A. Koda, T. U Ito
Local Electronic Structure of Interstitial Hydrogen in MgH_2 Inferred from Muon Study
J. Phys. Condens. Matter, **35** 285503 (2023).

112 Y. Sakaguchi, S. Takata, Y. Kawakita, Y. Fujimura, K. Kondo
Direct Observation of Concentration Fluctuations in Au–Si Eutectic Liquid by Small-Angle Neutron Scattering
J. Phys. Condens. Matter, **35** 415403 (2023).

113 K. Horie, M. Mihara, S. Shimizu, K. Kamada
Measurement of Muon Spin Relaxation Time in Various Scintillating Materials
J. Phys. Conf. Ser., **2446** 012040 (2023).

114 M. Tampo, Y. Miyake, T. Kutsuna, T. Saito, S. Takeshita, I. Umegaki, K. Shimomura
Developments of Muonic X-Ray Measurement System for Historical-Cultural Heritage Samples in Japan Proton Accelerator Research Complex (J-PARC)
J. Phys. Conf. Ser., **2462** 012002 (2023).

115 I.-H. Chiu, K. Terada, O. Takahito, C. Park, S. Takeshita, Y. Miyake, K. Ninomiya
Non-Destructive Elemental Analysis of Lunar Materials with Negative Muon Beam at J-PARC
J. Phys. Conf. Ser., **2462** 012004 (2023).

116 Y. Miyake, M. Tampo, S. Takeshita, I. Umegaki, P. Strasser, S. Doiuchi, A. Hashimoto, K. Shimomura, T. Kutsuna, T. Saito, K. Kubo, K. Ninomiya
Integration of Arts and Sciences Using Negative Muon Non-Destructive Analysis at J-PARC MUSE
J. Phys. Conf. Ser., **2462** 012005 (2023).

117 A. D. Pant, K. Ishida, A. Koda, S. Matoba, S. Nishimura, N. Kawamura, K. Shimomura
Search of Ultracold Muonium Generation Material: Muon Spin Rotation and Relaxation Study in SiC

J. Phys. Conf. Ser., **2462** 012016 (2023).

118 I. Umegaki, Y. Kondo, M. Tampo, S. Nishimura, S. Takeshita, Y. Higuchi, H. Kondo, T. Sasaki, K. Shimomura, Y. Miyake
Non-Destructive Operando Measurements of Muonic x-Rays on Li-Ion Battery
J. Phys. Conf. Ser., **2462** 012018 (2023).

119 R. Iwai, M. Abe, S. Fukumura, M. Hiraishi, S. Kanda, S. Kawamura, S. Nishimura, H. Okabe, K. Sasaki, P. Strasser, K. Shimomura, H. Tada, N. Teshima, H. A. Torii
Precise Measurement of the Hyperfine Splitting in Muonium with a High Intensity Pulsed Muon Beam at J-PARC
J. Phys. Conf. Ser., **2462** 012019 (2023).

120 P. Strasser, S. Fukumura, T. Ino, R. Iwai, S. Kanda, S. Kawamura, M. Kitaguchi, S. Nishimura, T. Oku, T. Okudaira, S. Seo, H. M. Shimizu, K. Shimizu, K. Shimomura, H. Tada, T. Tanaka, H. A. Torii, H. Yamauchi, H. Yasuda
Status of the New Muonic Helium Atom HFS Measurements at J-PARC MUSE
J. Phys. Conf. Ser., **2462** 012023 (2023).

121 Y. Oishi, T. Adachi, N. Saito, Y. Ikedo, K. Ishida, S. Kanda, T. Umezawa, S. Kamioka, N. Teshima, J. Nakamura, S. Nakamura, Y. Miyake, M. Iwasaki, S. Wada, K. Shimomura
Intense Lyman-Alpha Light Source for Ultra-Slow Muon Generation
J. Phys. Conf. Ser., **2462** 012026 (2023).

122 S. Kanda
In-Flight Muon Spin Resonance and Muonium Interferometry
J. Phys. Conf. Ser., **2462** 012029 (2023).

123 S. Kanda, N. Teshima, T. Adachi, Y. Ikedo, Y. Miyake, Y. Nagatani, S. Nakamura, Y. Oishi, K. Shimomura, P. Strasser, T. Umezawa
The Ultra-Slow Muon Beamline at J-PARC: Present Status and Future Prospects
J. Phys. Conf. Ser., **2462** 012030 (2023).

124 S. Matoba, N. Kawamura, S. Makimura
Development of Monitoring System for the Muon Rotating Target at J-PARC Using an Infrared Camera
J. Phys. Conf. Ser., **2462** 012031 (2023).

125 K. Shimomura, A. Koda, A. D. Pant, H. Natori, H. Fujimori, I. Umegaki, J. Nakamura, M. Tampo, N. Kawamura, N. Teshima, P. Strasser, R. Kadono, R. Iwai, S. Matoba, S. Nishimura, S. Kanda, S. Takeshita, T. Yuasa, T. Yamazaki, Y. Miyake, Y. Kobayashi, Y. Oishi, Y. Nagatani, Y. Ikedo, W. Higemoto, T. Ito
Present Status of J-PARC MUSE
J. Phys. Conf. Ser., **2462** 012033 (2023).

126 N. Teshima, S. Kanda, T. Adachi, Y. Ikedo, Y. Miyake, Y. Nagatani, Y. Oishi, K. Shimomura, P. Strasser
A Simulation Study of Muon Transport in the Ultra-Slow Muon Beamline at J-PARC
J. Phys. Conf. Ser., **2462** 012036 (2023).

127 J. Sugiyama, I. Umegaki, S. Takeshita, T. Nakano, K. Ninomiya, K. Shimomura, M. Kenya Kubo
Negative Muon Spin Rotation and Relaxation on Li Metal
J. Phys. Conf. Ser., **2462** 012045 (2023).

128 K. Ohishi, D. Igarashi, R. Tatara, Y. Kawamura, K. Hiroi, J. Suzuki, I. Umegaki, S. Nishimura, A. Koda, S. Komaba, J. Sugiyama
Sodium Diffusion in Hard Carbon Studied by Small- and Wide-Angle Neutron Scattering and Muon Spin Relaxation
J. Phys. Conf. Ser., **2462** 012048 (2023).

129 D. P. Sari, M. Kaito, Y. Someya, U. Widyaiswari, I. Watanabe, H. Taniguchi, Y. Ishii
Superconductivity Nearby Quantum Critical Region in Hole-Doped Organic Strange Metal κ-(ET)$_4$Hg$_{3-\delta}$Br$_8$, δ=11%
J. Phys. Conf. Ser., **2462** 012061 (2023).

130 S. Takahashi, R. Kiyanagi, R. Kobayashi, T. Okudaira, T. Ino, J. Suzuki, K. Kakurai, T. Oku
The First Polarized Neutron Diffraction Experiment at the Time-of-Flight Single Crystal Neutron Diffractometer SENJU at J-PARC
J. Phys. Conf. Ser., **2481** 012005 (2023).

131 T. Dang Vu, H. Shishido, K. Aizawa, T. Oku, K. Oikawa, M. Harada, K. M. Kojima, S. Miyajima, K. Soyama, T. Koyama, M. Hidaka, S. Y. Suzuki, M. M. Tanaka, M. Machida, S. Kawamata, T. Ishida
Superconducting Neutron Transmission Imaging for Investigating a Sequential Change in Phase Separations of Low-Melting Wood's Metal
J. Phys. Conf. Ser., **2545** 012019 (2023).

132 K. Oikawa, H. Sato, K. Watanabe, Y. H. Su, T. Shinohara, T. Kai, Y. Kiyanagi, H. Hasemi
Update of Bragg Edge Analysis Software "GUI-RITS"
J. Phys. Conf. Ser., **2605** 012013 (2023).

133 Y. Tsuchikawa, T. Kai, Y. Abe, K. Oikawa, J. D. Parker, T. Shinohara, I. Sato
Development of an Areal Density Imaging for Boron and Other Elements
J. Phys. Conf. Ser., **2605** 012022 (2023).

134 E. Nocerino, O. K. Forslund, H. Sakurai, A. Hoshikawa, N. Matsubara, D. Andreica, A. Zubayer, F. Mazza, T. Saito, J. Sugiyama, I. Umegaki, Y. Sassa, M. Månsson
Unusually Large Magnetic Moment and Tricritical Behavior of the CMR Compound $NaCr_2O_4$ Revealed with High Resolution Neutron Diffraction and μ^+ SR
J. Phys. Mater., **6** 035009 (2023).

135 H. Okabe, M. Hiraishi, A. Koda, Y. Matsushita, T. Ohsawa, N. Ohashi, R. Kadono
Local Magnetism in the Spin-singlet State of VO_2
JPS Conf. Proc., **38** 011117 (2023).

136 A. Shimoda, K. Iwasa, K. Kuwahara, H. Sagayama, H. Nakao, M. Ishikado, T. Ohhara, A. Nakao, A. Hoshikawa, T. Ishigaki
Magnetic Ordering and Structural Phase Transitions of $Nd_3T_4Sn_{13}$ (T = Rh and Ir)
JPS Conf. Proc., **38** 011091 (2023).

137 M. Maeda, M. Segawa, Y. Toh, S. Endo, S. Nakamura, A. Kimura
Development of Correction Method for Sample Density Effect on PGA
J. Radioanal. Nucl. Chem., **332** 2995–2999 (2023).

138 E. Nocerino, U. Stuhr, I. San Lorenzo, F. Mazza, D. G. Mazzone, J. Hellsvik, S. Hasegawa, S. Asai, T. Masuda, S. Itoh, A. Minelli, Z. Hossain, A. Thamizhavel, K. Lefmann, Y. Sassa, M. Månsson
Q-Dependent Electron-Phonon Coupling Induced Phonon Softening and Non-Conventional Critical Behavior in the CDW Superconductor $LaPt_2Si_2$
J. Sci. Adv. Mater. Devices, **8** 100621 (2023).

139 K. Yoshida, J. Abe, Y. Matsumoto, K. Mishima
In Situ Observation of the Decomposition Process of Woodchips in Subcritical- and Supercritical Water by Neutron Imaging
J. Solut. Chem., **53** 680–688 (2023).

140 M. Kaneko, K. Ninomiya, T. Hishida, Y. Takeuchi, K. Otani, M. Nishibori
Enhanced Li-ion Conductivity of Strontium Doped Li-excess Garnet-type $Li_{7+x}La_{3-x}Sr_xZr_2O_{12}$
J. Am. Ceram. Soc., **106** 4480–4487 (2023).

141 T. Nakanishi, Y. Hori, Y. Shigeta, H. Sato, R. Kiyanagi, K. Munakata, T.

Ohhara, A. Okazawa, R. Shimada, A. Sakamoto, O. Sato
Development of an Iron(II) Complex Exhibiting Thermal- and Photoinduced Double Proton-Transfer-Coupled Spin Transition in a Short Hydrogen Bond
J. Am. Chem. Soc., **145** 19177–19181 (2023).

142 Y. Oba, H. Sasaki
Neutron Imaging Technology and Diverse Applications: Observation of Microstructures in Cu Using Bragg Edge Imaging
J. At. Energy Soc. Jpn., **65** 499–502 (2023).

143 T. Taniguchi, S. Kitayama, H. Okabe, J. G. Nakamura, A. Koda, M. Ishikado, M. Fujita
Magnetic Instability of $Pr_3Ru_4Sn_{13}$
J. Phys. Soc. Jpn., **92** 124703 (2023).

144 Y. Liu, N. Miyata, T. Miyazaki, A. Shundo, D. Kawaguchi, K. Tanaka, H. Aoki
Neutron Reflectometry Analysis of Condensed Water Layer Formation at a Solid Interface of Epoxy Resins Under High Humidity
Langmuir, **39** 10154–10162 (2023).

145 H. Iwase, M. Akamatsu, Y. Inamura, Y. Sakaguchi, K. Kobayashi, H. Sakai
Time-Resolved Structural Analysis of Fast-Photoresponsive Surfactant Micelles by Stroboscopic Small-Angle Neutron Scattering
Langmuir, **39** 12357–12364 (2023).

146 S. Yada, M. Kuroda, M. Ohno, T. Koda, T. Yoshimura
Stability and Structural Analysis Using Small-Angle Neutron Scattering for Foam of Homogeneous Polyoxyethylene-Type Nonionic Surfactants with Multibranched Chains
Langmuir, **39** 15355–15361 (2023).

147 K. J. Bichler, B. Jakobi, A. Klapproth, T. Tominaga, R. A. Mole, G. J. Schneider
Side Chain Dynamics of Poly(norbornene)-g-Poly(propylene oxide) Bottlebrush Polymers
Macromol. Rapid Commun., **44** 2200902 (2023).

148 Y. Song, K. Fukuzawa, T. Hirayama, N. Yamashita, N. L. Yamada, S. Itoh, N. Azuma, H. Zhang
Effects of Polarity of Polymers on Conformation and Lubricating Film Formation of Adsorbed Films
Macromolecules, **56** 1954–1964 (2023).

149 Y. Shiraki, M. Saito, N. L. Yamada, K. Ito, H. Yokoyama
Adhesion to Untreated Polyethylene and Polypropylene by Needle-like Polyolefin Crystals
Macromolecules, **56** 2429–2436 (2023).

150 M. Hibino, S. Takata, K. Hiroi, H. Aoki, T. Terashima
Dynamic Exchange of Amphiphilic Random Copolymers between Micelles in Water: Kinetics and Mechanism Analyzed by TR-SANS
Macromolecules, **56** 2955–2964 (2023).

151 M. Saito, N. L. Yamada, K. Ito, H. Yokoyama
Mechanical Properties and Swelling Behaviors of Ultrathin Chemically Cross-Linked Polybutadiene Films
Macromolecules, **56** 4000–4011 (2023).

152 R. Sujita, S. Imai, M. Ouchi, H. Aoki, T. Terashima
Microphase Separation of Cationic Homopolymers Bearing Alkyl Ammonium Salts into Sub-4 Nm Lamellar Materials with Water Intercalation Channels
Macromolecules, **56** 9738–9749 (2023).

153 T. Wakui, Y. Takagishi, M. Futakawa
Cavitation Damage Prediction in Mercury Target for Pulsed Spallation Neutron Source Using Monte Carlo Simulation
Materials, **16** 5830 (2023).

154 Z. Zhang, X. Jiang, T. Hattori, X. Xu, M. Li, C. Yu, Z. Zhang, D. Yu, R. Mole, S. Yano, J. Chen, L. He, C.-W. Wang, H. Wang, B. Li, Z. Zhang
A Colossal Barocaloric Effect Induced by the Creation of a High-Pressure Phase
Mater. Horiz., **10** 977–982 (2023).

155 P. Thirathipviwat, S. Nozawa, M. Furusawa, Y. Onuki, M. Hasegawa, K. Matsumoto, S. Sato
A Correlation between Texture Evolution and Dislocation Density in Al-Mg Alloys during Uniaxial Tensile Deformation
Mater. Lett., **349** 134829 (2023).

156 R. B. Figueiredo
In-Situ Heating Observations on Microstructure Relaxation of Ultrafine-grained High-Entropy Alloys Using Neutron Diffraction and Laser-scanning Confocal Microscopy
Materials Research Proceedings, **32** 235–243 (2023).

157 N. Tsuchida, Y. Wada, H. Minami, Y. Toji
Role of Retained Austenite in Improving the Mechanical Properties of 1.5 GPa-Grade High-Strength Martensitic Steels
Mater. Sci. Eng. A, **873** 144989 (2023).

158 Y. Wang, H. Wang, Y. Su, P. Xu, T. Shinohara
Cryogenic Impact Fracture Behavior of a High-Mn Austenitic Steel Using Electron Backscatter Diffraction and Neutron Bragg-Edge Transmission Imaging
Mater. Sci. Eng. A, **887** 145768 (2023).

159 N. Tsuchida, R. Ueji, W. Gong, T. Kawasaki, S. Harjo
Effects of Pre-Strain and Tempering on Mechanical Properties in High-Strength Martensitic Steels
Mater. Sci. Forum, **1105** 129–133 (2023).

160 Y. Fang, L. Kong, R. Wang, Z. Zhang, Z. Li, Y. Wu, K. Bu, X. Liu, S. Yan, T. Hattori, N. Li, K. Li, G. Liu, F. Huang
Pressure Engineering of van Der Waals Compound RhI_3: Bandgap Narrowing, Metallization, and Remarkable Enhancement of Photoelectric Activity
Mater. Today Phys., **34** 101083 (2023).

161 S. Harjo, W. Gong, K. Aizawa, T. Kawasaki, M. Yamasaki, T. Mayama, Y. Kawamura
Effect of Extrusion Ratio in Hot-Extrusion on Kink Deformation during Compressive Deformation in an aMg/LPSO Dual-Phase Magnesium Alloy Monitored by In Situ Neutron Diffraction
Mater. Trans., **64** 766–773 (2023).

162 M. Kawasaki, J.-K. Han, X. Liu, S.-C. Moon, K.-D. Liss
Synchrotron High-Energy X-Ray & Neutron Diffraction, and Laser-Scanning Confocal Microscopy: In-Situ Characterization Techniques for Bulk Nanocrystalline Metals
Mater. Trans., **64** 1683–1694 (2023).

163 T. Tsuru, K. Nishimura, K. Matsuda, N. Nunomura, T. Namiki, S. Lee, W. Higemoto, T. Matsuzaki, M. Yamaguchi, K. Ebihara, K. Shimizu, H. Toda
Identification of Hydrogen Trapping in Aluminum Alloys Via Muon Spin Relaxation Method and First-Principles Calculations
Metall. Mater. Trans. A, **54** 2374–2383 (2023).

164 I. Chiu, K. Terada, T. Osawa, C. Park, S. Takeshita, Y. Miyake, K. Ninomiya
Non-destructive Elemental Analysis of Lunar Meteorites Using a Negative Muon Beam
Meteorit. Planet. Sci., **58** 1333–1344 (2023).

165 M. Hirai, S. Arai, H. Iwase
Fibrillization Process of Human Amyloid-Beta Protein (1–40) under a Molecular Crowding Environment Mimicking the Interior of Living Cells Using Cell Debris
Molecules, **28** 6555 (2023).

166 M. Teshigawara, Y. Ikeda, M. Yan, K. Muramatsu, K. Sutani, M. Fukuzumi, Y. Noda, S. Koizumi, K. Saruta, Y. Otake
New Material Exploration to Enhance Neutron Intensity below Cold Neutrons: Nanosized Graphene Flower Aggregation
Nanomaterials, **13** 76 (2023).

167 Y. Yasui, M. Tansho, K. Fujii, Y. Sakuda, A. Goto, S. Ohki, Y. Mogami, T. Iijima, S. Kobayashi, S. Kawaguchi, K. Osaka, K. Ikeda, T. Otomo, M. Yashima
Hidden Chemical Order in Disordered $Ba_7Nb_4MoO_{20}$ Revealed by Resonant X-Ray Diffraction and Solid-State NMR
Nat. Commun., **14** 2337 (2023).

168 S. Bao, Z.-L. Gu, Y. Shangguan, Z. Huang, J. Liao, X. Zhao, B. Zhang, Z.-Y. Dong, W. Wang, R. Kajimoto, M. Nakamura, T. Fennell, S.-L. Yu, J.-X. Li, J. Wen
Direct Observation of Topological Magnon Polarons in a Multiferroic Material
Nat. Commun., **14** 6093 (2023).

169 K. Saito, M. Yashima
High Proton Conductivity within the 'Norby Gap' by Stabilizing a Perovskite with Disordered Intrinsic Oxygen Vacancies
Nat. Commun., **14** 7466 (2023).

170 P. Park, W. Cho, C. Kim, Y. An, Y.-G. Kang, M. Avdeev, R. Sibille, K. Iida, R. Kajimoto, K. H. Lee, W. Ju, E.-J. Cho, H.-J. Noh, M. J. Han, S.-S. Zhang, C. D. Batista, J.-G. Park
Tetrahedral Triple-Q Magnetic Ordering and Large Spontaneous Hall Conductivity in the Metallic Triangular Antiferromagnet $Co_{1/3}TaS_2$
Nat. Commun., **14** 8346 (2023).

171 I. Konuma, D. Goonetilleke, N. Sharma, T. Miyuki, S. Hiroi, K. Ohara, Y. Yamakawa, Y. Morino, H. B. Rajendra, T. Ishigaki, N. Yabuuchi
A near Dimensionally Invariable High-Capacity Positive Electrode Material
Nat. Mater., **22** 225–234 (2023).

172 Q. Ren, M. K. Gupta, M. Jin, J. Ding, J. Wu, Z. Chen, S. Lin, O. Fabelo, J. A. Rodríguez-Velamazán, M. Kofu, K. Nakajima, M. Wolf, F. Zhu, J. Wang, Z. Cheng, G. Wang, X. Tong, Y. Pei, O. Delaire, J. Ma
Extreme Phonon Anharmonicity Underpins Superionic Diffusion and Ultralow Thermal Conductivity in Argyrodite Ag_8SnSe_6
Nat. Mater., **22** 999–1006 (2023).

173 H. Takagi, R. Takagi, S. Minami, T. Nomoto, K. Ohishi, M.-T. Suzuki, Y. Yanagi, M. Hirayama, N. D. Khanh, K. Karube, H. Saito, D. Hashizume, R. Kiyanagi, Y. Tokura, R. Arita, T. Nakajima, S. Seki
Spontaneous Topological Hall Effect Induced by Non-Coplanar Antiferromagnetic Order in Intercalated van Der Waals Materials
Nat. Phys., **19** 961–968 (2023).

174 C. Kim, S. Kim, P. Park, T. Kim, J. Jeong, S. Ohira-Kawamura, N. Murai, K. Nakajima, A. L. Chernyshev, M. Mourigal, S.-J. Kim, J.-G. Park
Bond-Dependent Anisotropy and Magnon Decay in Cobalt-Based Kitaev Triangular Antiferromagnet
Nat. Phys., **19** 1624–1629 (2023).

175 S. Han, S. Dai, J. Ma, Q. Ren, C. Hu, Z. Gao, M. Duc Le, D. Sheptyakov, P. Miao, S. Torii, T. Kamiyama, C. Felser, J. Yang, C. Fu, T. Zhu
Strong Phonon Softening and Avoided Crossing in Aliovalence-Doped Heavy-Band Thermoelectrics
Nat. Phys., **19** 1649–1657 (2023).

176 F. Wu, S. Bao, J. Zhou, Y. Wang, J. Sun, J. Wen, Y. Wan, Q. Zhang
Fluctuation-Enhanced Phonon Magnetic Moments in a Polar Antiferromagnet
Nat. Phys., **19** 1868–1875 (2023).

177 Y. Shangguan, S. Bao, Z.-Y. Dong, N. Xi, Y.-P. Gao, Z. Ma, W. Wang, Z. Qi, S. Zhang, Z. Huang, J. Liao, X. Zhao, B. Zhang, S. Cheng, H. Xu, D. Yu, R. A. Mole, N. Murai, S. Ohira-Kawamura, L. He, J. Hao, Q.-B. Yan, F. Song, W. Li, S.-L. Yu, J.-X. Li, J. Wen
A One-Third Magnetization Plateau Phase as Evidence for the Kitaev Interaction in a Honeycomb-Lattice Antiferromagnet
Nat. Phys., **19** 1883–1889 (2023).

178 P. Wu, N. Murai, T. Li, R. Kajimoto, M. Nakamura, M. Kofu, K. Nakajima, K. Xia, K. Peng, Y. Zhang, W. Zhao
Experimental Evidence for the Significance of Optical Phonons in Thermal Transport of Tin Monosulfide
New J. Phys., **25** 013032 (2023).

179 K. Yadav, K. P, S. Singh, M. Hagihala, K. Mukherjee
Existence of Complex Magnetic Ground State and Topological Hall Effect in Centrosymmetric Silicide DyScSi
New J. Phys., **25** 123030 (2023).

180 N. Sumi, G. Ichikawa, K. Mishima, Y. Makida, M. Kitaguchi, S. Makise, S. Matsuzaki, T. Nagano, M. Tanida, H. Uehara, K. Yano, H. Otono, T. Yoshioka
The LiNA Experiment: Development of Multi-Layered Time Projection Chamber
Nucl. Instrum. Methods Phys. Res. Sect. Accel. Spectrometers Detect. Assoc. Equip., **1045** 167586 (2023).

181 H. Akatsuka, T. Andalib, B. Bell, J. Berean-Dutcher, N. Bernier, C. P. Bidinosti, C. Cude-Woods, S. A. Currie, C. A. Davis, B. Franke, R. Gaur, P. Giampa, S. Hansen-Romu, M. T. Hassan, K. Hatanaka, T. Higuchi, C. Gibson, G. Ichikawa, I. Ide, S. Imajo, T. M. Ito, B. Jamieson, S. Kawasaki, M. Kitaguchi, W. Klassen, E. Korkmaz, F. Kuchler, M. Lang, M. Lavvaf, T. Lindner, M. Makela, J. Mammei, R. Mammei, J. W. Martin, R. Matsumiya, E. Miller, K. Mishima, T. Momose, S. Morawetz, C. L. Morris, H. J. Ong, C. M. O'Shaughnessy, M. Pereira-Wilson, R. Picker, F. Piermaier, E. Pierre, W. Schreyer, S. Sidhu, D. Stang, V. Tiepo, S. Vanbergen, R. Wang, D. Wong, N. Yamamoto
Characterization of Electroless Nickel-Phosphorus Plating for Ultracold-Neutron Storage
Nucl. Instrum. Methods Phys. Res. Sect. Accel. Spectrometers Detect. Assoc. Equip., **1049** 168106 (2023).

182 M. Sato, T. Kurihara, F. Naito, T. Sugimura, H. Kumada, S. Tanaka, T. Ohba, N. Nagura
Non-Destructive Measurement of the Beryllium Thickness of the iBNCT Neutron-Generation Target Using Negative Muons
Nucl. Instrum. Methods Phys. Res. Sect. Accel. Spectrometers Detect. Assoc. Equip., **1052** 168291 (2023).

183 M. Tsunoda, T. Honda, K. Ikeda, H. Ohshita, W. Kambara, T. Otomo
Radial Collimator Performance and Future Collimator Updates for the High-Intensity Total Scattering Diffractometer NOVA at J-PARC
Nucl. Instrum. Methods Phys. Res. Sect. Accel. Spectrometers Detect. Assoc. Equip., **1055** 168484 (2023).

184 S. Nishimura, H. Okabe, M. Hiraishi, M. Miyazaki, J. G. Nakamura, A. Koda, R. Kadono
Development of Transient μSR Method for High-Flux Pulsed Muons
Nucl. Instrum. Methods Phys. Res. Sect. Accel. Spectrometers Detect. Assoc. Equip., **1056** 168669 (2023).

185 S. Itoh, S. Fukumura, T. Fujiie, M. Kitaguchi, H. M. Shimizu
Demonstration of Simultaneous Measurement of the Spin Rotation of Dynamically-Diffracted Neutrons from Multiple Crystal Planes Using Pulsed Neutrons
Nucl. Instrum. Methods Phys. Res. Sect. Accel. Spectrometers Detect. Assoc. Equip., **1057** 168734 (2023).

186 S. Endo, A. Kimura, S. Nakamura, O. Iwamoto, N. Iwamoto, G. Rovira, Y. Toh, M. Segawa, M. Maeda
Measurements of the Neutron Total and Capture Cross Sections and

Derivation of the Resonance Parameters of ^{181}Ta
Nucl. Sci. Eng., **198** 786–803 (2023).

187 Y. Nakazawa, E. Cicek, H. Ego, Y. Fukao, K. Futatsukawa, K. Hasegawa, T. Iijima, H. Iinuma, K. Inami, K. Ishida, N. Kawamura, R. Kitamura, Y. Kondo, T. Mibe, Y. Miyake, T. Morishita, M. Otani, N. Saito, K. Shimomura, Y. Sue, K. Sumi, K. Suzuki, T. Takayanagi, Y. Takeuchi, J. Tojo, T. Yamazaki, H. Yasuda, M. Yotsuzuka
Interdigital H-Mode Drift Tube Linear Accelerator for a Muon Linear Accelerator
Phys. Sci. Forum, **8** 20

188 T. Nakanishi, Y. Hori, Y. Shigeta, H. Sato, S.-Q. Wu, R. Kiyanagi, K. Munakata, T. Ohhara, O. Sato
Observation of Proton-Transfer-Coupled Spin Transition by Single-Crystal Neutron-Diffraction Measurement
Phys. Chem. Chem. Phys., **25** 12394–12400 (2023).

189 S. K. Dey, K. Ishida, H. Okabe, M. Hiraishi, A. Koda, T. Honda, J. Yamaura, H. Kageyama, R. Kadono
Local Spin Dynamics in the Geometrically Frustrated Mo Pyrochlore Antiferromagnet $Lu_2Mo_2O_{5-y}N_2$
Phys. Rev. B, **107** 024407 (2023).

190 M. Fujihala, M. Hagihala, K. Morita, N. Murai, A. Koda, H. Okabe, S. Mitsuda
Spin Gap in the Weakly Interacting Quantum Spin Chain Antiferromagnet $KCuPO_4{\cdot}H_2O$
Phys. Rev. B, **107** 054435 (2023).

191 Z. Liu, Y. Araki, T. Arima, S. Itoh, S. Asai, T. Masuda
Spin Excitation in the Coupled Honeycomb Lattice Compound Ni_2InSbO_6
Phys. Rev. B, **107** 064428 (2023).

192 M. Pardo-Sainz, A. Toshima, G. André, J. Basbus, G. J. Cuello, V. Laliena, T. Honda, T. Otomo, K. Inoue, Y. Hosokoshi, Y. Kousaka, J. Campo
New (αβγ)-Incommensurate Magnetic Phase Discovered in the $MnCr_2O_4$ Spinel at Low Temperatures
Phys. Rev. B, **107** 144401 (2023).

193 H. Tamatsukuri, K. Fukui, S. Iimura, T. Honda, T. Tada, Y. Murakami, J. Yamaura, Y. Kuramoto, H. Sagayama, T. Yamada, M. Matsuura, K. Shibata, M. Kofu, Y. Kawakita, K. Ikeda, T. Otomo, H. Hosono
Quasielastic Neutron Scattering Probing H^- Dynamics in the H^- Conductors $LaH_{3-2x}O_x$
Phys. Rev. B, **107** 184114 (2023).

194 H. Kikuchi, S. Asai, H. Manaka, M. Hagihala, S. Itoh, T. Masuda
Inelastic Neutron Scattering in the Weakly Coupled Triangular Spin Tube Candidate $CsCrF_4$
Phys. Rev. B, **107** 184405 (2023).

195 S. Yano, C.-W. Wang, J. S. Gardner, W.-T. Chen, K. Iida, R. A. Mole, D. Louca
Weak Trimerization in the Frustrated Two-Dimensional Triangular Heisenberg Antiferromagnet $Lu_yY_{1-y}MnO_3$
Phys. Rev. B, **107** 214407 (2023).

196 S. Aji, T. Oda, Y. Fujishiro, N. Kanazawa, H. Saito, H. Endo, M. Hino, S. Itoh, T. Arima, Y. Tokura, T. Nakajima
Direct Observations of Spin Fluctuations in Hedgehog–Anti-Hedgehog Spin Lattice States in $MnSi_{1-x}Ge_x$ (x = 0.6 and 0.8) at Zero Magnetic Field
Phys. Rev. B, **108** 054445 (2023).

197 T. Kitazawa, Y. Ikeda, T. Sakakibara, A. Matsuo, Y. Shimizu, Y. Tokunaga, Y. Haga, K. Kindo, Y. Nambu, K. Ikeuchi, K. Kamazawa, M. Ohkawara, M. Fujita
Observation of Field-Induced Single-Ion Magnetic Anisotropy in a Multiorbital Kondo Alloy (Lu, Yb) Rh_2Zn_{20}
Phys. Rev. B, **108** 085105 (2023).

198 H. Saito, F. Kon, H. Hidaka, H. Amitsuka, C. Kwanghee, M. Hagihala, T. Kamiyama, S. Itoh, T. Nakajima
In-Plane Anisotropy of Single-q and Multiple-q Ordered Phases in the Antiferromagnetic Metal $CeRh_2Si_2$
Phys. Rev. B, **108** 094440 (2023).

199 T. U. Ito, W. Higemoto, K. Shimomura
Understanding Muon Diffusion in Perovskite Oxides below Room Temperature Based on Harmonic Transition State Theory
Phys. Rev. B, **108** 224301 (2023).

200 T. Okudaira, Y. Tani, S. Endo, J. Doskow, H. Fujioka, K. Hirota, K. Kameda, A. Kimura, M. Kitaguchi, M. Luxnat, K. Sakai, D. C. Schaper, T. Shima, H. M. Shimizu, W. M. Snow, S. Takada, T. Yamamoto, H. Yoshikawa, T. Yoshioka
Angular Distribution of γ Rays from a Neutron-Induced p-Wave Resonance of ^{132}Xe
Phys. Rev. C, **107** 054602 (2023).

201 S. Imajo, H. Akatsuka, K. Hatanaka, T. Higuchi, G. Ichikawa, S. Kawasaki, M. Kitaguchi, R. Mammei, R. Matsumiya, K. Mishima, R. Picker, W. Schreyer, H. M. Shimizu
Diffuse Scattering Model of Ultracold Neutrons on Wavy Surfaces
Phys. Rev. C, **108** 034605 (2023).

202 T. Okumura, T. Azuma, D. A. Bennett, I. Chiu, W. B. Doriese, M. S. Durkin, J. W. Fowler, J. D. Gard, T. Hashimoto, R. Hayakawa, G. C. Hilton, Y. Ichinohe, P. Indelicato, T. Isobe, S. Kanda, M. Katsuragawa, N. Kawamura, Y. Kino, K. Mine, Y. Miyake, K. M. Morgan, K. Ninomiya, H. Noda, G. C. O'Neil, S. Okada, K. Okutsu, N. Paul, C. D. Reintsema, D. R. Schmidt, K. Shimomura, P. Strasser, H. Suda, D. S. Swetz, T. Takahashi, S. Takeda, S. Takeshita, M. Tampo, H. Tatsuno, Y. Ueno, J. N. Ullom, S. Watanabe, S. Yamada
Proof-of-Principle Experiment for Testing Strong-Field Quantum Electrodynamics with Exotic Atoms: High Precision X-Ray Spectroscopy of Muonic Neon
Phys. Rev. Lett., **130** 173001 (2023).

203 W. G. F. Krüger, W. Chen, X. Jin, Y. Li, L. Janssen
Triple-q Order in $Na_2Co_2TeO_6$ from Proximity to Hidden-SU(2)-Symmetric Point
Phys. Rev. Lett., **131** 146702 (2023).

204 P. Strasser, S. Fukumura, R. Iwai, S. Kanda, S. Kawamura, M. Kitaguchi, S. Nishimura, S. Seo, H. M. Shimizu, K. Shimomura, H. Tada, H. A. Torii, MuSEUM Collaboration
Improved Measurements of Muonic Helium Ground-State Hyperfine Structure at a Near-Zero Magnetic Field
Phys. Rev. Lett., **131** 253003 (2023).

205 Q. Li, A. Ahadi, Y. Onuki, Q. Sun
Role of Thermal Expansion Anisotropy on the Elastocaloric Effect of Shape Memory Alloys with Slim-Hysteresis Superelasticity
Phys. Rev. Mater., **7** 013606 (2023).

206 K. Iwasa, K. Suyama, S. Ohira-Kawamura, K. Nakajima, S. Raymond, P. Steffens, A. Yamada, T. D. Matsuda, Y. Aoki, I. Kawasaki, S. Fujimori, H. Yamagami, M. Yokoyama
Weyl–Kondo Semimetal Behavior in the Chiral Structure Phase of $Ce_3Rh_4Sn_{13}$
Phys. Rev. Mater., **7** 014201 (2023).

207 S. Tanaka, R. Kiyanagi, Y. Ishikawa, Y. Amako, T. Iiyama, R. Futamura, K. Maruyama, S. Utsumi
Incommensurate Helimagnetic Structure of $Ba(Fe_{1-x}Sc_x)_{12}O_{19}$ Determined by Single-Crystal Neutron Diffraction
Phys. Rev. Mater., **7** 014403 (2023).

208 H. Yoshioka, Y. Aoki, K. Nonaka, N. L. Yamada, M. Kobayashi
Effect of Molecular Weight Distribution on the Thermal Adhesion of

Polystyrene and PMMA Brushes
Polymer, **264** 125561 (2023).

209 Z. Huang, Y. Bajaj, J.-M. Y. Carrillo, Y. Nakanishi, K. Uchida, K. Mita, T. Yamada, T. Miyazaki, B. G. Sumpter, M. Endoh, T. Koga
Local Conformations and Heterogeneities in Structures and Dynamics of Isotactic Polypropylene Adsorbed onto Carbon Fiber
Polymer, **265** 125584 (2023).

210 D. Kawaguchi
Aggregation States, Thermal Molecular Motion and Carrier Properties in Functional Polymer Thin Films
Polym. J., **55** 1237–1245 (2023).

211 T. Matsumoto, M. Yorifuji, R. Hori, M. Hara, N. L. Yamada, H. Seto, T. Nishino
Selective Acetylation of Amorphous Region of Poly (Vinyl Alcohol) in Supercritical Carbon Dioxide
Polym. J., **55** 1287–1293 (2023).

212 P. Goux, F. Glessgen, E. Gazzola, M. S. Reen, W. Focillon, M. Gonin, T. Tanaka, K. Hagiwara, A. Ali, T. Sudo, Y. Koshio, M. Sakuda, G. Collazuol, A. Kimura, S. Nakamura, N. Iwamoto, H. Harada, M. Wurm
Angular Correlation of the Two Gamma Rays Produced in the Thermal Neutron Capture on Gadolinium-155 and Gadolinium-157
Prog. Theor. Exp. Phys., **2023** 063H01 (2023).

213 M. Watanabe, T. Kihara, H. Nojiri
Automated Pulsed Magnet System for Neutron Diffraction Experiments at the Materials and Life Science Experimental Facility in J-PARC
Quantum Beam Sci., **7** 1 (2023).

214 S. Koizumi, Y. Noda, T. Inada, T. Maeda, S. Yada, T. Yoshimura, H. Shimosegawa, H. Fujita, M. Yamada, Y. Matsue
Microscopic Depictions of Vanishing Shampoo Foam Examined by Time-of-Flight Small-Angle Neutron Scattering
Quantum Beam Sci., **7** 4 (2023).

215 S. Harjo, W. Gong, T. Kawasaki
Stress Evaluation Method by Neutron Diffraction for HCP-Structured Magnesium Alloy
Quantum Beam Sci., **7** 32 (2023).

216 S. Machiya, K. Osamura, Y. Hishinuma, H. Taniguchi, S. Harjo, T. Kawasaki
Measurement of Mechanical Behavior of 11B-Enriched MgB_2 Wire Using a Pulsed Neutron Source
Quantum Beam Sci., **7** 34 (2023).

217 J. Abe, Y. Matsumoto, T. Miyazaki, T. Noma
A High-Temperature and High-Pressure Cell for In Situ Visualization of Reaction Processes by Neutron Imaging
Rev. Sci. Instrum., **94** 083904 (2023).

218 Y. Goto, M. Kikugawa, K. Kobayashi, Y. Manaka, T. Nanba, H. Matsumoto, M. Matsumoto, M. Aoki, H. Imagawa
Facile Formation of Barium Titanium Oxyhydride on a Titanium Hydride Surface as an Ammonia Synthesis Catalyst
RSC Adv., **13** 15410–15415 (2023).

219 E. Nakamura, H. Iwase, H. Arima-Osonoi, M. Sakuragi
Effect of Water Content on Stratum Corneum Penetration Mechanism of W/O Type Microemulsions
RSC Adv., **13** 17742–17749 (2023).

220 Y. Li, S. Song, H. Kim, K. Nomoto, H. Kim, X. Sun, S. Hori, K. Suzuki, N. Matsui, M. Hirayama, T. Mizoguchi, T. Saito, T. Kamiyama, R. Kanno
A Lithium Superionic Conductor for Millimeter-Thick Battery Electrode
Science, **381** 50–53 (2023).

221 Z. Jin, Y. Li, Z. Hu, B. Hu, Y. Liu, K. Iida, K. Kamazawa, M. B. Stone, A. I. Kolesnikov, D. L. Abernathy, X. Zhang, H. Chen, Y. Wang, C. Fang, B. Wu, I. A. Zaliznyak, J. M. Tranquada, Y. Li
Magnetic Molecular Orbitals in MnSi
Sci. Adv., **9** eadd5239 (2023).

222 H. Mamiya, Y. Oba, N. Terada, K. Hiroi, T. Ohkubo, T. Shinohara
Neutron Imaging for Magnetization inside an Operating Inductor
Sci. Rep., **13** 9184 (2023).

223 Y. Oba, R. Motokawa, K. Kaneko, T. Nagai, Y. Tsuchikawa, T. Shinohara, J. D. Parker, Y. Okamoto
Neutron Resonance Absorption Imaging of Simulated High-Level Radioactive Waste in Borosilicate Glass
Sci. Rep., **13** 10071 (2023).

224 T. Kozawa, M. Fujihala, T. Uchihara, S. Mitsuda, S. Yano, H. Tamatsukuri, K. Munakata, A. Nakao
Atomic Reconstruction Induced by Uniaxial Stress in MnP
Sci. Rep., **13** 13750 (2023).

225 N. Yamashita, T. Hirayama, M. Hino, N. L. Yamada
Neutron Reflectometry under High Shear in Narrow Gap for Tribology Study
Sci. Rep., **13** 18268 (2023).

226 H. Nozaki, H. Kondo, T. Shinohara, D. Setoyama, Y. Matsumoto, T. Sasaki, K. Isegawa, H. Hayashida
In Situ Neutron Imaging of Lithium-Ion Batteries during Heating to Thermal Runaway
Sci. Rep., **13** 22082 (2023).

227 X. Wen, L. Zhu, M. Naeem, H. Huang, S. Jiang, H. Wang, X. Liu, X. Zhang, X.-L. Wang, Y. Wu, Z. Lu
Strong Work-Hardenable Body-Centered-Cubic High-Entropy Alloys at Cryogenic Temperature
Scr. Mater., **231** 115434 (2023).

228 W. Mao, S. Gao, W. Gong, S. Harjo, T. Kawasaki, N. Tsuji
Quantitatively Evaluating the Huge Lüders Band Deformation in an Ultrafine Grain Stainless Steel by Combining In Situ Neutron Diffraction and Digital Image Correlation Analysis
Scr. Mater., **235** 115642 (2023).

229 H. Dannoshita, H. Hasegawa, S. Higuchi, H. Matsuda, W. Gong, T. Kawasaki, S. Harjo, O. Umezawa
Effects of Dislocation Arrangement and Character on the Work Hardening of Lath Martensitic Steels
Scr. Mater., **236** 115648 (2023).

230 K. Wu, E. Zhao, P. Ran, W. Yin, Z. Zhang, B. Wang, K. Ikeda, T. Otomo, X. Xiao, F. Wang, J. Zhao
Localizing Oxygen Lattice Evolutions Eliminates Oxygen Release and Voltage Decay in All-Mn-Based Li-Rich Cathodes
Small, **19** 2300419 (2023).

231 K. Aomura, Y. Yasuda, T. Yamada, T. Sakai, K. Mayumi
Quasi-Elastic Neutron Scattering Study on Dynamics of Polymer Gels with Controlled Inhomogeneity under Uniaxial Deformation
Soft Matter, **19** 147–152 (2023).

232 K. Shimokita, K. Yamamoto, N. Miyata, Y. Nakanishi, M. Shibata, M. Takenaka, N. L. Yamada, H. Seto, H. Aoki, T. Miyazaki
Neutron Reflectivity Study on the Nanostructure of PMMA Chains near Substrate Interfaces Based on Contrast Variation Accompanied with Small Molecule Sorption
Soft Matter, **19** 2082–2089 (2023).

233 T. Kimura, R. Izawa, C. Hotehama, K. Fujii, A. Sakuda, M. Yashima, M. Tatsumisago, A. Hayashi
Synthesis and Ionic Conductivity of an Argyrodite-Type Li_6SbS_5I Electrolyte

Solid State Ion., **399** 116287 (2023).

234 C. Micheau, Y. Ueda, K. Akutsu-Suyama, D. Bourgeois, R. Motokawa
Deuterated Malonamide Synthesis for Fundamental Research on Solvent Extraction Systems
Solvent Extr. Ion Exch., **41** 221–240 (2023).

235 Md. K. Rahman, T. Yamada, N. L. Yamada, M. Hishida, Y. Higuchi, H. Seto
Quasi-Elastic Neutron Scattering Reveals the Relationship between the Dynamical Behavior of Phospholipid Headgroups and Hydration Water
Struct. Dyn., **10** 044701 (2023).

236 H. Gu, T. Hirayama, N. Yamashita, T. Okano, J. Xu, N. Sato, M. Yamada
Tribological Performance of a Surfactant Derived from Its Structure of Molecular Aggregates in Water
Tribol. Int., **188** 108881 (2023).

Editorial Board - MLF Annual Report 2023

J-PARC

JAPAN PROTON ACCELERATOR RESEARCH COMPLEX

High Energy Accelerator Research Organization (KEK)
Japan Atomic Energy Agency (JAEA)

http://j-parc.jp/

Materials and Life Science Division
J-PARC Center

https://mlfinfo.jp/en

Comprehensive Research Organization for Science and Society
https://neutron.cross.or.jp/en

J-PARC 24-02